University of Bath

UNIVERSITY OF
BATH

**PHD**

**Composite photoanodes for artificial leaves**

Zhang, Jifang

*Award date:*
2019

*Awarding institution:*
University of Bath

[Link to publication](Link to publication)

**University of Bath**

**UNIVERSITY OF BATH**

**PHD**

**Composite photoanodes for artificial leaves**

Zhang, Jifang

*Award date:*
2019

*Awarding institution:*
University of Bath

[Link to publication](Link to publication)

# COMPOSITE PHOTOANODES FOR ARTIFICIAL LEAVES

Jifang Zhang

A thesis submitted for the degree of Doctor of Philosophy

University of Bath

Department of Chemical Engineering

December 2018

**COPYRIGHT NOTICE**

**RESTRICTION ON THE USE AND LICENSING**

**DECLARATION OF AUTHORSHIP**

I am the author of this thesis, and the work described therein was carried out by myself personally. Contribution from other researchers in each individual work is detailed in "Declaration of Authorship" sections.

Candidate's signature

# Abstract

The quest for clean and sustainable energy has been ongoing since we realize that fossil fuels will be depleted in future generations due to our ever-increasing demand for energy, while causing serious environmental problems. A major branch of tackling this problem is developing the usage of sunlight, which is easily accessible and vastly abundant. Converting solar energy into clean fuels (e.g. hydrogen), mimicking natural photosynthesis, is an elegant way that illustrates how research can be inspired by nature. Such conversion can be done in a photoelectrochemical (PEC) cell, which is a device that can carry out solar water splitting to produce hydrogen and oxygen in two separate electrodes. The oxygen evolution, taking place on the photoanode electrode, is much more kinetically demanding than the hydrogen evolution. As such, there has been extensive research for efficient and stable photoanodes since the first report on $TiO_2$. Tungsten trioxide ($WO_3$) and hematite ($\alpha$-$Fe_2O_3$) are two of the most stable candidates whose band gaps can be overcome with visible light.

In this PhD thesis, Chapter 1 introduces the background and motivation of photoelectrochemical water splitting. Chapter 2 and 3 illustrate the concepts and methodologies to evaluate and understand the effectiveness of photoelectrodes. Chapter 4 includes a comprehensive literature survey of hematite as photoanode material. It is selected as an example to reveal the roles of crystal defects in regard to both bulk and surface properties combining a wide range of research focuses. One type of surface states is identified by examination of experimental results and theoretical predictions over the years. Chapter 5 provides a more in-depth study of the impact of overlayers on hematite photoanodes. Two types of overlayers are investigated here: first, an intrinsically grown amorphous iron oxide layer ($FeO_x$) that is introduced by addition of lactic acid in the precursor formation step; second, one of the most efficient transition metal (oxy)hydroxide oxygen evolution catalyst, $CoFeO_x$ coated by electrodeposition. The electrodes are examined using multiple PEC techniques, including PEC impedance spectroscopy, transient photocurrent spectroscopy and intensity modulated photocurrent spectroscopy. Chapter 6 explores a simple way of fabricating nanostructured $WO_3$ photoanodes. We studied the oxide growth in the process of anodization in citric acid

solution, along with the influence of morphology on photoactivity. Finally, Chapter 7 concludes this PhD work and gives perspectives for future research.

# Acknowledgement

First and foremost, my main supervisor Dr. Salvador Eslava is greatly acknowledged for every bit of support and advice he gave me through the three years. His dedication and patience for research has always inspired me. He is also a successful group leader that cares about every member in our group, not to mention our lab equipment! I am also very thankful to my two other supervisors, Prof. Davide Mattia and Dr. Petra Cameron for their help on my experiments and publications. I also appreciate the occasional but fruitful conversations with Prof. Frank Marken and Prof. Laurie Peter of Department of Chemistry. Many thanks to the Eslava group members who have always been very nice to me and willing to help me.

The technicians of microscopy and analysis suite in our university (Mrs. Ursula Potter, Dr Philip Fletcher and Ms. Diana Lednitzky) are always very helpful whenever I need them. Dr David Morgan from Cardiff University should be notably thanked not only for his exceptional XPS analysis skills that impressed me but more because of the level of support. The writing center and career service of our university are also acknowledged for their professional service that indeed has made a difference.

I would also like to thank my family and best friends who have been an equally important part of my PhD life and prevented me from being a science geek!

# Publication List

- Zhang, J., Eslava, S., Understanding charge transfer, defects and surface states at hematite photoanodes, Under peer review

- Zhang, J., García-Rodríguez, R., Cameron, P. J., Eslava, S., Role of Cobalt−Iron (Oxy)Hydroxide ($CoFeO_x$) as Oxygen Evolution Catalyst on Hematite Photoanodes, Energy & Environmental Science, 2018, 11, 2972-2984

- Park, M. S., Walsh, D., Zhang, J., Kim J. H., Eslava, S., 2018, Efficient hematite photoanodes prepared by hydrochloric acid-treated solutions with amphiphilic graft copolymer, Journal of Power Source, 2018, 404, 149-158

- Walsh, D., Zhang, J., Dassanayake, R., Regue, M., and Eslava, S., Simultaneous Formation of FeOx Electrocatalyst Coating within Hematite Photoanodes for Solar Water Splitting, ACS Applied Energy Materials, 2019, 2, 2043−2052

- Zhang, J., Salles, I., Pering, S., Cameron, P. J., Mattia, D. and Eslava, S., Nanostructured $WO_3$ photoanodes for efficient water splitting via anodization in citric acid. RSC Advances, 2017, 7(56), 35221-35227.

- Hammond, O. S., Eslava, S., Smith, A. J., Zhang, J., and Edler, K. J., Microwave-assisted deep eutectic-solvothermal preparation of iron oxide nanoparticles for photoelectrochemical solar water splitting. Journal of Materials Chemistry A, 2017, 5(31), 16189-16199.

# Table of Contents

# Chapter 1 Introduction

## 1.1 Resources of Sustainable Energies

The reliance on fossil fuels for energy has lasted for over two centuries. More than 80% of the world's total energy consumption comes from burning fossil fuels.[1] As climate issues, especially global warming, exacerbate over the years, it has become critical that clean and sustainable energy sources must be developed. A handful of options are available including wind, biomass, geothermal, nuclear and solar energies, all abundant and therefore with potential to meet global energy demand. Among these options, solar energy technology has been advancing at an unprecedented pace, offering suitable solutions for both small and large-scale power generation systems.

There are two main ways to make solar energy usable. First, using photovoltaic systems that convert sunlight directly into electricity and feed it into the power grid. However, the intermittency of sunlight requires vast quantities of batteries, which is not a realistic option for the gigawatts or terawatts scale needed to tackle energy problems globally. The second option is to produce solar fuels such as hydrogen and hydrocarbons. These fuels not only possess higher power density but can be transported more easily compared to batteries. For example, the mass density of hydrogen is about 180 higher than the best batteries.[2,3] The relationship between solar energy, electricity and hydrogen is demonstrated in Fig. 1-1.
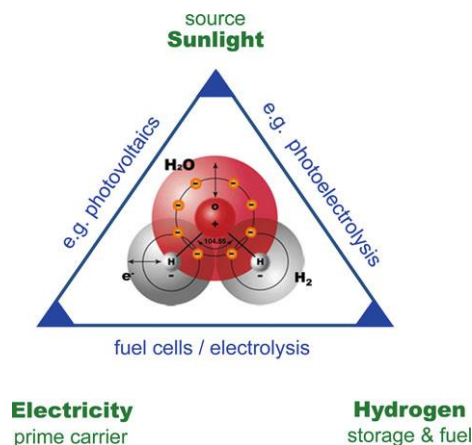


Fig. 1-1 Relation between three main types of energy sources and their conversion.[4] Reprinted by permission from Springer Nature: Springer, Photoelectrochemical Hydrogen Production by Roel van de Krol and Michael Grätzel, COPYRIGHT 2012.

Some debate has been raised over which is the most desirable chemical compound to store renewable energy sources, hydrogen ($H_2$) or carbon-based compounds including methane ($CH_4$), methanol ($CH_3OH$), formic acid (HCOOH) and carbon monoxide (CO).[5,6] The motivation to use these carbon-based compounds are two-fold. First, they can be used as feedstocks to produce other chemicals.[6] Second, they can be combusted as fuels. The latter is not an ideal route because to close the carbon cycle, $CO_2$ needs to be captured, but carbon capture efficiency currently is far from ideal.[7] Therefore, a fair amount of carbon footprint will be generated by each cycle. Hydrogen, in contrast, is an advantageous candidate mainly because water is the only by-product. 96% of hydrogen is currently made via a high carbon footprint method called steam reforming (13.7 kg $CO_2$ emitted for 1 kg $H_2$), so replacing its production with a clean approach would be significant to reduce $CO_2$ emissions worldwide.[8,9] However, using hydrogen is not straightforward. Its low volumetric energy density renders hydrogen storage and distribution problematic. The traditional way of compressing it into a high-pressure cylinder requires extra energy for the compression and poses safety issues. To solve this problem, a variety of classes of materials for $H_2$ storage are currently being developed, such as activated carbon and promising metal organic frameworks .[10]

## 1.2 Solar Hydrogen Production

Solar hydrogen production can be realized via (a) photovoltaic modules in combination with electrolyzers (PV+E), (b) photoelectrochemical cells (PEC), and (c) photocatalysts. Each of them has a set of pros and cons.

The most technologically feasible method is PV+E.[11] Its advantage is the compatibility with the existing infrastructure since photovoltaics and electrolysis have both been industrialized. Reasonable efficiencies can be achieved as a result of available 20%-efficiency PV cells and 70%-efficiency electrolyzers. Additionally, it has a high degree of freedom, i.e., operating conditions for modules can be individually tuned. The levelized cost of hydrogen when shining concentrated sunlight is halved to \$6.1 kg$^{-1}$ from \$12.1 kg$^{-1}$ at 1 sun illumination assuming 10% $\eta_{STH}$.[12] In laboratory, a recent work has demonstrated a record-high solar-to-hydrogen efficiency of over 30% that is stable for 48 h, although an irradiation intensity of 42 suns is required for two electrolyzers to reach the desired maximum power-point.[13] To our knowledge, the highest solar-to-hydrogen efficiency achieved is 19% without

concentrated sunlight. There are a few setbacks too, the major one being elevated balance-of-system costs. For example, more than one PV module is possibly required for electrolyzers to be operating optimally. Expensive electrolyzers are another factor that prevents reduction in costs. At present, iridium compounds are the only known acid-stable oxygen evolution catalysts; but Ir is unfortunately the least abundant element in the Earth's crust.[14]

Another promising method is PEC water splitting. The setup is simpler compared to PV+E and usually operates at atmospheric pressure and room temperature. Since PEC cell combines both processes of electricity conversion and gas evolution into a single device, it entails less balance-of-systems costs as described above.[12] In addition, most electrode materials studied are elementally earth abundant and non-toxic. The levelized cost of hydrogen (at 10% $\eta_{STH}$) is slightly lower than PV+E at \$11.4 kg$^{-1}$ under standard illumination.[12] As for the record $\eta_{STH}$ of PEC devices under standard illumination, it remains at 12.4% but with poor stability.[15]

The less developed system for solar $H_2$ production is particulate photocatalysis. Although the estimated cost is lower than PV+E and PEC, there are more associated technological and market risks. The outstanding problem with photocatalysis is the mixture of $H_2$ and $O_2$ gases that will involve safety issues as well as costs for separation potential. Solar thermolysis and thermochemical hydrogen production are two other options that have been studied.[11] Due to the high temperatures required and complicated process design, they are less investigated. These methods fall out of the scope of this thesis.

In short, PV+E and PEC are in my opinion the most promising ways for solar fuels production. It should be noted that solar water splitting is not always strictly designed in these two types. PV+PEC and PEC+E are also readily found in the literature. Since PEC and PV materials are technically interchangeable, there is not a clear distinction between PV+E and PEC+E. Therefore, for unambiguous classification, we define PEC water splitting devices to possess at least one semiconductor-liquid junction in this thesis.

The combination of PV and PEC cells have been often reported to have $\eta_{STH}$ around 10%.[16] In order to boost this number, Rothschild and Dotan evaluated PEC+PV and PV+E using a hematite photoanode in their setup.[17] The authors first pointed out that

due to the late onset potential of photoanodes, PV units can be connected in series to multiply the output voltage for a better match with PEC material. Despite this, the low photocurrent density by hematite greatly limits the operating power output if a PV cell is to provide the applied bias potential. The difference in power output at this operating condition and maximum power-point is called coupling loss (Fig. 1-2a). By adding an external ohmic load, which could be peripheral system components, the device can operates at minimal point, thus making use of coupling loss (Fig. 1-2b).[17] But before diving into engineering approaches, optimizing the performance of PEC devices are of priority, which is the focus of following chapters.
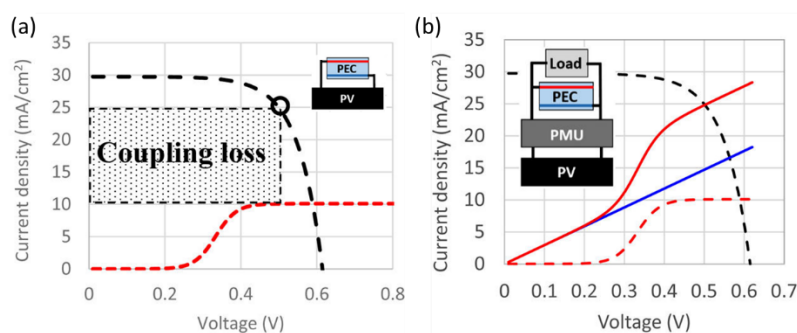


Fig. 1-2 (a) The J−V curves for a Si PV back cell (black dashed) and an ideal PEC front cell (red dashed). The black circle marks the maximum power point of the PV cell, and the dotted rectangle represents the energy loss due to non-ideal coupling. (b) Device J-V curves for the circuit shown in the inset. The blue line represents the resistance of an ohmic load connected in parallel to the PEC cell. In the device shown in insets, PV unit is the main power supply for PEC cell, peripheral load, and power management unit (PMU). Reprinted with permission from ref. [17]. Copyright 2017 American Chemical Society.

# Chapter 2 Photoelectrochemical Cells

## 2.1 Configuration

The main components of PEC cells are the (photo)anode, (photo)cathode, electrolyte solution and external electrical connection. The photocathode carries out the reduction reaction such as the hydrogen evolution reaction and the photoanode electrode the oxidation reaction such as the oxygen evolution reaction. Hydrogen is produced through:

$$2H^+ + 2e^- \rightarrow H_2 \text{ (low pH)} \qquad \text{Eq. 2-1}$$

$$2H_2O + 2e^- \rightarrow H_2 + 2OH^- \text{ (high pH)} \qquad \text{Eq. 2-2}$$

Oxygen is produced through:

$$2H_2O + 4h^+ \rightarrow O_2 + 4H^+ \text{ (low pH)} \qquad \text{Eq. 2-3}$$

$$4OH^- + 4h^+ \rightarrow O_2 + 2H_2O \text{ (high pH)} \qquad \text{Eq. 2-4}$$

The overall water splitting reaction is

$$2H_2O \rightarrow 2H_2 + O_2 \quad \Delta G = 237 \text{ kJ mol}^{-1} \qquad \text{Eq. 2-5}$$
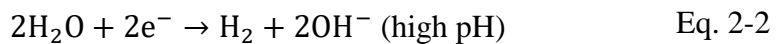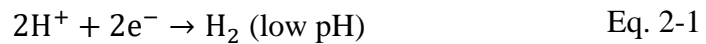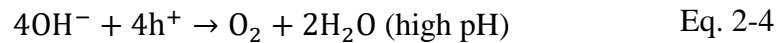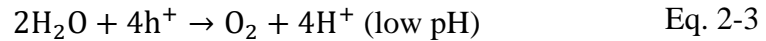
PEC cells can be configured in several ways assisted or unassisted by external voltages. In an assisted cell, the external bias is expected to be provided by a PV unit, a power supply, or a potentiostat. Taking a photoanode as the working electrode (WE), holes are generated in the valence band of n-type semiconductors to oxidize water. However, the electrons excited to the conduction band may not have enough energy to reduce water into hydrogen, so a bias voltage is typically applied. A reference electrode (RE) is used to accurately control the bulk Fermi level of the semiconductor for diagnostic purposes in PEC measurements, while establishing a three-electrode system. The potential difference between WE and RE is accurately monitored by a potentiostat. The aim of this auxiliary electrode is to avoid the influence of polarization potential drop at the counter electrode (CE). A typical three electrode system is displayed in Fig. 2-1.
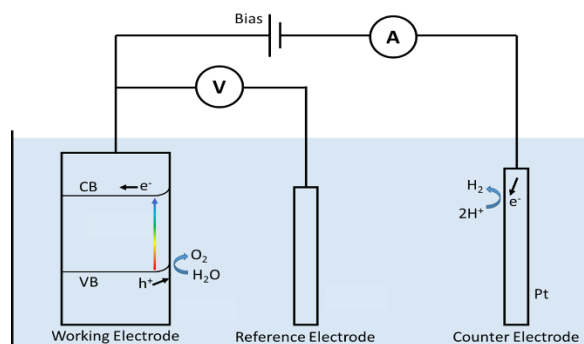
Fig. 2-1 Illustration of a typical three-electrode PEC cell, where the semiconductor is the photoanode and Pt is the counter electrode.

An unassisted PEC cell can be assembled by coupling a photoanode and a photocathode without any bias. It is often referred to as D4 system, meaning four photons absorbed by two photosystems (semiconductors) for one molecule of $H_2$.[18] In a D4 system, electrons excited into the conduction band (CB) of the photoanode recombine with holes left in the valence band (VB) of the photocathode, while holes in the VB of the photoanode can carry out OER and electrons in the CB of the photocathode can carry out HER. In such case, the quantum yield is halved compared to a two-photon single photosystem (S2).[18] The two semiconductors can be either stacked or arranged side-by-side. The STH efficiency of the latter will be halved again because of twice the illumination area. If stacked, the band gap of top irradiated semiconductor should be large enough to allow lower energy photons to reach the bottom semiconductor.

## 2.2 Steps of PEC Water Splitting

A PEC cell usually consists of one WE (although two WE devices have been reported too[19]), which are usually n-type and p-type for the photoanode and photocathode, respectively. A counter electrode is used for the other half reaction. The process of water splitting taking place at the electrodes of a PEC cell involves three steps: excitation, diffusion and reaction. First, the semiconductor absorbs a photon, followed by an electron being excited from VB to CB. The excited electron first relaxes to the CB edge (sub-picoseconds scale).[20,21] This photo-generated electron-hole pair can then recombine at sub-microsecond scale.[22] For the holes that do not recombine, they must live long enough to diffuse to the semiconductor-liquid junction (SCLJ) before oxidizing water. This diffusion length is usually characteristic of a

material, which varies from a few nanometers to micrometers, depending on the charge lifetime and mobility.[23,24] The diffusion length can be calculated by Eq. 2-6.[25]

$$L_D = \sqrt{D\tau} \qquad \text{Eq. 2-6}$$

$$D = \frac{\mu k_B T}{q} \qquad \text{Eq. 2-7}$$

In these equations, $L_D$ is the diffusion length, $\tau$ is the charge lifetime and $D$ is the diffusion coefficient, which correlates to the minority-carrier mobility ($m^2$ $V^{-1}$ $s^{-1}$). Boltzmann constant, temperature and elementary charge are $k_B$, $T$ and $q$, respectively.

The distance that a charge that can be collected and travel to SCLJ is extended by the existence of band bending, in which the electric field formed can considerably assist the migration to the surface. In the estimation of maximal photocurrent to be obtained from a certain irradiation, recombination at space charge region is often omitted, as described in the Gärtner model.[26] However, this condition might not apply either at a relatively low potential due to light induced Fermi level pinning or at very fine structures (e.g. nanoparticles) where band bending cannot fully develop.[27] More explanation is provided later in Chapter 3.

The last step is the reaction between charges and water molecules. The thermodynamic energy requirement for water splitting is 237 kJ mol^{-1} as shown in Fig. 3-2, which correlates to a band gap ($E_g$) minimum of 1.23 eV for the semiconductor. Moreover, the CB and VB edges of a semiconductor must straddle the energy levels (standard reaction potentials) for hydrogen and oxygen evolution from water. In addition, it must overcome overpotentials of the reactions and thus a much higher $E_g$ is needed, meaning significantly less light from the wide solar spectrum can be utilized. According to simulations, the maximal power conversion efficiencies for a dual band-gap PEC (D4) cell is indeed higher than a single band-gap one.[18] As such, single semiconductor PEC cells that could realize both oxidation and reduction of water are not actively pursued in recent years. Instead, studies of individual photoanode/photocathode or the construction of tandem cells have been the major targets.

## 2.3 Figures of Merit

According to description in Section 2.2, water splitting takes place in multiple stages, each giving an efficiency:

$$\eta_{overall} = \eta_{abs} \times \eta_{sep} \times \eta_{ct} \times \eta_F \qquad \text{Eq. 2-8}$$

First, the fraction of effective light absorption is given by $\eta_{abs}$, which can be limiting when the absorption coefficient is low and film thickness is low too. For example, p-GaP is known to have a light penetration depth (ca. 0.3 μm at 442 nm) shorter than the diffusion length of minority carriers (ca. 8 μm).[28] Therefore, all charges can be collected given an appropriate film thickness. Second, when electron-hole pairs are generated after absorption, the probability of charge carriers undergoing bulk recombination is represented by $\eta_{sep}$. For a material with very small minority-carrier diffusion length, $\eta_{sep}$ can severely restrict photocurrent. Thirdly, for the long-lived holes that arrive at electrode surface, the probability for them to successfully undergo charge transfer is $\eta_{ct}$. Finally, the fraction of photocurrent that conducts OER is indicated by Faradaic efficiency, $\eta_F$.

Common efficiencies to reflect the performance of a photoelectrode can be usually seen as individual efficiencies selectively grouped together. Some of them are for benchmarking purposes and others for diagnostic purposes. Solar-to-hydrogen conversion efficiency ($\eta_{STH}$), being the most important benchmark number for overall water splitting devices, is equivalent to $\eta_{overall}$, and is calculated by the energy of hydrogen produced against the power input of the irradiation, as shown in Eq. 2-9.[29]

$$\eta_{STH} = \left[ \frac{(G \text{ mmol H}_2 \text{ s}^{-1}) \times (237{,}000 \text{ J mol}^{-1})}{P_{\text{total}}(\text{mW cm}^{-2}) \times Area \text{ (cm}^{-2})} \right]_{\text{AM1.5G}} \qquad \text{Eq. 2-9}$$

The $\eta_{STH}$ should be measured by recording the $H_2$ gas evolution rate $G$ under 1-sun simulation (AM 1.5G, $P_{\text{total}}$ =100 mW cm$^{-2}$) in a two-electrode setup. In a $\eta_{STH}$ measurement, no difference in pH should be present between the electrolyte environments at the two electrodes, to avoid an extra chemical potential drop.[29] In addition, $\eta_{STH}$ is only valid when $H_2$ and $O_2$ are produced stoichiometrically, suggesting no side reactions.

Photocurrent density is conventionally used as a benchmarking number for a certain electrode. For photoanodes, the photocurrent is usually taken and compared at 1.23 V$_{\text{RHE}}$, because beyond this point, external voltage is likely to initiate electrocatalytic water oxidation, and contribution from photocurrent may not be

precisely distinguished. Likewise, 0 $V_{RHE}$ is often adopted to compare photocathodes. Irradiation standard for photocurrent is the same with the measurement of $\eta_{STH}$. Photocurrent density is sometimes recorded applying a low wavelength cut-off filter for diagnostic purposes.[30] When Faradaic efficiency is known, $\eta_{STH}$ can be expressed as a function of photocurrent density

$$\eta_{STH} = \left[ \frac{\left| J_{ph}(\text{mA cm}^{-2}) \right| \times 1.23 \text{ V} \times \eta_F}{P_{total}(\text{mW cm}^{-2})} \right]_{\text{AM1.5G}} \qquad \text{Eq. 2-10}$$

For a PEC cell assisted by an external bias, the efficiency can be calculated after removing the bias from 1.23 V, resulting in an applied bias photon-to-current efficiency (ABPE).[29]

$$ABPE = \left[ \frac{\left| J_{ph}(\text{mA cm}^{-2}) \right| \times (1.23 - |V_b|) \times \eta_F}{P_{total}(\text{mW cm}^{-2})} \right]_{\text{AM1.5G}} \qquad \text{Eq. 2-11}$$

To be strict, ABPE should be measured with two electrodes for a characterization of a standalone water splitting device. A three-electrode setup results in interface measurement rather than a device measurement. Nevertheless, it is good approximation when potential drop at cathode is small and has been widely used in the literature.

The incident photon-to-current efficiency (IPCE), or external quantum efficiency (EQE) can be calculated by

$$IPCE = \frac{J_{ph}(\text{mA cm}^{-2}) \times 1239.8 \text{ (V nm)}}{P_{total}(\text{mW cm}^{-2}) \times \lambda \text{ (nm)}} \qquad \text{Eq. 2-12}$$

When $\eta_{abs}$ is discounted from IPCE, we have absorbed photon-to-current efficiency (APCE), or internal quantum efficiency (IQE), which is more characteristic of charge transport and charge transfer properties.

$$APCE = \frac{IPCE}{\eta_{abs}} \qquad \text{Eq. 2-13}$$

Both IPCE and APCE are very useful diagnostic parameters. For example, they contain information about charge collection in varied electrode microscopic structures (e.g., planar vs. nanoporous).[31,32] These two numbers do not include faradaic efficiency since current generation is the final step of interest rather than gas production.

It is noteworthy that there are other potential factors limiting power conversion efficiencies. In hematite, for example, onsite single and pair ligand field transitions do not generate electron-hole pairs.[33] Consequently, IPCE profile would not match absorption profile (Fig. 2-2). To my knowledge, this issue is unfortunately often overlooked and there is currently no tactics against these unhelpful transitions in the literature.
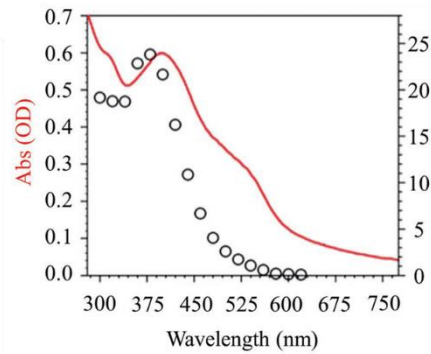


Fig. 2-2 UV–vis absorption spectrum (red line) and IPCE (black open circles, measured at 1.43 $V_{RHE}$) of a hematite thin film. Reprinted by permission of John Wiley & Sons, Inc. from ref. [33].

Although a higher photocurrent is always pursued for any photoelectrode, it does not reflect the effectiveness of the electrode unless the band gap of the material is taken into consideration. In other words, a semiconductor with lower a band gap can in theory produce more photocurrent. Therefore, the relative efficiency of a photoanode can be evaluated by the ratio of measured photocurrent density to its theoretical maximum (e.g., at 1.23 $V_{RHE}$), which is directly converted from solar power without assuming any losses. The conversion is performed by Eq. 2-14 and plotted in Fig. 2-3 showing integrated theoretical photocurrent density alongside solar irradiance spectrum (AM1.5G) as a function of photon energy.

$$J_{max} = \frac{\int P_{AM1.5G}(\lambda)\mathrm{d}\lambda}{E} \qquad \text{Eq. 2-14}$$
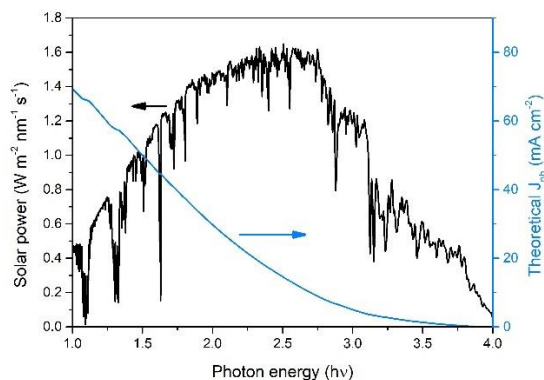
Fig. 2-3 Solar irradiance spectrum (black) and theoretical maximum photocurrent at 1.23 $V_{RHE}$ (blue) as a function of photon energy.

For example, hematite has a band gap of 2 eV while $WO_3$ 2.7 eV, which correspond to ca. 30 and 10 mA cm$^{-2}$, respectively. If both electrodes have the same photocurrent density, the relative efficiencies would be three times superior for $WO_3$.

## 2.4 Requirements and Challenges

There are several requirements for a PEC material to be industrially viable, which are directly associated with each step. The first selection rule is a relatively small band gap to absorb more visible light. As the first reported PEC material in 1972, $TiO_2$ has an $E_g$ of ca. 3.0 eV so that only the UV region of the solar spectrum can be used, which takes up 4% of sunlight.[34] Despite extensive effort to reduce the band gap of $TiO_2$ by dopant inclusion, it still remains a major problem.[35,36] Some semiconductors, including $TiO_2$, have a direct band gap as opposed to an indirect type. An indirect band gap is less desirable since it requires coupling with a phonon to absorb a photon, usually giving lower absorption coefficients ($\alpha$). In the case of hematite that has an indirect band gap, its poor $\alpha$ means it needs an absorption depth of several hundreds of nanometers, which mismatches the diffusion lengths of a few nanometers as well as the space charge width.[37] Doping of Sn was sometimes regarded as improving the absorption of hematite,[38,39] but sometimes the opposite was observed or no changes at all.[40,41] Therefore, systematic studies on techniques to enhance absorption capability are required.

Rapid recombination of photogenerated charges is a major cause for limited activity. Efforts have been spent on reducing recombination by improving conductivity as well as band engineering. For bulk doping, aliovalent dopants are known to increase donor

or lower acceptor level, enhancing the conductivity thus the average charge lifetime.[42] Creating homo- or heterojunctions where electrons flow to one end and holes to the other end has proved to be effective.[43,44] Surface recombination can also be treated with band engineering such as manipulating piezoelectric and ferroelectric effects.[45,46] Surface recombination can also be greatly reduced by accelerating the catalysis kinetics, which is further discussed below and later sections.

Optimization of surface reaction kinetics not only involves lowering overpotential but also retarding charge accumulation and subsequent recombination. It has been found that band bending in space charge region can thus be better developed and more bulk charges can migrate to the surface via the strong gradient of the electric field. [47] For instance, silicon has been studied as a photocathode, but it does not possess fast water reduction kinetics at SCLJ. A common solution is to coat a thin layer of electrocatalyst.[48] Although improvements in photocurrent density are often reported with such coatings, the interaction between the semiconductor and the catalyst is not yet well understood.

In addition to attempts to increasing the device efficiencies, there are other factors to make PEC systems competitive. The first concern is stability. A number of materials including $Cu_2O$, Si and group III-V compounds have been reported to have high theoretical maximum photocurrent densities but poor stability in the meantime.[49,50] A uniform protecting layer can be achieved by vacuum deposition methods whereas more difficult by wet chemistry methods.

Elemental abundancy should be taken into consideration if PEC systems are to be used in large scale. In this respect, first row transition metals are desirable candidates to select from. Likewise, the photoelectrode fabrication methods should be simple and less energy consuming. Vacuum deposition methods such as chemical vapour deposition (CVD) and atomic layer deposition (ALD) can produce high quality and reproducible results but requires complicated setups.[51] Last but not least, highly toxic materials should be avoided for safety reasons.

## 2.5 Electrode Materials

### 2.5.1 Photocathode

Research on p-Si has been continuing for decades and still remains an active topic.[52–54] It has a small band gap of 1.12 eV and very negative CB edge. In spite of strong light absorption, the performance of Si electrodes can be further enhanced by morphological control. Wire arrays fabricated by electroless etching were found to considerably suppress reflectance and improve photocurrent.[48] Another issue with p-Si is photocorrosion that transform Si into Si ions. When Si(0) is oxidized to Si(I) by photogenerated holes, further oxidation can also take place by spontaneous ejection of electrons to form higher oxidation states. This phenomenon is known as photocurrent multiplication and has been carefully studied with intensity modulated photocurrent spectroscopy in $NH_4F$ electrolyte.[55,56] The stability issue can be addressed by depositing a protection layer, such as $TiO_2$ and $Al_2O_3$ via ALD.[57] The latter has been frequently used for protection layers both in photocathodes and photoanodes as the deposition can be extremely thin and uniform. Since p-Si and these protection layers do not possess efficient HER kinetics, the presence of an electrocatalyst is necessary. For example, Pt and NiMoZn, have been found exceptionally effective.[48,54] In addition, one must be aware of the stringent conditions to make high quality p-Si, which raises fabrication expenses.

In the history of solar water splitting research, III-V semiconductors frequently set the records. Traditional examples such as GaP and InP have shown unique advantages, but each possesses its own drawbacks. InP has a small and direct band gap (1.35 eV) but indium is a scarce element.[25] If Ga and In are mixed in combination with phosphorous or arsenic as anions, record-setting devices are more likely to be produced, as evidenced by reports throughout the years. Efficiencies above 10% and up to 30% have been achieved, many of which have demonstrated stability for tens of hours.[13,15,58,59]

Chalcogenides are another class of low band gap semiconductors which have been heavily investigated as photocathodes. Some photovoltaic materials have been attempted at PEC water splitting, including CdTe, $CuIn_{1-x}Ga_xSe_2$ (CIGS), $Cu_2ZnSn(S,Se)_4$ (CZTS). The state-of-the-art photocurrent densities of these materials have frequently exceeded 15 mA $cm^{-2}$.[60,61] For CIGS and CZTS, band gaps can be controlled by modifying the anionic composition of the multinary chalcogenides. Before practical application, their poor stability must first addressed.

Copper oxides ($Cu_2O$ and $CuO$) have demonstrated great potential for high photocurrent densities. For $Cu_2O$, in particular, the chemical integrity is readily affected by a number of factors. According to $Cu$-$H_2O$ Pourbaix diagram (Fig. 2-4), $Cu_2O$ could only exist at pH between 5 and 14. In addition, it only exists in a relatively short potential window due to either reduction or oxidation:
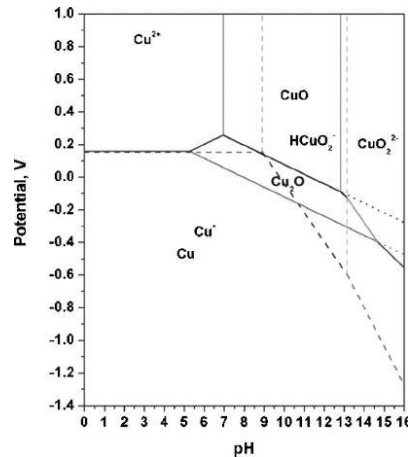


Fig. 2-4 Pourbaix diagram of copper in $Cu$-$H_2O$ system at 25 °C.[62] Reproduced with permission from J. Electrochem. Soc., 153(7), G617 (2006). Copyright 2006, The Electrochemical Society.

$$Cu_2O + H_2O + 2e^- = 2Cu + 2OH^- \qquad \text{Eq. 2-15}$$

$$Cu_2O + 2OH^- = 2CuO + H_2O + 2e^- \qquad \text{Eq. 2-16}$$
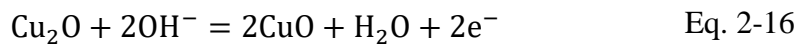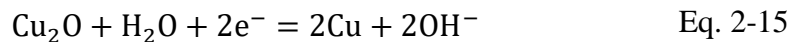
Note that under illumination both excited electrons and holes have enough energy to reduce and oxidize $Cu_2O$ if it is in contact with electrolyte, thereby speeding up the degradation. Carefully designed protection layers coupled with charge transport layers extended the lifetime of $Cu_2O$ but it still remains challenging.[63] Additionally, the electrical conductivity of $Cu_2O$ is limited.[25] $CuO$ has a lower band gap in the range of 0.7-1.6 eV with high absorption coefficient and is more stable compared with $Cu_2O$, but its photocurrent density is severely limited by charge recombination.[64] For $Cu_2O$ and $CuO$, photocurrent densities are much lower than complex chalcogenides, giving only about 7 mA cm$^{-2}$ at best with protection measures.[65,66]

## 2.5.2 Photoanode

Since photoanodes operate at a more oxidizing condition, many photoresponsive materials suitable for photocathode cannot function as photoanodes. The research started from binary oxides such as $TiO_2$ and $WO_3$,[34,67] which are decided to be uneconomical candidates considering their realistic maximal STH efficiency

achievable. The band gap of hematite is lower (~2 eV), but it has some major disadvantages, which will be the focus of Chapter 4 and Chapter 5.

Some multinary oxides have been introduced for similar reasons, such as $BiVO_4$ and spinel compounds. The CB and VB edge of $BiVO_4$ consist of V 3d orbitals, and the hybridization of Bi 6s and O 2p orbitals, respectively.[68] $BiVO_4$ has a higher band gap than $Fe_2O_3$ but has longer charge diffusion length (70 nm) due to its long lifetime.[69] When aligned along (001) facet, 16 times higher photocurrent density can be extracted than randomly orientated structure.[70] Like hematite, $BiVO_4$ also has poor surface OER kinetics, making the addition of co-catalysts highly beneficial.[71,72] Multi-layered electrocatalysts of FeOOH/NiOOH/Co-(bpy-P)$_2$ were found not only to reduce the onset potential by 0.3 V but also to more than double the plateau photocurrent.[73]

Spinel ferrites $MFe_2O_4$ (e.g., M = Cu, Mg, Zn) are an emerging class of metal oxide photoanodes with remarkable thermal and chemical stability as well as tunable band gaps. An early work by Sivula group reported three types of spinel ferrites with photocurrent densities all smaller than 1 mA cm$^{-2}$.[74] Rapid-scan voltammetry found the presence of surface states, which caused prominent Fermi level pinning and limited photovoltages to 0.1-0.2 V. The same group later changed film annealing temperature of $ZnFe_2O_4$ and thus largely removed these surface states.[75] As a result, charge injection (charge transfer) efficiency improved considerably. Such removal of surface states by high temperature annealing has also been observed in the case of hematite.[76] However, for spinel ferrites, high temperature (especially at 800 °C) caused undesirable drops in charge separation efficiency as it increases crystallinity and lowered spinel inversion degree.[75]

Another novel multinary metal oxide for photoanodes is $Fe_2TiO_5$. The research originates from Ti doping at $Fe_2O_3$ that improves conductivity, thereby charge separation efficiency.[77] Stoichiometric $Fe_2TiO_5$, compared with hematite, has a similarly low band gap but higher conductivity.[78] However, its performance is rather low when operating independently. Coupling with hematite has produced near 2 mA cm$^{-2}$ and higher if co-catalysts are added.[77] In addition, a more promising combination is attained when $Fe_2TiO_5$ is deposited onto $TiO_2$ nanotubes.[79] The photocurrent curve maintained the onset potential for $TiO_2$ along with overall enhancement. Moreover, a

surprisingly high fill factor is obtained after a simple electrodeposition step for a cobalt based electrocatalyst.

Non-oxide metal photoanodes are relatively scarcer. A promising example is $Ta_3N_5$ (with a direct band gap of 2.1 eV) but like many other non-oxide semiconductors, it shows poor stability.[80] Good understanding of $Ta_3N_5$ electrodes have been recently acquired, with the record photocurrent density (12.1 mA cm$^{-2}$) approaching the theoretical maximum (12.9 mA cm$^{-2}$).[81] It was found that a 3 nm surface oxide layer lead to total Fermi level pinning. This layer can be largely avoided by coating $Co(OH)_2$ because of the establishment of interactions between $Ta_3N_5$ and $Co(OH)_2$. Meanwhile, stability was much better for $Ta_3N_5$/$Co(OH)_2$/Co-Pi than $Ta_3N_5$/CoPi.[82] Similarly, a thin interlayer of MgO between $Ta_3N_5$ and $Co(OH)_x$ can also substantially improve electrode stability.[80] Although there is still much work to be done, the knowledge gained on $Ta_3N_5$ is valuable to other photoelectrodes.

Every material discussed and not discussed above for photoelectrodes possess its own set of advantages and disadvantages. Many of these important characteristics such as charge transfer and stability are SCLJ-related. Therefore, it is essential to discuss in more depth the physics and chemistry at SCLJ and tools capable of investigating it.

# Chapter 3 Theories and Techniques for PEC research

## 3.1 Schottky Junction and Semiconductor-Liquid Junction

The electronic structure of semiconductors consists of a conduction band (CB) and a valence band (VB), with a gap known as band gap ($E_g$) where no electrons are found. In solid state physics, all materials have a Fermi level ($E_F$), which is be the highest energy level that electrons could be found at absolute zero temperature. Since $E_F$ lies within this gap, this definition needs to be adapted. According to band theory, $E_F$ is defined to be the level where the possibility of finding an electron is one half. Above 0 K, The possibility function is dependent on temperature $T$, as described by Fermi-Dirac distribution:[83]

$$f(E) = \frac{1}{1 + \exp\left(\frac{E - E_F}{k_B T}\right)}$$ 

Eq. 3-1

where $k_B$ is Boltzmann's constant. Due to the presence of unintentional or intentional defects in the crystal structure, the Fermi level is often shifted above or below the center of the band gap, giving an n-type (negatively doped) or p-type (positively doped) semiconductor. Electrons are the majority charge carriers in an n-type semiconductor, while holes in a p-type semiconductor. Doping by introducing aliovalent atoms is the most common way of tuning the electronic properties, for example, boron and phosphorous in silicon. The intrinsic defects in metal oxides that gives conductivity typically involve the presence of oxygen vacancies.[84] These impurities can become ionized upon thermal excitation:[85]

$$D \rightarrow D^+ + e_{CB}$$ 

Eq. 3-2

$$A \rightarrow A^- + h_{VB}$$ 

Eq. 3-3

D and A represent donor and acceptor species, respectively. The thermal excitation consequently renders the shifting of $E_F$. For an n-type semiconductor, Eq. 3-2 is far easier than Eq. 3-3, making $E_F$ closer to CB. Here, electrons are the majority charge carrier, and concentration of free electrons increases if the semiconductor is more heavily doped.

Charge carrier pairs (e⁻-h⁺) can also be generated by photon absorption. In this process, an electron from the VB is excited to the CB and rapidly relax at the CB edge

(fs), while leaving a hole in VB.[20,21] The conductivity caused by irradiation is known as photoconductivity. This charge generation process is the principle and prerequisite for PV and PEC research.

Contact between a semiconductor and a metal creates a Schottky junction if the work function of the semiconductor is smaller than the metal. This scenario is illustrated with an n-type semiconductor here in Fig. 3-1. To begin with, $E_F$ of two materials will line up by electron flow from the semiconductor to the metal. Because of the low density of states in the semiconductor, electrons not only come from the surface but also some distance into the material, thus causing positive charge accumulation. This region is called space charge region (or depletion region), where $E_F$ is shifted downward. On the metal side, negative charges are built up and give rise to an electric field, which acts as a barrier to stop further electron transfer across the interface. More detailed description is provided in the following section.
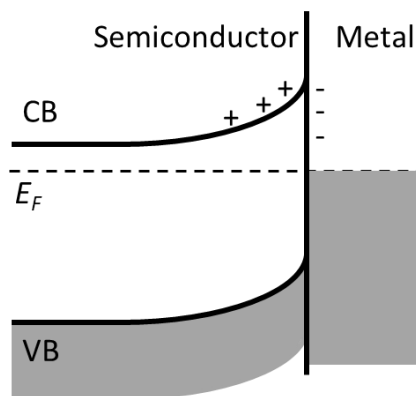


Fig. 3-1 Energy diagrams of a metal-semiconductor system when they are (a) separated, (b) connected, (c) brought close, and (d) in contact.[86]

The situation is similar when a semiconductor is in contact with an electrolyte solution compared with a metal. The space charge properties in the semiconductor can be calculated in the same way but the electron transfer processes are more complex and requires the knowledge of electrochemical dynamics.

The space charge properties at the semiconductor can be studied starting with an abrupt depletion approximation, which assumes total depletion of free electrons within the region $W_{SC}$. Subsequently, a series of important values can be calculated from Poisson's law in electrostatics, which relate the potential to the net amount of charge:[85]

$$\frac{\partial^2 \varphi}{\partial x^2} = \frac{-\partial \xi}{\partial x} = \frac{-\rho(x)}{\varepsilon_r \varepsilon_0} \qquad \text{Eq. 3-4}$$

In this equation, $x$ is one-dimensional distance from the surface, $\varepsilon_0$ is vacuum permittivity $8.854 \times 10^{-12}\,\mathrm{F\,m^{-1}}$, $\varepsilon_r$ is the relative dielectric constant of the semiconductor. $\xi$ and $\rho(x)$ represent electric field and charge density, respectively. As the charge density $\rho(x)$ is constant ($N_D$ in depletion region according to the assumption), electric field is linear and electric potential is parabolic against distance away from the SCLJ, as shown in Fig. 3-2.
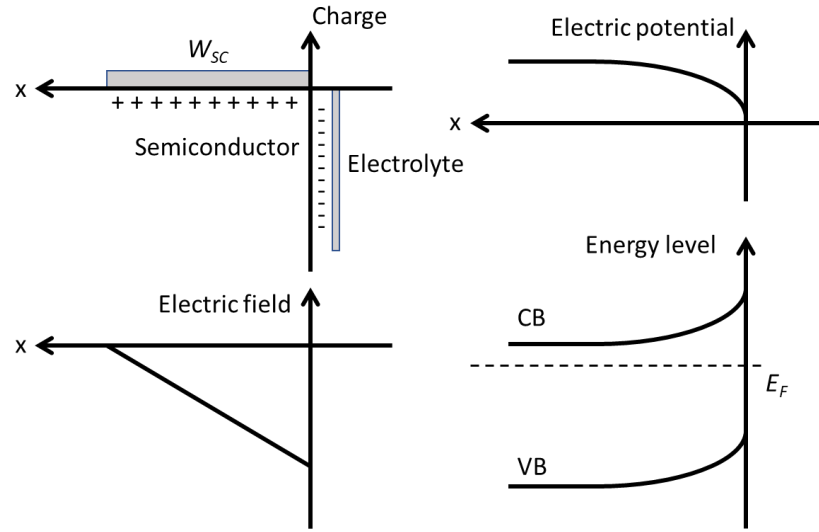


Fig. 3-2 Distribution of (a) charge, (b) electric field, (c) electric potential, and (d) energy diagram of a electrochemical system.[85]

The total amount of charge in the space charge region can be obtained by integration of Eq. 3-4 in a simplified form if the potential drop across space charge region is larger than 0.1 V, which is typically the case in PEC operating conditions[4]

$$Q_{SC} = \sqrt{2\varepsilon_r \varepsilon_0 q N_D A^2 \left(\Delta\phi_{SC} - \frac{kT}{q}\right)} \qquad \text{Eq. 3-5}$$

where $\Delta\phi_{SC}$ is the potential drop across the space charge region, $N_D$ is the donor density, and $A$ is the surface area. Given the total charge can also be approximated as

$$Q_{SC} = q N_D A W \qquad \text{Eq. 3-6}$$

space charge width is then calculated by

$$W = \sqrt{\frac{2\varepsilon_r \varepsilon_0}{q N_D} \left( \Delta\phi_{SC} - \frac{kT}{q} \right)} \qquad \text{Eq. 3-7}$$

The famous Mott-Schottky equation can also be derived by differentiating Eq. 3-5 with respect to $\Delta\phi_{SC}$

$$\frac{1}{C_{SC}^2} = \left( \frac{\partial Q_{SC}}{\partial \phi_{SC}} \right)^{-2} = \frac{2}{\varepsilon_r \varepsilon_0 q N_D A^2} \left( \Delta\phi_{SC} - \frac{kT}{q} \right) \qquad \text{Eq. 3-8}$$

By plotting $\frac{1}{C_{SC}^2}$ with respect to applied potential, the donor density can be determined by working out the slope. $C_{SC}$ can be approximated by total interface capacitance, which is relatively easily measured by impedance spectroscopy. Note that this is theoretically only applicable when Helmholtz double layer capacitance ($C_H$) is significantly higher and potential drop across it is negligible. In practice, large errors can be easily introduced when the electrode conditions deviate from ideal.

## 3.2 Interfacial Charge Transfer

The situation is similar when a semiconductor is in contact with electrolyte solution as opposed to a metal. However, the electrolyte is not an electronically conducting phase and have localized energy levels in the solvent and ions.[85] Consequently, Fermi level equilibrium can only be achieved if a redox couple is present:

$$O + e^- \leftrightarrow R \qquad \text{Eq. 3-9}$$

where O and R stand for oxidised and reduced species, respectively. The reaction described here not only involves electron transfer but also the reconfiguration of the solvent around the ions, which brings a reorganization energy $\lambda$. This reorganization step causes the energy separation between O and R. Depending on the state and configuration, a certain redox species has the probability of having energy $E$ following a Gaussian distribution:[4]

$$W_O(E) = \frac{1}{\sqrt{4\pi\lambda k_B T}} \exp\left( \frac{-(E - E_{redox}^o + \lambda)^2}{4 k_B T \lambda} \right) \qquad \text{Eq. 3-10}$$

$$W_R(E) = \frac{1}{\sqrt{4\pi\lambda k_B T}} \exp\left( \frac{-(E - E_{redox}^o - \lambda)^2}{4 k_B T \lambda} \right) \qquad \text{Eq. 3-11}$$

Here $E_{redox}^o$ is the center of the overlapped part of the two functions. This distribution originates from the fluctuating energy levels of ionic species surrounded by oriented polar solvent molecules and interaction with farther ions and solvent molecules in the

solution. The distribution of these fluctuating energy levels is shown in Fig. 3-3. Note that this probability function should be distinguished from DOS that only allows one electron to be occupied at each energy level.[4] It can be calculated by multiplying probability function W(E) by species concentration. According to Marcus theory, electron transfer can only occur when the energy level of O and R is the same by tunnelling.[87,88] For a photoanode, electrons can be either accepted in valence band or surface states. Therefore, the matching of energy levels would be essential to maximize charge transfer rate.
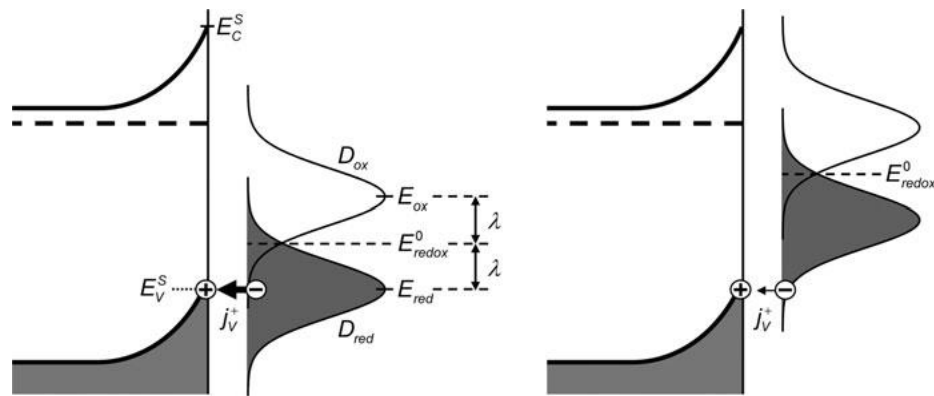


Fig. 3-3 Energy diagrams for electron transfer from a redox species in the electrolyte to a photogenerated hole in the semiconductor valence band. A larger overlap of the redox DOS with the energy levels of the hole gives higher transfer rate.[4] Reprinted by permission from Springer Nature: Springer, Photoelectrochemical Hydrogen Production by Roel van de Krol and Michael Grätzel, COPYRIGHT 2012.

## 3.3 Helmholtz Layer, Surface States and Fermi Level Pinning

Since the space charge layer is positively charged, there will be electrons accumulated on the other side, which is typically the case in contact with metals. However, for metal oxides, it is more often the case that water molecules from the air or in the solution dissociatively adsorb onto the surface.[4] The hydroxylated layer becomes inner Helmholtz layer and solvated ions form outer Helmholtz layer. This hydroxide layer can get protonated or deprotonated depending on the pH of solution (Eq. 3-12 and Eq. 3-13). The latter scenario is illustrated in Fig. 3-4. If the surface is uncharged, it reaches the point of zero charge.[4]

$$\text{M} - \text{OH} \overset{k_a}{\longleftrightarrow} \text{MO}^- + \text{H}_{aq}^+ \qquad\qquad \text{Eq. 3-12}$$

$$\text{M} - \text{OH} + \text{H}_{aq}^+ \overset{k_b}{\longleftrightarrow} \text{M} - \text{OH}_2^+ \qquad\qquad \text{Eq. 3-13}$$
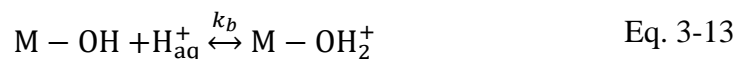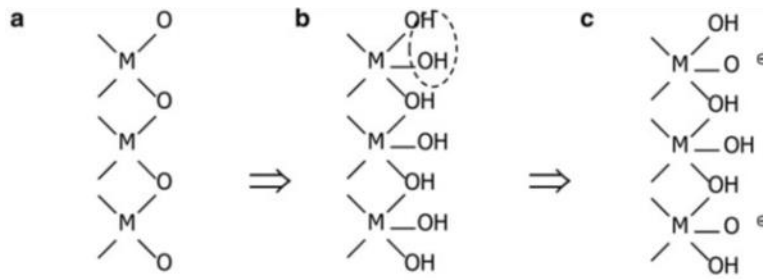
Fig. 3-4 Surface representation of a (a) intrinsic metal oxide termination, (b) H2O dissociatively adsorbed OH termination, and (c) deprotonated termination.[4] Adapted by permission from Springer Nature: Springer, Photoelectrochemical Hydrogen Production by Roel van de Krol and Michael Grätzel, COPYRIGHT 2012.

Because the space charge layer and Helmholtz layer have the same total charge associated with them, the potential distribution is inversely correlated to their capacitances[4]

$$\frac{\Delta V_{SC}}{\Delta V_H} = \frac{C_H}{C_{SC}} \qquad \text{Eq. 3-14}$$

As the Helmholtz layer width is considerably smaller than space charge region, meaning $C_H \gg C_{SC}$, the potential drop across Helmholtz layer would be much smaller. However, it is often not negligible in the presence of surface states. For example, if a hematite electrode is submerged in strong alkaline solution, as often used in PEC operating conditions, the surface states filled with electrons now hinder the formation of a hydroxylate ion layer, meaning the Helmholtz capacitance will be less than without surface states.[6] Notably, it has been pointed out that high donor density increases Helmholtz potential drop. The additional potential drop brought by surface states is calculated by Eq. 3-15 and illustrated in Fig. 3-5.[85]

$$\Delta V_{H,ss} = \frac{\Delta Q_{ss}}{C_H} = \frac{q}{C_H} \int_{E_V}^{E_C} f(E - E_F) g_{ss}(E) dE \qquad \text{Eq. 3-15}$$

Here $f(E - E_F)$ is Fermi-Dirac distribution and $g_{ss}(E)$ is the energy distribution of surface states.
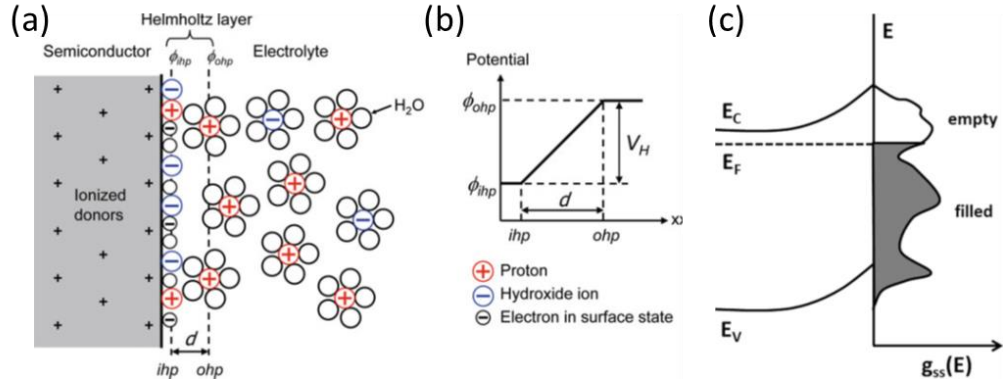
Fig. 3-5 (a) A schematic model of the semiconductor/electrolyte interface and the Helmholtz layer. The inner Helmholtz plane (ihp) consists of adsorbed $H^+$ and $OH^-$ ions with possible presence of electron-trapped surface states. The outer Helmholtz plane (ohp) marks the solvated counter ions from the solution. (b) An electric potential plot for (a).[4] Reprinted by permission from Springer Nature: Springer, Photoelectrochemical Hydrogen Production by Roel van de Krol and Michael Grätzel, COPYRIGHT 2012. (c) The distribution of filled and empty surface states.[85] Reprinted by permission from Springer Nature: Springer, Photoelectrochemical Solar Fuel Production From Basic Principles to Advanced Devices by Sixto Gimenez and Juan Bisquert, COPYRIGHT 2016.

As the charge of inner Helmholtz layer cannot fully develop due to the extra electrons accommodated by surface states, electric field in the space charge region will not be as high, leading to a lower barrier height. The band edge will be unpinned upon applying reverse bias because the additional charges will be partly used to empty surface states. This effect is known as Fermi level pinning.[86]

## 3.4 Quasi Fermi Level and Photovoltage

In practice, the maximum driving force of a PEC device is not the barrier height but is determined by the gain in internal energy. As the system is no longer in equilibrium, the use of a single Fermi level is no longer appropriate. Generation of electrons and holes cause the divergence in their energy levels that are now called quasi Fermi levels ($E_{F,n}$ for electrons and $E_{F,p}$ for holes). They can be calculated by[89]

$$n = N_C \left( \frac{1}{1 + \exp\left(\frac{E_C - E_{F,n}}{k_B T}\right)} \right) \qquad \text{Eq. 3-16}$$

$$p = N_V \left( \frac{1}{1 + \exp\left(\frac{E_{F,p} - E_V}{k_B T}\right)} \right) \qquad \text{Eq. 3-17}$$

In the two equations above, in which $n$ and $p$ stand for concentrations of free electrons and holes, respectively; $N_C$ and $N_V$ represent density of states of conduction band and valence band, respectively. For an n-type semiconductor, the majority charge carriers are electrons and its number only increases slightly, so the quasi Fermi level of electrons is hardly shifted. On the other hand, holes have a significant rise in numbers, pushing its quasi Fermi level close to the valence band. While under some debate, it is useful to associate the OER rate constant with the overlapped region between $E_{F,p}$ and standard reaction potential.[85] For every order of magnitude increase in light intensity, photovoltage increases by 59 mV until flat band condition is reached.[85] It should be noted that in many reports, $E_{F,p}$ close to the surface is often depicted to rise to some degree as holes are consumed by recombination as well as OER.
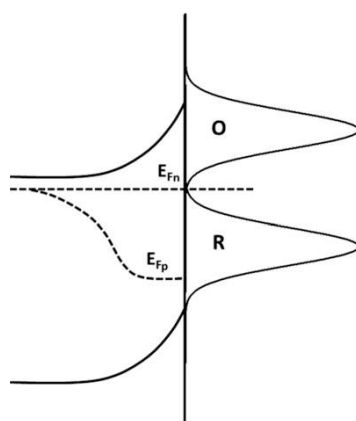


Fig. 3-6 Schematic diagram of a semiconductor in contact with electrolyte with redox couple R/O, showing quasi Fermi level of electrons ($E_{f,n}$) and holes ($E_{f,p}$).[85] Reprinted by permission from Springer Nature: Springer, Photoelectrochemical Solar Fuel Production From Basic Principles to Advanced Devices by Sixto Gimenez and Juan Bisquert, COPYRIGHT 2016.

## 3.5 PEC Characterizations

There are many techniques to characterize a photoelectrode, from basic physical methods including X-ray diffraction, scanning electron microscopy, UV-visible absorption spectroscopy, X-ray photoelectron spectroscopy to photoelectrochemical approaches. Fundamentals of these physical characterization methods have been thoroughly introduced in many textbooks and therefore skipped in this thesis. On the other hand, emphasis is put on PEC characterizations.

The PEC characterizations for the studies of photoelectrodes are normally represented by linear sweep voltammetry (that typically measures the photocurrent

density of a film), chronoamperometry (that evaluates the stability), as well as photoelectrochemical impedance spectroscopy (PEIS) and intensity modulated photocurrent spectroscopy (IMPS), which will be explained briefly in the following sections. In addition, other advanced methods such as dual working electrode, transient spectroscopy and in-situ X-ray absorption have had significant contribution of understanding reactions at photoanodes.

### 3.5.1 Photocurrent-Voltage Characteristics

An n-type semiconductor behaves like a diode in the electrolyte. If the applied potential is more negative than its flat-band potential, it falls into accumulation regime.[4] The CB edge soon crosses Fermi level, meaning rapid charge transfer across interface. In contrast, when a more positive potential is applied, opposite charge transfer is allowed when Fermi level is lower than redox potential of the reactive species. Under illumination, Fermi level can be elevated without external potential input until flat band potential is reached, which in practice cannot be achieved due to severe recombination especially when band edges are more flattened.[25] Higher surface roughness of the electrode also leads to reduced photovoltage because less charges will be distributed per unit area, although higher surface area is known to improve charge collection ratio. For every order of magnitude increase in roughness, photovoltage drops by 59 mV.

A widely known model to rationalize photocurrent-potential curve is the Gärtner model, in which several assumptions must be made: (a) photons with energy larger than band gap are absorbed as a function of absorption coefficient α; (b) all photo-generated holes generated within space charge layer plus a diffusion length of $L_p$ can reach the surface; (c) Faradaic efficiency is unity. A one-dimensional illustration is shown in Fig. 3-7.[26] The photocurrent density is then given by

$$J_{\mathrm{ph}} = qI_0 \left[ 1 - \frac{\exp(-\alpha W_{SC})}{1 + \alpha L_{\min}} \right] \qquad \text{Eq. 3-18}$$

where $I_0$ is incident photon flux. The part in the square bracket indicates the fraction of holes that are collected and reacted at the surface. Thus, external quantum efficiency (or IPCE) is readily known by taking away $qI_0$.
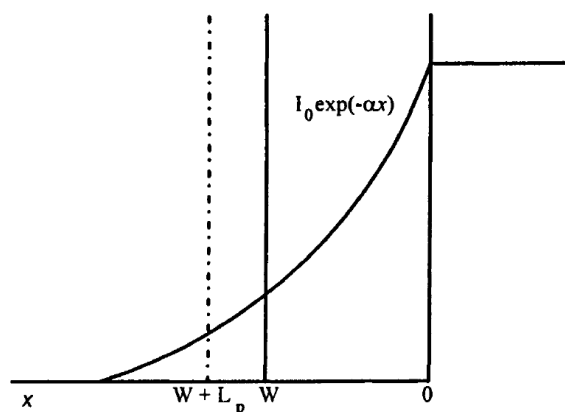
Fig. 3-7 Profile of light penetration into the semiconductor, showing crucial distances: space charge width $W$ and hole diffusion length $L_p$.[90] Reprinted from Comprehensive Chemical Kinetics: Applications of Kinetic Modelling, 1st Edition, G. Hancock and R.G. Compton, Chapter 8, Copyright (1999), with permission from Elsevier.

The Gärtner model is an oversimplified description. A more complex model considering charge recombination has been developed by Reichman.[91] Later Peter and co-workers showed kinetic analysis with surface recombination.[92] In recent years, researchers have investigated numeric representation of photocurrent characteristics.[93]

### 3.5.2 Surface Charge Recombination vs. Charge Transfer

Since hole consumption rate of OER cannot keep up with charge generation rate, excessive holes will inevitably accumulate near the SCLJ, leading to higher possibilities to recombine with majority charge carriers. In this case, band edges will be unpinned and appear to be more pronounced near flat-band potentials. This phenomenon is also referred to as light induced Fermi level pinning.

Introduction of surface states that trap holes and electrons allows one to more conveniently depict the destiny of them in action. Surface recombination can be assumed to take place only at these trapping states. Generalized surface reaction equations in the present of surface states (X) can expressed as[90]

$$R + h^+ \rightarrow 0 \qquad\qquad \text{Eq. 3-19}$$

$$X + h^+ \rightarrow X^+ \qquad\qquad \text{Eq. 3-20}$$

$$X^+ + e^- \rightarrow X \qquad\qquad \text{Eq. 3-21}$$

$$X^+ + R \rightarrow 0 \qquad\qquad \text{Eq. 3-22}$$

26

On a photoanode, R could be adsorbed $H_2O$ or $OH^-$ species or intermediate species, while O could be intermediate species too (oxidized relative to R) or $O_2$. The true identities of R and O are not very important for following kinetic calculations. An uncharged surface trap site takes up a hole and becomes charged, which is likely to recombine with an electron. Alternatively, if holes are instantaneously trapped at surface states, followed by OER, the direct charge transfer is omitted. This alternative route is often seen as more appropriate for hematite photoanodes.

Now it is apparent that three processes at semiconductor surface determine photocurrent: trap states charging, surface recombination and charge transfer, each of which being directly associated with surface charge:[90]

$$J_{\text{ch}} = \frac{dQ_s}{dt} \qquad\qquad \text{Eq. 3-23}$$

$$J_{\text{ct}} = k_{ct}Q_s \qquad\qquad \text{Eq. 3-24}$$

$$J_{\text{rec}} = k_{rec}Q_s \qquad\qquad \text{Eq. 3-25}$$

Surface charging current $J_{ch}$ is the differential of surface charge with time ($Q_s$). Recombination and charge transfer are proportional to surface charge, each corresponded by a rate constant $k_{ct}$ and $k_{rec}$, respectively. The sum of the three currents represents the total hole flux to the surface ($g$), while the sum of $J_{ct}$ and $J_{ch}$ gives the measurable photocurrent density[90]

$$J_{\text{ph}} = J_{\text{ct}} + J_{\text{ch}} = g - J_{\text{rec}} \qquad\qquad \text{Eq. 3-26}$$

The time dependent photocurrent density is then expressed in the differential equation:

$$qg(t) = \frac{dQ_s(t)}{dt} + (k_{ct} + k_{rec})Q_s(t) \qquad\qquad \text{Eq. 3-27}$$

If light is illuminated at time t=0, the above equation can be solved, defining $Q_s(0)=0$. Thus, $Q_s(t)$ is known as well as each current component:

$$Q_s(t) = \frac{qg\left(1 - e^{-(k_{ct}+k_{rec})t}\right)}{k_{ct} + k_{rec}} \qquad\qquad \text{Eq. 3-28}$$

and

$$J_{\text{ch}} = qg\, e^{-(k_{ct}+k_{rec})t} \qquad\qquad \text{Eq. 3-29}$$

$$J_{\text{ct}} = \frac{qgk_{ct}\left(1 - e^{-(k_{ct}+k_{rec})t}\right)}{k_{ct} + k_{rec}} \qquad\qquad \text{Eq. 3-30}$$

$$J_{\text{rec}} = \frac{qg k_{rec}\left(1 - e^{-(k_{ct}+k_{rec})t}\right)}{k_{ct} + k_{rec}} \qquad \text{Eq. 3-31}$$

The above formulas are plotted after normalization in Fig. 3-8. Their behavior is described in detail in the following section.
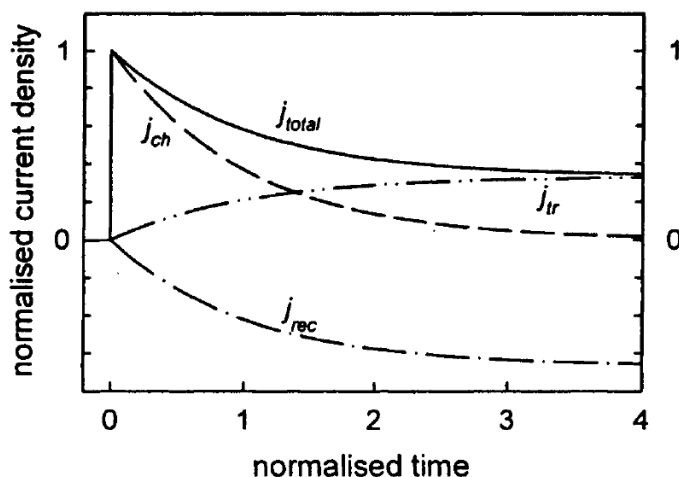


Fig. 3-8 Components of the current response ($j_{total}$) of a photoanode to an illumination step, which consists of charging current $j_{ch}$, recombination current $j_{rec}$, and charge transfer current $j_{tr}$.[90] Reprinted from Comprehensive Chemical Kinetics: Applications of Kinetic Modelling, 1st Edition, G. Hancock and R.G. Compton, Chapter 8, Copyright (1999), with permission from Elsevier.

### 3.5.3 Transient Photocurrent Spectroscopy

When the photoanode starts being irradiated, there is no surface charge so both charge transfer and recombination take up no contribution. The hole flux is entirely used for surface charging. As surface states become filled with holes, charge transfer and recombination become appreciable with opposite signs because electrons are moved toward to the surface for recombination. At steady state, surface charge is constant therefore no charging current. The measured photocurrent density only comes from charge transfer. The characteristics of transient photocurrent curves can be used to reveal the kinetic rate constants in a simpler way:[89]

$$\frac{J(t) - J(\infty)}{J(0) - J(\infty)} = e^{-t/\tau} \qquad \text{Eq. 3-32}$$

where $J(0)$ is initial photocurrent read at the maximum of the spike and $J(\infty)$ is the steady state photocurrent density; $\tau = (k_{ct} + k_{rec})^{-1}$. Also,

$$\frac{J(\infty)}{J(0)} = \frac{k_{ct}}{k_{ct} + k_{rec}} \qquad \text{Eq. 3-33}$$

However, this technique may not result accurate estimations for two reasons. First, chopped light method involves the shutter opening time that causes a delay in photocurrent response. This so-called step time was found to be 20 ms for a common solar simulation system but less than 1μs for LED.[94] Second, the spike maximum is not easily defined due to the short time interval of data acquisition required, or could be attenuated by the time constant of the cell. Moreover, the drastic change in light intensity cannot assure the linear response of photocurrent.[95]
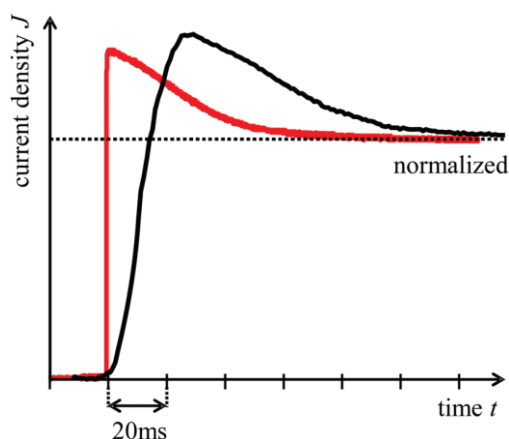


Fig. 3-9 Comparison of transient photocurrent responses taken with a mechanical shutter in front of a solar simulator (black curve), and a white LED controlled by a fast intensity transient (FIT) module (red curve). Both curves were recorded with the same photoanode at a potential of 1.35 $V_{RHE}$.[94] Reproduced from ref. [94] with permission from the PCCP Owner Societies.

**3.5.4 Photoelectrochemical Impedance Spectroscopy**

Impedance spectroscopy (IS) is a very useful tool in electrochemistry. Its measurement involves the application of a small sinusoidal perturbation of potential (or much less often, current) provided by a waveform generator that is imposed on a constant potential.

$$E(t) = E_0 + E_m\sin(\omega t) \qquad \text{Eq. 3-34}$$

Here $E_m$ is the magnitude of the imposed wavefunction, which must be limited below the thermal voltage (25 mV at 25 °C) in order to preserve the linearity of the system, thereby the legitimate use of Fourier transformation. $\omega$ is angular frequency. The magnitude and phase of current is then measured by the potentiostat with a frequency response analyzer (FRA).

$$I(t) = I_0 + I_m\sin(\omega t + \theta) \qquad \text{Eq. 3-35}$$

The impedance is then designated as[96]

$$Z(f) = \frac{E(t)}{i(t)} = Z' + iZ''$$ 
<span style="float:right">Eq. 3-36</span>

Its modulus is $|Z|$, projecting to a real part $Re(Z) = Z' = |Z|\cos(\theta)$ and an imaginary part $Img(Z) = Z'' = |Z|\sin(\theta)$ in an orthogonal coordinate system, where $\theta = \tan^{-1}(Z''/Z')$. A Nyquist plot is obtained when all experimental data points are mapped in this coordinate system. Another commonly seen graph is the Bode plot, which has frequency in logarithm scale as horizontal axis and $|Z|$ as vertical axis.
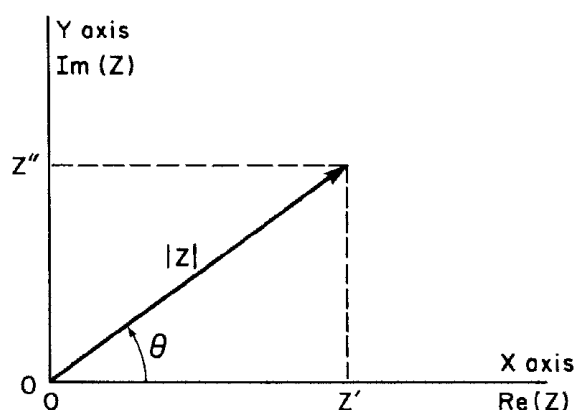


Fig. 3-10 The impedance $Z$ plotted as a planar vector using rectangular and polar coordinates.[96] From Evgenij Barsoukov and J. Ross Macdonald, Impedance Spectroscopy Theory, Experiment, and Applications, 2nd Edition. Copyright © 2005 by John Wiley & Sons, Inc. Reprinted by permission of John Wiley & Sons, Inc.

The total impedance of a system can be matched with impedance of a simple or complex combination of electrical elements, such as resistors and capacitors, arranged in a specific way, known as an equivalent circuit (EC). Nonetheless, an infinite number of ECs can yield exactly the same overall impedance, as exemplified in Fig. 3-11.[96] This is known as the transformability problem. Therefore, the choice of EC is dependent on physical intuition of the researcher. Several sets of IS can be measured with different conditions for a more reliable diagnosis. In the case of PEC studies, impedance results are often carried out at varied applied potentials.
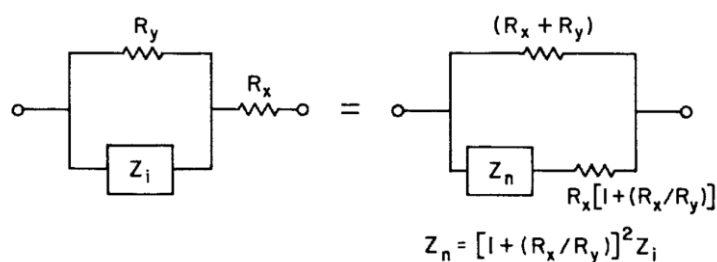
Fig. 3-11 Two example equivalent circuits with identical total impedance.[96] From Evgenij Barsoukov and J. Ross Macdonald, Impedance Spectroscopy Theory, Experiment, and Applications, 2nd Edition. Copyright © 2005 by John Wiley & Sons, Inc. Reprinted by permission of John Wiley & Sons, Inc.

A flow chart can represent the process of applying IS to electrochemistry. First, some theory and physical model should be established to account for the most fundamental procedures in the electrode-electrolyte system, which is then mapped into an EC via mathematical modelling. After the measurement of impedance, results are fitted using the proposed EC to check its validity. If the data do not fit well with the EC, the physical model should be modified. If a reasonable numeric match between measured and simulated data is obtained, a change in variable ensues, followed by further IS measurements to validate the model.
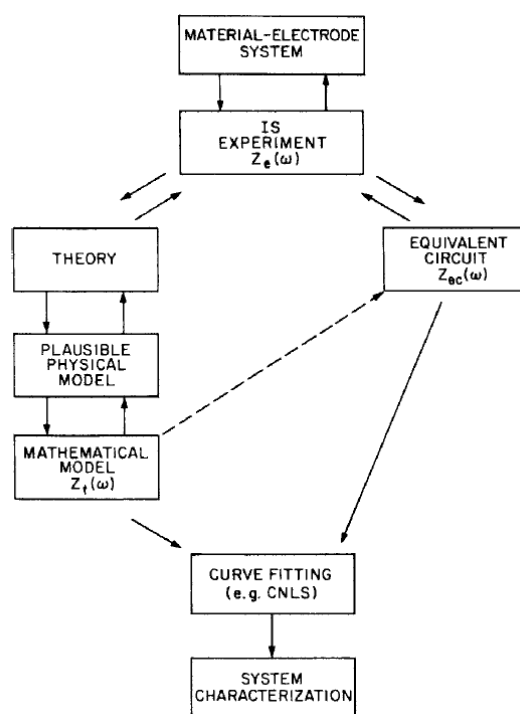


Fig. 3-12 A typical flow chart of using impedance spectroscopy to study electrochemical systems.[96] From Evgenij Barsoukov and J. Ross Macdonald,

Although IS is a useful tool to gain information of mass transport, reaction rates, and dielectric properties to defects and microstructure, it comes with inaccuracies in its interpretation. For example, since microscopic properties are independently distributed, it is found that ideal electrical elements are not capable of reproducing the impedance response, thus numerical elements such as constant phase elements (CPEs) are sometimes used instead of its ideal counterpart capacitance.[96] More specifically, for highly nanostructured electrodes, transmission line model is an effective tool. Description for mesoscopic oxide electrodes using semi-infinite number of elements can be found elsewhere.[97]

Several plausible ECs for water oxidation at hematite photoanodes have been proposed in Klahr et al.'s work with different assumptions.[98] The authors first considered the contribution from direct hole charge transfer as well as through surface states. Although it is highly possible that both reaction routes are participating, impedance data cannot be unambiguously interpreted due to its complexity. It is therefore inevitable to assume that one route dominates. Klahr and co-workers argued that surface states mediated route is more probable for hematite electrodes whereas some other research groups prefer the direct transfer model,[99] as ECs in Fig. 3-13b and Fig. 3-13c are mathematically indistinguishable.
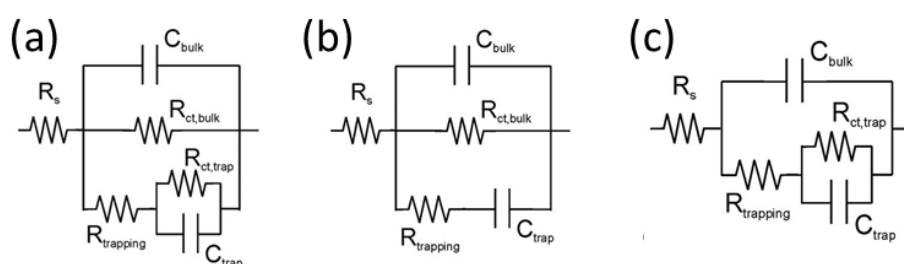


Fig. 3-13 Equivalent circuits for PEIS analysis assuming contribution from (a) both direct VB charge transfer and surface states charge transfer, (b) only direct VB charge transfer, and (c) only surface states charge transfer.[98] Reprinted with permission from ref. [98]. Copyright 2012 American Chemical Society

In an ideal SCLJ scenario, modulation of potential can cause corresponding changes in electron density in semiconductors and hence the recombination rate constants according to the correlations:[90]

$$k_{rec} = k_{rec}^0 e^{\frac{-q\left(E - E_{fb}\right)}{k_B T}}$$
<div align="right">Eq. 3-37</div>

$$k_{rec}^0 = N_D \sigma_n v_n$$
<div align="right">Eq. 3-38</div>

where $k_{rec}^0$ is the recombination rate constant at $E = E_{fb}$ and the product of doping density $N_D$, the thermal velocity of electrons $v_n$ and the electron capture cross section of $X^+$ $\sigma_n$. This perturbation of potential influences both recombination and charging current but not the hole flux reaching the surface and charge transfer current. Assuming $C_{SC} \ll C_H$, two semicircles can be seen in a Nyquist plot at higher and lower frequency domains. Their parameters can be extracted by the following equations derived by Peter and co-workers:[89]

$$R_{LF} = \frac{k_B T}{q^2 g} \left(\frac{k_{ct} + k_{rec}}{k_{ct}}\right)$$
<div align="right">Eq. 3-39</div>

$$C_{LF} = \frac{q^2 g}{k_B T} \left(\frac{k_{ct} + k_{rec}}{k_{ct}}\right)$$
<div align="right">Eq. 3-40</div>

$$\omega_{max,LF} = \frac{1}{R_{LF} C_{LF}} = k_{ct}$$
<div align="right">Eq. 3-41</div>

The higher frequency semicircle has

$$R_{LF} = \frac{k_B T}{q^2 g} \left(\frac{k_{ct} + k_{rec}}{k_{rec}}\right)$$
<div align="right">Eq. 3-42</div>

$$C_{HF} = C_{SC}$$
<div align="right">Eq. 3-43</div>

$$\omega_{max,HF} = \frac{q^2 g}{k_B T C_{SC}} \left(\frac{k_{ct} + k_{rec}}{k_{ct}}\right)$$
<div align="right">Eq. 3-44</div>

These equations are fully compatible with the Klahr's model, which will be corroborated in Note S1 of Section 5.1.5.

Previous equations have been validated on hematite photoanodes, in which the presence of intermediate surface states has been validated with in-situ infrared spectroscopy.[100] However, the usage of surface states is sometimes regarded unnecessary or unsupported for photoelectrodes whose surface kinetics is little known or is very fast. In these cases, the space charge region is connected in series with solid-liquid interface, as represented by two RC units (Fig. 3-14).
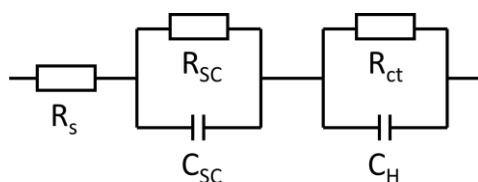
Fig. 3-14 Equivalent circuit for PEIS analysis without the assumption of surface states.

### 3.5.5 Intensity Modulated Photocurrent Spectroscopy

Intensity modulated photocurrent spectroscopy (IMPS) is another powerful technique particularly useful for PV and PEC research developed by Peter and co-workers in the 1980s.[101,102] As a frequency resolved spectroscopy, it is similar to PEIS, while replacing potential perturbation with illumination perturbation. A schematic illustration is shown in Fig. 3-15. Notable is the addition of a beam splitter and a photodiode, which are to avoid the acoustic delay in the modulator that leads to a phase lag in the LED.[90] They are, however, not used in some instruments with less accuracies of measurement.
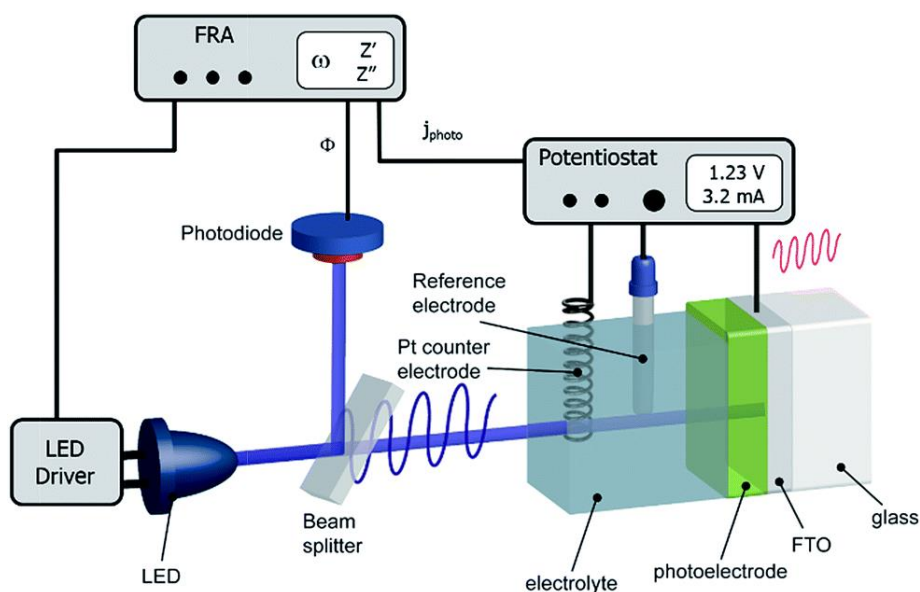


Fig. 3-15 Schematic diagram of the IMPS setup.[72] Reproduced from ref. [72] with permission from The Royal Society of Chemistry.

When light intensity is modulated in a sinusoidal pattern, hole flux is modulated correspondingly according to the Gärtner model

$$g(t) = g_0 + g_m \sin(\omega t + \theta) \qquad \text{Eq. 3-45}$$

Instead of impedance, the purpose of IMPS is to obtain the admittance of the cell:

34

$$IMPS(\omega) = \frac{I(t)}{g(t)} \qquad \text{Eq. 3-46}$$

The response of a photoanode in the complex plane can be derived following the assumptions used before by first expressing surface charge $Q_s(t)$ in its periodic form:[90]

$$Q_s(t) = \frac{qg_0}{k_{ct} + k_{rec}} + \frac{qg_m(k_{ct} + k_{rec})}{(k_{ct} + k_{rec})^2 + \omega^2}\sin(\omega t)$$
$$- \frac{qg_m\omega}{(k_{ct} + k_{rec})^2 + \omega^2}\cos(\omega t) \qquad \text{Eq. 3-47}$$

Photocurrent is thus known according to Eq. 3-48.

$$J_{\text{ph}}(t) = \frac{qg_0 k_{ct}}{k_{ct} + k_{rec}}$$
$$+ \frac{qg_m(k_{ct}(k_{ct} + k_{rec}) + \omega^2)}{(k_{ct} + k_{rec})^2 + \omega^2}\sin(\omega t) \qquad \text{Eq. 3-48}$$
$$- \frac{qg_m\omega k_{rec}}{(k_{ct} + k_{rec})^2 + \omega^2}\cos(\omega t)$$

which can be expressed in a dimensionless form

$$\Phi(J_{\text{ph}}) = \frac{J_{\text{ph}}(\omega)}{qg_m} = \frac{k_{ct} + i\omega}{k_{ct} + k_{rec} + i\omega} \qquad \text{Eq. 3-49}$$

and can be plotted in the complex plane as a semicircle as shown in Fig. 3-16.
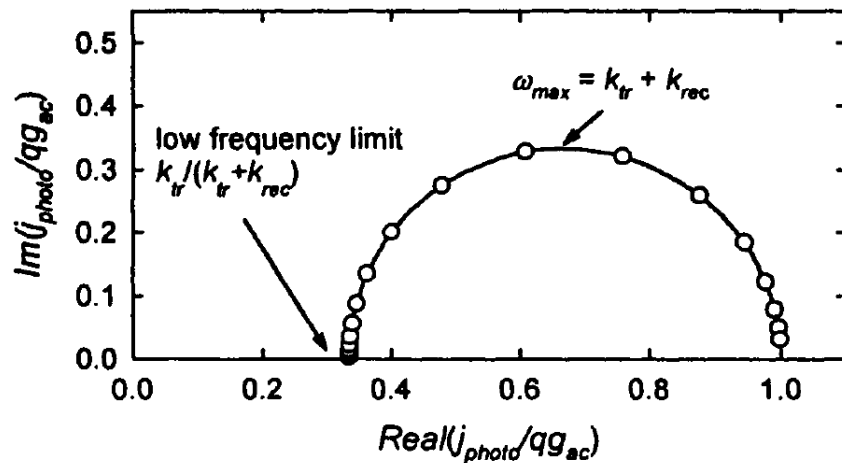


Fig. 3-16 Normalised IMPS signal for a photoanode shown in complex plane. Features of the fitted curve can be used to derive rate constants.[90] Reprinted from Comprehensive Chemical Kinetics: Applications of Kinetic Modelling, 1st Edition, G. Hancock and R.G. Compton, Chapter 8, Copyright (1999), with permission from Elsevier.

The real and imaginary parts of this response are:[90]

$$Re\left(\frac{J_{\text{ph}}}{qg_m}\right) = \frac{k_{ct}(k_{ct} + k_{rec}) + \omega^2}{(k_{ct} + k_{rec})^2 + \omega^2} \qquad \text{Eq. 3-50}$$

$$Img\left(\frac{J_{\text{ph}}}{qg_m}\right) = \frac{k_{rec}\omega}{(k_{ct} + k_{rec})^2 + \omega^2} \qquad \text{Eq. 3-51}$$

This semicircle has two intercepts with real axis, which can be interpreted as follows. The high frequency end crosses at unity, meaning all holes are converted to current. Here, the delay of electron motion cannot catch up with the high frequency of change in hole flux, therefore recombination is effectively 'frozen out'. On the other hand, it approaches DC conditions when frequency is low, where the intercept is $k_{ct}/(k_{ct}+k_{rec})$. Overall, IMPS can be seen as a frequency-resolved version of transient photocurrent spectroscopy with a much smaller light perturbation. More detailed steps for the interpretation of IMPS results are described in Section 5.1.5 to calculate charge transfer rate constant and surface recombination rate constant on a hematite photoanode.

An additional semicircle is often observed experimentally in the lower quadrant. It appears as a result of cell shunting, limiting the time resolution achievable for IMPS measurements. Li and Peter first assumed that the space charge capacitance is much smaller than Helmholtz layer capacitance, then pointed out that photocurrent is attenuated by the series resistor coupled with space charge capacitance by the factor[90]

$$A(\omega) = \frac{1}{1 + i\omega R_s C_{SC}} = \frac{1}{1 + i\omega \tau_{cell}} \qquad \text{Eq. 3-52}$$

Application of this factor to the IMPS response described by Eq. 3-52 suggests that the high frequency intercept with real axis will be less than unity. Later, Ponomarev and Peter gave more generalized equations when space charge capacitance and Helmholtz capacitance are of comparable magnitude,[103] which will not be expanded herein.
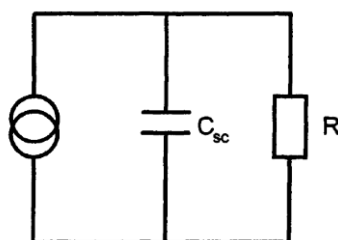


Fig. 3-17 Equivalent circuit for a PEC cell under potentiostatic condition. Photocurrent is shunted by the cell resistance.[90] Reprinted from Comprehensive

The calculated rate constants by IMPS, unfortunately, almost always turn out to be non-ideal. The surface recombination rate constant, $k_{rec}$, decreases considerably less than one order of magnitude per 59 mV as predicted by Eq. 3-37. The explanation can be that $E$-$E_{fb}$ is no long equal to $\Delta\phi_{sc}$ due to Fermi level pinning. Charge transfer rate constant in both photocathodes and photoanodes have also been found to deviate from ideal situations and become dependent with applied potential, which has been ascribed to the fact that water reduction and oxidation are multi-step reactions. The $k_{ct}$ thus contains a term related to recombination via the intermediates.[90]

Some remarks are necessary to compare PEIS and IMPS. It has been suggested that if these two methods are applied differentially (i.e., with small perturbation), they should yield identical information.[104] Impedance spectroscopy gives discrete values of each polarization process, at the price of transformability (different circuits may result in identical data fits). In contrast, IMPS only offers suggestions on the relation between components (e.g., time constants) without data scaling. An in-depth comparison of the two techniques using p-InP photocathodes was reported by Schefold.[104] In addition, the much less used intensity modulated photovoltage spectroscopy (IMVS) contains equivalent information as PEIS but without the influence of surface recombination. These three complementary techniques are called photoelectrochemical immittance triplets, making empirical analysis of operation mechanisms possible.

# Chapter 4 Literature Review and Analysis of Hematite Photoanodes

## 4.1 Overview

Hematite is the only known form of binary iron oxides that can carry out water oxidation. It has a trigonal-hexagonal scalenohedral corundum structure (class $\bar{3}$ 2/m).[105] The $O^{2-}$ anions are arranged in a hexagonal close-packed lattice along [001]. The $Fe^{3+}$ cations regularly occupy two thirds of the octahedral interstitial sites in the (001) planes, while leaving the tetrahedral interstitial sites unoccupied. The effective charges of Fe and O are +1.8 and -1.2, respectively, according to density functional theory (DFT) calculation.[33] Hematite is known for its poor electronic transport, which has been partly ascribed to small polaron formation and losses at grain boundaries.

### 4.1.1 Light Absorption and Charge Diffusion

In terms of its optoelectronic properties, hematite has an indirect band gap of ca. 2.0 eV and absorbs 16.8% of sunlight theoretically.[106] There are four types of transitions upon light irradiation, which will be discussed more in detail in Section 4.3.3. The absorption coefficient α has been measured by Marusak in 1980.[107] The absorption length of light with a certain wavelength can be estimated simply with $\alpha^{-1}$: for instance, 50 nm at λ=350 nm and 300 nm at λ=550 nm.[108] Such long absorption lengths, especially at longer wavelengths, raised a major mismatch with the order of the diffusion length minority charge carriers (2-4 nm).

An effective way to overcome this discrepancy between is to orthogonize these two processes by morphological control.[25] Vertically aligned nanorods, nanotubes or nanosheets are most reasonable and popular options. In contrast, mesoporous nanoparticlate network is inferior owing to the longer path that charge carriers need to traverse.

Due to the high thickness of film required for strong light absorption, direction of illumination must be considered to maximize photocurrent output. For a compact film, front illumination offers an advantage because holes generated near the surface need to travel less distance, especially for those generated by long wavelengths light. (Fig. 4-1) However, the situation is reversed for a porous electrode. Now as the electrolyte

reach the substrate, diffusion of holes to reach water is less of a problem. Therefore, back (substrate) side illumination shows better results when the film thickness is sufficiently high. Front illumination, on the other hand, gives a much longer distance for electrons to be collected, meaning a higher chance of recombination with surface-trapped holes, intermediate species, or donation to dissolved oxygen (Fig. 4-1).[31] The illumination direction loses impact on photocurrent when the film is very thin.
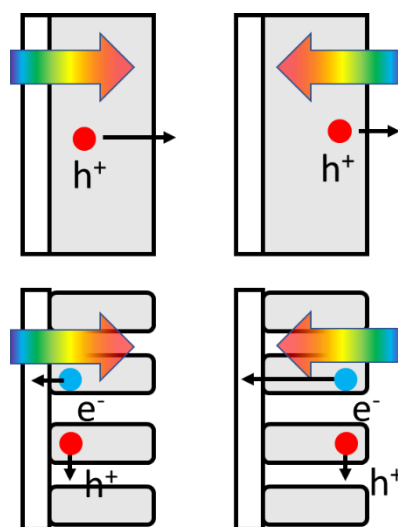


Fig. 4-1 Schematic illustration of charge movements with front and back illumination for a compact and nanorods photoanodes.

Surprisingly, if one assumes the diffusion length of minority charge carrier is $L_{min}$=2-4 nm as mentioned above, in addition to a space charge region of $W_{SC}$=5-10 nm, holes generated outside $L_{min} + W_{SC}$ should not be measurable in a thicker film according to the Gärtner model. Nevertheless, compact films of 1 µm have demonstrated noticeable photocurrent. This unusual phenomenon has been recently investigated by Kay et al.[109] The authors have used their 1 µm films to test the dependence on the wavelength of incident light. In spite of having about 300 nm shorter penetration depth for 450 nm light than 530 nm light, the former shows higher photocurrent density even with back illumination. (Fig. 4-2) They conclude that photo-generated holes can in fact travel at least 700 nm. The heavily cited values of 2-4 nm are, in contrast, are extracted by fitting measured photocurrent curve to the Gärtner model, and hence questionable. By definition, the diffusion length is obtained by Eq. 2-6. Time-resolved microwave conductivity measurement is often used to experimentally determine µ and τ, thereby the diffusion length, although it has not been successfully deployed on hematite due to anomalous Hall effect. According to

the charge mobility value measured from microwave conductivity ($\sim 10^{-4}$ cm$^2$ V$^{-2}$ s$^{-1}$)[33,110] and lifetime measured from TAS ($\sim 10^{-5}$ s at 0.6 V$_{RHE}$),[111] the estimated diffusion length would be about 3 nm, which agrees with the majority. Therefore, future research should shed more light to explain the unusually long charge collection length.
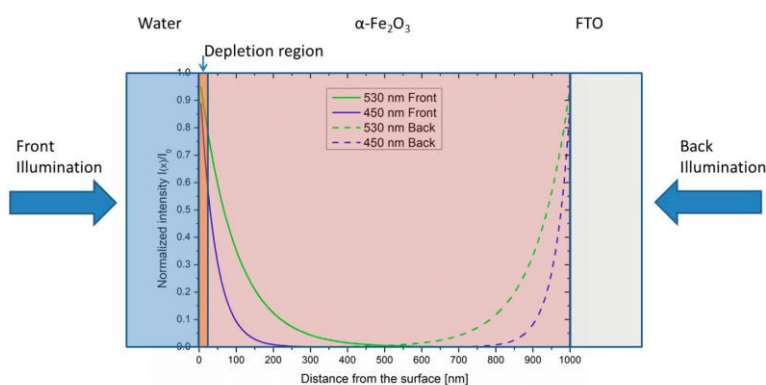


Fig. 4-2 Light penetration profile of a 1 μm thick hematite photoanode for front and back illumination at wavelengths of 450 and 530 nm.[109] Reprinted with permission from ref. [109]. Copyright 2017 American Chemical Society

More clues have been suggested by Peter and co-workers recently, who displayed the internal quantum efficiency (IQE, or APCE) as a function of wavelength (Fig. 4-3).[31] The linear correlation between IQE and photon energy means that the excess kinetic energy provided upon excitation is crucial to the hole diffusion length.
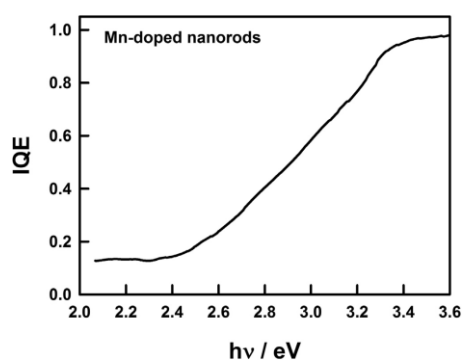


Fig. 4-3 Calculated IQE as a function of photon energy for Mn-doped hematite nanorods.[31] Reproduced with permission from J. Electroanal. Chem. 819, 447 (2018). Copyright 2018, The Electrochemical Society.

### 4.1.2 Synthesis

Despite the controversies on diffusion length, nanostructuring has displayed significant improvements in photocurrent density. For the single crystal case, it has afforded an increase of performance by a factor of 10.[112] Various types of structures

have been synthesized by physical/chemical deposition, thermal oxidation, anodization, electrodeposition, hydrothermal and other methods. Some representative examples are shown in Fig. 4-4 and described in Table 4-1.[113] More examples can be found in a review by Zhang's group.[114]
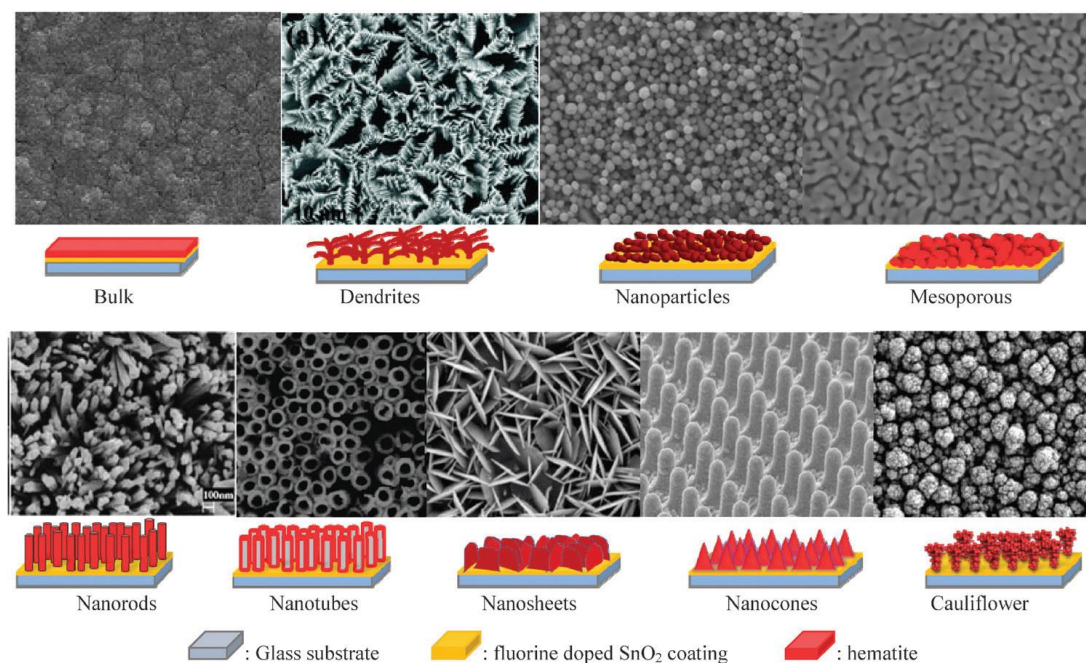


Fig. 4-4 SEM images and representative schemes of hematite photoanodes with different morphologies.[113] Reproduced from ref. [113] with permission from The Royal Society of Chemistry.

Table 4-1 Compilation of representative hematite photoanodes with various morphologies.

| Type of nanostructure | Synthesis method | Highest annealing temperature ($^{o}$C) | J (mA cm$^{-2}$) at 1.23 V$_{RHE}$, 1sun | Ref. |
|---|---|---|---|---|
| Bulk | Electrodeposition | 450 | No | 115 |
| Bulk | Drop casting | 700 | 0.1 | 116 |
| Dendrites | Electrodeposition | 500 | ~0.018 | 117 |
| Nanoparticles | Electrodeposition | 500 | 0.05 | 118 |
| Mesoporous | Colloidal | 820 | 1.1 | 119 |
| Nanorods | Hydrothermal | 800 | 1.26 | 120 |
| Nanotubes | Anodization | 500 | ~0.8 (87 mW cm$^{-2}$) | 121 |
| Nanosheet | Anodization | 450 | 1.5 | 122 |
| Cauliflower | APCVD | 545 | 2.2 | 123 |

In Table 4-1, highest annealing temperature during film fabrication is specially noted because it can drastically influence both the morphological and electronic behavior compared to moderately annealed samples (below 700 °C). Compact hematite films and nanosheet showed no photocurrent when annealed at 450 °C[115] but around 0.1 mA cm$^{-2}$ at 750 °C.[116] Nanoparticle-based films listed in Table 4-1 showed very small photoresponse, but if heated at 800 °C and transformed into mesoporous network, their photocurrent increases considerably.[108,118] Likewise, nanosheets were found to give noticeable photocurrent only when annealed above 700 °C, while at the cost of losing its 2D features.[124] A more convincing case has been shown by comparing intentionally and unintentionally Sn-doped hematite electrodes. The authors found that unintentional Sn doping owing to atomic diffusion from FTO by annealing at 800 °C produced better results than intentionally doped sample annealed at 650 °C, while undoped sample treated at 650 °C showed negligible photocurrent density (Fig. 4-5).[38] However, there are exceptions. For instance, samples made by CVD demonstrate champion photocurrent densities, possibly because of better crystallinity formed during synthesis. It is plausible that CVD produced samples that have less grain boundaries.[125]
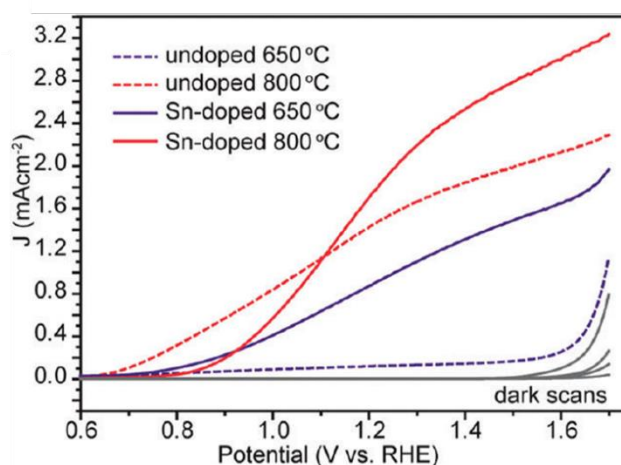


Fig. 4-5 Comparison of J-V scans collected for hematite photoanodes with (solid) and without (dashed) intentional doping, calcined at 650 (blue) and 800 °C (red).[38] Reprinted with permission from ref. [38]. Copyright 2011 American Chemical Society

It should be noted that the most widely adopted method in the literature to prepare a hematite base layer is based on Vayssieres's report in 2001.[126] The advantage of this hydrothermal synthesis method is the formation of vertically aligned nanorods, which are favorable for charge diffusion, while the procedure is relatively simple. Papers

focusing on both performance enhancement and kinetic researches can be frequently found to adopt this method in the literature.

## 4.2 Surface Kinetics of Oxygen Evolution Reaction

### 4.2.1 Mechanism of OER on hematite surface

One reaction route to explain the dissociation of water molecules at $Fe_2O_3$ (0001) proposed by Norskov and co-workers has been widely accepted.[127] First, one water molecule is adsorbed onto the active sites of hematite at the surface (*), followed by two consecutive deprotonation steps by taking two holes. The dangling oxygen attracts another water molecule and forms an oxyhydroxide group. According to Bockris and Otagawa, the third step can also be regarded as the formation of surface adsorbed $H_2O_2$, followed by its deprotonation.[128] Finally, the reaction is completed by the release of an oxygen molecule.

$$H_2O + * \rightarrow *OH_2 \qquad \text{Eq. 4-1}$$

$$*OH_2 \rightarrow *OH + H^+ + e^- \qquad \text{Eq. 4-2}$$

$$*OH \rightarrow *O + H^+ + e^- \qquad \text{Eq. 4-3}$$

$$H_2O + *O \rightarrow *OOH + H^+ + e^- \qquad \text{Eq. 4-4}$$

$$*OOH \rightarrow O_2 + * + H^+ + e^- \qquad \text{Eq. 4-5}$$
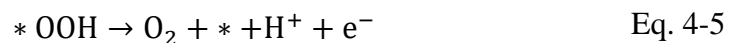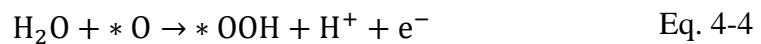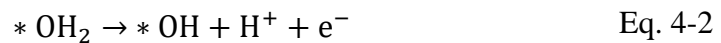
Computational methods have been used to estimate the changes in free energy for each step and subsequently the overpotential.[129,130] The overpotential of OER in computational chemistry is often defined to be the difference between the highest free energy change of one step and the average free energy change, although it lacks experimental association.[131]

$$\eta = \Delta G_{max} - \Delta G_{avg} \qquad \text{Eq. 4-6}$$

Experimentally, $\Delta G_{avg}$ is 1.23 eV but it may vary in computations depending on the method used.[129,132] In this way, one can easily determine the rate limiting step and even tell the physical implications when hematite surface is modified in certain ways, such as introducing vacancies, dopants, and different orientations. For example, $\eta$ is 0.71 eV for undoped $Fe_2O_3$ (0001) surface but rises to 2.16 eV when doped with Ti because Ti is an electron donor, favoring the first steps but unfavoring the third deprotonation step.[129] Alternatively, dual site mechanism has been proposed to occur

at other planes, e.g. (110) and (104). In this case, O-O coupling across two surface sites are crucial.[132]

The chemical nature of active surface states seems to be heavily controversial over the years. This is understandable considering the variety of possibilities OER can happen. Propositions of highly oxidized Fe species including Fe(IV), Fe(V) and even Fe(VI) are dominant OER intermediates in the literature:[37]

$$Fe(III) + h^+ \rightarrow Fe(IV) \qquad \text{Eq. 4-7}$$

$$Fe(IV) + h^+ \rightarrow Fe(V) \qquad \text{Eq. 4-8}$$

$$2Fe(V) + 4OH^- \rightarrow 2Fe(III) + 2H_2O + O_2 \qquad \text{Eq. 4-9}$$

Or

$$Fe(VI) + 4OH^- + 4h^+ \rightarrow Fe(III) + 2H_2O + O_2 \qquad \text{Eq. 4-10}$$
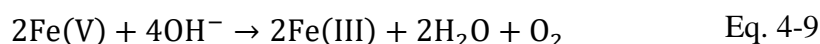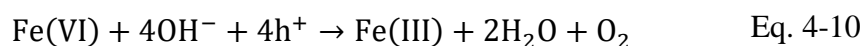
Zandi and Hamann applied operando infrared spectroscopy and confirmed the existence of Fe(IV)=O as an intermediate, which agrees with a previous kinetic model based on PEIS and IMPS data suggesting the accumulation of holes in the form of oxidized surface states.[133] Their proposed steps are in accordance with the single site mechanism of Eq. 4-1 to Eq. 4-5.

$$R - Fe^{III} + H_2O \xrightarrow{h^+} R - Fe^{III} - OH + H^+ \qquad \text{Eq. 4-11}$$

$$R - Fe^{III} - OH \xrightarrow{h^+} R - Fe^{IV} = O + H^+ \qquad \text{Eq. 4-12}$$

$$R - Fe^{IV} = O + H_2O \xrightarrow{h^+} R - Fe^{III} - O - O - H + H^+ \qquad \text{Eq. 4-13}$$

$$R - Fe^{III} - O - O - H \xrightarrow{h^+} R - Fe^{III} + O_2 + H^+ \qquad \text{Eq. 4-14}$$
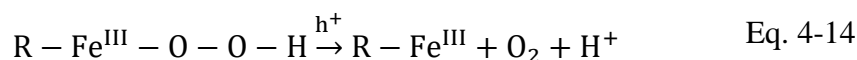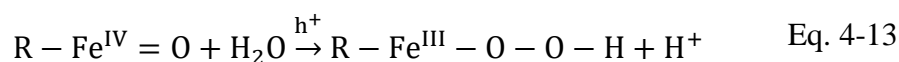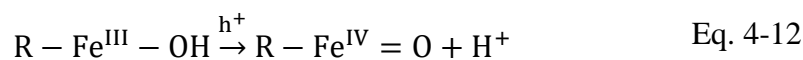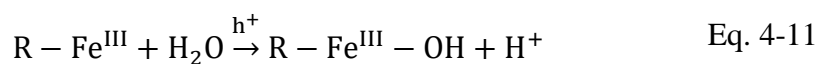
However, one cannot rule out the presence of Fe(V) or Fe(VI) because the difficulty of detecting them experimentally. Notably, Fe(VI) was observed in a spectroscopic study of NiFe-LDH electrocatalyst.[134]

A widely-used term called "trapping states" has raised plenty of confusion in the literature. Trapping states generally refer to one or more types of surface species that can trap charge carriers. However, the roles of trapping states have highly inconsistent interpretations. If trapping states trap electrons, they may either grasp electrons very tightly, so recombination becomes more difficult; or, they just extend the lifetime of electrons at the surface to a degree that the likelihood of recombination becomes higher. On the other hand, trapping states may either trap holes in order to prevent

charge transfer, or serve as an alternative platform for charge transfer. A more rational way to refer to surface states is to indicate their function, such as "recombination surface states" or "intermediate surface states" as suggested by Wang et al.[135]

### 4.2.2 Surface Treatments

Although OER at hematite surface is notoriously poor, there are many ways to address this problem. Here, a few other simple approaches without the inclusion of other compounds are first introduced, followed by more common ways such as coating electrocatalysts and non-catalytic layers.

The photoactivity of hematite electrodes are not only affected by morphology but also crystal orientation. Hematite has four orders of magnitude higher conductivity along [110] axis than [001].[136] Surprisingly, the hole flux that arrive at the electrode surface do not differ for several selected orientations by measuring photocurrent in the presence of hole scavenger and IMPS results.[137] The difference in performance, therefore, comes from the advantageous surface kinetics at (110) for OER. For example, DFT simulation suggests that (110) has smaller overpotentials both at bridge and terminal oxygen sites.[132] In Grave et al's work, onset potential for water oxidation under illumination cathodically shifted by up to 170 mV for (110) and (100) oriented hematite photoanodes compared to (001) oriented films.[137] The crystal orientation can be manipulated by carefully choosing the substrate to grow on, or sometimes by Si doping.[138,139]
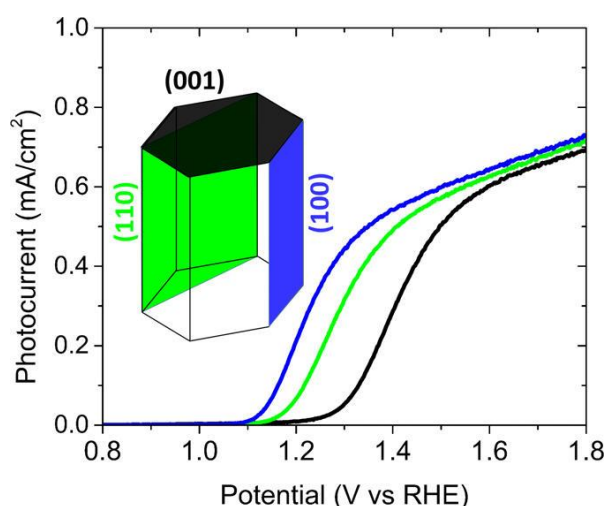


Fig. 4-6 Photocurrent density curves of hematite photoanodes with dominant orientation of (001) (black), (100) (blue), and (110) (green).[137] Reprinted with permission from ref. [137]. Copyright 2016 American Chemical Society

A second approach to modify low quality hematite surface is to recoat a layer. After the hydrothermal synthesis described above, if iron acetylacetonate is sprayed onto the FeOOH before calcination, a high quality crystalline $Fe_2O_3$ will be formed after heating, as observed by TEM and SAED.[140] This layer was found to cover surface states that act as recombination centers, further leading to one order of magnitude lower recombination rate constants measured by IMPS. Similarly, Wang's group revealed that photovoltage can be increased by more than 0.2 V upon repeated regrowth of hematite, indicating the removal of surface states.[141]

The search for efficient electrocatalysts for water oxidation has been a hotspot of materials research by itself. There are thousands of reported oxygen evolution catalysts in the literature. Noble metal compounds have been recognized as the most efficient candidates. Considering their elemental scarcity, research has been attempting to improve the utilization of noble metals.[142] Nanostructured catalysts have been dominating for decades, before being recently chased by single atom catalysts.[143] Meanwhile, non-noble transition metals (e.g., Co, Ni, Mn) are taking the place of noble metals (e.g., Pd, Ir, Ru) in recent years too.[144,145] Oxides, hydroxides and molecular species are most common compounds in metal-based catalysts. Additionally, there are a few non-metal catalysts, such as doped low dimensional carbon materials.[146] When applied to photoanodes, oxides and hydroxides are the most common choices due to the simplicity of preparation. Molecular catalysts are often synthesized via organic chemical reactions rather than in-situ growth, hence firm attachment with the electrodes cannot be readily achievable.[147] To name a few of most studied co-catalysts in combination with hematite, they are $IrO_x$, cobalt phosphate, cobalt oxide, iron oxyhydroxide.[123,148–150] An increasingly popular choice is nickel/cobalt (oxy)hydroxide, which has demonstrated competitive electrocatalytic performance compared with noble metal oxides.[151–154]

Since early this decade, researchers have noticed that coating cobalt-based electrocatalysts (typically CoPi) does not accelerate charge transfer at photoanodes using different spectroscopic techniques.[72,155,156] However, there is still much dispute over whether charge transfer takes place through the co-catalyst or hematite.[157–159] Barroso et al. used TAS and found no evidence of charge transfer through $CoO_x$. Instead, it acts as an electron reservoir and enhances band bending so that surface recombination is reduced.[157] In stark contrast, Klahr et al. confirmed the constant band

bending upon addition of CoPi and claimed that the co-catalyst does accept holes and conduct OER based on their transient photocurrent and PEIS results.[158] Such major discrepancies were ascribed to different film preparation techniques and geometry.[158] A reconciliation was gained by considering the structure of the electrode. For a compact hematite layer, electrons tend to move perpendicularly toward the conductive substrate. Consequently, recombination is not impacted by the thickness of CoPi. For a mesoporous structure, due to the retention of holes within CoPi, electrons have a higher propensity to recombine with those accumulated holes en route toward the substrate. Therefore, an optimal thickness (2.3 nm) was observed.[160] If OER does occur at the co-catalyst, it follows a Co oxidation cycle. An example is depicted in Fig. 4-7, where Co(II) and Co(III) are oxidized to Co(IV), which can occur via a fast surface site or a slow surface site.[148] Note these two mechanisms resemble dual site or single site mechanism for hematite. The OO bond-forming step with $H_2O$ in the fast cycle (Fig. 4-7) features the cooperative effect of adjacent electronically coupled Co(IV)=O sites, which is absent in the slow reaction regime.
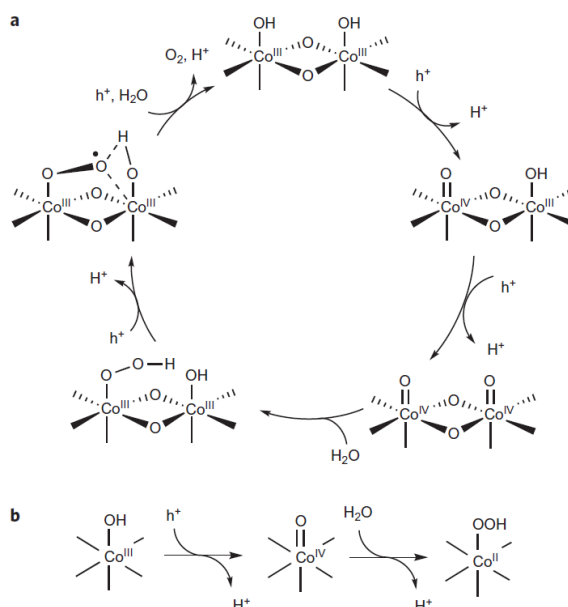


Fig. 4-7 Water oxidation mechanism of (a) the fast $Co_3O_4$ surface site and (b) the slow $Co_3O_4$ surface site.[148] Reprinted by permission from Springer Nature: Nature, Nature Chemistry, Time-resolved observations of water oxidation intermediates on a cobalt oxide nanoparticle catalyst, Zhang et al. COPYRIGHT 2014

More intriguingly, Tsyganok et al. have noticed different roles of the same co-catalyst on different types of hematite photoanodes.[47] They discovered that $FeNiO_x$ not only retards surface recombination, but also increases the hole flux to the surface

by IMPS for a Zn doped electrode, leading to higher photocurrent at more anodic potential when surface recombination is negligible. One explanation is that CoPi covers surface states of hematite and partly negates Fermi level pinning. Consequently, asymmetry in energetic profile is introduced, enhancing the built-in electric field. Another probable cause is a faster charge transfer that draws more holes to the surface.

The most common non-catalytic overlayers are 13-group element oxides, represented by $Al_2O_3$, $Ga_2O_3$ and $In_2O_3$. Compared to co-catalysts, the roles of these oxide layers have raised much less disagreement, since they do not possess catalytic or photocatalytic advantages.[161] Hence, it is apparent that these overlayers lower onset potential due to the passivation of surface states.[135,157,161,162]

This result has been frequently observed over many years experimentally and studied from different perspectives. Experimental and computational studies have both pointed out necessity to distinguish intermediate and recombination surface states (i-ss and r-ss respectively), and it is the passivation of the latter by overlayers that account for reduced onset potential. Photoluminescence spectra of $Al_2O_3$ coated hematite film showed weak and broad emission between 580 nm and 720 nm compared to the uncoated film, which indicates the removal of surface trap states responsible for non-radiative recombination.[163] These trap states are located from valence band maximum to 0.4 eV above it. Furthermore, we also notice that several reports have pointed out that by coating $Ga_2O_3$ or $Al_2O_3$, surface concentration of oxygen vacancies is decreased, which might be a cause for recombination.[161,163] Another factor for reduced surface recombination is because $Ga_2O_3$/$Al_2O_3$ has higher CB edge that stops electron flow toward solid-liquid interface.[162]

Due to the inactivity for catalysis of these 13-group oxides, OER is sometimes thought not to occur on their surfaces but still at $Fe_2O_3$ exposed to water through cracks of the overlayer. Given this, the benefit would come from electron depletion, which is supported by TAS.[157] This conclusion is supported by the fact that even ALD does not always produce highly uniform coatings considering the extremely low thicknesses of 2-3 nm. In order to confirm this proposition, IMPS could be conducted on high quality $Fe_2O_3$ film with $Ga_2O_3$ or $Al_2O_3$ coating. Observation of two conjugated semicircles which represent two time constant of OER would ensue.

The choice of 13-group metal oxides is mainly because they are expected to crystallize in the same way as hematite does, which would not lead to additional interfacial recombination loss. However, there are also problems, the main one being instability in alkaline environment. Hence the quest for effective overlayer materials continues. The two works in the next Chapter will investigate the influences of various surface treatments but before that, a critical analysis of literature allows us to attain some deeper insights into hematite photoanodes.

## 4.3 Publication: Understanding Charge Transfer, Defects and Surface States at Hematite Photoanodes
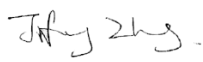
### 4.3.1 Preface

As a promising photoanode material, hematite ($\alpha$-Fe$_2$O$_3$) has a theoretical maximum photocurrent of 12.6 mA cm$^{-2}$. Although a multitude of studies have been carried out to optimize its performance, it is still quite far from being commercialized. In the past decades, researchers have been actively pursuing higher performance by various methods such as doping and surface treatment. However, even the best hematite electrodes only display less than 6 mA cm$^{-2}$. To understand the causes for such limited photoactivity, several major techniques have been developed or employed by physicists, chemists and material scientists. Electrochemical, computational and X-ray characterization methods are three main branches to gain mechanistic knowledge of photoelectrode processes; they are represented by Prof. Bisquert (PEIS), Prof. Peter and Prof. Wang (IMPS), Prof. Durrant (transient absorption spectroscopy, TAS), Prof. Braun and Prof. Constable (near edge X-ray absorption fine structure spectroscopy, NEXAFS), and Prof. Carter and Prof. Caspary Toroker (density functional theory simulations). Although each of these researchers has gained considerable understanding, the links between them are missing. To our knowledge, few papers apply a combination of these techniques in their research, possibly due to significant complexity. Therefore, we believe it is necessary at this moment to take a critical overview of current literature to clarify the progress and reveal the synergies.

Thanks to those existing mechanistic interpretations of photoelectrochemical responses of hematite electrodes, our Perspective manages to provide a more insightful view of the causes for good and poor performance of hematite photoanodes fabricated via various methods, in terms of bulk and surface properties. In this Perspective, after briefly describing the electronic transitions in hematite that are associated with photoresponse, we first examine the influence of oxygen vacancies regarding their defect chemistry. We then demonstrate the similarities between the oxygen vacancies and cation doping. Subsequently, we turn our focus on the surface dynamics, and corroborate the identity of major type of surface recombination, followed by its implication in the response of NEXAFS and impedance spectra. Several surface

treatment methods, including co-catalyst deposition are also compared. Two main complementary conclusions are made. First, oxygen vacancies, despite causing charge recombination, can create more positively charged oxygen anions and facilitate the transport of O 2p holes. Second, Fe(II) sites, potentially coupled with oxygen vacancies, are one main type of surface recombination sites, which consume O 2p holes and hinder water oxidation. Here we propose the most effective approaches to improve surface kinetics for oxygen evolution reaction, and suggest that the key step for efficient hematite photoanodes is to improve the bulk charge transport properties.

## 4.3.2 Declaration of Authorship

| This declaration concerns the article entitled: |||||
|---|---|---|---|---|
| Understanding Charge Transfer, Defects and Surface States at Hematite Photoanodes |||||
| Publication status |||||
| In preparation | Manuscript | Submitted | <u>In review</u> | Accepted | Published |
| Publication details (reference): | Sustainable Energy & Fuels ||||
| Candidate's contribution to the paper (detailed, and also given as a percentage). | <ul><li>Formulation of ideas: 100%<br>The candidate conducted both intensive and extensive literature survey of hematite photoanodes. I then proposed the theory as described in the manuscript.</li><li>Design of methodology: n/a<br>(This work does not involve laboratory work.)</li><li>Experimental work: n/a<br>(This work does not involve laboratory work.)</li><li>Manuscript writing and editing: 90%<br>The candidate independently drafted the manuscript. Some edits were done by Dr. Salvador Eslava but mostly by me.</li></ul> ||||
| Statement from Candidate: This paper reports on original research I conducted during the period of my Higher Degree by Research candidature. |||||
| Signed | *Jtfhy 2hg.* | | | Dec. 2018 |

**4.3.3 Manuscript**

# Understanding charge transfer, defects and surface states at hematite photoanodes

**Jifang Zhang, Salvador Eslava**

*Department of Chemical Engineering, University of Bath, Claverton Down, Bath, UK*

**ABSTRACT:** Hematite ($\alpha$-$Fe_2O_3$) has been widely investigated as a promising photoanode candidate in photoelectrochemical cells for solar water splitting. Although significant advances have been made to improve bulk charge properties as well as surface catalytic activity for oxygen evolution reaction, it still remains challenging to meet the standards for practical applications. As such, deeper understanding and analysis is necessary to guide efforts to achieve higher activities. This Perspective reviews and analyzes the important progress on hematite photoanodes from multiple angles. We highlight the critical role of defect chemistry in terms of bulk properties and surface reaction kinetics. Careful manipulation of the quantity of oxygen vacancies and majority/minority charge carriers is shown to be essential for higher activity. One major type of surface recombination site, which can be readily removed, is identified to be an $Fe^{2+}$ species based on multiple photoelectrochemical and spectroscopic observations. Analyzing X-ray absorption spectroscopy and electrochemical energy diagrams, we present a clear picture of water oxidation dynamics at different operating conditions, revealing the relationship between photo-generated holes and surface recombination states. Finally, we conclude that to make hematite photoanodes commercially viable, tuning the minority charge transport properties should be regarded as the priority.

---

Hydrogen production from solar water splitting has been an active research field in recent years with great promise to solve energy and environmental problems. It can be carried out in photoelectrochemical (PEC) cells with semiconductor materials, in which hydrogen and oxygen evolve at separate electrodes, hence making it convenient

for their collection. The choice of these electrode materials is key to efficient water splitting devices. Of its two electrode reactions, the oxygen evolution reaction (OER) is more challenging than the hydrogen evolution reaction (HER), since the OER involves four electrons to be transferred to produce each $O_2$ molecule. This process is known to take place in seconds, competing with much faster charge recombination processes in the semiconductor bulk material and at its surface.[164–166] Hematite (α-$Fe_2O_3$) has been one of the most extensively investigated photoanode materials due to its relatively small band gap, remarkable stability and great elemental abundance. However, it also comes with some notorious drawbacks such as low conductivity, small absorption coefficient, poor minority charge mobility (~$10^{-4}$ $cm^2V^{-1}s^{-1}$) as well as OER kinetics at the semiconductor-liquid junction (SCLJ).[167–169]

A large number of attempts to tackle these issues, including defect engineering, band engineering and surface treatment, have led to better performance.[170–173] Unfortunately, the underlying reasons for such improvements are not always well understood. For example, using perturbation-modulated techniques such as photoelectrochemical impedance spectroscopy (PEIS) and intensity modulated photocurrent spectroscopy (IMPS), one can obtain the rate constants for surface charge transfer and surface charge recombination.[166,174,175] However, the physical implications of differences in these rate constants with and without modifications of interest, even if calculated correctly, are often not obvious. Band or defect engineering via doping, in spite of being one of the most commonly used methods to improve bulk charge transport properties, is also frequently found to significantly change OER kinetics.[170,176–178] Therefore, PEC behavior must be interpreted by more advanced physical characterizations, such as X-ray absorption spectroscopies and infrared spectroscopy (ideally carried out *in situ* or *in operando*).[179,180]

This Perspective aims to provide an insight into the effect of defect engineering of hematite photoanodes not only on bulk properties but also on surface reactions, by gathering information from all aspects of PEC research, both computational and experimental. We prove here that direct control of oxygen vacancies and tuning dopant level follow practically the same principle to change the photoresponse of hematite electrodes, while their differences are also discussed. We also show that the presence of defects is highly associated with two types of electronic bands for charge transfer and how they are influenced by overlayers. Moreover, we reveal one possible

explanation for the chemical basis of recombination surface states and demonstrate the electrode dynamics at different voltages. Finally, we provide our opinion on future research directions.

## Charge Transfer in Hematite

Upon irradiation, there are four types of transitions in hematite as shown in Eq. 4-8a: (a) single ligand field (LF) transitions; (b) pair LF transitions; (c) ligand to metal charge transfer (LMCT); (d) metal to metal charge transfer (MMCT). The first two transitions do not generate electron-hole pairs thus they will not be discussed here. Detailed description of them can be found elsewhere.[167,181] The LMCT transition is prevalently recognized as the main, or sometimes, the only source of photocurrent.[182,183] According to the reaction

$$Fe^{3+} + O^{2-} \rightarrow Fe^{2+} + O^{-} \qquad \text{Eq. 4-15}$$
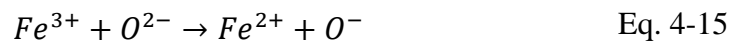
the excited electron resides at an Fe 3d orbital while the hole resides at an O 2p orbital, which is active for water oxidation. The MMCT indicates an electron transfer from one Fe site to another, resulting in split valences. This process is represented by

$$2Fe^{3+} \rightarrow Fe^{2+} + Fe^{4+} \qquad \text{Eq. 4-16}$$

In this case, a hole is generated in an Fe 3d orbital. These two transitions, the LMCT and the MMCT, are also responsible for the electron conduction of hematite; the former is known as $O^{2-}$-$Fe^{3+}$ electron hopping and the latter as charge disproportionation.[179,184]

Although MMCT has often been seen as not participating in solar water splitting by some early researchers,[183,185] a more recent work by Braun et al. has found evidence that it does account for a significant proportion of photocurrent.[179] They have used near-edge X-ray absorption fine structure (NEXAFS) spectroscopy to study the electronic structure of a hematite photoanode in a PEC cell *in operando*. The researchers discovered that only under illumination did the NEXAFS spectra of the same film contain two pre-edge peaks that represent O 2p holes through charge transfer band ($t_{1u\uparrow}^{CTB}$) as well as Fe 3d holes through upper Hubbard band ($a_{1g\uparrow}^{UHB}$), separated by about 1.3 eV. These peaks become apparent at applied potentials near and above the photocurrent onset potential only when irradiated (Eq. 4-8b). According to transient absorption spectroscopy (TAS) results, bulk recombination is found to be

ultrafast and a high percentage of holes are lost within 1 ns,[186] so only the rest which migrate to the surface can be detected by NEXAFS. The spectral weight distribution of CTB and UHB for illuminated samples versus applied bias is depicted in Eq. 4-8c. Interestingly, the spectral sum of these two has a peak located near the onset potential, which closely resembles surface capacitance (often referred to as trap states capacitance) measured using PEIS.[170,174,187] The relationship between these two curves will be discussed in later sections.
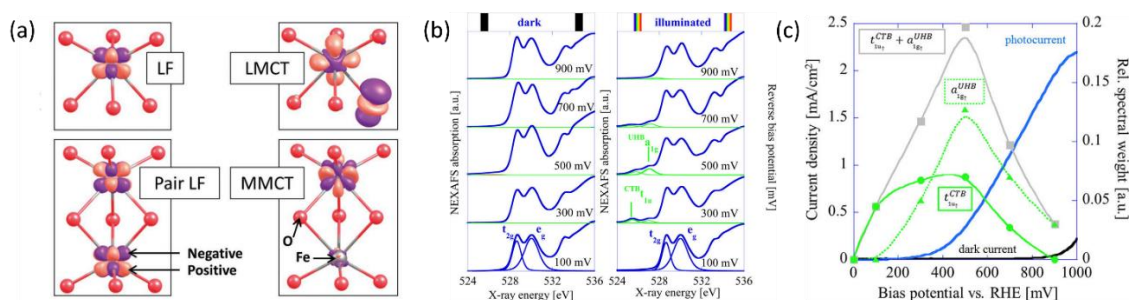


Fig. 4-8 (a) Calculated charge density difference isosurfaces (purple) of four types of transitions in hematite upon irradiation: single ligand field (LF) transition, pair LF transition, ligand to metal charge transfer (LMCT) and metal to metal charge transfer (MMCT). Red and grey atoms represent O and Fe atoms. From ref. [167]. Reprinted by permission of John Wiley & Sons, Inc. Also adapted with permission from ref.[181]. Copyright 2014 American Chemical Society. (b) O 1s NEXAFS spectra recorded at bias from 100 to 900 mV in the dark (left) and under illumination (right) conditions. (c) The spectral weight of $t_{1u\uparrow}^{CTB}$ (green squares) and $a_{1g\uparrow}^{UHB}$ (green triangles) measured by NEXAFS under illumination in relation to photocurrent density of a hematite photoanode. Bias potential can be converted to applied potential vs. RHE by adding flat-band potential of roughly 0.5-0.6 V. Reprinted with permission from ref. [179]. Copyright 2014 American Chemical Society.

Since holes from both CTB and UHB can directly contribute to photocurrent, it would be desirable to increase their density of states at PEC operational conditions. Judging from the relative positions and spectral weight of CTB and UHB, it is reasonable to hypothesize that CTB holes influence the low potential performance and even onset potential while UHB holes are associated with the high potential performance. As shown in Eq. 4-8b, the CTB peak is located at 525.8 eV, which is lower than the UHB peak at 527.1 eV. This means less X-ray energy is needed to inject a core electron into CTB than UHB, in turn proving that the energy level of the former is located lower. The CTB holes are found to be more reactive at lower potentials because their reaction is thermodynamically more favorable, as we will expand later. At higher potentials, more contribution must come from UHB holes as a majority of

CTB holes have already been participating in OER. More specifically, CTB contribution has dropped to none above 900 mV bias while photocurrent density is still rapidly increasing, meaning UHB contribution is dominating at this stage. Depending on the characteristics of the measured film, the total contribution of UHB holes can be much less if most holes prefer to present themselves in the CTB band. As such, the task of improving photocurrent densities relies on finding the determinants that change the spectral weights of these two bands.

**Oxygen Vacancies**

Two similar investigations in recent years have examined the effect of oxygen plasma on hematite photoanodes.[188,189] This treatment, in both cases, leads to increased photocurrent densities but higher onset potential too. Hu et al. observes a decrease in the concentration of surface $Fe^{2+}$ species upon oxygen-plasma treatment accompanied by an increase of $OH^-$ species by X-ray photoelectron spectroscopy (XPS).[189] Pyeon et al. observes the same but also shows that after a posterior short annealing step the photocurrent is recovered and moreover enhanced (Eq. 4-9a).[188] Both groups propose that oxygen plasma fills oxygen vacancies and attracts more $OH^-$ species as the oxidation state of Fe increases. After short-annealing, the newly formed oxygen vacancies are closer to the surface (Eq. 4-9b). Since both the oxygen vacancies and the CTB/UHB density have a direct influence on the photocurrent curves, we believe there could be a connection between the concentration of oxygen vacancies and the CTB/UHB density.

The link between photoelectrochemistry and the presence of oxygen vacancies can be explained by examining XPS results of hematite before and after annealing treatment.[188] The binding energy of 530.10 eV for lattice oxygen O 1s electrons for untreated hematite is higher than the 529.40 eV for oxygen plasma-treated hematite, then returning to 530.00 eV after short annealing in air at 750 °C. These shifts indicate the possible presence of slightly more positively charged oxygen near oxygen vacancies. Such changes of O 1s binding energy, paired with the increased photocurrent density after oxygen plasma and post-annealing (Eq. 4-9a), are an indication that upon irradiation and LMCT transition (Eq. 4-15), transport of O 2p (CTB) holes near the surface is facilitated by virtue of oxygen vacancies. Conversely, the MMCT (Eq. 4-16) is favored upon irradiation if $Fe^{2+}$ species from pristine hematite

have been converted into $Fe^{3+}$ by oxygen plasma, reducing the likelihood of recombination of a UHB hole ($Fe^{4+}$) with $Fe^{2+}$ (reversed Eq. 4-16). Although $Fe^{2+}$ might also induce recombination with CTB holes (reversed Eq. 4-15), MMCT is more negatively affected because total Fe concentration is constant and $Fe^{2+}$ ions directly suppress the generation of UHB holes ($Fe^{4+}$).

Contrary to oxygen-plasma treatment, annealing in an oxygen deficient environment creates oxygen vacancies, as can be illustrated by the defect equilibrium of the standard oxygen reduction reaction for n-type oxides (Kröger–Vink notation is adopted in this article):[190]

$$O_O^\times \leftrightharpoons V_O^{\bullet\bullet} + 1/2 O_2(g) + 2e^-$$  Eq. 4-17
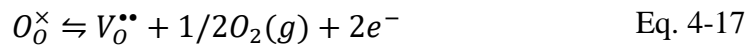
As the partial pressure of oxygen decreases, the reaction proceeds toward the right-hand side, creating more oxygen vacancies. Lower onset potentials have indeed been frequently measured after annealing in low partial $O_2$ concentration (Eq. 4-9c) or in $N_2$, or after air-plasma treatment, which gives the opposite effect of oxygen plasma treatment. However, the plateau photocurrent densities have also been improved.[172,176,191] It can be noticed in Eq. 4-17 that creating more $V_O^{\bullet\bullet}$ is accompanied by an increase in the concentration of electrons, leading to higher bulk conductivity. Therefore, plateau photocurrent still increases in spite of less contribution from UHB holes. However, excessive oxygen vacancies are detrimental, as evidenced by lower photocurrent densities.[176,192] This has been associated with lattice distortion and crystallographic phase mixing of α-$Fe_2O_3$ and $Fe_3O_4$. A computational study has predicted an optimal concentration of surface oxygen vacancies of 1.26 $nm^{-2}$ at (0001) surface, as a result of balancing its opposite effects of overpotential on hydroxyl terminated sites and oxygen terminated sites.[193]
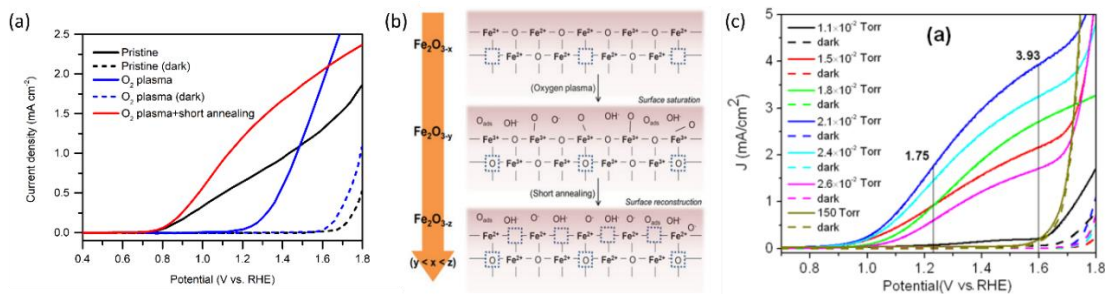


Fig. 4-9 (a) Photocurrent density curves of pristine (black), oxygen-plasma treated (blue) and short-annealed after oxygen-plasma treated hematite photoanodes (red). (b) Scheme showing filling and reintroduction of oxygen vacancies after oxygen-

plasma treatment and re-introduction after short-annealing. Adapted from ref. [188], reproduced with permission. (c) Current density curves of hematite photoanodes after annealing at different partial oxygen pressure. Dashed lines indicate measurements in the dark. Reproduced from ref. [176] with permission from The Royal Society of Chemistry.

**Cation Doping**

In addition to oxygen vacancies, doping also has an impact on bulk electronic properties as well as on surface kinetics. This Perspective focuses on cation doping of hematite, to which a majority of studies are dedicated. We emphasize aliovalent doping (n-type and p-type) here but isovalent and dual-element doping will also be covered briefly.

One of the most common n-type cation dopants for hematite photoanodes is titanium.[170,176,194–199] Electronic (Eq. 4-18) and ionic (Eq. 4-19) compensation are competing processes upon Ti doping:[190]

$$6TiO_2 \rightarrow 6Ti^{\bullet}_{Fe} + 9O^{\times}_O + 3/2O_2(g) + 6e^-  \qquad \text{Eq. 4-18}$$

$$6TiO_2 \rightarrow 6Ti^{\bullet}_{Fe} + 12O^{\times}_O + 2V'''_{Fe} \qquad \text{Eq. 4-19}$$
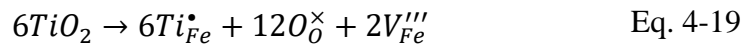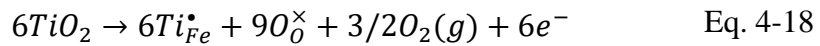
Each of them is irreversible but the resulting equilibrium obtained by subtracting one from the other can be seen as reversible:

$$3O^{\times}_O + 2V'''_{Fe} \leftrightharpoons 3/2O_2(g) + 6e^- \qquad \text{Eq. 4-20}$$
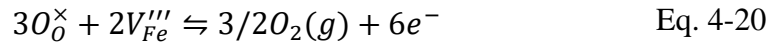
Here we only focus on substitutional rather than interstitial doping since the former was found to be more stable by simulation.[168] The equations above deserve careful examination as they have implications in both bulk electronic properties and surface kinetics. The conductivity of Ti-doped hematite does not necessarily increase unless electronic compensation outweighs ionic compensation.[190] Moreover, simulation by Liao et al. has compared the conductivities of several 4-valence cation doped hematite structures and has argued that electrons are more localized at Ti sites, which means they behave like traps.[168] In contrast, dopants such as germanium and silicon form more covalent bonds with oxygen and free electrons occupy the anti-bonding orbitals, which become more mobile. However, we could not find experimental validation in the literature.

The equilibrium of Eq. 4-20 (applicable for other n-type dopants) is influenced by multiple factors including dopant concentration, partial pressure of oxygen during

annealing, and annealing temperature.[190] At high dopant levels, ionic compensation dominates electronic compensation, meaning a maximum of conductivity is only achieved at low dopant concentration. This phenomenon has been studied for Sn doping, where maximal conductance is achieved at 3 at.%.[177] Low oxygen pressure annealing is preferred (confirmed by DFT+U simulation) as more electrons can be generated.[194] The transition from electronic compensation to ionic compensation has been theoretically illustrated with a Brower diagram as a function of oxygen partial pressure $pO_2$.[200] The authors demonstrate that at high oxygen level, negative charges are predominantly compensated by iron vacancies therefore free electron concentration falls. In the low $pO_2$ region, this compensation is also present, causing the increase of majority charge carrier concentration to be dependent on the doping density by a power of 1/3. Hence, the authors appeal that researchers should take $V_{Fe}'''$ compensation into consideration when doping hematite. The roles of $V_{Fe}'''$ on hematite band structures and for OER have been computationally examined elsewhere but will not be elaborated here.[201,202] It is worth noting that the optimal photocurrent has been achieved at a doping level of Sn different to 3%: 0.7 at.% for $5\times10^{-1}$ Torr $pO_2$ and 0.1 at.% for $5\times10^{-5}$ Torr $pO_2$ annealing.[177] Therefore, doping requires fine tuning to obtain optimal photocurrent. Finally, high annealing temperature (above 700 °C for hematite electrodes in practice) drives Eq. 4-20 to the right-hand side because of an increase in entropy, which means electronic compensation expressed by Eq. 4-18 is more favored. Unintentional doping from diffusion of Sn from the fluorine-doped tin oxide (FTO) conductive support can be introduced to improve conductivity, only if the total dopant concentration is within the peak level. Furthermore, high annealing temperature also has an impact on surface properties, which will be discussed in more detail later.

Due to the Schottky defects equilibrium as shown in Eq. 4-21, iron vacancies created through the ionic compensation upon Ti doping (Eq. 4-19) inevitably reduce the amount of oxygen vacancies:

$$nil \leftrightharpoons 2V_{Fe}''' + 3V_O^{\bullet\bullet} \qquad\qquad \text{Eq. 4-21}$$

Thus, Ti doping is expected to have a similar impact on surface kinetics to oxygen-plasma treatment that reduces oxygen vacancies. Indeed, it is frequently observed in photocurrent curves of Ti-doped samples (e.g., Fig. 4-10a) that the plateau photocurrent increases while onset potential also shifts anodically.

The plateau photocurrent is associated with a number of factors described above so the degree of improvements would vary. The onset potential, associated with surface kinetics, is more interesting to investigate. Often it is anodically shifted by 0.1 to 0.2 $V_{RHE}$ for films with n-type dopants, but only when annealed at high temperatures (700-800 °C).[173,178,203] This is in good agreement with the distribution shift between CTB and UHB, and it is additionally proved by the fact that even with the presence of hole scavenger $Na_2SO_3$, the onset potential also has a noticeable shift (Fig. 4-10b and c).[172] For films annealed at relatively lower temperatures, photocurrent is considerably lower or negligible for solution-processed electrodes.[195,203,204] In contrast, films prepared by atmospheric-pressure chemical vapor deposition show appreciable photocurrent at the same annealing temperature.[204] Given this, we believe that the consequences of high temperature annealing are two-fold: (a) enhancing the hematite crystallinity and (b) removing recombination surface states (r-SS). Zandi and Hamann have identified two types of surface states by rapid scan cyclic voltammetry and have shown that r-SS centered near 0.75 $V_{RHE}$ are removed upon 800 °C annealing (Fig. 4-11a).[205] Notably, a bare hematite photoanode with a record low onset potential of 0.58 $V_{RHE}$ has been fabricated by 10 s of $H_2$-$O_2$ flame treatment at 1700 K.[206] Coincidentally, Brillet and co-workers' study on functional annealing gives indirect evidence of r-SS oxidation.[108] When their hematite electrode is calcined in a $SiO_2$ template to preserve nanoporosity, the onset potential is 160 mV lower than without template, indicating unsuccessful removal of r-SS.
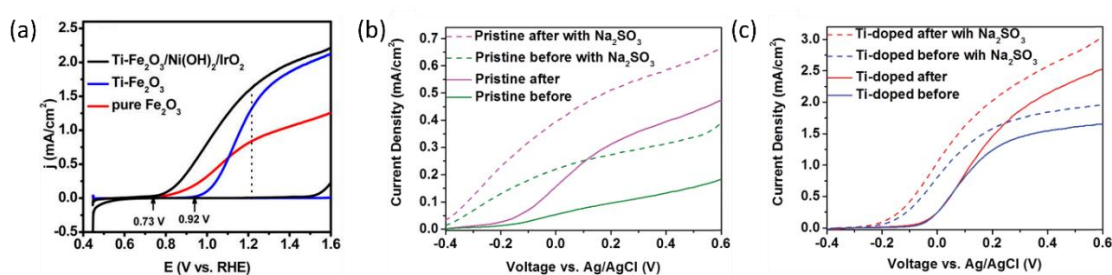


Fig. 4-10 (a) (Photo)current density curves of pure (red) Ti doped (blue), and Ti doped $Ni(OH)_2$-$IrO_2$ coated (black) hematite photoanodes. Reprinted with permission from ref.[173]. Copyright 2015 American Chemical Society. (b) Photocurrent density curves of pristine hematite photoanodes before (green) and after (purple) $N_2$ annealing. (c) Photocurrent density curves of Ti doped hematite photoanodes before (blue) and after (red) $N_2$ annealing. Dashed lines in (b) and (c) indicate measurements with $Na_2SO_3$ in the electrolyte. Reproduced from ref. [172] with permission from the PCCP Owner Societies.

Amongst the n-type dopants, manganese is an exception that negatively shifts onset potential. In spite of an increase of predicted reaction energy (related to overpotential),[207] the surface charge transfer accelerates and charge recombination slows down according to IMPS results.[166] It has been postulated that Mn forms multivalent oxidation states that leads to a low (O-Mn-O) energy barrier for hole transfer.[208] Vibronic superexchange effect is also possibly playing a part, since it has been recently found to enhance electrocatalytic performance of $La_2NiMnO_6$.[209]

Acceptor-type (p-type) dopants such as Zn and Cu create more oxygen vacancies as a result of the dissolution reaction:[190]

$$2ZnO \rightarrow 2Zn'_{Fe} + 2O^{\times}_O + V^{\bullet\bullet}_O \qquad \text{Eq. 4-22}$$
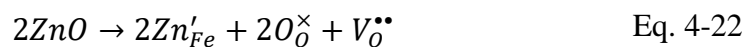
If oxygen is present, it also proceeds via

$$2ZnO + 1/2O_2(g) + 2e^- \rightarrow 2Zn'_{Fe} + 3O^{\times}_O \qquad \text{Eq. 4-23}$$
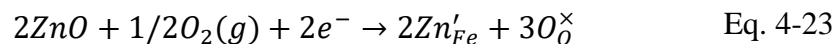
which depletes electrons in n-type $\alpha$-$Fe_2O_3$ and reduces conductivity. When dopant level is sufficiently high, mobile holes will be generated, forming a p-type $\alpha$-$Fe_2O_3$. A bulk p-type $\alpha$-$Fe_2O_3$ is unsuitable for photoanodes because downward band bending is formed at SCLJ junction and holes tend to move away from the surface. The opposite effects of n-type doping by p-type doping are initially expected. Liao et al. has calculated the volcano plot of reaction energy for OER at a hematite (0001) surface doped with a selection of dopants.[207] The dopants were found to alter the stabilities of holes on the active O anions. As a consequence, Co and Ni p-type doping yield lower reaction energies whilst Ti and Si n-type doping yield higher ones. Multiple other experimental and computational works with p-type dopants also support the improvements of surface kinetics.[171,197,210] Although extra $V^{\bullet\bullet}_O$ introduced by doping indirectly assist OER, the downside is the drop of bulk conductivity (Eq. 4-17 and Eq. 4-23). For example, doping of Be at 6% can reduce the plateau photocurrent by nearly 30% at 1.6 $V_{RHE}$,[178] and therefore the dopant concentration should be limited, preferably close to the surface.

It can be seen now that overall improvement of photocurrent cannot be easily achieved by using only one treatment. Although annealing in an oxygen deficient atmosphere seems to be one possibility as we have mentioned, the improvement in plateau photocurrent is often quite limited compared to n-type doping (Fig 3b and 3c).[172] Dual-element doping has been attempted by adding a mixture of n-type and p-

type dopants. Mirbagheri et al. has co-doped Ti and Zn into hematite and characterized films with PEIS.[197] The advantages of each individual doping, i.e., decreased bulk charge transport resistance for Ti-Fe$_2$O$_3$ and decreased surface charge transfer resistance for Zn-Fe$_2$O$_3$, are both obtained in Ti/Zn-Fe$_2$O$_3$ film at 1.0 V$_{RHE}$ (Fig. 4-11b). The plateau photocurrent exceeds films doped with either Ti or Zn, which can be attributed to released lattice strain (Fig. 4-11c).[178] Interestingly, its onset potential is maintained at 0.9 V$_{RHE}$ as opposed to shifting toward 0.8 V$_{RHE}$ for Zn-Fe$_2$O$_3$. This result implies that dopant or oxygen vacancy concentration is not simply linearly related to onset potential. In another work in which Sn and Be is co-doped, a similar behavior is recorded. Enhancement in plateau photocurrent density exceeds that of individual doping but onset potential ($E_{on}$) is also unchanged compared with Sn-Fe$_2$O$_3$.[178] A plausible explanation is that n-type dopants prefer to dominate electrode surface; this has been confirmed in works on Sn and Mn doping, which reveal a gradient of dopant concentration across the film as well as in individual particles (Fig. 4-11d).[166,211]
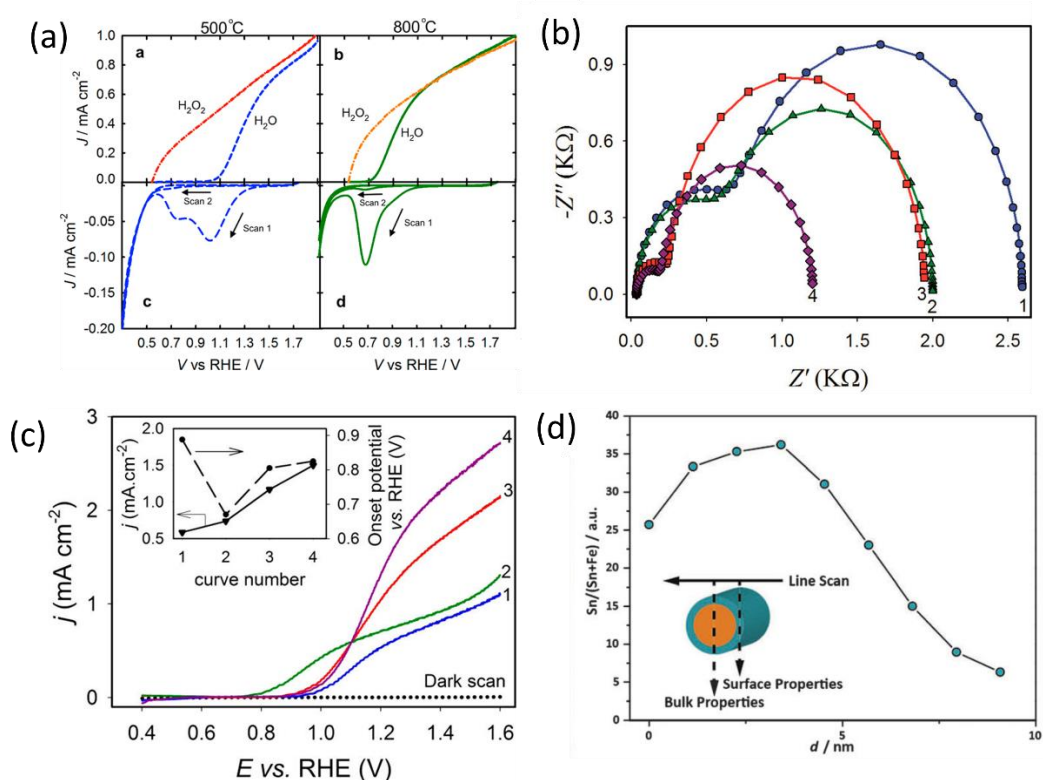


Fig. 4-11 (a) Linear sweep voltammograms for hematite electrodes annealed at (top left) 500 °C and (top right) 800 °C in air measured in H$_2$O and H$_2$O$_2$. Cyclic voltammograms scanned at 1 V/s in the dark of the electrodes annealed at 500 °C (bottom left) and 800 °C (bottom right). Reprinted with permission from ref. [212]. Copyright 2014 American Chemical Society. (b) Nyquist plots for and (c)

photocurrent density curves of (1) pristine hematite, (2) 10.71% Zn, (3) 1.96% Ti, and (4) 1.40% Ti + 5.58% Zn-modified hematite electrodes. Reprinted with permission from ref. [197]. Copyright 2014 American Chemical Society. (d) Atomic concentration of Sn as a function of position for a 20% Sn-Fe$_2$O$_3$ photoanode. Reproduced from ref. [211] with permission from the PCCP Owner Societies.

A more desirable configuration combining both n-type and p-type doping has been fabricated by Kay et al. to produce layered single-junctions (Fig. 4-12a).[213] Photocurrents improve at both potential ends when hematite is divided into three layers where top layer is doped with Zn and bottom layer with Ti, although $E_{on}$ is not as low as with individual Zn doping (Fig. 4-12b). An interesting feature to note here is that $E_{on}$ drops with increasing thickness of Zn doped layer. This means that p-type doping should not merely be placed at the outermost layer but also somewhat deeper so that O 2p holes transport more easily through slightly positively charged oxygen anions. On the other hand, this penetration depth should not be too high because, as seen before with Ti/Zn-Fe$_2$O$_3$, bulk co-doping does not reduce $E_{on}$. Therefore, control of surface doping of lower valence elements appears to be intricate and challenging.
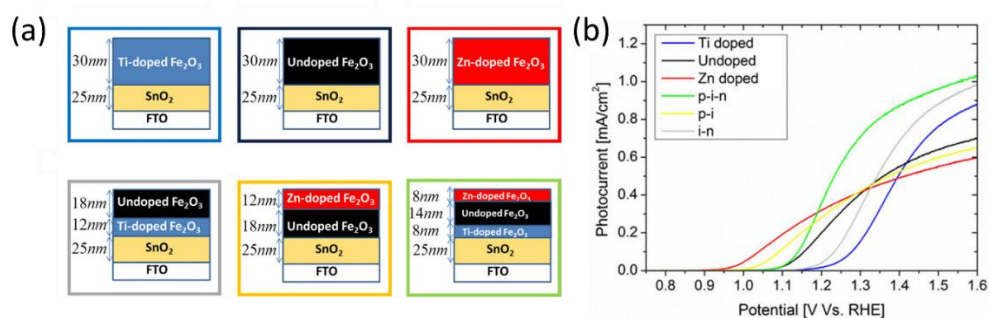


Fig. 4-12 (a) homogeneously Ti-doped (~1 cation%) hematite film (blue), undoped hematite film (black), homogeneously Zn-doped (~1 cation%) hematite film (red), heterogeneously doped i−n stack (grey) heterogeneously doped p−i stack (yellow), and heterogeneously doped p−i−n stack (green). (b) photocurrent density curves of films in (a), following color scheme of boxes in (a). Reprinted with permission from ref. [213]. Copyright 2016 American Chemical Society.

The less researched dopants are isovalent elements such as Al and Ga. They also show some promise of improving plateau photocurrent density which is attributed to better conductivity due to small polaron migration.[214,215] When doped with Al, there is no apparent change in defect chemistry other than cation replacement and hence no change in $E_{on}$.

**Surface States**

The origin of surface states as intermediate species or as recombination centers has been under heavy debate. In this Perspective, we attempt to combine several existing theories and construct a clearer picture. Durrant group has previously summarized some of their pioneering TAS research and has suggested that recombination centers exist and lie a few hundred millivolts below CB of a Si-$Fe_2O_3$ (annealed at 500 $^{\circ}$C).[164] Their dynamic model based on TAS is shown in Fig. 4-12a.[164] At low potentials, when Fermi level is above r-SS level, electrons are intrinsically trapped. Thus, further trapping becomes more difficult ($\mu$s) compared to recombination from VB holes (ps-ns). As applied potential becomes more anodic, band bending depletes these states near the surface, and electron trapping (ps-ns) becomes faster than hole trapping ($\mu$s-ms). The population of depleted r-SS is reflected by the bleach signal detected at 580 nm (electronic transition illustrated in Fig. 4-13b and signal in Fig. 4-13c). Notably, its intensity follows the square root relationship with applied potential, meaning the r-SS are formed within space charge layer. These states are tentatively assigned to $Fe^{2+}$-$V_o$ that turn into $Fe^{3+}$-$V_o$ when become depleted.[164] They have also been previously regarded as chromophores in Fe-$TiO_2$.[216] We have found further evidence in the literature from recent years supporting this assignment, as we shall illustrate below.

The positive signal above 650 nm on TAS results indicates the population and lifetime of holes (electronic transition illustrated in Fig. 4-13b and signal in Fig. 4-13d).[164,188] Its intensity at short time domains doubles after oxygen-plasma treatment, likely due to the reduction in the quantity of oxygen vacancies, which are ultrafast recombination centers.[188] This is supported by a simulation demonstrating that oxygen vacancies are even faster charge recombination centers than direct VB-CB recombination by 10 and 30 times for charged and neutral forms, respectively.[217] The timescale (ps-ns) of electron trapping from CB to r-SS measured by another work of Durrant group[186] is also computationally supported by Zhou et al.[217] Consequently, oxygen vacancies are very likely to be an integral component of r-SS.
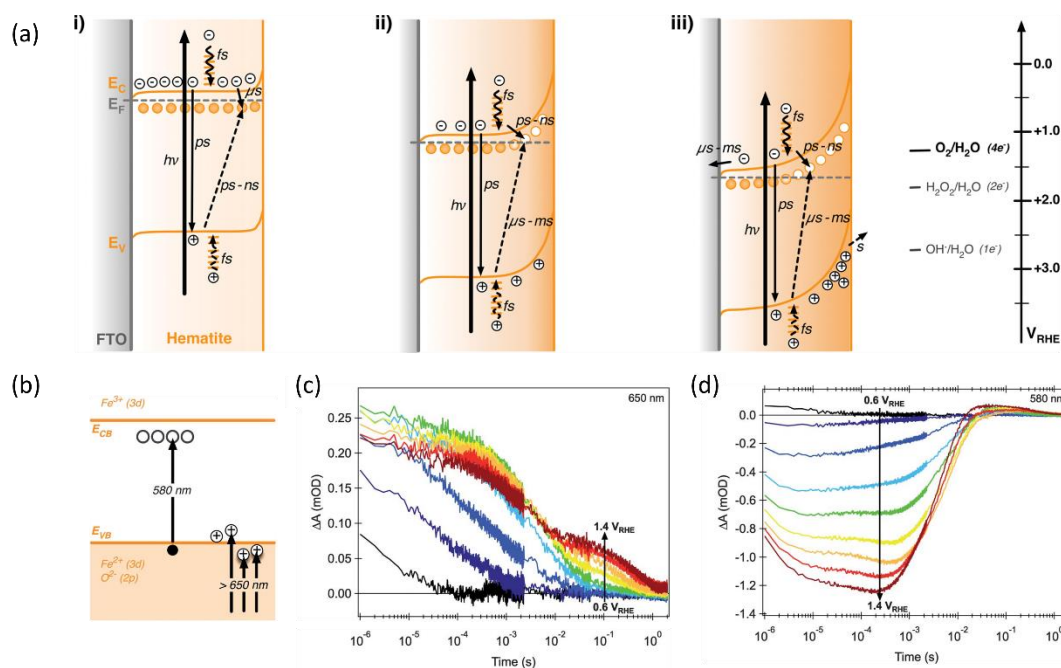
Fig. 4-13 Energy diagrams and processes involving photogenerated charge carriers for a hematite photoanode at various applied potentials at i) 0.5, ii) 1.1 and iii) 1.6 $V_{RHE}$. Circles indicate electron trap states. (b) Scheme of electronic transitions responsible for the Vis-NIR transient absorption spectra of hematite photoanodes. Reproduced from ref. [164] with permission from The Royal Society of Chemistry. (c) Transient absorption decay dynamics of 650 nm. (d) Transient absorption decay dynamics of 580 nm. Reproduced from ref. [218] with permission from The Royal Society of Chemistry.

The other part of r-SS, $Fe^{2+}$, can be more confidently confirmed with several approaches. Hu et al. has found a numeric match between the density of states and surface $Fe^{2+}$ species concentration, thus confirming that r-SS are highly associated with $Fe^{2+}$.[219] As previously mentioned, high temperature annealing is capable of removing this type of r-SS ($Fe^{2+}$-$V_o$), presumably by oxidation of $Fe^{2+}$ to $Fe^{3+}$. For a 500 $^{o}C$ treated sample, the empty form of electron traps can live up to 10 ms indicated by 580 nm bleach signals, whereas the signal disappears for a 750 $^{o}C$ treated sample for a wide range of applied potentials.[188] Although a feature emerges at 1.5 $V_{RHE}$, the timescale is 100 µs as opposed to 10 ms, so it must originate from recombination surface states of a different nature.[188] Hence, high temperature treatment can successfully reduce the population of $Fe^{2+}$, not to mention the improvement in crystallinity. Here, we should note that although high temperature introduces more oxygen vacancies, they are not as influential as $Fe^{2+}$, which act as redox centers. Although oxidation potential of $Fe^{2+}$ at hematite surface is undefined, we notice that the standard redox potential of $Fe^{3+}/Fe^{2+}$ (0.77 $V_{RHE}$) is located several hundred

millivolts below CB edge (0.3-0.4 $V_{RHE}$) and extremely close to that observed by Zandi et al (0.75 $V_{RHE}$).[205] Moreover, the computationally predicted position of $V_O^{\bullet\bullet}$ at 400 mV below CB by Zhou et al.[48] suggests possible interaction between $V_o$ and $Fe^{2+}$ due to their close proximity in energy alignment.

The spectral weight distribution of CTB, interestingly, follows a square root dependence on bias potential, in line with the development of 580 nm signal in TAS.[164] It suggests strengthened band bending with applied potential, while r-SS is consequently being depleted (Fig. 4-13a). However, it is hard to judge which of the two types of holes is performing the depletion. Although we believe it is more likely to be the UHB holes due to their closer proximity in energy and the absence of its spectral weight at low bias, possibility of recombination between CTB and r-SS cannot be ruled out. This question could be readily answered by NEXAFS measurements on the same samples after r-SS removal by high temperature annealing, although it remains unexplored in literature.

The surface states directly detected by TAS suggest that they are not only at the top surface layer but extend into the bulk as the space charge region builds up as a function of applied bias. However, since the space charge region is only a few nanometers wide, these states can be still termed as "surface states". This point has been previously mentioned by Barroso et al.[204]

Knowing the chemical origin of r-SS, we now focus on the crucial different effects that annealing and cation doping can have on the presence of oxygen vacancies and the relative amounts of CTB and UHB holes. N-type dopants (for example, Ti, Si and Sn) increase the concentration of nearby $Fe^{2+}$.[178,220,221] On the other hand, filling oxygen vacancies by oxygen plasma treatment or likewise reduces $Fe^{2+}$ concentration.[189] Although the increase of $Fe^{2+}$ is known to assist polaron hopping and subsequently electrical conductivity,[222] its existence near the surface (forming r-SS) would quench both CTB and UHB holes. An amorphous layer of $Fe_xSn_{1-x}O_4$ of 1-2 nm reduces the charge injection efficiency below ca. 1.1 $V_{RHE}$.[223] But more efficient charge injection was recorded at higher potentials, where $Fe^{2+}$ (r-SS) species are oxidized by the bias, so that UHB can be effectively used for OER. Such response is a firm proof of our theory on the role of UHB and CTB holes as there are no bulk effects involved in this case. Conversely, p-type doping would reduce $Fe^{2+}$

concentration, therefore expected to enhance both CTB and UHB hole fluxes. At lower potentials, in particular, the removal of r-SS allows for a much higher generation of effective CTB holes for water oxidation. Hence, lowered onset potential is often observed.[171,197,224] Direct evidence can be found in a work where an Ni-doped overlayer of $Ni_xFe_{2-x}O_3$ cathodically shifts onset potential of hematite by 100 mV while surprisingly enhancing photocurrent density by 2-3 fold.[224] Creating a p-type $\alpha$-$Fe_2O_3$ layer by 3% Mg doping on the top 20 nm layer has reduced onset potential by more than 200 mV, while slightly raising plateau saturation too.[171] Although the establishment of internal fields by homojunctions is claimed responsible for the improvement in the latter case, we believe changes in the contribution of holes are also playing a role here since uniform bulk p-type doping sometimes produces similar effects (Fig. 4-11c).[197]

In contrast to r-SS, the forms and chemistry of intermediate surface states (i-SS) that mediate OER are far more complicated and are still under heavy debate. Multiple oxidation states of Fe, such as IV, V, and even VI have been proposed to be present during OER, some of which have been experimentally observed.[180,225–227] It is also possible for a variety of OER mechanisms to occur simultaneously with either single or multiple oxidation states of Fe.

Regardless of the nature of i-SS, a procedural scheme can be demonstrated to show the fate of CTB and UHB holes in hematite photoanodes when r-SS are present. Figure 7 shows a schematic illustration of mixed energy diagrams of hematite photoanodes with CTB (red) and UHB (blue) and with the presence of r-SS at three applied potentials (0.55, 0.9, and 1.3 $V_{RHE}$). The X-ray energy scale is also displayed, where peak edge is simply set to be at half-height (528.2 eV), matching the CB minimum at electrode surface. A few basic assumptions were made in Fig. 4-14 for a typical hematite photoanode: (a) a band gap of 2.2 eV;[218] (b) CB minimum at 0.3 $V_{RHE}$,[228] (c) a flat band potential of 0.5 $V_{RHE}$,[229] and (d) r-SS at 0.75 $V_{RHE}$. As shown in Fig. 4-14a at $E_F$=0.55 $V_{RHE}$, which is close to the flat-band potential, the holes at the surface are very limited because they come from only a short diffusion layer of about 2 nm into the surface with little assistance from band bending. [179] Holes can easily recombine with r-SS since they lie below Fermi level and will be immediately refilled with electrons (Fig. 4-14a). As potential is swept anodically, r-SS near the surface begin to be depleted primarily by UHB holes because of smaller energy differences (marked

by thin purple arrow in Fig. 4-14b). Dare-Edwards and co-workers has pointed out that VB holes arrive at surface in $Fe^{3+}$ orbitals; these $Fe^{3+}$ have negligible rate constants for water oxidation.[229] Meanwhile, CTB holes do not generate photocurrent as well because of their low surface concentration. They mostly undergo surface recombination (illustrated by a thick purple arrow, Fig. 4-14b). Therefore, even if r-SS are removed by high temperature annealing, photocurrent onset still cannot approach the same value in $H_2O_2$ (c.f. green curve, Fig. 4-14d). When potential increases further, r-SS near the surface soon become fully depleted above 0.9 $V_{RHE}$ according to constant 650 nm signal intensity below $10^{-3}$ s from TAS results shown in Fig 6c.[164] At this point, CTB holes reach a critical concentration, leading to photocurrent onset as holes arriving in O 2p have a facile faradaic route to $O_2$ formation (thin red arrow in Fig. 4-14b).[229] A small amount of UHB holes also exist but do not yet contribute to photocurrent.[179,230] As bias is further swept anodically, rapid water splitting kinetics is capable of dissipating the CTB (O2p) accumulated holes, reducing its spectral weight observed with NEXAFS (Fig. 4-14c). Likewise, this trend appears for UHB holes but approximately 0.1-0.2 V more positive (Fig. 4-14d). Note that the peak intensity is much higher than that of CTB, which is possibly due to the lower overpotential of UHB holes compared to 1.23 $V_{RHE}$. Information about surface OER kinetics of excessive long-lived holes can be extracted from the second decay phase of 650 nm signal (Fig. 4-13c).[164] Fig. 4-14d shows the J-V responses of a typical hematite electrode (produced at 500 °C) marking out the points where each scenario projects to. The presence of r-SS is partly responsible for the strong contrast between J-V curves measured in $H_2O$ and $H_2O_2$.
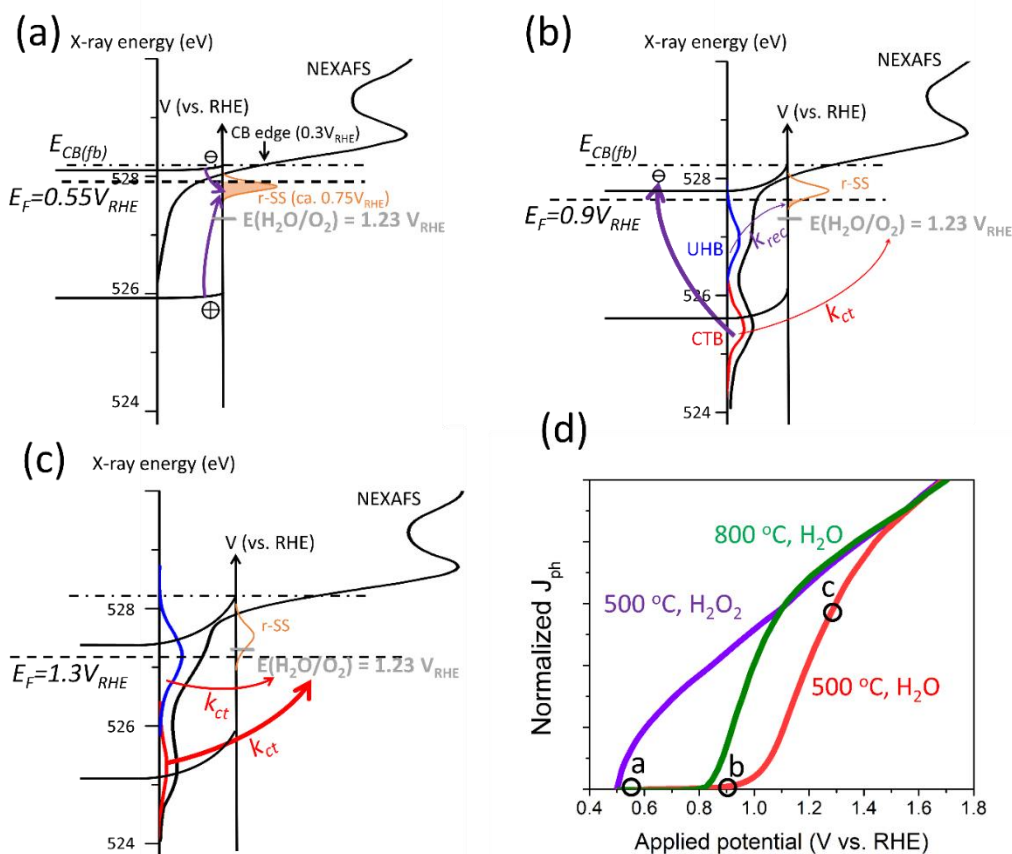
Fig. 4-14 Schematic illustration of mixed energy diagrams of hematite photoanodes at operating conditions with CTB (red) and UHB (blue) and with the presence of r-SS at applied potentials of (a) 0.55, (b) 0.9, and (c) 1.3 $V_{RHE}$. Arrows of different thicknesses indicate relative rates of important charge transfer and surface recombination processes. Purple arrows indicate surface recombination processes; red arrows indicate charge transfer processes. Grey dashes indicate OER potential of 1.23 $V_{RHE}$. NEXAFS data obtained from ref. 16. (d) Normalized typical J-V responses of a hematite photoanode calcined at 500 °C in $H_2O$ (red) and $H_2O_2$ (purple) and calcined at 800 °C in $H_2O$ (green). The position of the scenarios presented in (a), (b) and (c) are marked out in the J-V red curve of (d).

A better understanding of the photoelectrochemistry of a hematite photoanode in operation from spectroscopic findings allows for more rational investigation of PEIS outcomes. It is apparent that the overall spectral weight curve from NEXAFS closely resembles surface capacitance measured by PEIS. We believe that the surface capacitance is a reflection of CTB and UHB holes, in the form of both intermediate species and possibly positively charged r-SS but further investigation on this topic remains worthwhile.

At present, PEIS data is commonly interpreted following different models. In one model, charge transfer takes place directly from VB holes and surface states only

account for recombination (Fig. 4-15a). In an alternative model, both charge transfer and recombination take place via the same surface states (Fig. 4-15b). Deciding which model is more appropriate depends on the relative quantities of i-SS and r-SS as well as applied potential. Equivalent circuits of these two models are mathematically indistinguishable, and calculation of rate constants by either method produces same values.[230] However, Klahr et al. points out that the latter model is more physically meaningful because a peak maximum corresponds to a dip in charge transfer resistance.[187] We agree with this statement but moreover, we believe that the other model is possibly not suitable at all for hematite on the basis of more experimental evidence, as follows. For hematite films calcined at intermediate temperatures (around 500 °C), surface capacitance $C_{ss}$ peaks were not observed to start from 0.6 V, which would be the case if charged r-SS were oxidized by CTB holes according to NEXAFS spectral weights. Instead, $C_{ss}$ only starts near the onset potential of 0.9 to 1 V.[165,187] In contrast, for 800 °C calcined samples, density of surface states $N_{ss}$ (derived directly from $C_{ss}$) does rise from 0.6 V as extrapolated from Fig. 4-15c,[170] which demonstrates the appearance of CTB holes for OER. This is also in line with the intense peak centered at 0.75 V in Fig. 4-11a(d) recorded using CV in the dark.[212] Furthermore, Ti-doped films heated at 800 °C that are known to have more $Fe^{2+}$ show depressed $C_{ss}$ at low potentials (Fig. 4-15c), which further proves that PEIS does not detect r-SS. Note at high potentials, $C_{ss}$ increases substantially, peaking at 0.2 V above non-doped samples, indicating a much higher maximum surface concentration of UHB.
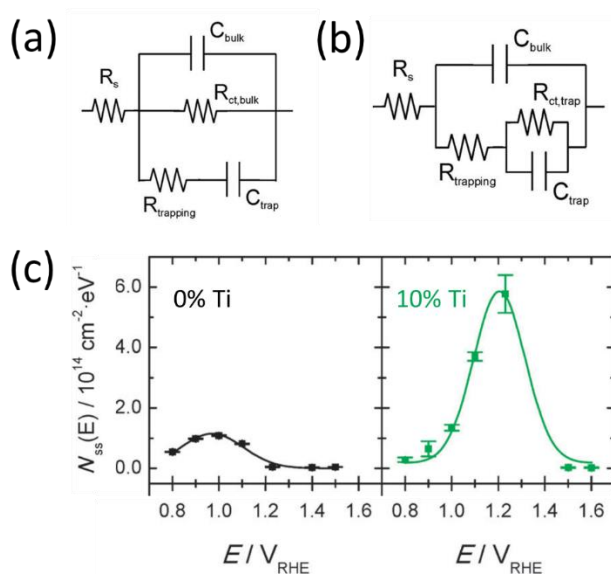
Fig. 4-15 Two types of equivalent circuit from PEIS to represent hematite photoanodes under illumination. Model in (a) suggests charge transfer through valence band and recombination through trap states. Model (b) suggests charge transfer and recombination both occur through surface trap states. Reprinted with permission from ref. [187]. Copyright 2012 American Chemical Society. (c) Density of surface states calculated from surface capacitance measured using PEIS with model (b) for pristine and Ti doped hematite photoanodes. Reproduced from ref. [170] with permission from The Royal Society of Chemistry.

Knowing the physical origin of r-SS, we are able to summarize the mixed effects of oxygen vacancies in hematite photoanodes. First, they discharge the surrounding oxygen atoms to yield more $O^-$ species that are beneficial for charge transfer of CTB holes. Second, they act as fast recombination sites either on their own or coupled with $Fe^{2+}$. Consequently, although the distribution of surface capacitance is located more cathodically, its intensity is lower than when there are less oxygen vacancies, as evidenced again in Fig. 4-15c. This trade-off is probably the source of difficulties when trying to improve the activity of a hematite photoanode, especially at low applied potentials. Apart from these roles already discussed, oxygen vacancies may also reduce the adsorption energy of $H_2O$ molecules, and subsequently reduce OER overpotential and Tafel slope, as observed for $NiCo_2O_4$.[201,231]

**Deposition of Overlayers**

It would be also helpful to consider the effect of overlayers on surface states, which is still under heavy debate. As Barroso has mentioned in an early report, there is some ambiguity regarding the definition of "surface state".[157] A majority of publications use this term for states that exist only at the top molecular layer, whereas $Fe^{2+}$-$V_o$ can spread deeper into the surface, for example, in the space charge region. This notion clarified, the roles of surface layers including co-catalysts, compact non-catalytic layers, and surface doped layers become clearer.

The deposition of an overlayer can partly or entirely cover the defects of the outermost hematite, including a fraction of $Fe^{2+}$-$V_o$ and other possible types of surface states. Here, we emphasize the difference between a co-catalyst (e.g., transition metal oxides and (oxy)hydroxides) and a compact non-catalytic layer (e.g., $Ga_2O_3$ and $Al_2O_3$). It has often been reported that the plateau photocurrent density drops with a $Ga_2O_3$ overlayer.[215,232] A possible justification is that when $Ga_2O_3$ covers $Fe^{2+}$ sites, it

influences O 2p (CTB) and UHB holes differently: (a) more O 2p (CTB) holes will be transferred to O atoms of $Ga_2O_3$ rather than used for oxidizing r-SS, improving the low potential performance; (b) as more Fe sites are covered, charge transfer through UHB holes is inhibited. In the case of cobalt-based co-catalysts such as CoPi, the increase in O 2p (CTB) hole flux toward Co sites does not lead to acceleration in catalysis.[157,165] Instead, recombination is retarded, which is associated with the low electrocatalytic activity of Co by itself compared with Fe sites, as reported by Boettcher group.[233] For instance, the measured turnover frequency was 0.035 s$^{-1}$ for $Co_3O_4$ at η=325 mV,[234] while 12 s$^{-1}$ for $CoFeO_x$ at η=350 mV.[153] Our group has recently reported a moderate improvement of charge transfer rate with $CoFeO_x$ coating only when the loading is extremely low;[174] and we have observed the same for thin $NiFeO_x$ coating. Thus, it can be said that the only part of the co-catalyst that assists OER is the layer where it connects to the hematite structure.

In contrast, if Co or Ni atoms are dispersed into hematite near the surface and interact with Fe atoms inside hematite structure, a far more significant benefit will be harnessed, in addition to reducing the number of $Fe^{2+}$. This comparison of surface doping and deposition has been made clear by Cheng et al. with Co;[224] the same prediction was also made through simulation in the same year by Liao et al.[207] Unfortunately, this approach has been considerably outnumbered in the literature by surface deposition methods to reduce onset potential.

**Bulk Charge Transport**

Currently, the best hematite-based photoanodes reported in the literature can only output photocurrents around 5 mA cm$^{-2}$ at 1.23 $V_{RHE}$ under 1-sun illumination (AM1.5G), which are much lower than the theoretical limit of 12.6 mA cm$^{-2}$.[235–238] It has frequently been reported that while charge injection efficiency can reach 90-100% with strong bias, charge separation efficiency is far lower regardless of applied potential.[172,223] Therefore, we and other researchers[166] believe that to further improve the performance of hematite as photoanodes and make them industrially viable, research should be mainly aiming at enhancing the bulk charge transport properties rather than surface OER kinetics, since researchers have established multiple tools to achieve this, e.g., by surface doping or controlled annealing.

To increase the electronic transport, or conductivity, the most obvious way is n-type doping. In Engel and Tuller's work, the conductivity of 1% Ti-doped hematite shows around four orders of magnitude higher conductivity at room temperature if calcined in air, which even reaches nine orders of magnitude higher in low $O_2$ concentration (0.1% and 0.01%).[200] In another work with the same doping level, photocurrent density for OER is indeed substantially increased. However, it only increases by less than three times at 1.23 $V_{RHE}$ in the presence of 0.5 M $H_2O_2$, which indicates that the hole flux increases by no more than one order of magnitude. The authors also confirmed that the surface hole concentration for water splitting reaction increases by only about four times using IMPS. The most probable reason for such low improvements in hole current as opposed to significant improvements in conductivity is the strengthened band bending due to the higher concentration of free electrons.

For hematite, conductivity along crystal orientation (110) has been reported to be four orders of magnitude higher than along (001).[136] However, these two orientations offer the same hole flux,[137] presumably because there is no difference in free electron density, giving a similar chance of bulk recombination.

Improving the hole (minority carrier) transport, i.e., mobility and lifetime, is a much more significant issue. For example, Peter et al. discovered that in stark contrast to the Gartner model, recombination is an apparent hindrance even within the space charge region.[31] Applied bias has been recognized as a way to retard ultrafast recombination in the bulk hematite, but not much progress has been made by means of film fabrication.[186] Another notable measure to enhance minority carrier mobility is by thermal energy, which can be achieved by concentrated solar illumination. Moreover, higher light intensity can also increase photovoltage and fill factor.[239] Future research in this direction would be highly meaningful.

**Conclusion and Outlook**

In summary, we have discussed the presence in hematite of charge transfer band (CTB) O2p holes and upper Hubbard band (UHB) Fe3d holes upon illumination and critically analyzed the role of oxygen vacancies and doping, as well as the origin of recombination surface states. Our main conclusion is that introducing oxygen vacancies at surfaces, by controlled annealing or p-type doping, gives rise to more

positively charged oxygen anions, which assist the transport of CTB holes; whereas reducing the amount of oxygen vacancies, by oxygen-plasma treatment or n-type doping, decreases the degree of Fe-O hybridization and facilitates charge transfer via UHB.[188] Additionally, concentration of near-surface $Fe^{2+}$ species is influenced differently upon annealing or doping. Among the methodologies covered here, the most promising way is to n-type dope in the bulk plus p-type dope near the surface. We then define one type of recombination surface states to be $Fe^{2+}$-$V_o$ that mainly consumes CTB holes and prevents early onset potential. These states are strongly affected by heating conditions: a short high temperature can readily remove them. On the basis of TAS findings, integration of NEXAFS results into photoelectrochemistry has led us to a far more clarified energy picture at hematite electrodes. Our theory is in agreement with a majority of theoretical and experimental data in the literature. The impacts of high temperature treatment, overlayer deposition and surface doping have also been discussed. We note that the key limiting factor of hematite as photoanodes is its poor hole transport properties instead of electronic transport (conductivity). If this issue is overcome, and given its remarkable stability, hematite would undoubtedly secure its progress toward commercial PEC application.

Finally, this Perspective has deepened the understanding of the PEC performance of hematite photoanodes by various surface or bulk modifications and provided a useful guide to more efficient photoanodes with other semiconductors for solar water splitting. More importantly, this methodology of interdisciplinary literature review has rarely been applied in materials science, but would be valuable in other fields to gain novel and original understanding from present knowledge.

# Chapter 5 Experimental Studies of Surface OER Kinetics at Hematite Photoanodes

## 5.1 Publication: Role of Cobalt–iron (oxy)hydroxide (CoFeO$_x$) as Oxygen Evolution Catalyst on Hematite Photoanodes

### 5.1.1 Preface
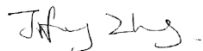
The commercial viability of hematite as photoanodes is mainly restricted by its short minority charge diffusion length and poor water oxidation kinetics. Attempts to address these problems have been introduced in the previous sections, amongst which adding oxygen evolution catalysts (OECs) is prevalent in the literature. However, despite apparent enhancement in photocurrent densities, the role of OECs has not been well understood, especially when complicated by the presence of surface states well-known for hematite. Among various techniques, PEIS and IMPS are particularly useful method to acquire insights into the surface reaction mechanism.

In this work, we have combined, for the first time, a traditional PEIS equivalent circuit method with a phenomenological approach to understand water oxidation kinetics on hematite coated with the OEC CoFeO$_x$. Our results suggest that different OEC loading levels lead to mechanistic changes and PEC performance. Although the effect of thickness has been investigated previously for CoPi/Fe$_2$O$_3$ composite photoanodes,[155] we advance the understanding by revealing the interplay between the OEC and the hematite and in particular, the surface states of hematite. Our conclusions are also supported by transient photocurrent spectroscopy and IMPS. We also demonstrate that an interlayer of catalytically inactive GaO$_x$ between hematite and the extremely thin layer of CoFeO$_x$ dramatically increases charge transfer rate.

In summary, our work has shed light on the role of CoFeO$_x$ when integrated with a surface-states-rich hematite photoanode. We expect this method to be applicable to other hematite-based PEC systems to study the reaction mechanisms at electrode-electrolyte interfaces. These breakthroughs will be of interest to material scientists, electrochemists, as well as theorists.

### 5.1.2 Declaration of Authorship

| This declaration concerns the article entitled: |
| --- |

| Role of Cobalt–iron (oxy)hydroxide ($CoFeO_x$) as Oxygen Evolution Catalyst on Hematite Photoanodes |
| --- |

<table>
<tr><td colspan="6">Publication status</td></tr>
<tr><td>In preparation</td><td>Manuscript</td><td>Submitted</td><td>In review</td><td>Accepted</td><td><u>Published</u></td></tr>
<tr><td>Publication details (reference):</td><td colspan="5">Energy and Environmental Science, 2018, 11, 2972-2984</td></tr>
<tr><td>Candidate's contribution to the paper (detailed, and also given as a percentage).</td><td colspan="5">

- Formulation of ideas: 100 %
  The candidate independently came up with research idea for this project.
- Design of methodology: 90%
  The design of methodology was mainly contributed by the candidate with a few suggestions from co-authors. Prof. Laurie Peter and Prof. Frank Marken from Department of Chemistry also offered advices in the course of this work.
- Experimental work: 90%
  The candidate performed most of the laboratory work, including sample preparation and photoelectrochemical measurements. I also participated in XPS data acquisition by HarwellXPS service and TEM images by MAS of Department of Physics. The setting up of IMPS was under assistance of Dr. Rodrigo García-Rodríguez.
- Manuscript writing and editing: 80%
  The manuscript was written by the candidate, then edited and approved by co-authors.
</td></tr>
<tr><td colspan="6">Statement from Candidate: This paper reports on original research I conducted during the period of my Higher Degree by Research candidature.</td></tr>
</table>

| Signed | | Dec. 2018 |
|---|---|---|
| | *Jhfy Zhg.* | |

## 5.1.3 Copyright Agreement

This article is licensed under a Creative Commons Attribution 3.0 Unported Licence. Reproduced from Energy Environ. Sci., 2018, 11, 2972 with permission from The Royal Society of Chemistry.

**5.1.4 Manuscript**

# Role of cobalt–iron (oxy)hydroxide (CoFeO$_x$) as oxygen evolution catalyst on hematite photoanodes

**Jifang Zhang**[a], **Rodrigo García-Rodríguez**[b], **Petra Cameron**[b] **and Salvador Eslava**\*[a]

[a]*Department of Chemical Engineering, University of Bath, Bath, BA2 7AY, UK. E-mail: S.Eslava@bath.ac.uk*

[b]*Department of Chemistry, University of Bath, Bath, BA2 7AY, UK*

**ABSTRACT:** Photoelectrochemical solar water splitting into hydrogen and oxygen offers an elegant and potentially efficient way to store solar energy in the chemical bonds of hydrogen, but the oxygen evolution rate is quite limited. The deposition of an oxygen evolution catalyst on the photoanode can enhance oxygen evolution, although the precise interplay between the semiconductor and the catalyst remains poorly understood and unoptimized. In this work, we use a combination of electrochemical approaches, including photoelectrochemical impedance spectroscopy and intensity modulated photocurrent spectroscopy, to unravel the nature of the interactions between different loadings of an electrocatalyst (CoFeO$_x$) and a hematite (α-Fe$_2$O$_3$) semiconductor. A thin layer of CoFeO$_x$ mainly reduces surface charge recombination, while an extremely thin layer enhances charge transfer kinetics. Moreover, an interlayer of GaO$_x$ modifies the surface state distribution and increases the charge transfer rate even further. These findings point to new opportunities for understanding and manipulating complex photoanodes for oxygen evolution.

## Broader Context

The increase in world population and its ever-increasing energy demands have made the use of fossil fuels a prominent threat to the global environment. Hydrogen fuel offers a clean and sustainable alternative, but current methods of production by steam reforming of natural gas creates a large carbon footprint. Photoelectrolysis of

water for the production of hydrogen (and oxygen) shows great promise and utilizes energy from sunlight. Unfortunately, the rate of water photoelectrolysis is considerably limited by the oxygen evolution reaction, which is a four electron charge transfer process. This is in stark contrast to far more rapid charge recombination processes taking place in the bulk (μs) or at the surface (ms) of the semiconductor. To alleviate bulk recombination, nanostructuring has proved to be effective. To reduce surface recombination, electrocatalysts are used to accelerate the oxygen evolution reaction. Although the outcomes of using electrocatalysts often appear encouraging, the underlying cause of improvements in surface kinetics still remains poorly understood. This paper aims to deepen this understanding by studying the photoelectrochemical response of hematite photoanodes coated with cobalt–iron (oxy)hydroxide layers of various thicknesses as well as the role of surface states.

---

**Introduction**

Photoelectrochemical (PEC) solar water splitting is a promising way to sustainably produce hydrogen.[112,240] The key to optimizing a PEC cell to achieve efficient water splitting for hydrogen and oxygen lies in the choice of materials and the design of photoelectrodes. In particular, developing efficient photoanodes for the water oxidation side has been a more challenging task due to the slow kinetics of the four-electron process ($2H_2O \rightarrow 4H^+ + O_2 + 4e^-$). Several approaches have been followed to enhance the intrinsic properties of the semiconductor (SC) light-absorbing layers in photoanodes, for example, doping and surface treatment.[141,241,242] In addition, the construction of heterojunctions to enhance electron–hole pair separation has been achieved using different semiconductors to form a cascade of band energy levels,[24,30,243] or adding other materials to make use of specific electronic phenomena such as piezoelectric or ferroelectric polarization.[45,46] Notably, passivation of the semiconductor absorbing layers by water oxidation electrocatalysts, also known as oxygen evolution catalysts (OECs) that are conventionally used for water electrolyzers, has shown to be a particularly effective method to improve the photocurrents in photoanodes.[244]

Mixed metal (oxy)hydroxides are promising candidates to replace noble metal oxides (*e.g.* $IrO_2$ and $RuO_2$) operating in alkaline solutions.[245,246] First-row transition

metal (*e.g.* Mn, Fe, Co, Ni) oxides or hydroxides attract widespread attention due to their elemental abundance and simple preparation techniques, including hydrothermal growth, photodeposition and electrodeposition.[145,153,154,247–251] Simulations have pointed out that binary or ternary (oxy)hydroxides composed of Fe, Co and Ni have the highest activities which relate to their optimized M–OH bond strengths.[246,252,253] This is supported by measured high turnover frequencies (TOFs) and low overpotentials.[153,233]

The deposition conditions for OEC on a semiconductor absorbing layer to obtain a better performing photoanode requires additional consideration compared to depositing on a highly conductive substrate (*e.g.* Au). For example, some electrodeposition methods using a strong negative potential at pH < 6 conditions on a hematite ($\alpha$-$Fe_2O_3$) layer can lead to deterioration or dissolution of the hematite.[145,152,249,250] Moreover, the loading level must be relatively low to prevent parasitic light absorption.[251] Some progress has been achieved using anodic electrodeposition,[153,154] but the understanding of the interaction between the OEC and semiconductor is still rather limited. Nellist *et al.* has modelled and observed experimentally that the permeability of electrolyte ions in an OEC plays an important role in the resulting photocurrent of a photoelectrode.[254,255] For example, in semiconductors with a high density of surface states, as in hematite, these surface states and OEC can be simultaneously charged during operation, which can increase surface recombination if the OEC is not very efficient.[255]

The idea of integrating OECs with hematite semiconductor absorbing layers for enhanced photocurrent attracts great attention.[154,256–261] The results often demonstrate a considerable improvement in photocurrent, which then leads to the conclusion that OECs accelerate the sluggish kinetics of the water oxidation reaction. The charge transfer efficiency when OECs are applied is commonly calculated relative to the assumed unity charge transfer efficiency where a hole scavenger ($Na_2SO_3$ or $H_2O_2$) is added in the electrolyte solution.[258,261,262] This method is a reasonable representation of the effectiveness of the OEC used. However, further insight can only be attained through more advanced techniques such as (photo)electrochemical impedance spectroscopy (PEIS), intensity modulated photocurrent spectroscopy (IMPS) and transient absorption spectroscopy (TAS).[72,165,230] These techniques show that surface electron–hole recombination is the dominating factor that accounts for a limited

photocurrent, instead of a limited charge transfer rate. However, much more work is required for a clear insight of the interplay between OECs and semiconductor layers in photoanodes.

In this work, we study the role of cobalt–iron (oxy)hydroxide (CoFeO$_x$, or cfox) as an OEC on mesoporous hematite (h) photoanodes. We use multiple electrochemical techniques to investigate h/CoFeO$_x$ composite photoanodes at varied applied voltages and different OEC loadings. A thin OEC layer leads to a cathodic shift in the onset potential due to inhibition of surface recombination and OEC charging but not due to a higher charge transfer rate to the electrolyte. However, we reveal that an extremely thin OEC layer achieves a higher hole transfer rate. We also show that the charge transfer process is further accelerated at low potentials with the assistance of an interlayer of GaO$_x$ that modifies the distribution of surface states.

**Experimental**

Preparation of photoanodes

Hematite films were prepared by a facile solution-based method. First, 2.16 g Pluronic 123 (P123, average $M_n \sim 5800$) was dissolved in 6 g tetrahydrofuran (THF, Fisher Chemicals, 99.99%). In a separate vial, 6.06 g Fe(NO$_3$)$_3$·9H$_2$O (Alfa Aesar, 98%) was dissolved in 6 g absolute ethanol (BDH Prolabo). The two solutions were mixed and stirred overnight. This precursor was then spin-coated onto fluorine-doped tin oxide (FTO) coated aluminoborosilicate glass (Solaronix, CH). The glass slides were previously cleaned by sonication in 2 vol% Hellmanex solution, 2-propanol and acetone, for 10 min each, sequentially. The spin coating was carried out at 1000 rpm for 5 s before ramping up to 6000 rpm and kept at this velocity for 30 s. The films were then calcined in air at 800 °C for 20 min in a preheated tube furnace. The spin coating and calcination were carried out twice to obtain sufficient thickness. The hematite films were then masked with black electric tape leaving a square area of 0.25 cm$^2$ for PEC measurements.

The loading method of CoFeO$_x$ was adapted from a previous study by Morales-Guio, using electrodeposition in a three-electrode system.[153] In the present study, a Pt wire was used as a counter electrode coupled with an Hg/HgO/1 M NaOH reference electrode. The electrodeposition electrolyte was composed of 10 mM FeCl$_3$·6H$_2$O (Sigma Aldrich, 99+%), 16 mM CoCl$_2$ (Alfa Aesar, anhydrous, 97%) and 0.1 M

NaOAc (Sigma, 99%), dissolved in deionized water, without adjusting its pH. $CoFeO_x$ was coated with this electrolyte by positively sweeping voltage from 1.35 to 1.65 $V_{RHE}$. The unidirectional linear sweeps were repeated for a controlled thickness. The sweeps were carried out three times for an extremely thin coating and up to thirty times for a standard thin coating. The bare hematite and 3–30 times $CoFeO_x$-coated hematite photoanodes are denoted as h/cfox0, h/cfox3, h/cfox9, h/cfox18, and h/cfox30, respectively. An Ivium Compactstat potentiostat was used for all electrodepositions. $GaO_x$ layer between hematite and $CoFeO_x$ layers was fabricated by following Hisatomi's procedure.[232] Briefly, hematite films were partly submerged into an aqueous solution containing 0.042 g $Ga(NO_3)_3 \cdot nH_2O$, where 0.6 g urea was slowly added and subsequently stirred at 75 °C for 15 min. The films were then rinsed with DI water and calcined at 500 °C for 2 h, before $CoFeO_x$ deposition.

Physical characterization

X-ray diffraction (XRD) patterns were collected using a BRUKER AXS D8 advance diffractometer with a Vantec-1 detector and Cu $K_\alpha$ radiation (1.5418 Å). Film morphologies were examined by field emission scanning electron microscopy (FESEM, JEOL JSM-6301F) with an acceleration voltage of 5 keV. X-ray photoelectron spectroscopy (XPS) was performed on a Thermo Fisher Scientific K-alpha[+] spectrometer. Samples were analyzed using a micro-focused monochromatic Al X-ray source (72 W) over an area of approximately 400 microns. Data was recorded at pass energies of 150 eV for survey scans and 40 eV for high resolution scans with 1 and 0.1 eV step sizes respectively. Charge neutralization of the sample was achieved using a combination of both low energy electrons and argon ions. No sputtering was carried out. Data analysis was performed in CasaXPS (2.3.19) using a Shirley type background and Scofield cross sections, with an energy dependence of −0.6. High-resolution transmission electron microscopy (HR-TEM) was used to examine the nanoparticles scraped from photoanode samples at 200 keV of electron beam energy (JEOL 2100 Plus).

(Photo)electrochemical characterization

Photocurrent density measurements were carried out in the same setup used for electrodeposition of $CoFeO_x$, replacing the electrolyte solution with 1 M NaOH (pH 13.4). Photocurrent densities were measured under chopped or continuous

illumination of 100 mW cm$^{-2}$ simulated sunlight (AM 1.5G) from the back side (glass side) using linear sweep voltammetry (LSV) at various scanning rates (5, 20 and 50 mV s$^{-1}$) or using chronoamperometry. Incident photon-to-current efficiency (IPCE) measurements were performed from 300 to 700 nm with the same light source passing a monochromator (MSH-300F LOT QuantumDesign) without the AM 1.5G filter. The intensity of monochromatic light was calibrated by a SEL033/U photodetector (International Light Technologies). Transient photocurrent spectroscopy (TP) was carried out in the same PEC setup with a data acquisition interval of 1 ms and chopped simulated sunlight. PEIS was carried out in a frequency range from 10$^5$ to 0.1 Hz, with an AC voltage amplitude of 10 mV. Impedance spectra were obtained in the range from 0.6 to 1.2 V$_{RHE}$, with 0.05 V steps, in 1 M NaOH, and under 1 sun irradiation unless otherwise specified. IMPS was conducted with a ModuLab XM PhotoEchem system (Solartron Analytical) under 470 nm LED (Thorlab M470L3) illumination (37.5 mW cm$^{-2}$) at varying potentials from 0.6 to 1.3 V$_{RHE}$ at a step of 0.05 V. A modulation of 10% in light intensity was applied, over a frequency range from 10$^3$ to 0.1 Hz at each potential step. PEIS and IMPS spectra were fitted using Zview software (Scribner).

**Results and discussion**

The facile photoanode preparation method used here produced high quality hematite films. The hematite phase was identified by XRD (Fig. 5-1). These photoanodes have a mesoporous worm-like morphology (Fig. 5-2), with feature sizes of 90±19 nm (analyzed using ImageJ software). Thickness was approx. 1 μm.
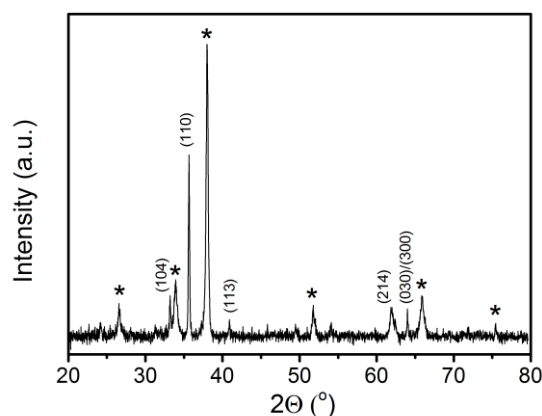
Fig. 5-1 XRD pattern of h/cfox0 showing hematite facet indices. Stars indicate diffraction peaks from FTO
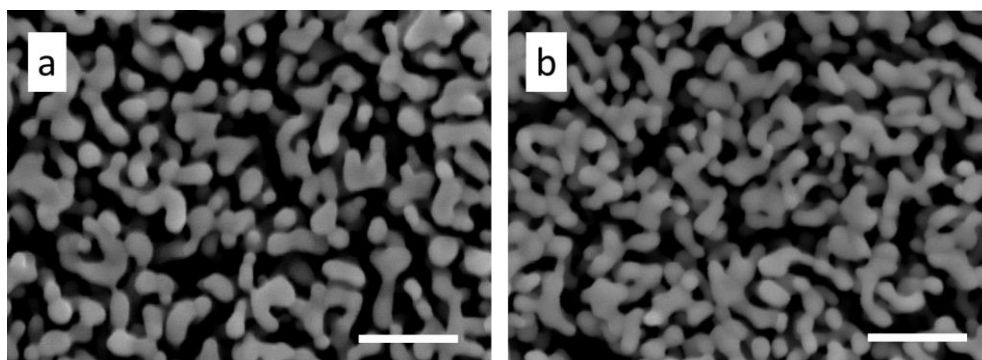


Fig. 5-2 FESEM images of (b) h/cfox0 and (c) h/cfox30. No morphological changes can be seen. Scale bars represent 500 nm.

CoFeO$_x$ was deposited onto the hematite layer using from three up to thirty unidirectional LSV sweeps, for controlled thickness. As shown in Fig. 5-3, the photocurrent densities at high potential reach the highest values after three sweeps (h/cfox3). The photocurrent density then gradually decreases for heavier loading. Low potential photocurrent densities apparently improve with higher deposition repetitions. To understand the differences in PEC performance, we examined the properties of three representative photoanodes with none, three and thirty coating sweeps (h/cfox0, h/cfox3 and h/cfox30).
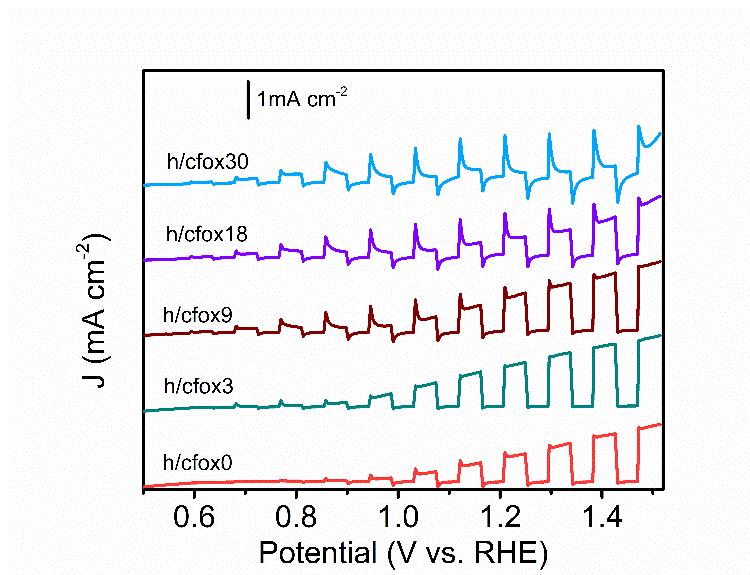


Fig. 5-3 Linear sweep voltammograms of hematite photoanodes with 0–30 times CoFeO$_x$ loadings: h/cfox0 (red), h/cfox3 (green), and h/cfox9 (brown), h/cfox18 (purple) and h/cfox30 (blue). Measured under chopped AM 1.5G (100 mW cm$^{-2}$) illumination at a scan rate of 20 mV s$^{-1}$.

The OEC on both h/cfox3 and h/cfox30 is very thin and parasitic light absorption is not observable. No apparent morphological changes in the hematite layer can be seen using FESEM even after thirty coating sweeps (Fig. 5-2). Successful electrodeposition of $CoFeO_x$ is observed however in HR-TEM (Fig. 5-4). The sample h/cfox0 shows hematite crystals with well-defined crystalline edges (Fig. 5-4a and b). The sample h/cfox3 shows hematite crystals with an extremely thin amorphous layer of *ca.* 0.7 nm, not ubiquitously covering all the hematite crystals (Fig. 5-4c and d). The sample h/cfox30 shows a highly uniform amorphous layer of 1.6 nm covering all the crystals (Fig. 5-4e and f). According to the current density maxima for each sweep during electrodeposition, the loading on h/cfox30 nearly approaches saturation, which corresponds to nearly 20 µg cm$^{-2}$ (Fig. 5-5).[153] This is comparable to or thinner than most OEC coatings in literature.[151,158,249,263]
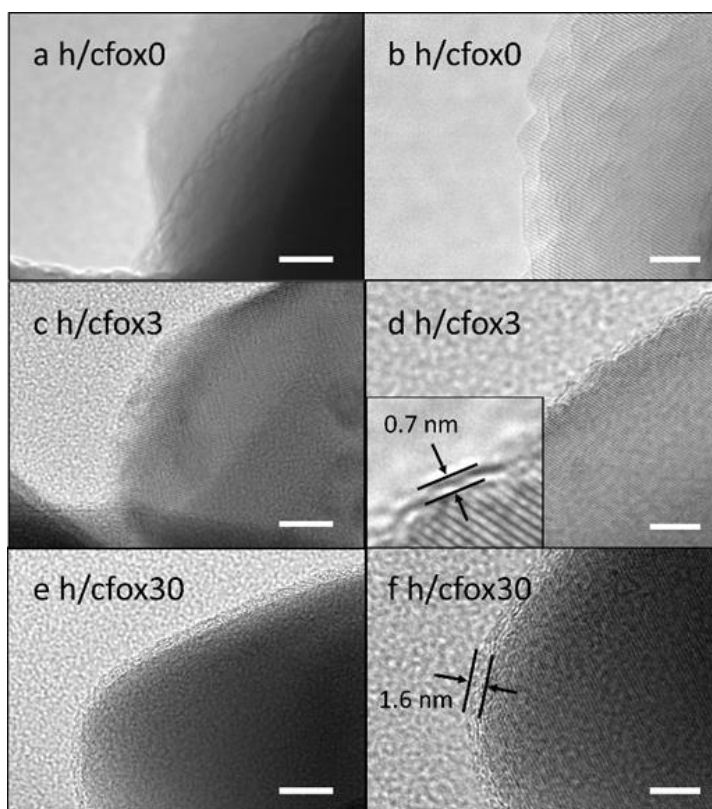


Fig. 5-4 HR-TEM images of photoanodes h/cfox0 (a and b), h/cfox3 (c and d) and h/cfox30 (e and f). Scale bars represent 10 nm for left column and 5 nm for right column.
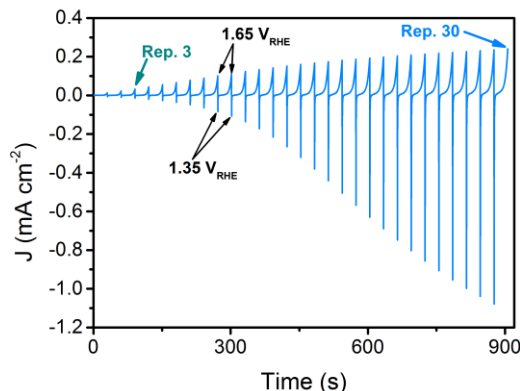
Fig. 5-5 Current density as a function of deposition time during repeated unidirectional LSV electrodeposition of CoFeO$_x$. Applied potential is repeatedly swept from 1.35 to 1.65 V$_{RHE}$.

CoFeO$_x$ deposition with thirty coating sweeps is also confirmed by characterizing the top surface of h/cfox30 with XPS and observing Co 2p peaks (Fig. 5-6a). A broad peak present between 775 and 795 eV in all photoanodes' XPS spectra is ascribed to Fe LMM Auger lines.[42] CoFeO$_x$ deposition with three coating sweeps (h/cfox3) is not confirmed by XPS on the top surface of h/cfox3, but confirmed following a direct deposition on solid FTO (Fig. 5-6b). Therefore, CoFeO$_x$ deposition on porous hematite layers must start closer to the FTO substrate, due to the gradient of potential across the porous hematite layer that requires multiple coating sweeps to cover the top surface with CoFeO$_x$. CoFeO$_x$ loading in FTO/cfox3 is approximately 20% of that in FTO/cfox30, based on the peak areas of Co 2p (Fig. 5-6b). Similar CoFeO$_x$ ratio between h/cfox3 and h/cfox30 is expected.
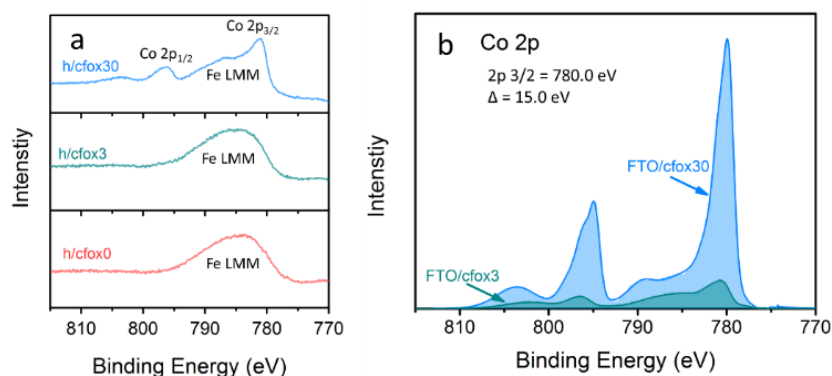


Fig. 5-6 (a) Co 2p XPS spectra of h/cfox0 (red), h/cfox3 (green), and h/cfox30 (blue). The broad peak present at 785 eV is ascribed to Fe LMM Auger lines.[264] (b) Co 2p XPS spectra (background subtracted) of CoFeO$_x$ coated three (green) or thirty times (blue) on FTO coated glass (FTO/cfox3 and FTO/cfox30, respectively).

The photocurrent densities of these photoelectrodes were initially measured by LSV at 20 mV s$^{-1}$ (Fig. 5-7a). The uncoated hematite sample (h/cfox0) shows a photocurrent density of 0.88 mA cm$^{-2}$ at 1.23 V$_{RHE}$ with an onset potential of *ca.* 0.8 V$_{RHE}$. When three layers of CoFeO$_x$ are coated (h/cfox3), the photocurrent density increases at all potentials, for example from 0.88 to 1.2 mA cm$^{-2}$ at 1.23 V$_{RHE}$. However, the onset potential has little shift. When thirty layers of CoFeO$_x$ are coated (h/cfox30), the photocurrent only increases at low potentials and there is a cathodic shift of the onset potential to approximately 0.6 V$_{RHE}$. It also displays a high dark current above 1.1 V$_{RHE}$ and a strong peak centered at 1.18 V$_{RHE}$. The IPCE of h/cfox0, h/cfox3 and h/cfox30 are shown in Fig. 5-8 with similar projected photocurrent densities to the measured by LSV.
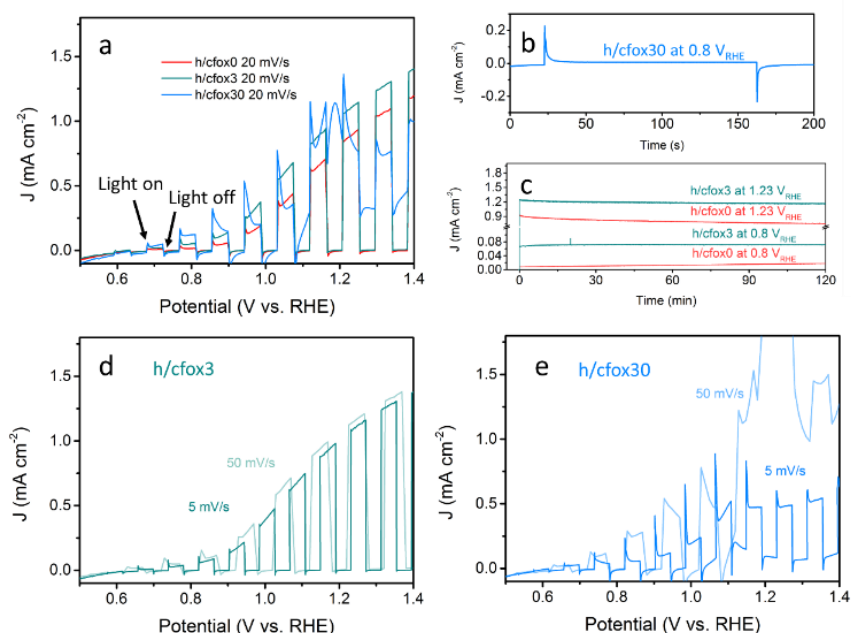


Fig. 5-7 (a) Linear sweep voltammograms of photoanodes h/cfox0 (red), h/cfox3 (green), and h/cfox30 (blue) under chopped AM 1.5G (100 mW cm$^{-2}$) illumination at a scan rate of 20 mV s$^{-1}$. (b) Chronoamperometry of sample h/cfox30 showing its short-term stability. (c) 2 h stability tests for samples h/cfox0 (red line) and h/cfox3 (green line) at constant potentials of 0.8 and 1.23 V$_{RHE}$. Linear sweep voltammograms of (d) h/cfox3 and (e) h/cfox30 under chopped light scanned at 5 mV s$^{-1}$ (darker line) and 50 mV s$^{-1}$ (lighter line).
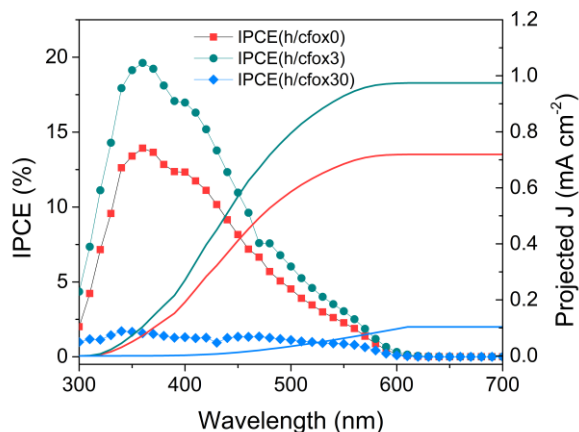
Fig. 5-8 IPCE of h/cfox0 (red squares), h/cfox3 (green circles) and h/cfox30 (blue diamonds) and their corresponding projected photocurrent density under AM1.5G (100 mW cm$^{-2}$) illumination at 1.23 $V_{RHE}$.

A short chronoamperometry test on h/cfox30 indicates that the enhancement at low potential (0.8 $V_{RHE}$) is totally lost within 10 s, after which it stabilizes at 8 μA cm$^{-2}$, a value almost identical to that on h/cfox0 at the same potential (Fig. 5-7b). In contrast, both h/cfox0 and h/cfox3 show remarkable stability over 2 h, and the significant improvement in h/cfox3 photocurrent over h/cfox0 is well maintained (Fig. 5-7c). We also performed LSV measurements at slower (5 mV s$^{-1}$) and faster (50 mV s$^{-1}$) scan rates. For h/cfox3, the *J–V* curves are consistent and independent of scanning rates (Fig. 5-7d). However, for h/cfox30, the current densities are highly dependent on the scanning rate (Fig. 5-7e). As scan rate increases, the intensity of the peak located near 1.18 $V_{RHE}$ increases roughly linearly (Table 5-1), which implies a surface immobilized redox reaction. Moreover, there is an anodic shift of the peak with increasing scan rate, indicating a potential driven process. Another feature to notice is that the position of the first photocurrent spikes are also dependent on the scan rate. The first relevant photocurrent spike is at 0.75, 0.85, and 0.92 $V_{RHE}$ for scan rates 5, 20 and 50 mV s$^{-1}$, respectively. All these features are ascribed to the likely oxidation of CoFeO$_x$ from its hydroxide form to oxyhydroxide form [Co(OH)$_2$ + OH$^-$ → CoOOH + H$_2$O + e$^-$].[265] This oxidation appears to start at low potentials driven by photo-generated holes (during irradiation), and continues at higher potentials driven by both the applied potential and more photo-generated holes.

Table 5-1 Peak intensity and peak position of the redox peak observed for h/cfox30

| Scan rate (mV s$^{-1}$) | Peak intensity (mA cm$^{-2}$) | Peak position (V$_{RHE}$) |
|---|---|---|
| 5 | 0.2 | 1.12 |
| 20 | 1.2 | 1.18 |
| 50 | 3.0 | 1.23 |

We start our investigation by PEIS. A representative Nyquist plot (Fig. 5-9a) for a bare hematite photoanode (h/cfox0) contains two semicircles that can be fitted using a two-RC-unit equivalent circuit, as proposed by Klahr *et al.*, where the oxygen evolution reaction (OER) is assumed to be driven by surface states.[187] In this equivalent circuit, three resistances are used: a series resistance attributed to the electrolyte and conductive substrate layer, $R_s$; a trapping resistance at surface states where electron–hole pairs recombine, $R_{trap}$; and a charge transfer resistance at the semiconductor–liquid junction, $R_{ct}$ (Fig. 5-9a inset). There are two capacitors used: a bulk capacitor mainly attributed to the space charge region, $C_{bulk}$, and a surface states capacitor, $C_{ss}$.
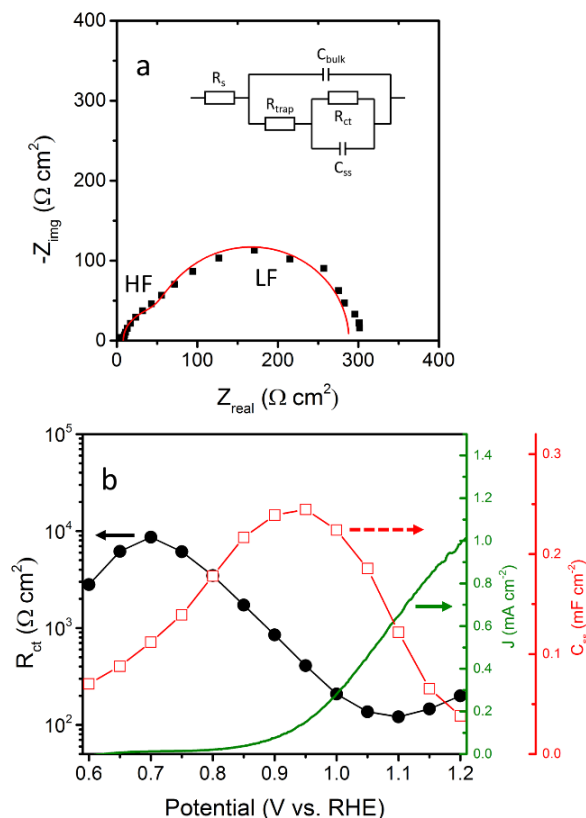


Fig. 5-9 (a) Nyquist plot for a typical PEIS measurement of h/cfox0 at 1.0 V$_{RHE}$ under 1 sun irradiation (AM 1.5G). Inset image shows the equivalent circuit used. HF and LF indicate high frequency and low frequency semicircles, respectively. (b) Fitting results of sample h/cfox0 as a function of applied potential.

Black circles represent $R_{ct}$; red squares represent $C_{ss}$; and green curve represents $J$–$V$ curve (under the same irradiation condition).

The PEIS spectra of h/cfox0 and h/cfox3 are similar (Fig. 5-10), so they are modelled using the same equivalent circuit depicted in the inset of Eq. 4-10a. However, the PEIS spectra of h/cfox30 shows different features (Fig. 5-11). Below 1.0 $V_{RHE}$, the h/cfox30 PEIS spectra are akin to those observed for h/cfox0 and h/cfox3, so they are modelled using the same equivalent circuit, while the term $C_{ss}$ is replaced with $C_{cat}$ because charge transfer in h/cfox30 must take place mainly through the OEC, as suggested by Boettcher and Bisquert.[159,263] Above 1.0 $V_{RHE}$, there is an additional peak in the phase angle at low frequencies in the Bode plots, *i.e.* a third semicircle in Nyquist plots (Fig. 5-11) which requires another RC unit in its equivalent circuit (Fig. 5-12). These extra features observed above 1.0 $V_{RHE}$ are also observed in dark EIS measurements above 1.0 $V_{RHE}$, coinciding with the peak onset in $J$–$V$ curves (Fig. 5-13), which can be assigned to the oxidation of $CoFeO_x$.[151] Consequently, for this extra RC unit, the capacitance ($C_{cfox}$) represents the main pseudocapacitance from the redox reaction and the resistance ($R_{cfox}$) the ion diffusion during electrolyte permeation.[266] Fitted parameters for h/cfox30 and the rest of the photoanodes studied are listed in Tables S1–S6 (Section 5.1.5).
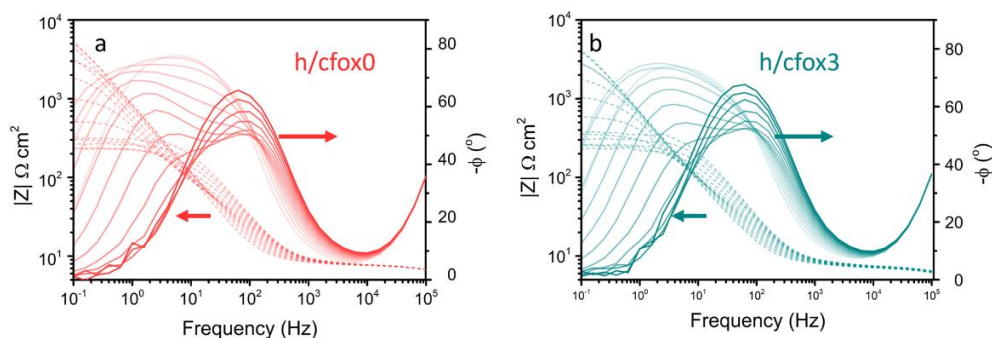


Fig. 5-10 Bode plot comparison of (a) h/cfox0 and (b) h/cfox3 measured at 1 sun illumination. Lighter line colors represent lower potentials (from 1.2 to 0.6 $V_{RHE}$). The non-zero phase angles at frequencies between $10^4$ and $10^5$ Hz may originate from the capacitance at electrode/sample interface.
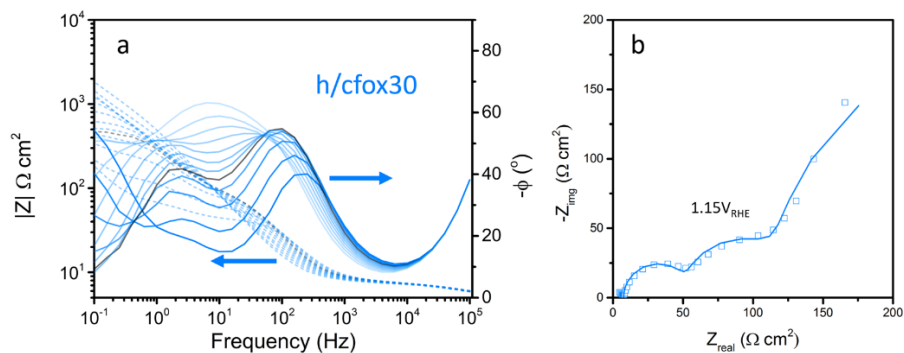
Fig. 5-11 Bode plots of h/cfox30 measured at 1 sun illumination. Lighter line colors represent lower potentials (from 1.2 to 0.6 $V_{RHE}$). An additional peak in phase angles can be observed compared to Figure S5 above 1.0 $V_{RHE}$ (marked in black), which corresponds to a new semicircle at low frequencies as exemplified in (b) in the case of 1.15 $V_{RHE}$.
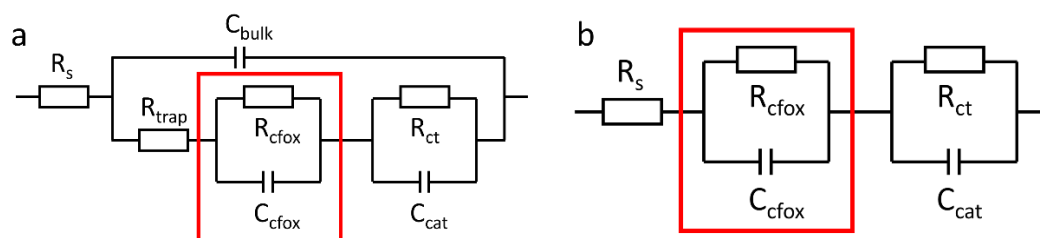


Fig. 5-12 Equivalent circuit used for h/cfox30 when (a) under 1 sun illumination or (b) in the dark. Elements in red box are only used when applied potential is larger than 1.0 $V_{RHE}$.
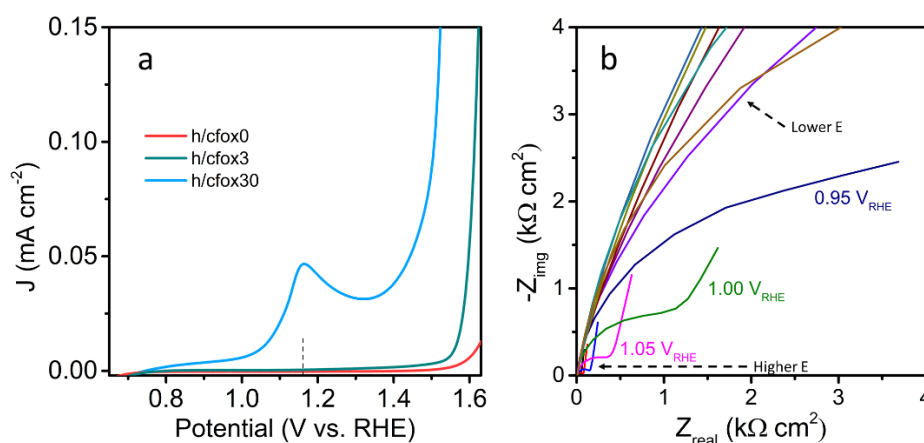


Fig. 5-13 (a) Dark *J-V* curve of h/cfox0 (red), h/cfox3 (green) and h/cfox30 (blue) scanned at 10 mV s$^{-1}$. (b) Nyquist plots from EIS results for h/cfox30 at various potentials in the dark. A new semicircle can be fitted from 1.00 $V_{RHE}$ on with strong capacitive character.

The PEIS spectra of our three representative electrodes (h/cfox0, h/cfox3, and h/cfox30) have good fit to the equivalent circuits and no constant phase elements are

necessary. To confirm the validity of PEIS measurements and fittings, the total resistance ($R_{tot}$) for each sample is plotted and compared against differential resistance ($dV/dJ$) obtained from LSV curves; the $R_{tot}$ of all three samples match the curves reasonably well (Fig. 5-14).
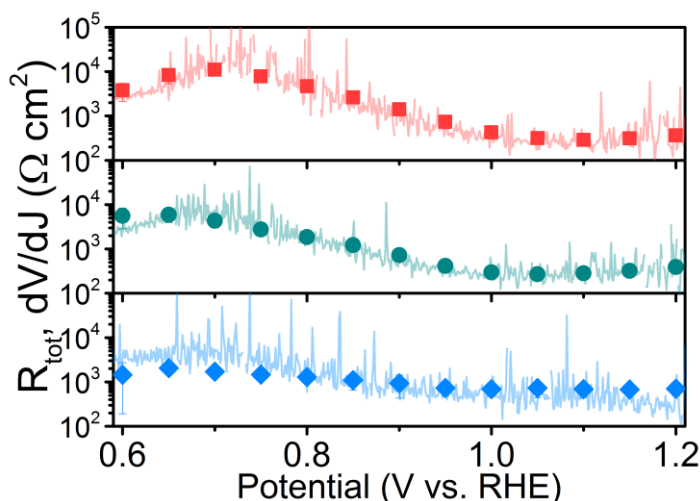


Fig. 5-14 Comparison of PEIS fitted total resistances $R_{tot}$ (scattered shapes) and differential resistances $dV/dJ$ (lines) of h/cfox0 (red squares), h/cfox3 (green circles) and h/cfox30 (blue diamonds).

Fig. 5-9b shows $R_{ct}$ and $C_{ss}$ fitted from PEIS and photocurrent measured at different potentials for h/cfox0. The presence of surface states, reported in literature for hematite,[187,267,268] is confirmed with $C_{ss}$ showing a Gaussian distribution centered at 0.95 V. This Gaussian distribution results from activation of OER intermediate species and appears close to the onset potential.[135] $R_{ct}$ also shows a local maximum at 0.7 $V_{RHE}$. We assign the early $R_{ct}$ bending to accumulation of electrons at the electrode surface near the flat band potential ($E_{fb}$),[269] which is estimated to be ~0.6 $V_{RHE}$ using Mott–Schottky equation (Note S2, 5.1.5). To avoid this accumulation effect, further impedance results are analyzed from 0.7 $V_{RHE}$.

Fig. 5-15 shows $R_{ct}$ and $C_{ss}$ or $C_{cat}$ at different potentials for the three representative hematite photoanodes (h/cfox0, h/cfox3, and h/cfox30). For h/cfox0 and h/cfox3, $R_{ct}$–$V$ curves show the same behavior from 0.7 to 1.2 $V_{RHE}$, but h/cfox3 has generally lower values than h/cfox0 below 1.05 $V_{RHE}$, suggesting easier charge transfer. The Gaussian distribution of $C_{ss}$ for h/cfox3 is depressed due to partial replacement of sluggish surface states with active CoFeO$_x$ sites.
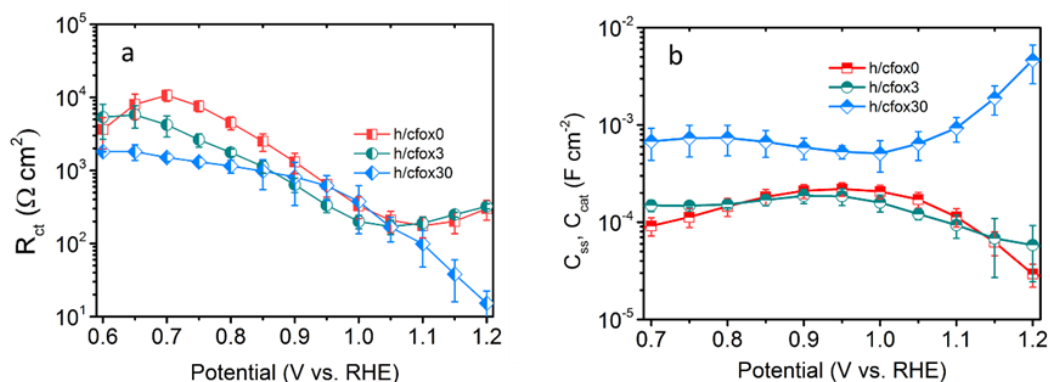
Fig. 5-15 (a) $R_{ct}$ and (b) $C_{ss}$, $C_{cat}$ obtained from EIS fitting as a function of applied potential for h/cfox0 (red squares), h/cfox3 (green circles) and h/cfox30 (blue diamonds).

The $C_{cat}$–$V$ curve of h/cfox30 is fundamentally different to the one of h/cfox3 (Fig. 5-15b). The curve shape observed for h/cfox30 is similar to that obtained for a NiFeO$_x$/Fe$_2$O$_3$ photoanode.[255] The high and flat region of $C_{cat}$ for h/cfox30 at lower potential indicates that almost all photogenerated holes are transferred to the CoFeO$_x$ layer as opposed to h/cfox3 where the loading is so low that only a small fraction of photogenerated holes is sufficient to oxidize the OEC. $R_{ct}$ of h/cfox30 decreases dramatically with potential. At voltages below 1.0 V$_{RHE}$, $R_{ct}$ decreases as photogenerated holes transform hydroxides into oxyhydroxides, which is known to be a more effective OEC.[148] Above 1.0 V$_{RHE}$, this process is further accelerated with the assistance of applied voltage. The significant decrease in $R_{ct}$ of h/cfox30 above 1.0 V$_{RHE}$ is, nevertheless, not accompanied by an improvement in photocurrent. Therefore, EIS data must be analyzed from a kinetic perspective.

In a simplified model, a hematite photoanode surface has two competing processes that determine the rate of water oxidation, namely charge transfer and surface recombination.[267] Its Nyquist plot typically exhibits two semicircles at different frequency domains [high frequency (HF) and low frequency (LF)] as shown in Fig. 5-9a. The rate constants of these two processes ($k_{ct}$ for charge transfer and $k_{rec}$ for surface recombination) can be calculated using a phenomenological model developed by Peter and co-workers.[267,270] The formal equivalence of this kinetic model and the EIS elements used previously is demonstrated in Note S1 of Section 5.1.5.

Assuming the space charge capacitance of the semiconductor is much smaller than the capacitance across the Helmholtz layer at electrode surface ($C_{SC} \ll C_H$), $k_{ct}$ is inversely related to the time constant of the low frequency semicircle:[53]

$$k_{ct} = \frac{1}{R_{LF}C_{LF}}$$ 

Eq. 5-1

$R_{LF}$ and $C_{LF}$, which are $R_{ct}$ and $C_{ss}$ in this work, respectively, can be calculated as:

$$R_{LF} = \frac{k_B T}{q^2 J_h}\left(\frac{k_{ct} + k_{rec}}{k_{ct}}\right)$$ 

Eq. 5-2

and

$$C_{LF} = \frac{q^2 J_h}{k_B T}\left(\frac{1}{k_{ct} + k_{rec}}\right)$$ 

Eq. 5-3

where $k_B$ is the Boltzmann constant, $T$ is temperature, $q$ is the elementary charge and $J_h$ is the flux of holes.

The resistance of the high frequency semicircle ($R_{HF}$) is $R_{trap}$ and can be calculated as:

$$R_{HF} = \frac{k_B T}{q^2 J_h}\left(\frac{k_{ct} + k_{rec}}{k_{rec}}\right)$$ 

Eq. 5-4

$k_{rec}$ can then be calculated using the following equation:

$$k_{rec} = \frac{R_{LF}}{R_{HF}}k_{ct}$$ 

Eq. 5-5

Once we have both $k_{ct}$ and $k_{rec}$, the charge transfer efficiency ($\phi_{ct}$) can be calculated as:

$$\phi_{ct} = \frac{k_{ct}}{k_{rec} + k_{ct}}$$ 

Eq. 5-6

Finally, the estimated photocurrent density is:

$$J_{est.} = J_h \phi_{ct}$$ 

Eq. 5-7

where $J_h$ is the hole flux that reaches the electrode surface, which can be calculated from Eq. 5-2 or Eq. 5-4.

The kinetic results estimated from Eq. 5-1 to Eq. 5-7 are plotted in Fig. 5-18. All measurements, where possible, are carried out on a single substrate for better comparability. According to Peter's model, at a high concentration of positively charged surface states, $k_{ct}$ first increases then saturates as limited by light intensity. In our case, the saturation point is not reached possibly because of strong light intensity

(100 mW cm$^{-2}$).[270] In contrast to the reported model that predicts a plummet of $k_{rec}$, our photoanodes show nearly constant values. Such unusual behavior is, again, an indication of strong light intensity that induces complete Fermi level pinning, where the band edge is unpinned and the degree of band bending is constant.[271] We also measured the impedance response under a weaker light intensity of 10 mW cm$^{-2}$ and $k_{ct}$ was indeed constant while $k_{rec}$ decreased with potential (Fig. 5-16), thereby proving that total Fermi level pinning happens under strong illumination which creates a high density of surface states. For our hematite photoanode, the extraordinary trend of increased $k_{rec}$ (Fig. 5-17) above 1.0 V$_{RHE}$ suggests a fundamental change to the semiconductor.
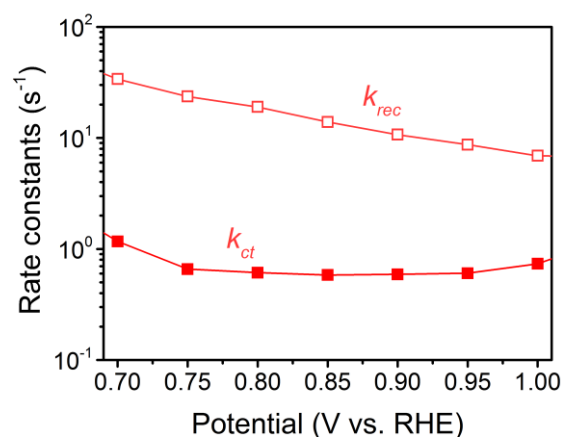


Fig. 5-16 Rate constants for h/cfox0 at light intensity of 10 mW cm$^{-2}$ (AM1.5G). Empty squares indicate $k_{rec}$ and filled squares indicate $k_{ct}$.
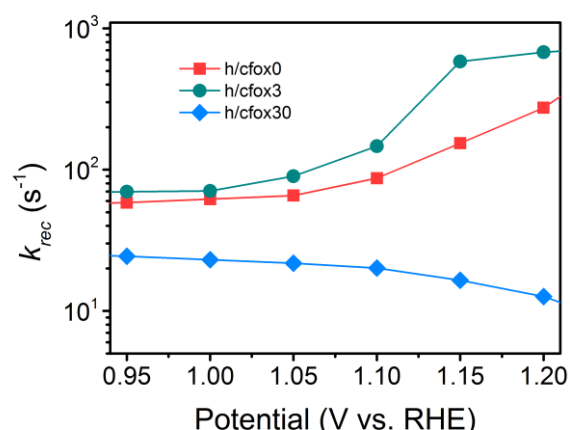


Fig. 5-17 Calculated $k_{rec}$ for photoanodes h/cfox0 (red squares), h/cfox3 (green circles) and h/cfox30 (blue diamonds). Unusual increases are observed for h/cfox0 and h/cfox3.

One explanation is the formation of a deep depletion region where the semiconductor surface behaves like an insulator, based on the observation that $C_{ss}$ starts to decrease at 0.95 $V_{RHE}$, and intensified band bending.[4] However, this explanation seems unlikely considering the strong Fermi level pinning effect. Another possible cause is a reversible modification of the surface states under strong illumination and high potential.[272] Under this circumstance, water oxidation mechanism is different and the kinetic model loses its continuity. As such, our kinetic analysis only considers potentials up to 1.0 $V_{RHE}$ for simplicity.
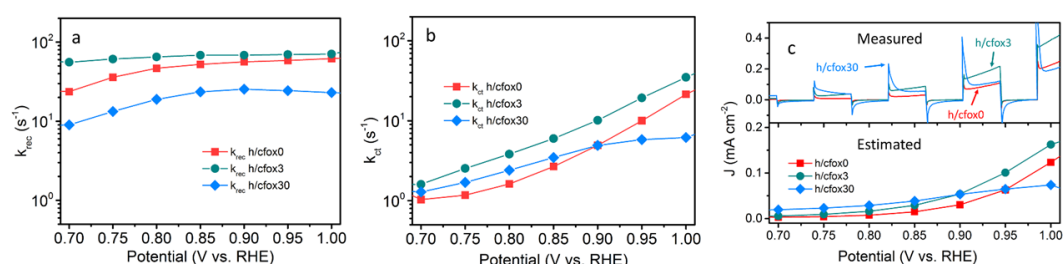


Fig. 5-18 Calculated (a) surface recombination and (b) charge transfer rates for photoanodes h/cfox0 (red squares), h/cfox3 (green circles) and h/cfox30 (blue diamonds) from PEIS. The estimated photocurrent densities are compared with measured *J–V* curves in (c).

To justify the applicability of this model for our photoanodes at relatively low potentials, the measured photocurrent densities were compared to estimated ones calculated using charge transfer efficiencies and hole fluxes (Fig. 5-18c and Fig. 5-19). Despite lower values, the estimated photocurrent densities follow the same trends of real *J–V* curves measured at 5 mV s$^{-1}$, showing that this model is at least useful to compare the trends of rate constants.
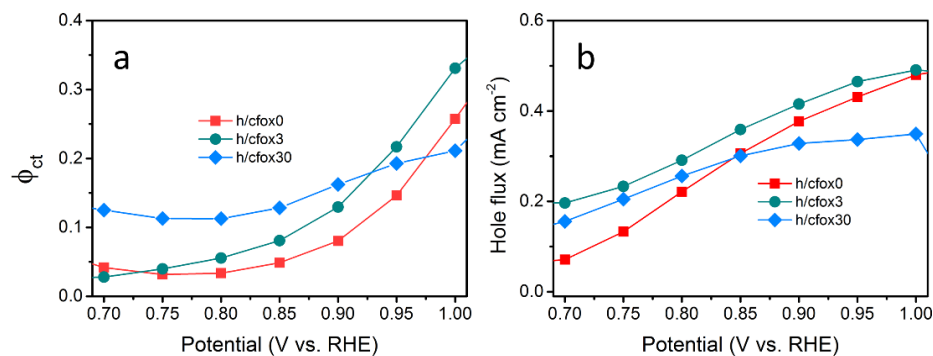


Fig. 5-19 Calculated (a) charge transfer efficiency and (b) hole flux for h/cfox0 (red squares), h/cfox3 (green circles) and h/cfox30 (blue diamonds) for the estimation of photocurrent density shown in Figure 7c.

Fig. 5-18and b show that both $k_{rec}$ and $k_{ct}$ of h/cfox3 increase with respect to h/cfox0 at all potentials, especially $k_{ct}$. Thus, the estimated photocurrent ($J_{est.}$) increases (Fig. 5-18c). The marginally increased $k_{rec}$ could be a result of interphase charge trapping or fitting error.[92] It should be noted that the moderate increase in $k_{rec}$ below 0.8 $V_{RHE}$ is unexpected but is a result of potential before photocurrent onset and therefore can be ignored. In contrast, both $k_{rec}$ and $k_{ct}$ of h/cfox30 have lower values. The higher estimated photocurrent density for h/cfox30 is mainly ascribed to the significantly reduced $k_{rec}$ and subsequently improved charge transfer efficiency, $\phi_{ct}$ (Fig. 5-19a). However, $k_{ct}$ increases much less with potential than lightly or even uncoated photoanodes especially above 0.85 $V_{RHE}$. The photocurrent thus falls behind the other two despite the subdued recombination. Therefore, the effect of $CoFeO_x$ is highly dependent on its thickness. These data, combined with chronoamperometry results shown previously, indicate that the characteristics of lowered onset potential and depressed photocurrent at high potential on h/cfox30 are associated with the relatively high thickness of $CoFeO_x$. In this situation, the OEC undergoes oxidation, stores charges and influences the photocurrent measured.

To confirm this hypothesis, transient photocurrents (TP) were investigated by converting it to a normalized parameter $D$ (Fig. 5-20), which can be calculated as:[273]

$$D = (J_t - J_{st})/(J_{in} - J_{st}) \qquad \text{Eq. 5-8}$$

where $J_t$, $J_{st}$ and $J_{in}$ are time-dependent, steady state and instantaneous photocurrent density, respectively. A transient time constant ($\tau$) can then be defined as the time when $\ln D = -1$. We then approximate $\tau$ as:[6]

$$\tau = (k_{rec} + k_{ct})^{-1} \qquad \text{Eq. 5-9}$$

The ratio of $J_{st}$ and $J_{in}$ is given by

$$\frac{J_{st}}{J_{in}} = \frac{k_{ct}}{k_{rec} + k_{ct}} \qquad \text{Eq. 5-10}$$
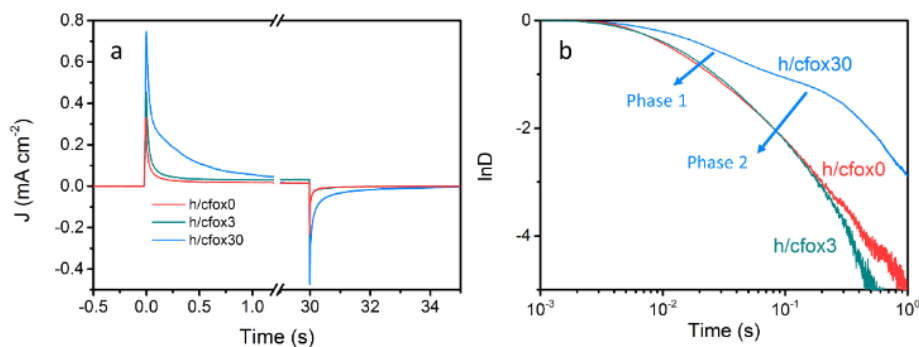
Fig. 5-20 (a) Photocurrent transients of photoanodes h/cfox0 (red), h/cfox3 (green) and h/cfox30 (blue) measured at 0.8 $V_{RHE}$. (b) ln($D$) as a function of time for h/cfox0 (red), h/cfox3 (green) and h/cfox30 (blue). Phase 1 and 2 represent surface charge recombination and OEC charging, respectively.

Thus, $k_{ct}$ and $k_{rec}$ can be estimated from photocurrent transients. We compare both rate constants using this simple method with those obtained from PEIS in Table 5-2. TP and PEIS methods produce good agreement overall except for $k_{ct}$ of h/cfox30, where PEIS gives a value nearly one magnitude higher than TP. The cause of such difference can be found in ln$D$–$t$ curves measured at 0.8 $V_{RHE}$. The shapes of these curves resemble TAS results (Fig. 5-20b).[230] For h/cfox30, two decay phases can be distinguished as opposed to only one for h/cfox0 and h/cfox3. The high frequency decay from 1 ms (recording limit) to about 50 ms is assigned to surface charge recombination (Phase 1 of Fig. 5-20b).[230] It is clear that CoFeO$_x$ in h/cfox30 effectively slows down this decay rate. The second decay stage in h/cfox30 is associated with the retention of photocurrent because of charging of CoFeO$_x$, which indicates this interfacial charge transfer from the semiconductor to the OEC is more rapid than the water oxidation (Phase 2 of Fig. 5-20b). In Table 5-2, charge transfer efficiencies calculated from rate constants by PEIS and TP (using Eq. 5-6) are compared with values obtained from the ratio of photocurrent densities measured in NaOH without and with a hole scavenger H$_2$O$_2$ (0.5 M). Notably, $\phi$(H$_2$O$_2$) are much lower compared to TP and PEIS methods. The differences can be understood by a stronger degree of band bending when H$_2$O$_2$ is present, where recombination at space charge region is minimized, hence giving a more accurate estimation of maximum photocurrent density. This effect is more pronounced in h/cfox0 due to its slower kinetics. PEIS and TP give similar results for h/cfox0 and h/cfox3 whereas TP has a more accurate approximation for h/cfox30. Therefore, we believe that the overestimation of $k_{ct}$ with PEIS is a result of the AC environment during

measurements which takes charging current of $CoFeO_x$ in h/cfox30 for water oxidation current. This analysis confirms that the higher photocurrent density is at least partly a result of OEC charging.

Table 5-2 Rate constants ($s^{-1}$) of photoanodes with different $CoFeO_x$ thicknesses calculated by TP and PEIS at 0.8 $V_{RHE}$

| Method | h/cfox0 | | h/cfox3 | | h/cfox30 | |
|---|---|---|---|---|---|---|
| | TP | EIS | TP | EIS | TP | EIS |
| $k_{ct}$ ($s^{-1}$) | 1.95 | 1.62 | 2.62 | 3.82 | 0.26 | 2.40 |
| $k_{rec}$ ($s^{-1}$) | 39.72 | 46.71 | 35.84 | 65.04 | 12.09 | 18.92 |
| $\phi$(est.) | 4.7% | 3.4% | 6.8% | 5.5% | 2.1% | 11.3% |
| $\phi$($H_2O_2$) | 0.6% | | 3.7% | | 0.6% | |

IMPS was also carried out to complement PEIS and TP outcomes. The theory behind IMPS is briefly introduced in Note S3 (Section 5.1.5) and more thoroughly explained elsewhere.[175,271] IMPS applies small perturbations of light intensity at a fixed potential and probes the photocurrent response from the PEC system. In contrast to PEIS, the redox reaction of $CoFeO_x$ by external voltage perturbation is avoided, which allows us to see if photo-generated holes are able to oxidize the OEC.

The complex IMPS plots of h/cfox0 and h/cfox3 show well defined low frequency semicircles at all potentials with no apparent flattening (Fig. 5-22a, with full dataset of IMPS in Fig. 5-21). The smaller low frequency semicircle of h/cfox3 clearly shows better charge transfer efficiency at high potentials. On the other hand, h/cfox30 shows distinct characteristics at 0.85 $V_{RHE}$. Two semicircles can be distinguished in the first quadrant, with the lower frequency part overlapping that of h/cfox0 and h/cfox3 and hence we attribute it to water oxidation. The appearance of another semicircle is indicative of an additional PEC process. Here, the only possible explanation is the oxidation of $CoFeO_x$ by holes. The high frequency intercept point of h/cfox30 is notably higher than the other two samples, meaning a higher hole flux to the surface. In h/cfox30, the band bending is more pronounced in the space charge region thanks to rapid charge transfer from hematite to $CoFeO_x$. Consequently, less recombination at the space charge region occurs and a higher hole flux reaches the surface. At 1.2 $V_{RHE}$, as most $CoFeO_x$ is oxidized by external bias, this is no longer an advantage, so high frequency intercepts become close again. Here only one semicircle is measured, meaning the absence of $CoFeO_x$ photo-oxidation. This semicircle is, however, the biggest among all, meaning a lower charge transfer efficiency. Its poor performance

with respect to the others can be understood by calculating the rate constants from these complex plots (steps illustrated in Note S3, Section 5.1.5).
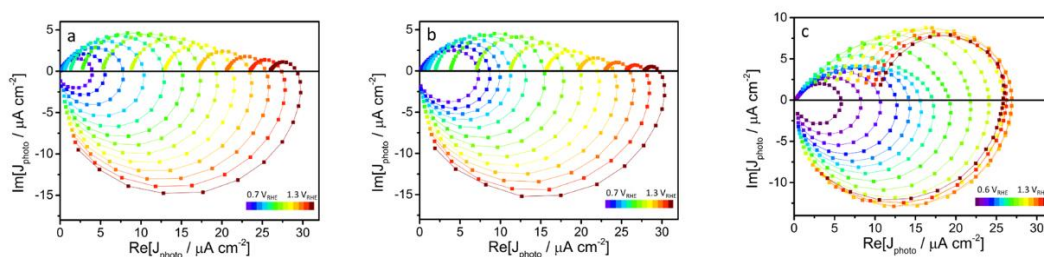


Fig. 5-21 Full IMPS complex plots of (a) h/cfox0, (b) h/cfox3 and (c) h/cfox30.
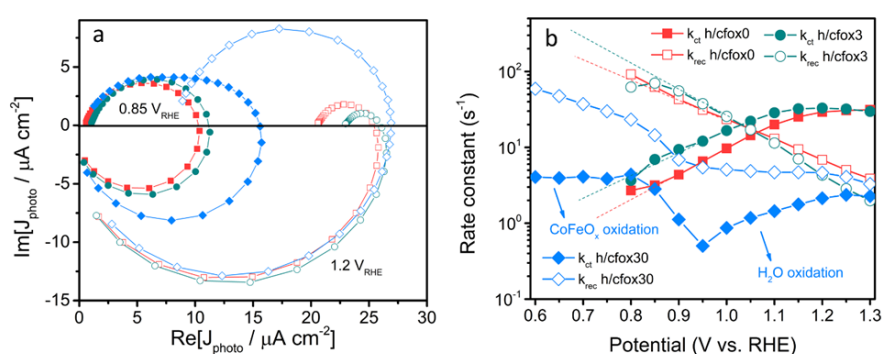


Fig. 5-22 (a) IMPS complex plots for h/cfox0 (red squares) h/cfox3 (green circles) and h/cfox30 (blue diamonds) at 0.85 (solid symbols) and 1.2 $V_{RHE}$ (open symbols). (b) Rate constants for h/cfox0, h/cfox3 and h/cfox30 (same color scheme) calculated with IMPS plots at various potentials. Solid symbols represent $k_{ct}$ and open symbols represent $k_{rec}$.

The rate constants calculated with IMPS are displayed in Fig. 5-22b. Unlike PEIS at 100 mW cm$^{-2}$ irradiation, IMPS gives decreasing $k_{rec}$ for h/cfox0 and h/cfox3. As discussed before, this is a result of a weaker light intensity used (37.5 mW cm$^{-2}$, *cf.* Fig. 5-16). The values of $k_{rec}$ for h/cfox0 and h/cfox3 are similar, while $k_{ct}$ is higher for h/cfox3 at all potentials, in excellent agreement with PEIS. Rate constants below 0.8 $V_{RHE}$ are not investigated since they are below the photocurrent onset potential. As applied potential increases, $k_{ct}$ for both h/cfox0 and h/cfox3 increase continuously until surpassing $k_{rec}$ at 1.05 $V_{RHE}$, beyond which charge transfer is more favored, which lead to high $\phi_{ct}$. The fitting for h/cfox30 requires more attention since the low frequency parts are convoluted with two semicircles at low voltages. To obtain meaningful rate constants, the lowest frequency semicircles must be disregarded. As such, the fitted rate constants are representative of photo-oxidation of CoFeO$_x$ rather than water. Above 0.95 $V_{RHE}$, water oxidation rate constants can be successfully fitted

again. From the plots it can be seen that the kinetics of $CoFeO_x$ oxidation is faster than water oxidation as previously suggested. When $CoFeO_x$ is fully functional after being oxidized, charge transfer is slowed as well as surface recombination, which agrees remarkably with PEIS results. The charge transfer efficiencies at 1.25 $V_{RHE}$ calculated from IMPS rate constants are, relatively, in good agreement compared to $\phi_{ct}$ obtained with the hole scavenging approach (Table 5-3). Higher values produced by IMPS result from differences in band bending as discussed before for PEIS.

Table 5-3 Charge transfer efficiencies calculated with IMPS and hole scavenging for different photoanodes at 1.25 $V_{RHE}$

|  | h/cfox0 (%) | h/cfox3 (%) | h/cfox30 (%) |
|---|---|---|---|
| $\phi$(IMPS) | 85.9 | 91.8 | 36.7 |
| $\phi$(H$_2$O$_2$) | 70.7 | 85.0 | 12.0 |

All four electrochemical methods applied in this work lead to the finding that photogenerated holes are used for $CoFeO_x$ oxidation. The results show that enhancement of charge transfer rate and reduction of surface recombination for water oxidation cannot be harnessed simultaneously. Therefore, in an attempt to decrease $k_{rec}$ without sacrificing the increase in $k_{ct}$, we passivated the hematite film by adding a layer of $GaO_x$ by chemical bath deposition (denoted as h/$GaO_x$).[215,232] Then, $CoFeO_x$ was electrodeposited with three coating sweeps as before (denoted as h/$GaO_x$/cfox3). The $J$–$V$ curves for h/cfox0, h/cfox3, h/$GaO_x$ and h/$GaO_x$/cfox3 are displayed in Fig. 5-23a. The improvement at low potentials with the $GaO_x$ coating is similar with cfox3 coating. When the two treatments are combined, the photocurrent density is significantly enhanced. We then conducted PEIS measurements and kinetic analyses for $GaO_x$ treated samples, which are compared with h/cfox3 (Fig. 5-23b).
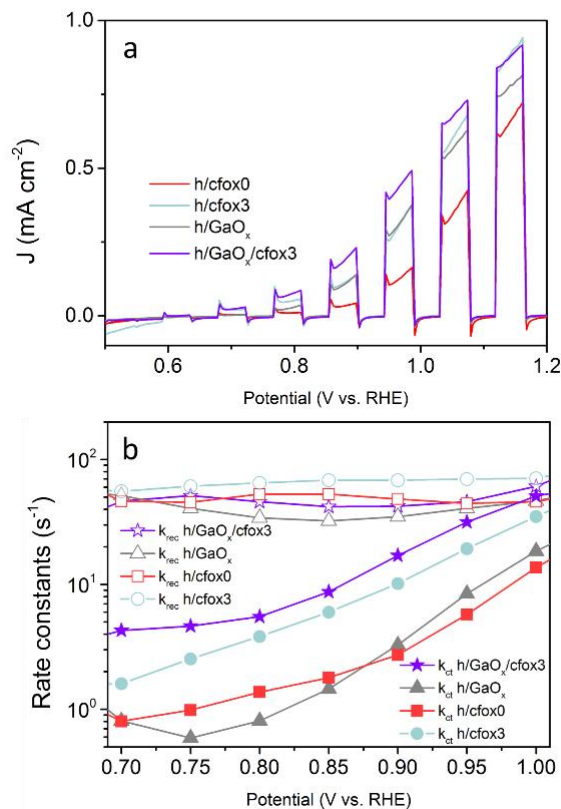
Fig. 5-23 (a) Linear sweep voltammograms under 1 sun chopped light of h/cfox0 (red), h/cfox3 (light green), h/GaO$_x$ (grey) and h/GaO$_x$/cfox3 (purple). (b) Rate constants calculated from PEIS for h/cfox0 (red squares), h/cfox3 (light green circles) h/GaO$_x$ (grey triangles) and h/GaO$_x$/cfox3 (purple stars). Empty symbols indicate $k_{rec}$ and filled symbols indicate $k_{ct}$.

Firstly, the effect of GaO$_x$ agrees with previously reported results obtained *via* IMPS, *i.e.* $k_{ct}$ remains similar and $k_{rec}$ drops.[274] However, when three sweeps of electrodeposition of CoFeO$_x$ are carried out on h/GaO$_x$, there is a marginal upshift in $k_{rec}$ possibly due to interphase recombination. On the other hand, $k_{ct}$ of h/GaO$_x$/cfox3 is much larger than that of h/cfox3 at any potential (Fig. 5-23b). This rise in $k_{ct}$ with a GaO$_x$ interlayer is a result of an alteration of the distribution of intermediate surface states (i-ss), as evidenced by a cathodic shift of $C_{ss}$ for h/cfox0 compared with h/GaO$_x$ and h/GaO$_x$/cfox3 (Fig. 5-24). A similar observation was reported by Wang *et al.* in the case of Al$_2$O$_3$ passivation of hematite photoanodes.[269] The energetics of altered surface states, as a consequence, may be more in favor of OER by CoFeO$_x$. This way, by adding a GaO$_x$ interlayer, the photocurrent density can be greatly improved at relatively low potentials ($\sim$0.5 mA cm$^{-2}$ at 1.0 V$_{RHE}$) owing to the additional enhancement of $k_{ct}$.
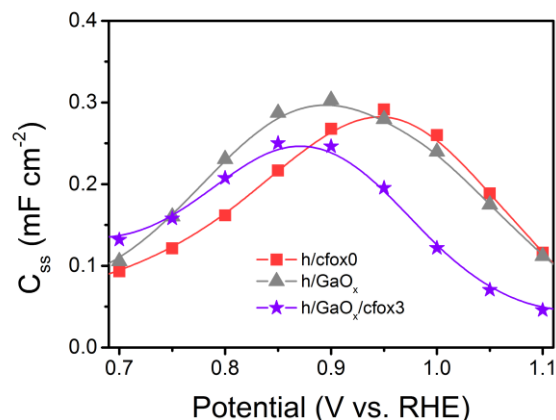
Fig. 5-24 Surface states capacitance $C_{ss}$ calculated from PEIS for h/cfox0 (red squares), h/cfox3 (light green circles), h/GaO$_x$ (grey triangles) and h/GaO$_x$/cfox3 (purple stars).

## Discussion

Our understanding of the role of CoFeO$_x$ on hematite photoanodes is summarized in Fig. 5-25. For a bare hematite photoanode, surface charge recombination takes place at a much faster time scale than charge transfer at semiconductor–liquid junction. Introducing CoFeO$_x$ is found to have different impact at different loading levels.
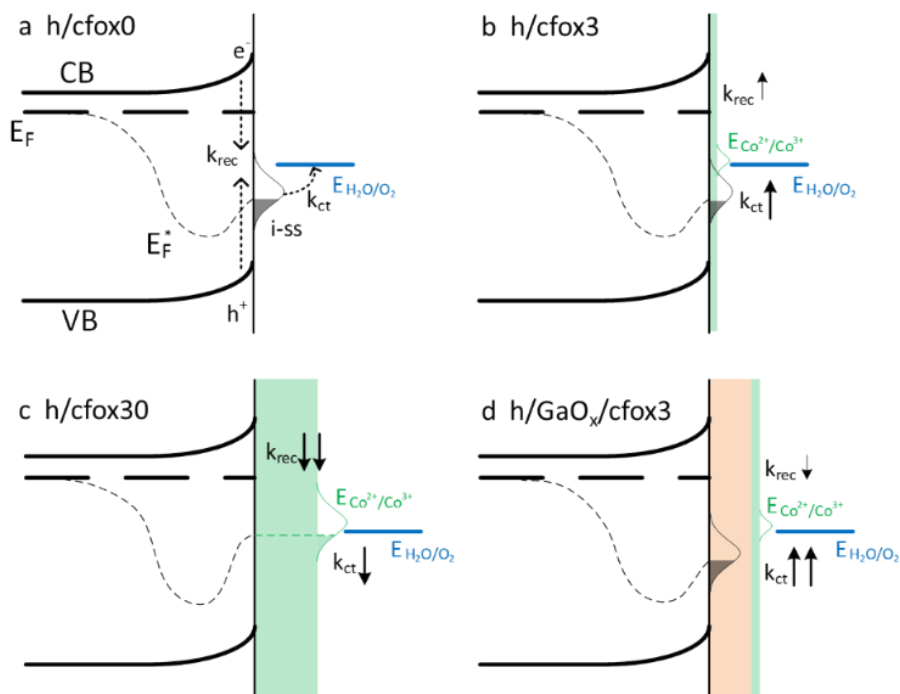


Fig. 5-25 Energetic schemes for (a) h/cfox0 showing surface recombination $k_{rec}$ and charge transfer $k_{ct}$ through i-ss; (b) h/cfox3 where $k_{ct}$ increase relative to h/cfox0 and density of i-ss reduces; (c) h/cfox30 where both rate constants are

decreased; (d) h/GaO$_x$/cfox3 with significantly increased $k_{ct}$ and increased density of i-ss.

An extremely thin layer of CoFeO$_x$ does not strongly affect recombination but significantly accelerates the charge transfer. In this case, CoFeO$_x$ assists the intermediate surface states by acting as a more efficient shuttle for holes thereby improving the OER charge transfer kinetics. When thickness is relatively higher, both the charge transfer and surface recombination slow down but especially the surface recombination, which is in good agreement with other studies on OECs of similar thickness on semiconductors.[165,175,274] Since CoFeO$_x$ fully covers the hematite electrode, as well as having a lower oxidation potential compared to i-ss, the photogenerated holes mainly charge the catalyst. The higher photocurrent density at low potential is partly attributed to a slower recombination but also to this pseudocapacitive OEC charging. In this situation, only the holes reaching the catalyst with energies between quasi-Fermi level ($E_F$*) and $E$(H$_2$O/O$_2$) are capable of carrying out water oxidation, which only takes a small proportion. This detrimental effect is, on the other hand, alleviated by the drop of $k_{rec}$, giving a photocurrent density comparable to h/cfox0. Accordingly, if CoFeO$_x$ loading is even higher, it is possible that all photogenerated holes oxidize the catalyst and $E_F$* moves higher than $E$(H$_2$O/O$_2$) (Fig. 5-26a). If that happens, photo-assisted water oxidation will become energetically impossible, which can be evidenced by the absence of net photocurrent after the catalyst is sufficiently oxidized. In this situation, photogenerated holes have no other pathways but recombination. Indeed, this expected $J$–$V$ behavior is observed on an h/cfox film containing a very thick CoFeO$_x$ layer deposited at 1.8 V$_{RHE}$ for 25 min (Fig. 5-26b). It shows little net photocurrent and strong spikes at higher applied potentials. Although higher applied potential can oxidize CoFeO$_x$ thus avoiding photo-charging of it, the low charge transfer rate constants prevent rapid improvement of photocurrent density.
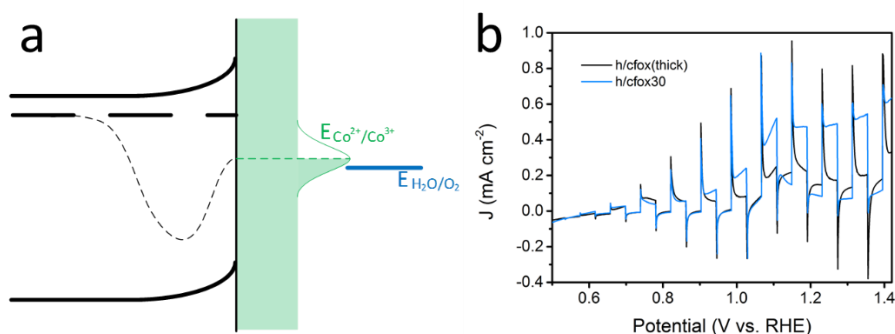
Fig. 5-26 (a) An energetic scheme of a hematite photoanode coated with excessive amount of $CoFeO_x$. (b) *J-V* curve (under 1 sun chopped illumination, 5 mV s$^{-1}$) of a hematite photoanode (black) coated with $CoFeO_x$ using electrodeposition at 1.8 $V_{RHE}$ for 25 min with same electrolyte composition for other $CoFeO_x$ coatings done in this work. Almost no net photocurrent density can be obtained at high applied potentials compared with h/cfox30 (blue).

Additional improvement of photoactivity can be achieved by adding an interlayer of $GaO_x$. The result is ascribed to remarkable enhancement of $k_{ct}$ without the strong OEC charging effect due to a redistribution of i-ss. This configuration can also be seen as an "adaptive junction" on top of a "buried junction" as proposed by Nellist and co-workers, although $GaO_x$ is not catalytically active.[255] Despite this promising improvement of photocurrent density, $GaO_x$ is unstable in strong alkaline solutions. Therefore, a more stable material to form a "buried junction" with the light absorbing layer is of research interest.

Our theory on the effect of different thicknesses has been tested to be applicable on some other Co or Ni containing OEC species (data not shown). Nevertheless, when CoPi is coated on our hematite photoanodes, the capacitive behavior is totally absent. We believe in this case, the $Co^{2+}/Co^{3+}$ reaction may be stabilized by phosphate ions and photo-charging is prevented. This topic deserves more attention.

**Conclusion**

We have investigated the effect of OEC coating thickness on hematite photoanodes using a promising OEC candidate, $CoFeO_x$. The research outcomes suggest that to improve interfacial charge transfer properties, the loading of the OEC must be carefully controlled to an extremely thin level as the oxidation current of $CoFeO_x$ can easily introduce an "illusion" of increase in photocurrent density. A slow scan rate is therefore preferred for LSV measurements, while light chopping sometimes provides extra information. According to our kinetic analysis, some traditional OEC coatings

are perhaps too thick to take advantage of the rapid water oxidation kinetics of the OEC. We have also revealed that an interlayer of $GaO_x$ between hematite and OEC can enhance hole transfer rates further compared to an OEC coating alone. Our work has found a new way of improving charge transfer kinetics at photoanode surfaces and helps understand the interplay between a semiconductor and an electrocatalyst. Future research will target at deeper understanding of semiconductor–catalyst junctions and creating more efficient complex photoanodes.

## Conflicts of interest

There are no conflicts of interest to declare.

## Data Access Statement

All data created during this research are available upon reasonable request.

## Acknowledgements

### 5.1.5 Supporting Information

## Note S1 Demonstration of formal equivalence between the phenomenological kinetic model and EIS equivalent circuit model

The kinetic analysis of impedance data by Wijayantha et al. suggested two semicircles of high frequency (HF) and low frequency (LF).[267] The intercepts of the two semicircles with $Z_{real}$ axis are $R_{ser}$, $R_{ser}+Z_2$ and $R_{ser}+Z_1$. This can be adapted to the equivalent circuit used in this paper for a bare hematite photoanode according to careful examination of Bode plots (Figure S4). It has been previously reported that charge transfer occurs on the scale of 0.1 to 1 s,[230] which matches the peaks of phase angles of lower frequency semicircles. Consequently, we attribute low frequency semicircle to interfacial charge transfer and the high frequency semicircle to surface charge recombination by trapping states. Series resistance remains the same physical meaning but is denoted as $R_s$ here. Therefore, the resistive equivalence can be described as

$$R_{ser} + Z_2 = R_s + R_{trap} \qquad \text{Eq. 5-11}$$

$$R_{ser} + Z_1 = R_{tot} = R_s + R_{trap} + R_{ct} \qquad \text{Eq. 5-12}$$

Now Equation 4 in Wijayantha's paper[267] can be re-written as

$$\frac{Z_1 - R_{ser}}{Z_2 - R_{ser}} = \frac{R_{trap} + R_{ct}}{R_{trap}} = 1 + \frac{R_{ct}}{R_{trap}} = 1 + \frac{k_r}{k_t} \qquad \text{Eq. 5-13}$$

Since the rate constants of charge transfer and recombination rate constant are $k_{ct}$ and $k_{rec}$ respectively in this paper (instead of $k_t$ and $k_r$), we have

$$\frac{R_{ct}}{R_{trap}} = \frac{k_{rec}}{k_{ct}} \qquad \text{Eq. 5-14}$$

or

$$k_{rec} = \frac{R_{ct}}{R_{trap}} k_{ct} \qquad \text{Eq. 5-15}$$

According to Wijayantha's model, $k_{ct}$ is equal to the frequency corresponding to the highest imaginary component of the low frequency semicircle, which is by definition, in the electrical circuit, the reciprocal of the time constant $\tau$(LF) of the $C_{ss}$&$R_{ct}$ unit (Figure 3a). This can be formulated as

$$k_{ct} = \frac{1}{\tau(LF)} = \frac{1}{C_{ss}R_{ct}}$$ 
<div align="right">Eq. 5-16</div>

The surface recombination rate constant $k_{rec}$ can now be expressed through Eq. 5-15

$$k_{rec} = \frac{1}{C_{ss}R_{trap}}$$ 
<div align="right">Eq. 5-17</div>

It can be immediately seen that the two rate constants share $C_{ss}$ but differ in resistance. This is understandable considering the kinetic model where charge transfer and surface recombination are two competing processes taking place at the interface that utilize charges stored in surface states (cf. Figure 1 of ref 1).

From the deductions shown above, we believe that the concepts of the phenomenological model and parameters in the equivalent circuit share the same root and our impedance data can be used for kinetic analyses.

**Note S2 Justification of PEIS and Mott-Schottky analyses.**

To confirm the validity of the EIS and Mott-Shottky analyses used on the porous nanostructured hematite photoanodes of this work, we need to ensure that nanostructuring does not significantly change the behavior within the space charge region and at interface. The behavior will not change if the space charge region thickness is much smaller than the nanostructure dimension.

We start with the estimation of doping density $N_d$ of hematite and flat band potential $E_{FB}$ by investigating a flat film using the same preparation method as reported in the Experimental but without P123 sacrificial pore templating. Capacitance is obtained by fitting impedance spectra of this film measured in the PEC setup as described in Experimental in the dark.
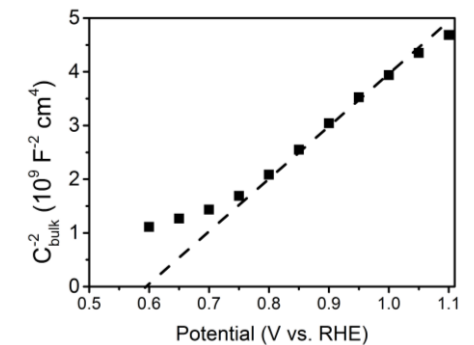
Fig. 5-27 Mott-Schottky plot for a flat hematite film.

The Mott-Schottky plot gives an intercept of 0.6 $V_{RHE}$ (approximated to be $E_{FB}$) and a slope of $9.13 \times 10^9$ $F^{-2}$ $V^{-1}$. Hence, doping density $N_d$ is given by

$$N_d = \frac{2}{q \varepsilon \varepsilon_0 A^2 k} = 1.64 \times 10^{20} \ cm^{-3} \qquad \text{Eq. 5-18}$$

where $q$ is the electronic charge ($1.6 \times 10^{-19}$ C); $\varepsilon$ is the relative permittivity of hematite (33),[275] $\varepsilon_0$ is the vacuum permittivity ($8.85 \times 10^{-12}$ F m$^{-1}$), $A$ is the geometric area (1.69 cm$^{-2}$), and $k$ is the slope of the linear fitting. Note this value is very high due to Sn diffusion from FTO after 800 °C treatment.

Assuming a potential drop at space charge region $\Delta \phi_{SC}$ of 0.6 V, using the *abrupt approximation*,[276] the differential space charge capacitance $C_{SC}$ is given by

$$C_{SC} = \left[ \frac{q N_d \varepsilon \varepsilon_0}{2 \left( \Delta \phi_{SC} - \frac{k_B T}{q} \right)} \right]^{1/2} = 8.2 \ \mu F \ cm^{-2} \qquad \text{Eq. 5-19}$$

where $k_B$ is the Boltzmann constant ($1.38 \times 10^{-23}$ m$^2$ kg s$^{-2}$ K$^{-1}$) and $T$ is the room temperature (298K).

It should also be noted that $C_{SC}$ is considerably smaller than Helmholtz capacitance ($C_H$), which can be estimated to be 200 µF cm$^{-2}$.[269] Therefore, the effect of potential drop at Helmholtz layer $\Delta \phi_H$ is negligible.

This result for $C_{SC}$ is in excellent agreement with experimental value (8.06 µF cm$^{-2}$ at 1.2 $V_{RHE}$). Therefore, the doping density $N_d$ of $1.64 \times 10^{20}$ cm$^{-3}$ used in our model is a good approximation and can be used for our nanostructured photoanodes to calculate potential drops.

The applicability of the kinetic model on nanostructures is demonstrated as follows. Since there is not an established model for mesoporous structures, we apply our nanostructure dimension (radius $R$=45 nm) to a model designed for nanorods recently developed by Peter et al.[269]

For a rod structure, the potential drop at space charge region is now calculated as

$$\Delta\phi_{SC,rod} = -\frac{qN_d}{2\varepsilon\varepsilon_0}[\frac{1}{2}(x^2 - R^2) + x^2 \ln\left(\frac{R}{x}\right)] \qquad \text{Eq. 5-20}$$

where $x$ is the distance from the edge of the space charge region to the center of the rod.

If $\Delta\phi_{SC,rod}$ is again assumed to be 0.6 V, $x$ is 41.3 nm, and the space charge region width is

$$W_{SC} = R - x = 3.7 \, nm \ll R \qquad \text{Eq. 5-21}$$

Here potential drop at Helmholtz layer $\Delta\phi_{H,rod}$ is given by equation:

$$\Delta\phi_{H,rod} = \frac{qN_d}{2C_H}(\frac{R^2 - x^2}{R}) \qquad \text{Eq. 5-22}$$

and is found to be less than 0.05 V for $C_H$=200 µF cm$^{-2}$. Again, this is negligible.

From the calculation above, we found that the depletion region is very shallow. Under illumination, strong Fermi level pinning is induced and $\Delta\phi_{SC}$ will be much lower so the depletion width will be smaller than 3.7 nm. Therefore, our impedance as well as Mott-Schottky analyses are valid in both dark and light conditions.

## Note S3 Brief introduction to IMPS measurement and data interpretation

IMPS serves as a tool to probe surface kinetics of photoelectrodes, which has been proved suitable for multi-step charge transfer reactions.[270] It has been successfully applied to hematite photoanode systems by Peter et al. with a simple model where charge transfer only occurs at surface states while competing with surface recombination,[225] which is also used in this paper for PEIS study. In an IMPS measurement, a base light illumination intensity is employed to reach steady-state conditions while a frequency-dependent sinusoidal illumination is imposed to the system and the corresponding modulated photocurrent response is measured.

The spectrum of a typical IMPS measurement for an n-type semiconductor photoanode consists of two semicircles located at first and fourth quadrant. The high frequency semicircle starts in the fourth quadrant that represents the attenuation by the total resistance of the cell and combined space charge capacitance and Helmholtz layer capacitance, giving an RC time constant of the cell. The high intercept with the real axis depicted in Figure S17 represents the modulated photocurrent that is reflective of

the hole flux arriving at the surface, which happens at a certain frequency such that recombination processes are effectively "frozen out".[225] By decreasing the frequency of perturbation even further surface recombination and charge transfer processes dominate, giving another semicircle in the first quadrant. The imaginary part reaches a maximum when the characteristic time constant of the system is met:[175]

$$\omega_{max} = k_{ct} + k_{rec} \qquad \text{Eq. 5-23}$$

The system then moves toward its steady state as frequency lowers further, giving a low intercept value that corresponds to steady state photocurrent. The ratio of low frequency and high frequency intercept represents the fraction of holes that arrives at surface and is injected to the electrolyte, which is effectively charge transfer (injection) efficiency.

$$\phi_{ct} = \frac{k_{ct}}{k_{ct} + k_{rec}} \qquad \text{Eq. 5-24}$$

The two rate constants $k_{ct}$ and $k_{rec}$ can then be extracted using Eq. 5-26 and Eq. 5-27. This frequency dependent measurement is particularly useful since it allows one to obtain phenomenological kinetic constants for charge transfer and recombination directly, without altering the band bending or charge distribution inside the semiconductor.
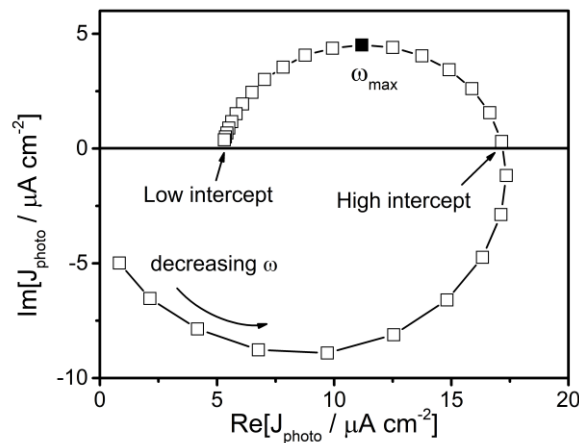


Fig. 5-28 A representative IMPS complex plot of a hematite photoanode.

Table 5-4 to Table 5-9 show original fitted EIS parameters obtained from Zview software. The working area of all electrodes is 0.25 cm$^2$.

Table 5-4 Results for h/cfox0.

| Scan | Potential (V$_{RHE}$) | R$_s$ (Ω) | C$_{bulk}$ (F) | R$_{trap}$ (Ω) | C$_{ss}$ (F) | R$_{ct}$ (Ω) |
|------|------------------------|-----------|-----------------|-----------------|---------------|---------------|
| 1 | 1.2 | 31.64 | 1.11E-05 | 381.9 | 9.56E-06 | 797.5 |
| 2 | 1.15 | 31.76 | 1.19E-05 | 398 | 1.63E-05 | 584 |
| 3 | 1.1 | 31.85 | 1.27E-05 | 377 | 3.05E-05 | 484.3 |
| 4 | 1.05 | 31.9 | 1.36E-05 | 328.8 | 4.64E-05 | 545.6 |
| 5 | 1 | 31.94 | 1.45E-05 | 288.6 | 5.60E-05 | 832.8 |
| 6 | 0.95 | 31.97 | 1.58E-05 | 279.4 | 6.12E-05 | 1633 |
| 7 | 0.9 | 32.01 | 1.73E-05 | 296.5 | 5.98E-05 | 3401 |
| 8 | 0.85 | 32.07 | 1.93E-05 | 353.1 | 5.42E-05 | 6908 |
| 9 | 0.8 | 32.16 | 2.17E-05 | 481 | 4.45E-05 | 13879 |
| 10 | 0.75 | 32.23 | 2.44E-05 | 799.4 | 3.48E-05 | 24505 |
| 11 | 0.7 | 32.23 | 2.73E-05 | 1509 | 2.80E-05 | 34662 |
| 12 | 0.65 | 32.09 | 3.02E-05 | 1812 | 2.20E-05 | 24708 |
| 13 | 0.6 | 31.85 | 3.38E-05 | 1134 | 1.75E-05 | 11231 |

Table 5-5 Results for h/cfox3.

| Scan | Potential (V$_{RHE}$) | R$_s$ (Ω) | C$_{bulk}$ (F) | R$_{trap}$ (Ω) | C$_{ss}$ (F) | R$_{ct}$ (Ω) |
|------|------------------------|-----------|-----------------|-----------------|---------------|---------------|
| 1 | 1.2 | 30.72 | 1.07E-05 | 238.7 | 6.18E-06 | 1192 |
| 2 | 1.15 | 30.72 | 1.12E-05 | 235 | 7.31E-06 | 915.6 |
| 3 | 1.1 | 30.72 | 1.28E-05 | 380.6 | 1.79E-05 | 587.7 |
| 4 | 1.05 | 30.73 | 1.36E-05 | 358.5 | 3.10E-05 | 529.1 |
| 5 | 1 | 30.66 | 1.46E-05 | 313.3 | 4.52E-05 | 633.3 |
| 6 | 0.95 | 30.58 | 1.57E-05 | 282.5 | 5.08E-05 | 1020 |
| 7 | 0.9 | 30.52 | 1.71E-05 | 284.5 | 5.15E-05 | 1913 |
| 8 | 0.85 | 30.46 | 1.89E-05 | 311.6 | 4.70E-05 | 3551 |
| 9 | 0.8 | 30.41 | 2.10E-05 | 374 | 4.11E-05 | 6360 |
| 10 | 0.75 | 30.36 | 2.36E-05 | 459.2 | 3.56E-05 | 11092 |
| 11 | 0.7 | 30.31 | 2.65E-05 | 539.4 | 3.33E-05 | 18782 |
| 12 | 0.65 | 30.16 | 2.93E-05 | 531 | 3.17E-05 | 20224 |
| 13 | 0.6 | 30 | 3.29E-05 | 568.8 | 2.94E-05 | 11076 |

Table 5-6 Results for h/cfox30.

| Scan | Potential ($V_{RHE}$) | $R_s$ ($\Omega$) | $C_{bulk}$ (F) | $R_{trap}$ ($\Omega$) | $C_{ss}$ (F) | $R_{ct}$ ($\Omega$) | $C_{cfox}$ (F) | $R_{cfox}$ ($\Omega$) |
|---|---|---|---|---|---|---|---|---|
| 1 | 1.2 | 29.98 | 1.16E-05 | 134.6 | 5.88E-04 | 93.88 | 0.0024 | 1839 |
| 2 | 1.15 | 30.33 | 1.26E-05 | 194.3 | 3.13E-04 | 243.2 | 0.00246 | 1454 |
| 3 | 1.1 | 30.4 | 1.35E-05 | 270.6 | 1.84E-04 | 555.6 | 0.00182 | 987.2 |
| 4 | 1.05 | 30.4 | 1.44E-05 | 326.3 | 1.41E-04 | 732.8 | 8.50E-04 | 740.1 |
| 5 | 1 | 30.41 | 1.55E-05 | 373.1 | 1.16E-04 | 1394 | | |
| 6 | 0.95 | 30.42 | 1.66E-05 | 378.3 | 1.09E-04 | 1585 | | |
| 7 | 0.9 | 30.42 | 1.80E-05 | 374.1 | 1.05E-04 | 1932 | | |
| 8 | 0.85 | 30.48 | 2.02E-05 | 392.4 | 1.08E-04 | 2668 | | |
| 9 | 0.8 | 30.6 | 2.33E-05 | 452.3 | 1.17E-04 | 3566 | | |
| 10 | 0.75 | 30.75 | 2.75E-05 | 565.6 | 1.33E-04 | 4446 | | |
| 11 | 0.7 | 30.87 | 3.26E-05 | 755 | 1.47E-04 | 5288 | | |
| 12 | 0.65 | 30.79 | 3.64E-05 | 970.3 | 1.21E-04 | 5978 | | |
| 13 | 0.6 | 30.42 | 3.82E-05 | 1134 | 7.73E-05 | 7173 | | |

Table 5-7 Results for h/cfox0 (under 10 mW cm$^{-2}$ illumination).

| Scan | Potential ($V_{RHE}$) | $R_s$ ($\Omega$) | $C_{bulk}$ (F) | $R_{trap}$ ($\Omega$) | $C_{ss}$ (F) | $R_{ct}$ ($\Omega$) |
|---|---|---|---|---|---|---|
| 1 | 1.2 | 27.95 | 1.53E-05 | 4339 | 2.33E-05 | 6668 |
| 2 | 1.15 | 27.97 | 1.61E-05 | 3955 | 3.14E-05 | 8277 |
| 3 | 1.1 | 27.97 | 1.70E-05 | 3905 | 3.50E-05 | 13120 |
| 4 | 1.05 | 27.96 | 1.79E-05 | 4179 | 3.50E-05 | 23215 |
| 5 | 1 | 27.95 | 1.90E-05 | 4398 | 3.30E-05 | 41239 |
| 6 | 0.95 | 27.92 | 2.01E-05 | 4215 | 2.73E-05 | 60522 |
| 7 | 0.9 | 27.9 | 2.13E-05 | 4150 | 2.24E-05 | 75518 |
| 8 | 0.85 | 27.88 | 2.27E-05 | 3971 | 1.81E-05 | 94701 |
| 9 | 0.8 | 27.85 | 2.43E-05 | 3375 | 1.56E-05 | 104530 |
| 10 | 0.75 | 27.87 | 2.63E-05 | 2833 | 1.50E-05 | 101320 |
| 11 | 0.7 | 27.8 | 2.88E-05 | 2043 | 1.44E-05 | 59414 |
| 12 | 0.65 | 27.69 | 3.19E-05 | 1161 | 1.44E-05 | 24678 |
| 13 | 0.6 | 27.6 | 3.11E-05 | 166.4 | 1.67E-05 | 10858 |

Table 5-8 Results for h/GaO$_x$

| Scan | Potential (V$_{RHE}$) | R$_s$ (Ω) | C$_{bulk}$ (F) | R$_{trap}$ (Ω) | C$_{ss}$ (F) | R$_{ct}$ (Ω) |
|---|---|---|---|---|---|---|
| 1 | 1.2 | 32.62 | 1.22E-05 | 333.5 | 9.29E-06 | 1152 |
| 2 | 1.15 | 32.77 | 1.31E-05 | 291.6 | 1.47E-05 | 835.6 |
| 3 | 1.1 | 32.88 | 1.42E-05 | 411.8 | 2.80E-05 | 658.9 |
| 4 | 1.05 | 32.91 | 1.52E-05 | 379.6 | 4.37E-05 | 657.7 |
| 5 | 1 | 32.96 | 1.64E-05 | 357.4 | 5.99E-05 | 902.7 |
| 6 | 0.95 | 32.97 | 1.78E-05 | 351.9 | 6.99E-05 | 1698 |
| 7 | 0.9 | 32.99 | 1.95E-05 | 378.3 | 7.58E-05 | 4033 |
| 8 | 0.85 | 32.98 | 2.15E-05 | 431.6 | 7.18E-05 | 9580 |
| 9 | 0.8 | 32.96 | 2.34E-05 | 507.9 | 5.77E-05 | 21441 |
| 10 | 0.75 | 32.9 | 2.52E-05 | 614.4 | 4.01E-05 | 42418 |
| 11 | 0.7 | 32.79 | 2.68E-05 | 735.9 | 2.64E-05 | 46948 |
| 12 | 0.65 | 32.63 | 2.86E-05 | 848.9 | 2.00E-05 | 21595 |
| 13 | 0.6 | 32.43 | 3.08E-05 | 732.7 | 1.89E-05 | 7499 |

Table 5-9 Results for h/GaO$_x$/cfox3

| Scan | Potential (V$_{RHE}$) | R$_s$ (Ω) | C$_{bulk}$ (F) | R$_{trap}$ (Ω) | C$_{ss}$ (F) | R$_{ct}$ (Ω) |
|---|---|---|---|---|---|---|
| 1 | 1.2 | 37.72 | 1.25E-05 | 175.4 | 1.11E-05 | 2179 |
| 2 | 1.15 | 37.59 | 1.13E-05 | 186.6 | 1.09E-05 | 1793 |
| 3 | 1.1 | 38.07 | 1.12E-05 | 359.2 | 1.14E-05 | 1339 |
| 4 | 1.05 | 38.02 | 1.13E-05 | 552.6 | 1.77E-05 | 881.6 |
| 5 | 1 | 37.79 | 1.17E-05 | 538.2 | 3.05E-05 | 643 |
| 6 | 0.95 | 37.74 | 1.25E-05 | 446 | 4.88E-05 | 647.5 |
| 7 | 0.9 | 37.71 | 1.36E-05 | 383.7 | 6.16E-05 | 952.3 |
| 8 | 0.85 | 37.69 | 1.50E-05 | 380.6 | 6.25E-05 | 1831 |
| 9 | 0.8 | 37.56 | 1.67E-05 | 419.4 | 5.19E-05 | 3497 |
| 10 | 0.75 | 37.28 | 1.85E-05 | 492.5 | 3.95E-05 | 5465 |
| 11 | 0.7 | 37.02 | 2.10E-05 | 652 | 3.30E-05 | 7089 |
| 12 | 0.65 | 36.85 | 2.46E-05 | 1082 | 3.41E-05 | 9687 |
| 13 | 0.6 | 36.62 | 2.93E-05 | 2351 | 4.34E-05 | 17748 |

### 5.1.6 Commentary

*On the timescale of OER*

In the manuscript, we have wrongly stated that OER is a "sluggish reaction that takes place in seconds", which can also be found sometimes in the literature. Although in transient absorption spectroscopy, the lifetime of photogenerated holes are observed to be seconds, which can be extended by anodic potential and co-catalysts, it does not represent the timescale of the reaction. Frequency resolved techniques, typically EIS, can produce a time constant for a polarization process. However, it may not be accurate to directly associate this time constant with reaction rate constant.

*Deposition of CoFeO$_x$*

Although we have shown TEM images where the top surface of hematite is covered by thin amorphous layers, its identity may be questioned. Therefore, more evidence is required to confirm whether this layer is CoFeO$_x$. Fortunately, this task has been accomplished by a newly published work where Hu's group used the same repetitious LSV electrodeposition method to coat CoFeO$_x$ on cauliflower hematite photoanodes.[277] In their work, high resolution STEM-EDX mapping (Fig. 5-29) shows evidence for well distributed cobalt, thereby proving the existence of CoFeO$_x$.
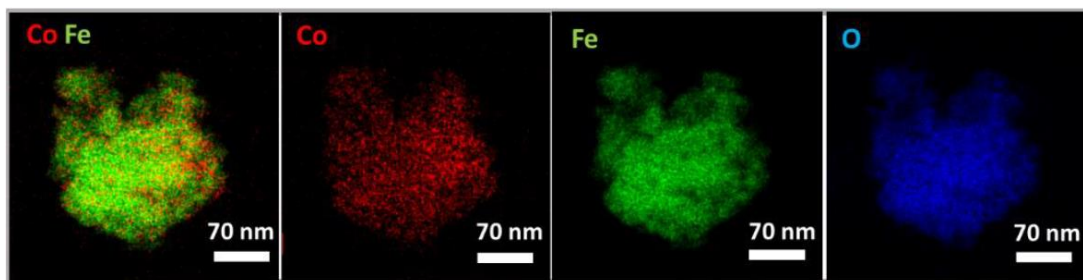


Fig. 5-29 STEM-EDX mapping (CoFe, Co, Fe and O) of hematite coated with electrodeposition of CoFeO$_x$. In particular, Co shows homogeneous distribution.[277] Reproduced from ref. [277] with permission from The Royal Society of Chemistry.

We must note the observation that repeated LSV deposition of CoFeO$_x$ did not result in apparent enhancement in OER peak currents in Fig. 5-5. Nevertheless, negative peaks continue to grow with each repetition, meaning that deposition process did not terminate within a few scans. The most possible explanation is that in the later stage of deposition, Co(OH)$_2$ was deposited instead of CoFeO$_x$ with the desired ratio. This speculation perfectly accounts for the low charge transfer rate constants

calculated from PEIS and IMPS. Unfortunately, trace metal elemental analysis on our TEM instrumentation during the course of this work was not possible.

*Reversed photocurrent density measurement*

In addition to the advanced PEC characterizations to prove the oxidation of $CoFeO_x$, a simple backward LSV measurement can further strengthen this finding. In Fig. 5-30, similar photocurrent density was recorded for backward scan compared with forward scan at high potentials because Co is in III oxidation state. However, the net photocurrent density become noticeably smaller near onset region upon backward scan, since $Co^{2+}/Co^{3+}$ conversion is irreversible, and the co-catalyst has not yet been reduced. This discrepancy is a strong evidence for involvement of photo-oxidation of $Co^{2+}$ during the forward scan.
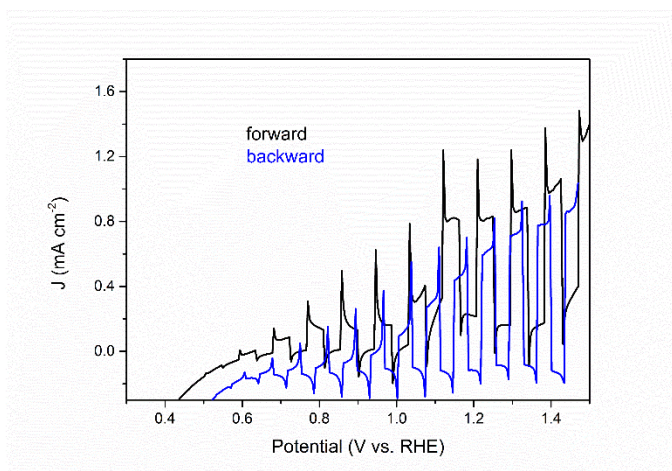


Fig. 5-30 Forward (black) and backward (blue) LSV measurements of h/cfox30

*Fermi level pinning at bare hematite photoanodes*

More comments are necessary here to illustrate the energetics of our photoanodes. In an ideal situation, band edge position is pinned at SCLJ. Enhanced band bending with higher applied potentials cause reduction in surface recombination, while charge transfer rate constant stays (Fig. 5-31a). Nevertheless, according to PEIS results, we found highly non-ideal behavior of our bare hematite electrodes, i.e., increasing $k_{ct}$ and nearly constant $k_{rec}$. This observation is a strong indication of total Fermi level pinning. For a photoanode with high concentration of surface states, back electron (surface) recombination becomes dominant, so it will heavily flatten the bands. According to Eq. 3-37, as applied potential is always close to flat band potential, the exponential term approaches 1, giving nearly constant $k_{rec}$ at all potentials. The quasi Fermi level

of holes also moves linearly with applied potential, and charge transfer rate increases correspondingly (Fig. 5-31b). This condition is akin to charge transfer across a metal electrode, which has a dependence of 120 mV per decade increment. However, for one magnitude rise in $k_{ct}$ in the case of our hematite photoanodes, the potential shift is 180 mV. Such high value can be ascribed to the fact that water oxidation is a multi-step reaction. Even higher values have been reported by other groups.[37,155]
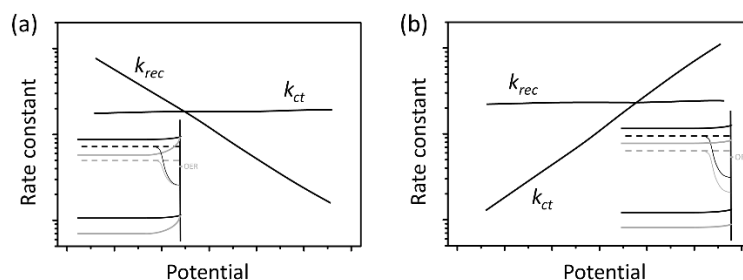


Fig. 5-31 Illustration of changes in rate constants as a function of applied potential for an ideal case and hematite electrodes with high surface states concentration. Insets show band diagrams with quasi Fermi level.

*Charge transfer from hematite to catalyst*

There are two possible ways for charge transfer from hematite to the OEC. The first way is by tunnelling, which is dominant when there is not much or no surface states. For our hematite electrodes, charge transfer via surface states becomes much more significant. This process has been discussed by Nellist et al., where the energetics is impacted by the effectiveness of the OEC.[255] Since surface states and catalyst are in quasi equilibrium, surface states have to be more heavily charged when in contact with a poor OEC due to the high overpotential required. Conversely, surface states do not charge as much when a good catalyst is deposited, leading to a smaller potential drop across Helmholtz layer. According to our previous speculations, a thicker layer (cfox30) of $CoFeO_x$ with less Fe concentration is a "poor catalyst". This is another cause for the much higher capacitance values of h/cfox30. For the same reason, cfox3, as a "good catalyst", reduced the surface capacitance peak compared to bare hematite (Fig. 5-15).
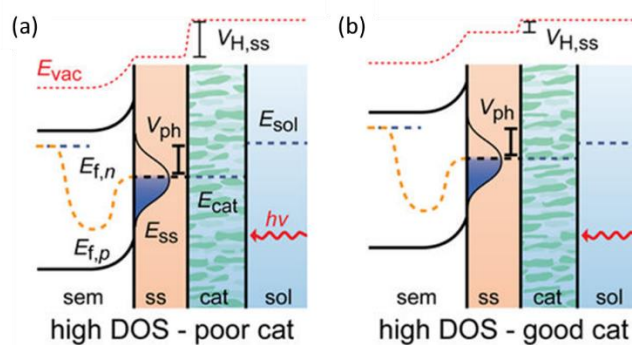
Fig. 5-32 Effect of high density of surface states on permeable catalysts. A poor catalyst (a) gives a higher Helmholtz layer potential drop than a good catalyst (b).[255] Reprinted with permission from ref. [255]. Copyright 2016 American Chemical Society

*Comparison of methods for measuring charge transfer efficiency*

Several methods to measure charge transfer efficiency have been attempted in this work, including hole scavenging TP, PEIS and IMPS. Although we stated that hole scavenging method is more reliable than others, it is perhaps not true as unexpected reactions are very likely to be present, as pointed out by Klotz in a recent publication.[94] What is most notable is the significant differences in charge transfer efficiencies for h/cfox30 measured by TP (2.1%) and PEIS (11.3%), as the latter is mistakenly taking co-catalyst oxidation current for water oxidation current. On the other hand, it happens that the time regime for $Co^{2+}/Co^{3+}$ reaction falls out of $\ln D = -1$ boundary. Although IMPS has been claimed the best way to measure $\eta_{ct}$, the differences in light source and intensity make the values not directly comparable with those obtained in front of solar simulators.[94]

*Changes in hole flux*

When a very thin layer of co-catalyst is electrodeposited, the rapid surface recombination process is not alleviated, unlike commonly observed outcomes for other Co-based co-catalysts. Instead, charge transfer is accelerated. The extra charges come from an increase of hole flux according to both PEIS and IMPS results. Similar trends of hole fluxes are observed when comparing Eq. 4-12 with Fig. 5-19b. In both figures, $J_h$ for h/cfox3 are slightly higher than h/cfox0 at low potentials, followed by convergence at higher potentials. This gap becomes more apparent when stronger illumination is applied. The convergence of hole flux for h/cfox30 and the other two electrodes happens at a much lower potential in PEIS results, also likely due to the stronger light intensity that oxidizes the co-catalyst charging more easily.
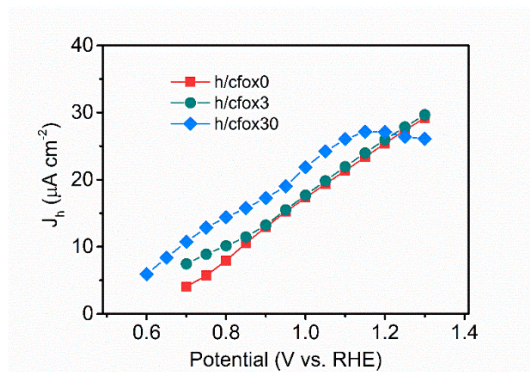
Fig. 5-33 Hole flux for h/cfox0 (red squares), h/cfox3 (green circles) and h/cfox30 (blue diamonds) derived from IMPS.

*Unresolved issues in PEIS*

In this publication, we believed that the kinetic model used in PEIS analysis does not apply above 1.0 $V_{RHE}$ as $k_{rec}$ starts to increase beyond this point, which is counter-intuitive. The same observation had been previously discovered by Cummings et al. via IMPS.[278] The authors carried out measurements up to very high potential and found a Gaussian peak located around 0.5 V vs. Ag/AgCl (1 M NaOH). This phenomenon was associated with distribution of surface states but more detailed explanation was absent. Further research on this issue would have been worthwhile.

Mott-Schottky analysis was used based on dark EIS data to determine the flat band potential and doping density of hematite. In Note S2 we assumed the Helmholtz to be 200 $\mu C\ cm^{-2}$ from a literature value, which is much greater than the space charge capacitance of 8.06 $\mu C\ cm^{-2}$. Consequently, the estimated potential drop across Helmholtz layer would be negligible. However, this $C_H$ value might not be true for our electrodes. Measurement of $C_H$ by impedance spectroscopy is difficult but could be estimated based on the assumption of total Fermi level pinning, where bias is exerted on $\Delta V_H$. However, the accurate determination of $\Delta V_H$, is of little interest in this work. What is more relevant is that the kinetic models we adopt to calculate rate constants is also based on the assumption of negligible $\Delta V_H$, and yet our study has showed plausible explanation for the data acquired. Therefore, it would be noteworthy for future research to explore deeper into the equivalent circuit model as well as the rate constant model.

## 5.2 Publication: Simultaneous Formation of FeO$_x$ Electrocatalyst Coating within Hematite Photoanodes for Solar Water Splitting

### 5.2.1 Preface

For hematite photoanodes, some kind of surface modification has been regarded as a necessity among this field. Common surface treatments include coatings of electrocatalysts or non-catalytic layers, which can sometimes damage the quality of hematite.[152] In this work, an alternative method is discovered by adding lactic acid during the precursor preparation. The resulting photoanodes are found to form a self-organized thin layer of FeO$_x$, which demonstrates improvement in photocatalytic activities. The effects of LA addition on FeOOH formation and photoanode quality are examined by XRD, SEM, TEM, XPS and Raman. Furthermore, electrochemical tools including Tafel plots, ECSA, PEIS and IPCE were employed to evaluate the performance and related properties. More interesting indications are obtained by IMPS measurements, which showed that the large improvement in photocurrent obtained with the hematite-FeO$_x$ photoanodes mainly derives from an increase of hole flux and the suppression of surface electron–hole recombination as a result of the amorphous layer.

This simplified auto-co-catalyst fabrication is a meaningful step toward the commercialization of hematite photoanode. Although some understanding has been gained of the role of carboxylate groups in the formation of $\alpha$-FeOOH and $\beta$-FeOOH,[279,280] more systematic research is required to understand the causes for FeO$_x$ formation as well as the influence of other additives.

### 5.2.2 Declaration of Authorship

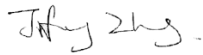| | | | | | |
|---|---|---|---|---|---|
| This declaration concerns the article entitled: Simultaneous Formation of FeOx Electrocatalyst Coating within Hematite Photoanodes for Solar Water Splitting | | | | | |
| Publication status | | | | | |
| In preparation | Manuscript | Submitted | In review | Accepted | <u>Published</u> |
| Publication details (reference): | ACS Appl. Energy Mater. 2019, 2, 2043−2052 | | | | |
| Candidate's contribution to the paper (detailed, and also given as a percentage). | <ul><li>Formulation of ideas: 0 %<br>The candidate was not engaged in the formulation of ideas.</li><li>Design of methodology: 30%<br>The candidate was responsible for the design of PEC characterizations in this work to gain deeper understanding of samples, such as the use of hole scavengers and PEIS.</li><li>Experimental work: 30%<br>The candidate conducted experiments in the PEC measurement section, including photocurrent measurements (Fig. 5-50) and PEIS (Fig. 5-51), as well as participation in IPCE measurement (Fig. 5-53) and gas evolution measurement (Fig. 5-54). IMPS for different samples were recorded by the candidate but not published. The candidate analysed most characterization outcomes and significantly contributed to gaining understanding of the electrode systems.</li><li>Manuscript writing and editing: 30%<br>The candidate participated in writing PEC sections of the manuscript and produced Fig. 5-50, Fig. 5-51 and</li></ul> | | | | |

| | Fig. 5-53. I also made edits throughout the manuscript and supporting information. |
|---|---|
| Statement from Candidate: This paper reports on original research I conducted during the period of my Higher Degree by Research candidature. | |

| Signed | | Dec. 2018 |
|---|---|---|
| | *Jifang Zhang* | |

### 5.2.3 Copyright Agreement

Title: Simultaneous Formation of FeOx Electrocatalyst Coating within Hematite Photoanodes for Solar Water Splitting

Author: Dominic Walsh, Jifang Zhang, Miriam Regue, et al

Publication: ACS Applied Energy Materials

Publisher: American Chemical Society

Date: Mar 1, 2019

Copyright © 2019, American Chemical Society

- Permission is granted for your request in both print and electronic formats, and translations.
- If figures and/or tables were requested, they may be adapted or used in part.
- Please print this page for your records and send a copy of it to your publisher/graduate school.
- Appropriate credit for the requested material should be given as follows: "Reprinted (adapted) with permission from (COMPLETE REFERENCE CITATION). Copyright (YEAR) American Chemical Society." Insert appropriate information in place of the capitalized words.
- One-time permission is granted only for the use specified in your request. No additional uses are granted (such as derivative works or other editions). For any other uses, please submit a new request.

**5.2.4 Manuscript**

# Simultaneous Formation of FeO$_x$ Electrocatalyst Coating within Hematite Photoanodes for Solar Water Splitting

**Dominic Walsh\*† , Jifang Zhang†, Miriam Regue§†, Ruchi Dassanayake†, and Salvador Eslava\*†**

*† Department of Chemical Engineering, University of Bath, Claverton Down, Bath BA2 7AY, United Kingdom*

*§ Centre for Sustainable Chemical Technologies, University of Bath, Claverton Down, Bath BA2 7AY, United Kingdom*

**ABSTRACT:** Depositing an oxygen evolution electrocatalyst on the intricate pores of semiconductor light-absorbing layers of photoanodes for photoelectrochemical solar water splitting is an efficient way to improve their performance, but it adds extra costs and difficulties. In this work, we present a synthesis of hematite ($\alpha$-Fe$_2$O$_3$) photoanodes with a self-derived conductive amorphous FeO$_x$ electrocatalyst coating. Hematite-FeO$_x$ photoanodes were prepared via FeOOH precursors modified with low levels of lactic acid additive. In the absence of lactic acid, FeOOH consisted of lepidocrocite nanorods that resulted in $\alpha$-Fe$_2$O$_3$ particulate photoanodes with sharp crystal edges upon doctor blading and calcination. Lactic acid addition, however, resulted in goethite and amorphous FeOOH that formed $\alpha$-Fe$_2$O$_3$ particulate photoanodes coated by a thin conductive amorphous FeO$_x$ layer. Electron microscopy studies revealed that the thickness of this layer was controlled with the addition of lactic acid in the preparation. Photoelectrochemical characterization including Tafel plots, impedance spectroscopy, and hole scavenger measurements confirmed that the FeO$_x$ layer behaved as an FeOOH electrocatalyst enhancing charge transfer efficiency and minimizing electron–hole surface recombination. Such coating and approach increased the electrochemically active surface area and amount of surface states. Photocurrent increased from 0.32 to 1.39 mA cm$^{-2}$ at 1.23 V$_{RHE}$ under simulated sunlight, remarkable results for an auto-co-catalyzed and simple solution-process deposition.

## Introduction

The world's energy consumption continues to increase above current ~13 Mtoe levels due to worldwide population growth and economic expansion.[281] To avoid the dependence on fossil fuels, there has been a sharp increase in research and commercialization of solar technologies in the past decade. Among these technologies, the research of photoelectrochemical (PEC) splitting of water to produce hydrogen fuel using low cost components and solar energy attracts much attention.[282–284] Candidate metal oxides for the photoanode component of a PEC cell include n-type semiconductors such as $TiO_2$, $ZnO$, $WO_3$, and $\alpha$-$Fe_2O_3$ (hematite), with the latter being especially promising due to its high elemental abundance, low cost, and solar light absorption properties.[285,286] For hematite to function effectively as a photoanode, films of a few hundred nanometers thick are required to overcome the low absorption coefficient, while nanoscale features better match short carrier diffusion lengths.[39,120,287–292] Materials and production methods that are economically viable and suitable for very large-scale implementation are a key target.

The formation of hematite photoanodes with intricate morphologies and features for water oxidation has been extensively investigated, but more progress is still needed to achieve the maximum theoretical limit of 12.6 mA $cm^{-2}$.[120,238,293] Hematite photoanodes have been prepared in the shapes of cauliflowers, nanocones, nanotubes, and worms, in attempts to increase the hematite area exposed to the electrolyte and minimize the diffusion path of holes facilitating their reaching the electrolyte.[113,121,294,295] Some of these approaches require vacuum deposition techniques which can increase costs. Solution processes such as doctor blading or spin coating are inexpensive and can be easily adopted by many researchers and laboratories.

PEC water oxidation is limited by both the high tendency of photoinduced electrons and holes to recombine in the photoanode semiconductor and the poor catalytic properties of semiconductor surfaces to evolve oxygen at the electrolyte interface. The pairing of a semiconductor light-absorbing layer with $O_2$ evolution electrocatalysts that mediate in the oxidation of water and collect the holes to avoid their recombination is a route to significantly enhance photocurrents.[296,297] Many different

electrocatalysts such as Pt, IrO$_x$, CoFeO$_x$, and CoPi have been directly functionalized on the surface of hematite.[263,298–300] They are typically deposited by electrodeposition, drop casting, or more expensive and sophisticated vacuum deposition techniques. This poses an extra deposition step that can increase costs, especially if precious metals are used, and in some cases deteriorate the semiconductor hematite if this is unstable under the deposition conditions.[145,250]

Herein, we introduce a solution-process method to prepare hematite photoanodes formed simultaneously with a self-derived amorphous surface FeO$_x$ coating that effectively works as an O$_2$ evolution electrocatalyst and minimizes losses from surface charge recombination. To generate the amorphous layer we employed the small monocarboxylated molecule lactic acid [CH$_3$CH(OH)COOH, LA] as a biodegradable, nontoxic, and low cost additive in the aqueous precipitation synthesis of FeOOH nanorod precursors.[301] When these LA-modified FeOOH species were readily coated onto transparent conductive supports by doctor blading and were heated, simultaneous formation of light-absorbing semiconductor hematite coated with FeO$_x$ electrocatalyst occurred. This simplified and inexpensive photoanode preparation that self-co-catalyzes with a surface coating reduces costs and boosts photocurrents from 0.32 up to 1.39 mA cm$^{-2}$ at 1.23 V$_{RHE}$ under simulated sunlight. Electron microscopy confirmed that the amorphous layer thickness could be controlled with the levels of LA addition to the solution process. Dark current water oxidations, hole scavenger measurements, and a range of photoelectrochemical analysis together showed that the amorphous layer was intrinsically more catalytic and suppressed surface electron–hole recombination.

**Experimental Section**

Preparation of FeOOH Precursor of Hematite Films

A 100 mL portion of N$_2$-degassed distilled water was used to dissolve 0.198 g of iron(II) chloride tetrahydrate and 0.5406 g of iron(III) chloride hexahydrate solution (0.02/0.04 M Fe$^{2+}$/Fe$^{3+}$) with stirring.[302] A 1 M sodium carbonate solution was then added dropwise to the stirred solution until the pH rose from 1.8 up to 6, while FeOOH precipitated. The mixture was left to stand for 24 h. Precipitated FeOOH in the presence of LA was alternatively prepared by adding the equivalent of 0.1, 0.2, 0.3, and 0.4 g (0.044 M) of LA (using adjusted weights from an 80% LA solution) to the

$Fe^{2+}/Fe^{3+}$ solution prior to dropwise addition of the sodium carbonate. For example, 0.2 g of LA was equivalent to a 2.73:1 molar ratio of Fe:LA. In all cases, a brown sediment was formed that was washed three times by repeated centrifugation at 3500 rpm for 5 min and redispersion in distilled water. A final 10 min centrifugation was carried out, followed by removal of the supernatant and addition of 3 mL of ethanol to form brown slurry mixtures that were stored in sealed vials.

Preparation of PEC Photoanode Slides

To prepare coated slides suitable for PEC measurements, 0.4 g of FeOOH/ethanol sediments (dry weight 0.025 g FeOOH) was mixed with 1 mL of a 2-propanol solution of 0.5 wt % acetylacetonate (acac) capping agent and 4 wt % polyvinylpyrollidone ($M_r$ 40k, PVP). This mixture was then sonicated for 5 min. An excess of two drops (~0.06 mL) of this mixture was placed onto thoroughly cleaned and washed $12 \times 25 \times 1.05$ mm$^3$ fluoridated tin oxide coated aluminoborosilicate glass slides (ABS-FTO, Solaronix, CH) and doctor bladed at 0.20 mm layer thickness, an overall setting of 1.25 mm including the 1.05 mm thick slide. Then, coatings were allowed to dry in air. The low level of PVP aided formation of regular thin continuous films that adhered firmly to the FTO slides. The slides were then placed directly into a tube furnace preheated to 800 °C and heated for 20 min followed by immediate removal and cooling to room temperature in air. Previous studies have shown these heating conditions to be optimal for diffusion of Sn into the hematite layer which increases conductivity and raises photocurrent.[39] Apart from Sn diffusion effects, previous studies have shown clearly the ABS-FTO glass is essentially otherwise unaltered by heating at 800 °C.[299,303] The yellow coating of the FeOOH material changed into red/orange hematite that was continuous and firmly adhered to the slide surface. The slides were washed in distilled water and air-dried. The following reaction took place during the heating at 800 °C for 20 min (Eq. 5-25):

$$2FeOOH \rightarrow Fe_2O_3 + H_2O \qquad \text{Eq. 5-25}$$

PEC Measurements

Photocurrent density (in mA cm$^{-2}$), PEC impedance spectroscopy (PEIS), incident photon-to-current efficiency (IPCE), and Faradaic efficiency were investigated in a three-electrode PEC quartz cell. Simulated sunlight on a circular 0.283 cm$^2$ area was supplied by a 300 W Xe Lamp (LOT Quantum Design) using an AM 1.5G filter

(which simulates the terrestrial solar spectrum at ground level). Illumination intensity was set to 1 sun (100 mW cm$^{-2}$) by calibration with a silicon photodiode linked to an ILT1400 radiometer photometer. An Ivium Compacstat.h mobile potentiostat was used with IviumSoft version.2.6 software. In the three-electrode system, the working electrode was the as-prepared hematite photoanode, the counter electrode a Pt wire, and a Ag/AgCl (in 3.5 M KCl) electrode the reference electrode. A 1 M KOH solution (pH 13.9) was used as an electrolyte. The working electrode was illuminated from the back side (glass side). Photocurrent density–potential ($J$–$V$) curves were recorded at a scan rate of 20 mV s$^{-1}$. The measured potentials vs Ag/AgCl ($E_{Ag/AgCl}$) were converted to RHE potential ($E_{RHE}^{\circ}$) following the Nernst equation (Eq. 5-26):

$$E_{RHE}^{o} = E_{Ag/AgCl}^{o} + E_{Ag/AgCl} + 0.059pH \qquad \text{Eq. 5-26}$$

where $E_{Ag/AgCl}^{o} = +0.205\ V$

In PEIS measurements, a potential perturbation of 10 mV was applied at a frequency range from $10^5$ to 0.1 Hz. The data were collected at direct current potentiostatic conditions from 0.7 to 1.3 V$_{RHE}$ at a step of 0.05 V and fitted using Zview software (version 3.5, Scribner). Simulated solar illumination (AM1.5G, 100 mW cm$^{-2}$) was used to illuminate the back (glass) faces of the FTO slide supports.

Stability of a Fe$_2$O$_3$–FeO$_x$ (0.2 g LA) photoanode was measured over 2.5 h under chopped simulated sunlight at an applied potential of 1.23 V$_{RHE}$.

Cyclic Voltammetry for Surface Area

The electrochemically active surface area (ECSA) of photoanodes was investigated using cyclic voltammetry (CV), scanning from 0 to 0.17 V$_{Ag/AgCl}$ at scan rates between 10 and 200 mV s$^{-1}$, in 1 M KOH solution (pH = 13.9).[304] ECSA is proportional to the double layer capacitance ($C_{dl}$), which is estimated from the slope of the plot $\Delta J$ vs scan rate and dividing by two $\Delta J$ is equal to ($J_a − J_c$),[305] where $J_a$ and $J_c$ are the anodic and cathodic current densities, respectively, in this case taken at 0.1 V$_{Ag/AgCl}$ in the CV scans.[306,307] Sample slides were measured in triplicate, and consistent $C_{dl}$ values were obtained.

Hole Scavenger Measurements

Underlying differences in charge transport properties and surface catalytic properties between samples prepared with different LA levels were studied by adding

0.5 M $H_2O_2$ as a hole scavenger into the 1 M KOH electrolyte to eliminate surface recombination.[308]

Measurement of oxygen evolution from photoanode

A custom-made 110ml square quartz cell with PFTE lid and air-tight ports for sample, Pt counter, reference electrode and $N_2$ bubble line was used. An $O_2$ sensor probe was used to measure $O_2$ evolution from the hematite photoanode. The sensor probe was a Pyroscience Firesting $O_2$ sensor housed in a robust tip, coupled with a temperature probe for continuous temperature compensation. The probe tip houses a fluorescent dye that fluoresces relative to $O_2$ presence on brief flash illumination. The sample photoanode, Pt counter and Ag/ AgCl reference electrode were placed in 1 M KOH electrolyte and air-tight sealed in the chamber lid. The chamber electrolyte and headspace were flushed with $N_2$ for 30 min before the photoanode ($0.55cm^{-2}$ exposed area) at an applied potential of 1.23V vs RHE was illuminated at 100 mW $cm^{-2}$ for 1 hour. Evolution of $O_2$ was continuously monitored with the Pyroscience probe and the $O_2$ generation rate used to calculate Faradaic efficiency. The best performing $Fe_2O_3$-$FeO_x$ (0.2g LA) and the $Fe_2O_3$ (0g LA) photoanodes were tested. However, the α-$Fe_2O_3$ (0g LA) photoanode generated poor $O_2$ evolution which was difficult to quantify, so results are not presented.

Faradaic efficiency calculation

To calculate the Faradaic efficiency, first the amount of $O_2$ evolved in the headspace of the PEC cell was calculated using the ideal gas law and measurements of the %$O_2$ and $O_2$ in the electrolyte solution was estimated using Henry's law and added to the measured values in the headspace.[309,310] Next, the theoretical amount of $O_2$ expected for a water oxidation reaction with 100% Faradaic efficiency was calculated. The following equation (Eq. 5-27) was used:

$$Q = n(e^-) \times F$$
<div align="right">Eq. 5-27</div>

where $Q$ is the charge in C, obtained from the photocurrent-time curve; $n$ $(e^-)$ is the number of electrons in mol; and F is the Faraday constant (96485.3329 C $mol^{-1}$). The theoretical amount of $O_2$ generated was calculated by dividing $n$ $(e^-)$ by four, which is the number of electrons involved in the oxidation of water. Finally, the Faradaic efficiency was calculated by dividing the amount of $O_2$ evolved in the headspace by

the theoretical amount of $O_2$ expected for 100% Faradaic efficiency (µmol / µmol x 100).

Further Characterization

Samples analyzed by powder X-ray diffraction (XRD) were recorded on a Bruker D8 powder diffractometer. FeOOH samples were dried in air and lightly ground by hand before measurement. Hematite photoanodes did not need any preparation for XRD. Crystal modeling and powder XRD diffraction pattern calculation were obtained with Crystalmaker 10.1.1 and CrystalDiffract 6.7.2 software, respectively, and by using published crystal structure cif files. Field-emission scanning electron microscopy (FESEM, JEOL JSM-6301F) was employed to observe photoelectrode surfaces and cross-sectional morphology and determine film particle sizes. Samples were not coated before SEM observation. Energy dispersive X-ray spectroscopy (EDXS) was conducted on a JEOL JSM-6480LV SEM at low magnification (~250 µm diameter sample area) for elemental composition (for elements heavier than N). Transmission electron microscopy (TEM) was carried on a JEOL 2100 Plus to characterize the morphology of the samples, the presence of amorphous material, and the lattice fringes of hematite crystals (using ImageJ). FeOOH samples on carbon coated copper TEM grids were prepared from suspensions diluted in 2-propanol followed by briefly sonicating, drop casting, and drying. Samples of hematite photoanodes for TEM imaging were prepared by carefully scraping hematite material from the ABS-FTO slide into 2-propanol, followed by brief sonication. Then, one drop of the suspension was placed onto the TEM grid and air-dried before TEM analysis. UV–vis spectroscopy of photoanode slides was conducted by diffuse reflectance light absorption measurements on an Agilent UV–vis Cary 100 spectrometer fitted with a diffuse reflection integrating sphere. Tauc plots were carried out to calculate direct and indirect band gap, using exponents $n = 2$ and $n = 1/2$, respectively. Raman spectroscopy was conducted with a Renishaw inVia system utilizing a 532 nm laser operating at 0.7 mW. Hematite photoanode slides were also analyzed by X-ray photoelectron spectroscopy (XPS) on a Thermo Fisher Scientific K-alpha[+] spectrometer using a microfocused monochromatic Al X-ray source (72 W) over an area of approximately 400 µm. Data was recorded at pass energies of 150 eV for survey scans and 40 eV for a high resolution scan with 1 and 0.1 eV step sizes, respectively. Data analysis was performed in CasaXPS using a Shirley-type

background and Scofield cross-sections, with an energy dependence of −0.6. Charge neutralization of the sample was achieved using a combination of both low energy electrons and argon ions.

## Results and Discussion

### XRD and Raman Spectroscopy Measurements

Powder XRD analysis was conducted on FeOOH precipitated from iron chlorides with sodium carbonate solutions. Samples showed broad reflections corresponding to γ-FeOOH, lepidocrocite (L) (ICDD 74-1877), and a low level of α-FeOOH, goethite (G) (ICDD 29-713) (Fig. 5-34a). Enhanced γ-FeOOH (X00) reflections could be observed compared to calculated standards. LA was selected as a mild binding agent that could potentially alter the morphology of the precipitated FeOOH and its surface properties, but without strongly chelating or sequestering Fe ions that would lead to entirely amorphous material.[311–313] With 0.1 g of LA added to the carbonate precipitation process, XRD reflections consisted of poorly crystalline γ-FeOOH (Fig. 5-34b). At 0.2 and 0.3 g of LA addition, poorly crystalline γ-FeOOH/α-FeOOH was obtained, with a lower γ-FeOOH proportion at 0.3 g of LA addition (Fig. 5-34c,d). At 0.4 g of LA addition, near amorphous α-FeOOH was formed (Fig. 5-34e).
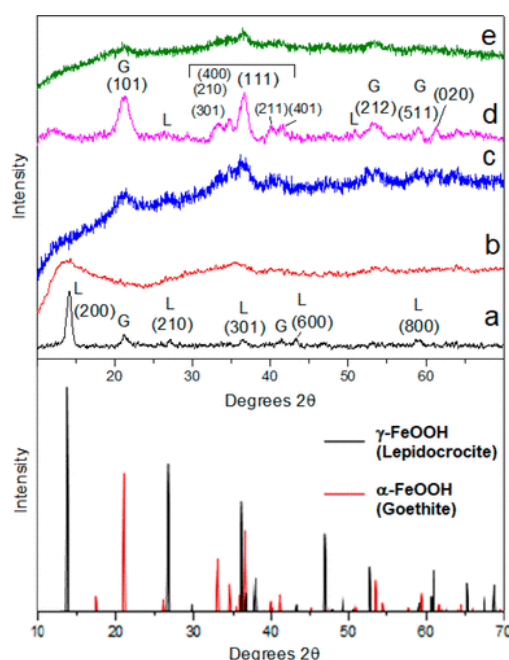


Fig. 5-34 XRD patterns of FeOOH prepared using different amounts of LA: (a) 0 g LA, (b) 0.1 g LA, (c) 0.2 g LA, (d) 0.3 g LA, and (e) 0.4 g LA. Calculated standards are shown below for comparison. L and G indicate lepidocrocite (γ-

FeOOH) and goethite (α-FeOOH), respectively. (Pattern d was smoothed to aid peak assignment.)

Raman spectra of dry powder samples prepared in the absence of LA match to a modified γ-FeOOH and a β-FeOOH (schwertmannite)-like phase,[314] again suggesting some interaction with carbonate anion. With increasing LA usage, a transition was observed from a mixture high in γ-FeOOH and low in α-FeOOH to the reverse composition (Fig. 5-35). Band assignments and comparison to database standards are shown in Table 5-10.[315,316] This phase change may be caused by LA interaction with α-FeOOH planes resulting in increased expression and promotion of this phase over γ-FeOOH. Carboxyl adsorption to α-FeOOH (100) has been suggested by computational study.[317]
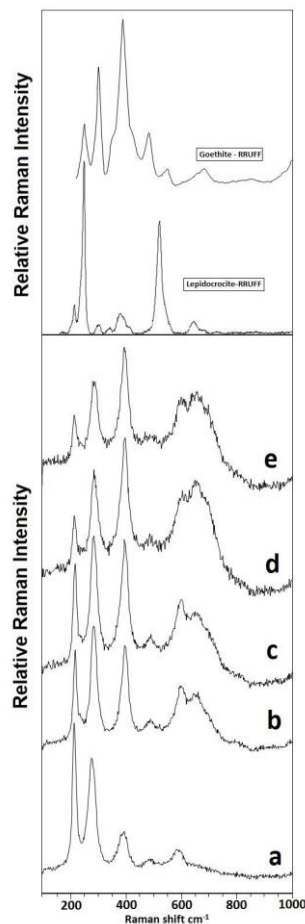


Fig. 5-35 Raman spectroscopy collected using 532nm laser source of FeOOH powders prepared with different levels of LA. (a) 0g LA; (b) 0.1g LA; (c) 0.2g LA; (d) 0.3g LA; (e) 0.4g LA. For comparison, two 532nm Raman spectra of known samples of (unoriented) goethite (α-FeOOH) and lepidocrocite (γ-FeOOH) from the RRUFF mineral database are also shown above.[318]

Table 5-10 Band positions (cm$^{-1}$) and relative intensities (in parenthesis: w = weak, m = medium, s = strong, vs = very strong) for the most significant bands in the Raman spectra of prepared FeOOH powders. Raman bands of γ-FeOOH and α-FeOOH from the RRUFF database and a β-FeOOH (schwertmannite) phase are shown for comparison.[314,318]

| Sample | Relative Raman Intensity | | | | | |
|---|---|---|---|---|---|---|
| γ-FeOOH (0g LA) | 214(s) | 275(s) | 394(m) | 487(w) | 585(w) | |
| γ/α -FeOOH (0.1-0.4g LA) | 217(s) | 290(s) | 400(vs) | 480(m) | 600(s) | 660(s) |
| γ -FeOOH (RRUFF) | 216(w) | 250(vs) | 396(s) | | 525(s) | 650(w) |
| α -FeOOH (RRUFF) | | 250(m) | 302(s) | 484(m) | 550(w) | 684(w) |
| 'β-FeOOH like'[2] | 212(s) | 278(m) | 390(w) | 477(w) | 587(w) | |

XRD analysis of the photoanode slides prepared by doctor blading FeOOH powders and heating to 800 °C showed reflections corresponding to rhombohedral α-Fe$_2$O$_3$ hematite (ICDD 24-0072), together with strong reflections due to the FTO underlayer (Fig. 5-36). Reflections due to other phases such as Fe$_3$O$_4$ were not observed. Relative reflection intensities with increasing LA use were complex due to differences in thickness of the hematite layer and increasing amorphous FeOOH levels in the precursor. However, the difference in the relative higher intensity of the (110) compared to the (104) reflection was notable. The (110):(104) ratios of the integrated peak areas were 1:0.67, 1.24:1, 1.27:1, 1.04:1, 0.49:1 for Fe$_2$O$_3$ (0 g LA), Fe$_2$O$_3$–FeO$_x$ (0.1 g LA), Fe$_2$O$_3$–FeO$_x$ (0.2 g LA), Fe$_2$O$_3$–FeO$_x$ (0.3 g LA), and Fe$_2$O$_3$–FeO$_x$ (0.4 g LA), respectively. It is probable that the hematite (110) originates from moderate atomic reorganization of the α-FeOOH (111) plane upon heating and dehydration to hematite. Recently, it has been shown that water splitting efficiency of hematite can be substantially increased by enhancement of the (110) crystal orientation due to increased charge transport along this iron-rich direction and/or lowered overpotentials (Fig. 5-37).[319,320]

Fig. 5-36 XRD patterns of hematite photoanodes prepared with FeOOH powders synthesized with different levels of LA: (a) $Fe_2O_3$ (0 g LA), (b) $Fe_2O_3$–$FeO_x$ (0.1 g LA), (c) $Fe_2O_3$–$FeO_x$ (0.2 g LA), (d) $Fe_2O_3$–$FeO_x$ (0.3 g LA), and (e) $Fe_2O_3$–$FeO_x$(0.4 g LA). Starred peaks indicate diffraction from FTO.
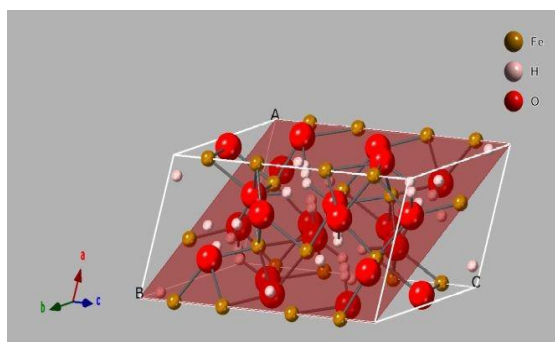


Fig. 5-37 Crystallographic diagram of α-$Fe_2O_3$ hematite showing iron rich (110) plane.

**Electron Microscopy**

TEM showed that FeOOH precipitated in the absence of LA generated rod crystals of 20–50 nm in length and 10 nm in width (Fig. 5-38a–f). Narrowing of the needle-shaped crystals with increasing LA was evident along with the presence of increasing levels of ill-defined amorphous material.
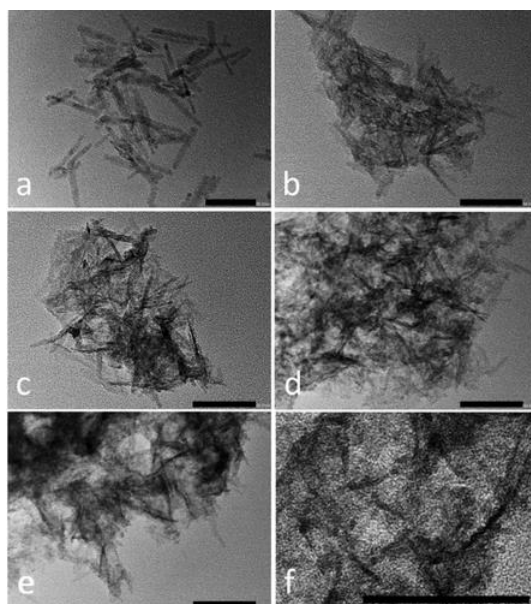


Fig. 5-38 TEM micrographs of FeOOH powders prepared with different levels of LA: (a) 0 g LA, (b) 0.1 g LA, (c) 0.2 g LA, (d) 0.3 g LA, (e) 0.4 g LA, and (f) 0.4 g LA, zoomed in. Scale bar: 50 nm.

Cross-sectional FESEM micrographs of resulting photoanodes showed the hematite crystal layer firmly bound to the FTO (Fig. 5-39). Hematite layer thicknesses varied

from 275 to 400 nm, due to subtle differences in the mixture concentration and doctor blading process.
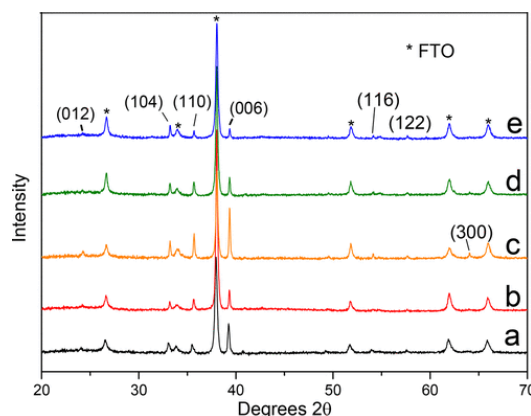


Fig. 5-39 FESEM micrographs of cross-sections of hematite photoanodes prepared with FeOOH powders synthesized with different levels of LA. (a) $Fe_2O_3$ (0g LA); (b) $Fe_2O_3$-$FeO_x$ (0.1g LA); (c) $Fe_2O_3$-$FeO_x$ (0.2g LA); (d) $Fe_2O_3$-$FeO_x$ (0.3g LA); (e) $Fe_2O_3$-$FeO_x$ (0.4g LA). Photoanodes were constructed using as a substrate aluminoborosilicate glass with conductive FTO layer.

FESEM of the top surface of the photoanodes prepared with FeOOH in the absence of LA showed irregular blocks of hematite size crystals (∼50–200 nm) that were often fused together (Fig. 5-41a). No notable differences can be observed for different levels of LA use, except for LA ≥ 0.3 g which led to a reduced number of crystals formed but more coupled and larger (Fig. 5-41d,e). A significant feature in the FESEM micrographs was the appearance of a continuous coating upon linked crystals with the use of LA (note the loss of sharpness in Fig. 5-41b–e insets). The lower contrast of the coating layer is suggestive of lower density and/or better conductivity. This coating was confirmed by TEM imaging. Fragments of the hematite photoanodes showed a sharp crystal edge with no LA use (Fig. 5-41f and Fig. 5-40). With the use of LA,

hematite crystals are, however, terminated with an amorphous coating absent of lattice fringes and of lower density. The average coating thickness was 5–10 nm for $Fe_2O_3$–$FeO_x$ (0.2 g LA) and 10–20 nm for $Fe_2O_3$–$FeO_x$ (0.4 g LA) (Fig. 5-41g,h and Fig. 5-40).
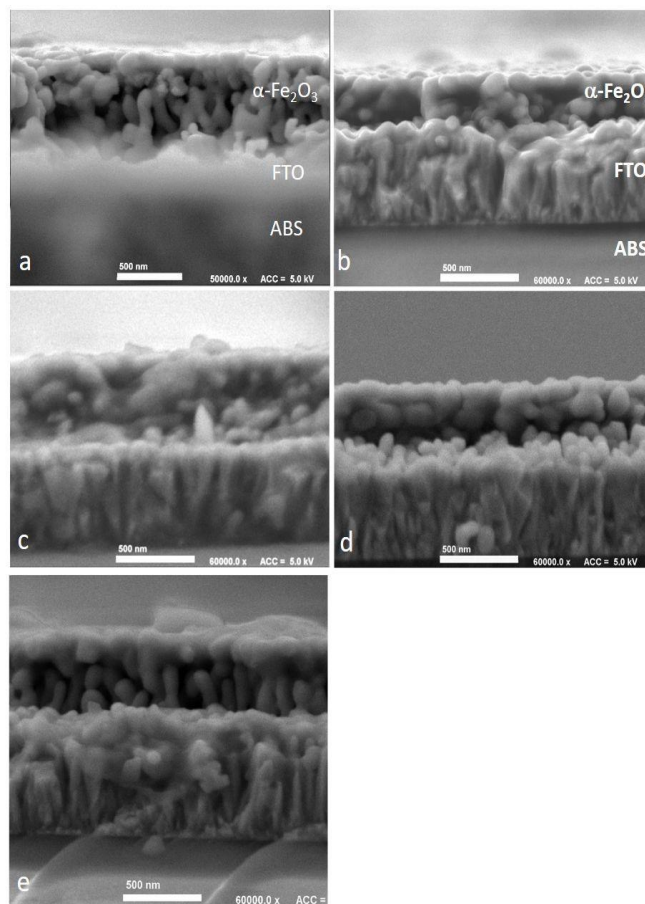


Fig. 5-40 TEM micrographs of material scraped from hematite photoanodes prepared with FeOOH powders synthesized with different levels of LA. (a) $Fe_2O_3$ (0g LA); (b) $Fe_2O_3$-$FeO_x$ (0.2g LA); and (c-d) $Fe_2O_3$-$FeO_x$ (0.4g LA). Upon using LA in the synthesis procedure, hematite crystal surfaces are terminated with a coating of amorphous $FeO_x$ material. Hematite lattice fringes were absent in this overlying amorphous layer. Occasional 2-3nm zones of graphitic carbon sheets between hematite and amorphous layer were also present (arrowed) in $Fe_2O_3$-$FeO_x$ (0.4g LA) sample.[3]

Also visible in the $Fe_2O_3$–$FeO_x$ (0.4 g LA) sample were occasional graphitic carbon layers between the crystalline hematite and amorphous $FeO_x$ layer and in a smaller amount at the surface of the amorphous $FeO_x$ layer (arrows in Fig. 5-41h). Since graphitic carbon was only observed for $Fe_2O_3$–$FeO_x$ (0.4 g LA) which had an excess of LA, we assign this graphitic carbon to the decomposition of LA and its trapping in the structure. Samples were heated at 800 °C, but they were only kept at this temperature for 20 min. Graphitic carbon on hematite has previously been observed on certain preparation conditions.[321] In any case, the amount of graphitic carbon was very low compared with the presence of amorphous $FeO_x$ surrounding hematite crystals, and no parasitic absorption due to carbon could be observed.
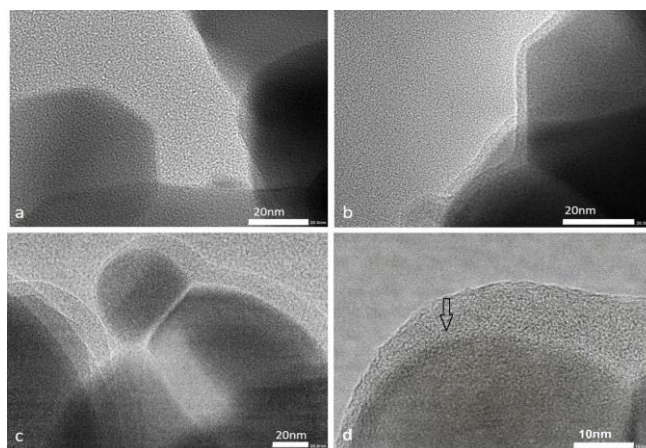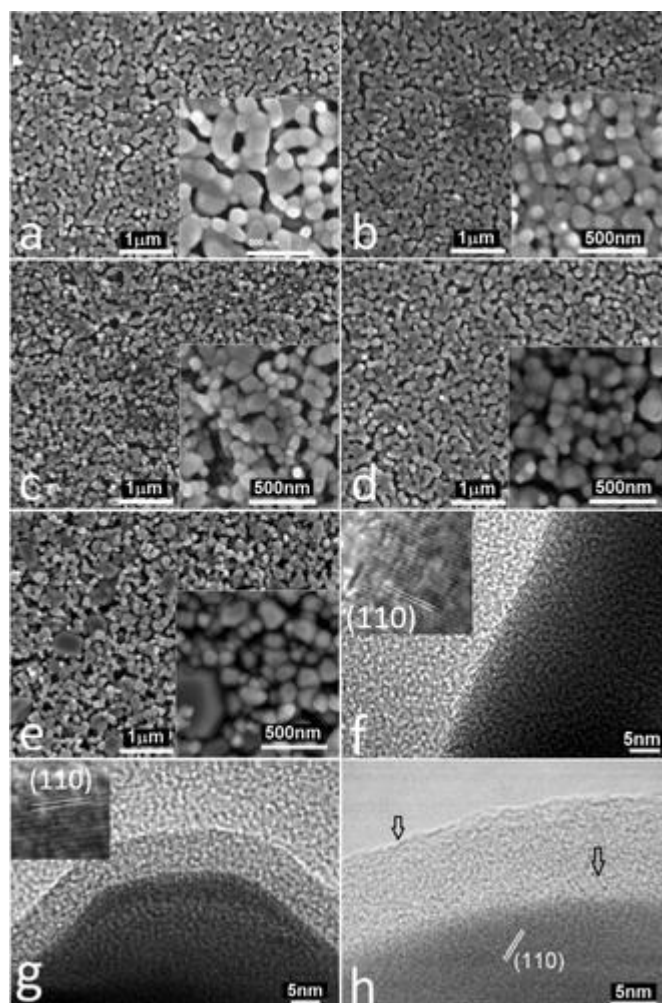
Fig. 5-41 FESEM micrographs of upper surface of hematite photoanodes prepared with FeOOH powders synthesized with different levels of LA: (a) $Fe_2O_3$ (0 g LA), (b) $Fe_2O_3$–$FeO_x$ (0.1 g LA), (c) $Fe_2O_3$–$FeO_x$ (0.2 g LA), (d) $Fe_2O_3$–$FeO_x$ (0.3 g LA), and (e) $Fe_2O_3$–$FeO_x$ (0.4 g LA). Insets show zoomed-in areas. TEM micrographs of material scraped from the hematite photoanodes: (f) $Fe_2O_3$ (0 g LA), (g) $Fe_2O_3$–$FeO_x$ (0.2 g LA), and (h) $Fe_2O_3$–$FeO_x$ (0.4 g LA). In the insets to parts f and g, and in part h, hematite 0.25 nm (110) lattice spacings are shown. Graphitic carbon layers between crystalline hematite and amorphous $FeO_x$ and trace surface carbon are indicated by arrows in part h.

**X-ray Photoelectron Spectroscopy (XPS) Analysis**

Fig. 5-42a shows a full XPS survey of a representative $Fe_2O_3$–$FeO_x$ (0.2 g LA) sample showing iron, oxygen, and carbon peaks. The C 1s band for every prepared hematite sample is shown in Fig. 5-42b. Carbon is ubiquitous, and adventitious carbon gave a significant C 1s peak centered at 285 eV for the $Fe_2O_3$ (0 g LA) sample. However, the intensity of this band increased with increasing precursor LA content indicating the presence of additional carbon in the final $Fe_2O_3$–$FeO_x$ photoanode sample surface. The O 1s peak was composed of two bands due to lattice O at 529.7

137

eV and surface hydroxyl at 531.4 eV. With increasing LA use, a reduction in peak level of lattice O was observed in comparison to the height of the surface hydroxyl band, indicating the presence of (less oxidized) $Fe^{2+}$ and/or a higher proportion of the contribution from hydroxyl bands (Fig. 5-42c).[321,322] The Fe 2p showed a spin–orbit component at $2p_{1/2} \sim 724.2$ eV and $2p_{3/2}$ at $\sim710.8$ eV consistent with $Fe_2O_3$ (Fig. 5-42). At the highest LA precursor level a trace peak at 716.2 eV associated with $Fe^{2+}$ is present. The difference in binding energy [$\Delta$(BE)] altered from 13.3 to 13.6 with increasing LA component of precursor.[291,323]
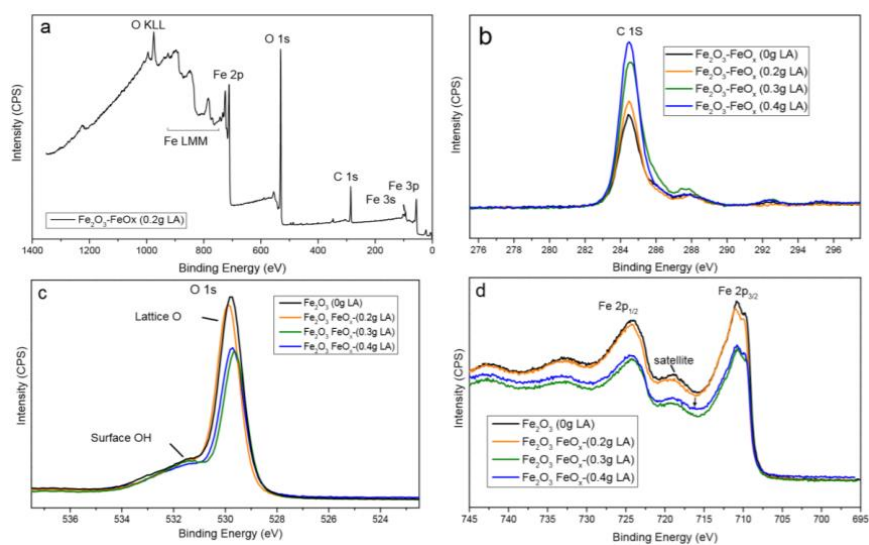


Fig. 5-42 XPS analysis of hematite photoanodes prepared with FeOOH powders synthesized with different levels of LA. (a) Representative XPS survey of a hematite photoanode, $Fe_2O_3$-$FeO_x$ (0.2g LA); (b) C 1s region with increasing intensities with increasing LA; (c) O1s region with increasing contribution of surface hydroxyl groups region with increasing LA; (d) Fe 2p region, where an arrow indicates a trace peak associated with $Fe^{2+}$ content for the $Fe_2O_3$-$FeO_x$ (0.4g LA) sample.

**Energy Dispersive X-ray Spectroscopy (EDXS)**

EDXS mapping carried out during the TEM showed that the coating is composed of iron oxide only; carbon detection was not reliable, and other elements were at background levels (Fig. 5-43). EDXS was also conducted at low magnification SEM ($\sim250$ μm diameter EDXS collection area), and elemental composition was measured. Oxygen, iron, tin, and trace potassium (from trace levels of remnant electrolyte) were detected (Fig. 5-44). For the $Fe_2O_3$–$FeO_x$ (0.4 g LA), a high Sn level was measured. This was most likely due to the presence of pores exposing the FTO glass surface (Table 5-11).
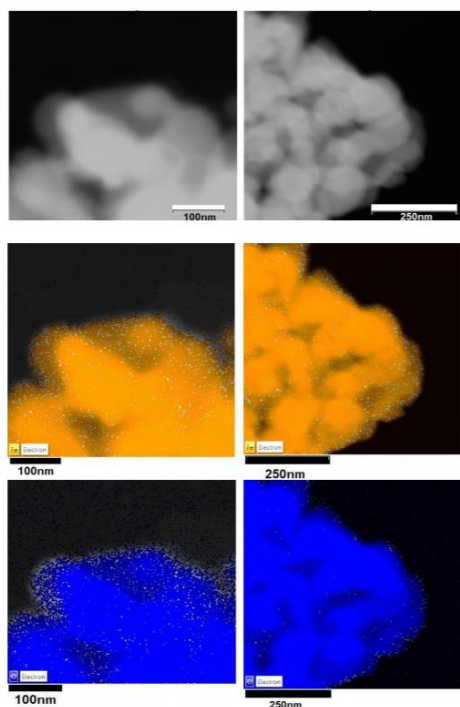
Fig. 5-43 STEM EDX elemental mapping of material scraped from $Fe_2O_3$-$FeO_x$ (0.4g LA) photoanode, showing Fe (orange) and O (blue). The coating layer regions gave emissions corresponding to iron (orange) and oxygen (blue) only, with all other elements at background levels.
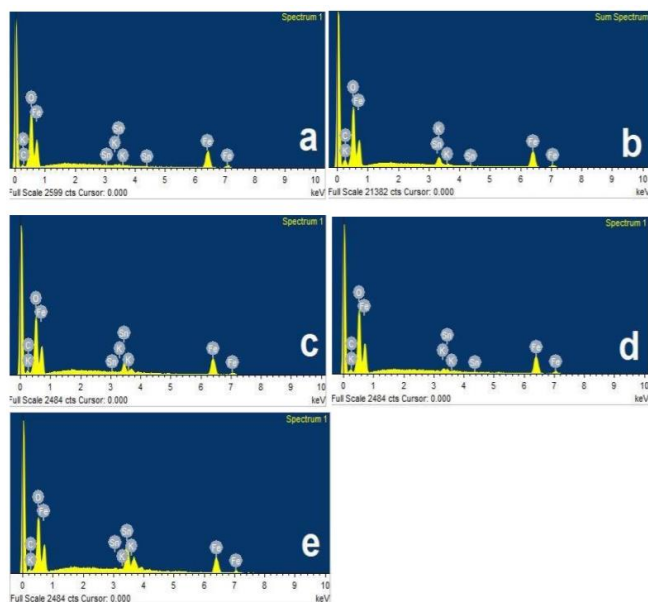


Fig. 5-44 EDXS spectra obtained at low magnification SEM of hematite photoanodes prepared with FeOOH powders synthesized with different levels of LA. (a) $Fe_2O_3$ (0g LA); (b) $Fe_2O_3$-$FeO_x$ (0.1g LA); (c) $Fe_2O_3$-$FeO_x$ (0.2g LA); (d) $Fe_2O_3$-$FeO_x$ (0.3g LA); and (e) $Fe_2O_3$-$FeO_x$ (0.4g LA).

Table 5-11 EDXS analysis of elemental composition (for elements of atomic weight > N) of hematite photoanodes prepared with FeOOH powders synthesized with different levels of LA.

| Element | $Fe_2O_3$ (0g LA) Wt % | At % | $Fe_2O_3$-$FeO_x$ (0.1g) Wt % | At % | $Fe_2O_3$-$FeO_x$ (0.2g) Wt % | At % | $Fe_2O_3$-$FeO_x$ (0.3g) Wt% | At% | $Fe_2O_3$-$FeO_x$ (0.4g) Wt% | At% |
|---|---|---|---|---|---|---|---|---|---|---|
| O K | 27.43 | 57.40 | 27.45 | 56.69 | 26.04 | 58.51 | 27.38 | 57.60 | 22.22 | 57.27 |
| K K | 0.49 | 0.42 | 6.67 | 5.64 | 0.00 | 0.00 | 2.18 | 1.88 | 0.00 | 0.00 |
| Fe L | 68.83 | 41.26 | 61.72 | 36.52 | 56.03 | 36.06 | 64.40 | 38.81 | 40.22 | 29.69 |
| Sn L | 3.24 | 0.91 | 4.16 | 1.16 | 17.93 | 5.43 | 6.04 | 1.71 | 37.56 | 13.04 |

With everything taken into consideration, the crystalline γ/β-FeOOH in the absence of LA converted upon deposition and heating to sharp well-defined hematite crystals, while more amorphous and surface disordered α-phase-rich FeOOH prepared with LA presence dehydrated to hematite crystals with an amorphous $FeO_x$ coating upon heating. Overall, during the short heating step a major morphological alteration from rods/amorphous material into crystalline or crystalline/amorphous blocks took place.

**PEC Performance**

Photocurrent density performances of hematite photoanodes prepared with different amounts of LA were measured with linear sweep voltammetry (LSV) under chopped simulated sunlight (100 mW cm$^{-2}$, with an AM1.5G filter) (Fig. 5-45a,b). A photocurrent of 0.32 mA cm$^{-2}$ was obtained at 1.23 V$_{RHE}$ for $Fe_2O_3$ (0 g LA) photoanode, typical of hematite formed from precursor solution coatings and without oxygen evolution electrocatalysts such as FeOOH or cobalt phosphate.[120,324,325] On addition of LA to the FeOOH precursor preparations, the photocurrent of the final photoanodes increased up to a maximum of 1.39 mA cm$^{-2}$ [$Fe_2O_3$–$FeO_x$ (0.2 g LA)] and then decreased back to 0.61 mA cm$^{-2}$ [$Fe_2O_3$–$FeO_x$ (0.4 g LA)], both at 1.23 V$_{RHE}$ (Fig. 5-45a,c).
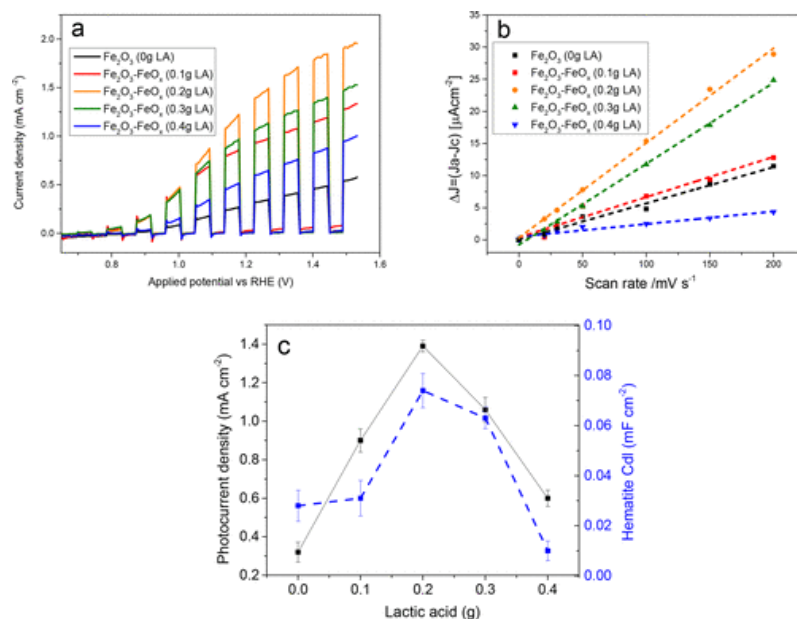
Fig. 5-45 Electrochemical characterization of hematite photoanodes prepared with FeOOH powders synthesized with different levels of LA. (a) Current density as a function of applied potential ($J$–$V$) carried out in 1 M KOH electrolyte under chopped simulated sunlight (AM1.5G, 100 mW cm$^{-2}$). (b) Scan rate dependence of current densities ($\Delta J$) for the calculation of ECSA values ($C_{dl}$). (c) Photocurrent density (solid line) at 1.23 $V_{RHE}$ and ECSA values $C_{dl}$ (dashed line) as a function of LA used in synthesis procedure. Error bars denote photocurrent, and $C_{dl}$ is the standard deviation of three replicate samples.

Surface activity was determined using CV measurements of the samples over the 20–200 mV s$^{-1}$ sweep rates (Fig. 5-46).
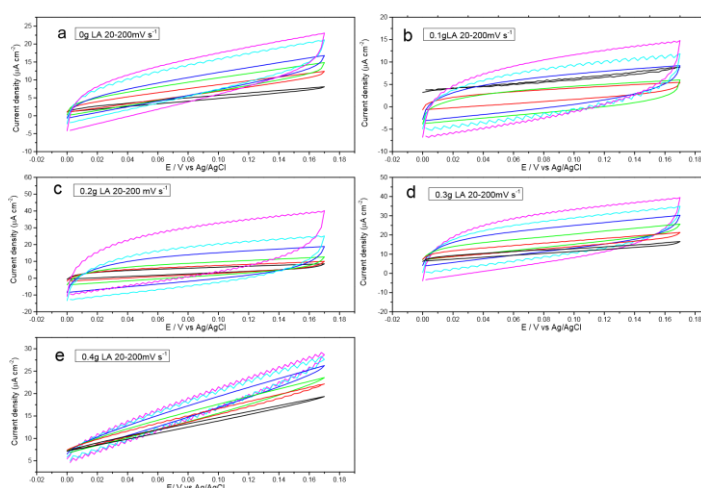


Fig. 5-46 Cyclic voltammetry curves of hematite photoanodes prepared with FeOOH powders synthesized with different levels of LA. (a) Fe$_2$O$_3$ (0g LA); (b) Fe$_2$O$_3$-FeO$_x$ (0.1g LA); (c) Fe$_2$O$_3$-FeO$_x$ (0.2g LA); (d) Fe$_2$O$_3$-FeO$_x$ (0.3g LA); and (e) Fe$_2$O$_3$-FeO$_x$ (0.4g LA). Curves were measured at 20 (black), 30 (red), 50 (green), 100 (blue), 150 (cyan) and 200 (magenta) mV s$^{-1}$ at applied potential of 0 to 0.17$V_{Ag/AgCl}$.

At lower sweep rate the applied charge had time to dissipate away. With an increasing rate, an increasing charge density at the surface was measured over the anodic/cathodic scans. The slopes of the current density vs scan rate can be related to the double layer capacitance ($C_{dl}$) directly proportional to the ECSA (Fig. 5-45b). The results indicate that the $Fe_2O_3$–$FeO_x$ (0.2 g LA) photoanode possesses the largest electrochemically active surface ($C_{dl} = 0.074$ mF cm$^{-2}$), followed by $Fe_2O_3$–$FeO_x$-0.3 g LA, $Fe_2O_3$–$FeO_x$-0.1 g LA, and $Fe_2O_3$–$FeO_x$-0 g LA, and finally the $Fe_2O_3$–$FeO_x$-0.4 g LA sample. Figure 5c compares photocurrents and ECSA values showing they follow the same rising and falling trend with increasing LA presence in FeOOH precursor preparation. The photocurrent obtained with the $Fe_2O_3$–$FeO_x$ (0.4 g LA) sample was however higher than what it would be expected considering its lowest $C_{dl}$. This can be ascribed to the presence of trace graphitic carbon observed by TEM at the $\alpha$-$Fe_2O_3$–$FeO_x$ interface increasing the electrical conductivity. Table 5-12 shows hematite particle sizes measured on the surface by FESEM, calculated surface areas, and photocurrent densities measured at 1.23 $V_{RHE}$. Photoactivity was related to the particle size and optimal photocurrent that occurred for $Fe_2O_3$–$FeO_x$ (0.2 g LA) which coincides with the smallest hematite particle size and a medium thickness of amorphous $FeO_x$ coating. Overall, these results show there exists an optimal addition of LA to the FeOOH precursor preparation to achieve the best hematite photoanode performance.

Table 5-12 Characteristics of Hematite Photoanodes Prepared with FeOOH Powders Synthesized with Different Levels of LA[a]

| sample | particle size (nm) | surface area (m$^2$/g) | ECSA $C_{dl}$ (mF cm$^{-2}$) | $FeO_x$ (nm) | J (mA cm$^{-2}$) |
|---|---|---|---|---|---|
| $Fe_2O_3$ (0 g LA) | 165 (45) | 6.9 | 0.028 (0.0062) | 0 | 0.32 |
| $Fe_2O_3$–$FeO_x$ (0.1 g LA) | 100 (30) | 11.4 | 0.031 (0.0071) | | 0.90 |
| $Fe_2O_3$–$FeO_x$ (0.2 g LA) | 95 (25) | 12.0 | 0.074 (0.0068) | 5−10 | 1.39 |
| $Fe_2O_3$–$FeO_x$ (0.3 g LA) | 140 (54) | 8.2 | 0.063 (0.0042) | | 1.06 |
| $Fe_2O_3$–$FeO_x$ (0.4 g LA) | 168 (125) | 6.8 | 0.010 (0.0039) | 10−20 | 0.60 |

[a]Particle size (and std deviation) on the surface analyzed by FESEM. Surface area (assuming spherical particles of previous sizes and hematite density of 5.26 g/cm$^3$). Measured ECSA values ($C_{dl}$) (and std deviation). $FeO_x$ amorphous overlayer thickness analyzed by TEM. Corresponding measured photocurrent (J) at 1.23 $V_{RHE}$ under simulated sunlight (back illumination).

Back illumination was used as this eliminates PEC variation due to sample thicknesses. Moreover, it also gave higher photocurrents than the front one in all cases, indicating that these porous hematite films have sufficient thickness to measure highest photocurrent possible for each condition assessed.[326] Depositions and

measurements were repeated more than five times showing reproducible trends and results (see example at optimal $Fe_2O_3$–$FeO_x$ (0.2 g LA) in Fig. 5-48, mean = 1.35 (($\sigma$ = 0.06) mA cm$^{-2}$ at 1.23 $V_{RHE}$). Photostability under 1 sun chopped illumination for a total of 2.5 h showed a decrease of 3% over the initial 20 min, followed by a constant photocurrent density, indicating high stability of the hematite film (Fig. 5-47).
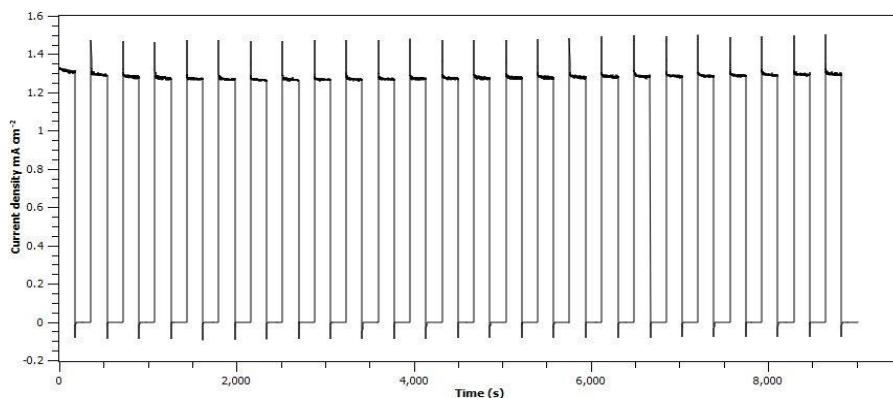


Fig. 5-47 Current density of $Fe_2O_3$-$FeO_x$ (0.2g) photoanode slide, over 2.5 h, conducted with chopped simulated sunlight (100mW cm$^{-2}$, AM1.5G filtered) in 1 M KOH at an applied potential 1.23$V_{RHE.}$
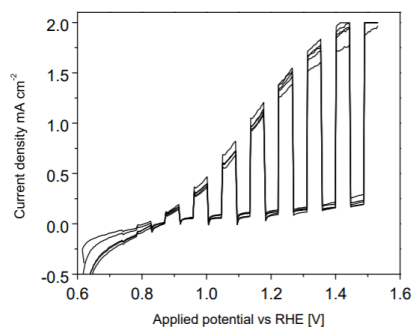


Fig. 5-48 Photocurrent for five $Fe_2O_3$-$FeO_x$ (0.2g LA) photoanode slides at different applied potentials. Measurements were made using 1M KOH as electrolyte under simulated sunlight (AM1.5G, 100mW cm$^{-2}$).

Intrinsic water oxidation capability of the anode surfaces was assessed measuring $J$–$V$ curves under dark conditions at elevated applied potential up to 2.0 $V_{RHE}$ (Fig. 5-49).[327] Tafel plots showed that the lowest onset potential and a clearly higher current density occurred with the $Fe_2O_3$–$FeO_x$ (0.2 g LA) anode (Fig. 5-49b). The $Fe_2O_3$ (0 g LA) sample showed the next lowest onset (Fig. 5-49b). These results further confirmed that the photoanodes with an optimal amorphous $FeO_x$ layer thickness and surface area can obtain higher currents for water oxidation.
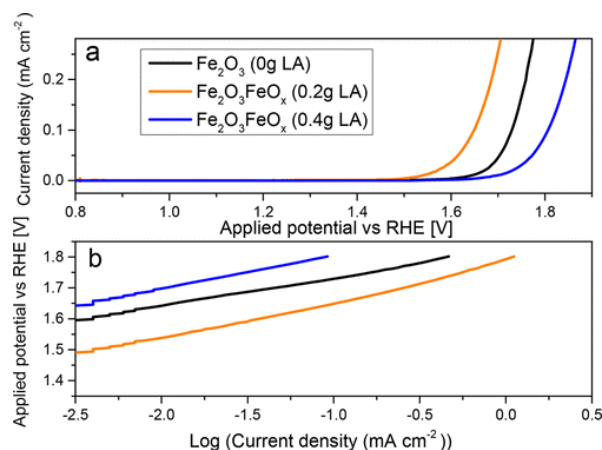
Fig. 5-49 (a) Current density as a function of applied potential (*J–V*) of hematite photoanodes prepared with FeOOH powders synthesized with different levels of LA, under dark conditions in 1 M KOH, showing intrinsic water oxidation ability. (b) Corresponding Tafel plots.

## Hole Scavenger Measurements

Sacrificial reagents such as $H_2O_2$ can be used as a hole scavenger to elucidate electron–hole surface recombination photocurrent losses, that among other factors hamper reaching the hematite photocurrent theoretical limit (12.5 mA cm$^{-2}$).[113] With measurements of photocurrents with and without $H_2O_2$ in the same electrolyte (KOH), charge transfer efficiencies ($\eta_{ct}$) can be calculated by the ratio of photocurrent densities (Table 5-13). In the presence of $H_2O_2$, the photocurrent density of the $Fe_2O_3$ (0 g LA) sample was higher at all potentials and more than doubled at 1.23 $V_{RHE}$ showing the high degree of surface recombination losses of photocurrent in 1 M KOH electrolyte ($\eta_{ct}$ of 49% at 1.23 $V_{RHE}$, Fig. 5-50 and Table 5-13). However, for $Fe_2O_3$–$FeO_x$(0.2 and 0.4 g LA) samples, higher charge transfer efficiencies were observed, for example, $\eta_{ct}$~80% at 1.23 $V_{RHE}$. We ascribe this higher efficiency to the presence of the amorphous $FeO_x$ coating, acting as an $O_2$ evolution electrocatalyst. Comparison of $\eta_{ct}$ for the $Fe_2O_3$ (0 g LA) photoanode against $Fe_2O_3$–$FeO_x$ (0.2 and 0.4 g LA) photoanodes shows some advantage at 0.95 $V_{RHE}$ (from 13.5% to 17.6% and 16.4% $\eta_{ct}$, respectively). However, enhancements became even more significant at 1.23 $V_{RHE}$ (from 49 to ~80% $\eta_{ct}$). This higher activity at higher potentials indicates that the amorphous $FeO_x$ coating behaves as an FeOOH electrocatalyst, whose conductivity has been measured to increase substantially with stronger applied potentials in its pure form or mixed with other metals.[151] From XPS results we noticed intensified Sn 2p signals with higher LA addition, meaning $FeO_x$ could also be mixed with Sn.
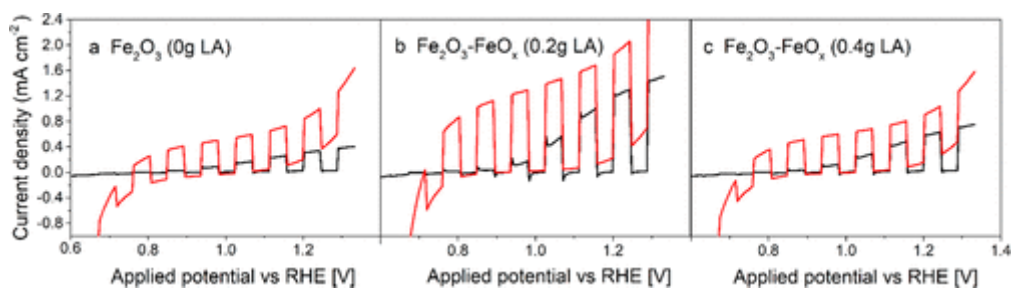
Fig. 5-50 Hole scavenger measurements of hematite photoanodes prepared with FeOOH powders synthesized with different levels of LA. Current density as a function of applied potential under chopped simulated sunlight (AM1.5G, 100 mW cm$^{-2}$). Electrolyte: 1 M KOH (black curve) and 1 M KOH containing 0.5 M H$_2$O$_2$(red curve). (a) Fe$_2$O$_3$ (0 g LA), (b) Fe$_2$O$_3$–FeO$_x$ (0.2 g LA), and (c) Fe$_2$O$_3$–FeO$_x$ (0.4 g LA).

Table 5-13 Analysis of Hole Scavenger Measurements of Hematite Photoanodes Prepared with FeOOH Powders Synthesized with Different Levels of LA[a]

|  | Fe$_2$O$_3$ (0 g LA) | | Fe$_2$O$_3$–FeO$_x$ (0.2 g LA) | | Fe$_2$O$_3$–FeO$_x$ (0.4 g LA) | |
|---|---|---|---|---|---|---|
| potential ($V_{RHE}$) | 0.95 | 1.23 | 0.95 | 1.23 | 0.95 | 1.23 |
| $J_{1MKOH}$ | 0.07 | 0.31 | 0.21 | 1.23 | 0.10 | 0.59 |
| $J_{1MKOH+0.5MH2O2}$ | 0.52 | 0.63 | 1.19 | 1.51 | 0.59 | 0.74 |
| $\eta_{ct}$ (%) | 13.5 | 49.2 | 17.6 | 81.4 | 16.4 | 79.7 |

[a]Table includes photocurrent densities measured in different electrolytes and under different applied potentials and charge transfer efficiency ($\eta_{ct}$(%)) at applied voltages of 0.95 and 1.23 $V_{RHE}$. Photocurrents in electrolytes with H$_2$O$_2$ are corrected for the dark current observed.

## PEIS Analysis

To further understand the differences in the surface kinetics of photoanodes having different FeO$_x$ coating thickness, photoelectrochemical impedance spectroscopy (PEIS) was employed. Nyquist plots were obtained at different potentials in 1 M KOH and fitted using an equivalent circuit proposed by Klahr et al. for hematite (Fig. 5-51a).[268] In this model, water oxidation is assumed to take place via surface states, which compete with surface charge recombination. The density of surface states is represented by the capacitor $C_{ss}$. The fitted $C_{ss}$ values are shown in Figure 8b, where peak maxima were located at 0.9–1.0 $V_{RHE}$, which coincide with the onset potential of hematite. Importantly, the $C_{ss}$ of the Fe$_2$O$_3$–FeO$_x$ (0.2 and 0.4 g LA) photoanodes was much higher than that of the Fe$_2$O$_3$ (0 g LA) reference photoanode, which can be attributed to the presence of amorphous FeO$_x$ conductive coating observed by FESEM and TEM. Moreover, the $C_{ss}$ of Fe$_2$O$_3$–FeO$_x$ (0.2 g LA) was double than that of Fe$_2$O$_3$–

FeO$_x$ (0.4 g LA), in agreement with the largest electrochemical current densities and PEC photocurrents observed (Fig. 5-45). Therefore, $C_{ss}$ values together with PEC results indicate that the amorphous FeO$_x$ coating helps store and shuttle photoinduced holes to the electrolyte, boosting photocurrents observed.
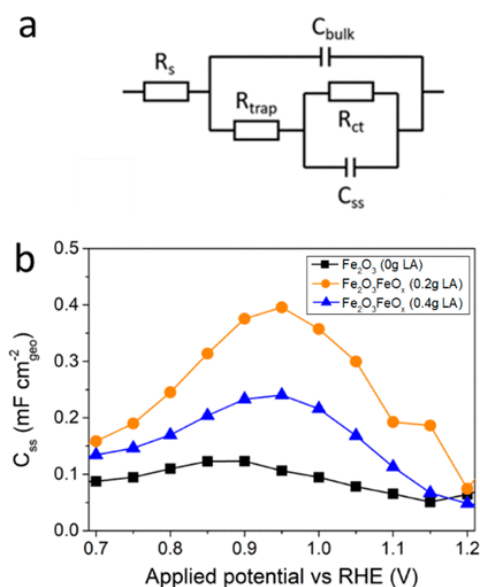


Fig. 5-51 (a) Equivalent circuit used for fitting PEIS data. (b) PEIS analysis. Surface state capacitances ($C_{ss}$) calculated as a function of applied potential for hematite photoanodes prepared with FeOOH powders synthesized with different levels of LA. Conditions: 1 M KOH electrolyte, simulated sunlight (AM1.5G, 100 mW cm$^{-2}$).

## Light Absorption and IPCE

UV–vis spectroscopy was used to measure the light absorbance of prepared photoanodes and confirm that the amorphous FeO$_x$ layer does not affect the band gap (Fig. 5-52a). A Tauc plot was applied to determine direct and indirect band gaps.[328] Direct band gaps were located at $E_g$2.05–2.08 eV ($\sim$600 nm) and indirect around $E_g$ 2.04 eV (608 nm), both in accordance with submicron sized hematite (Fig. 5-52b,c).[328,329]
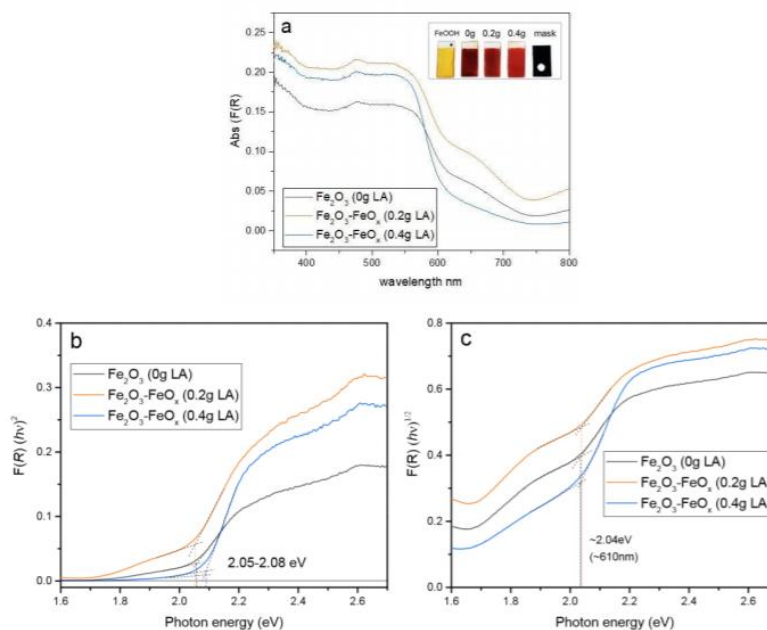
Fig. 5-52 (a) UV-visible light $(F(R).h\nu)^n$ diffuse reflectance absorbance of hematite photoanodes prepared with FeOOH powders synthesized with different levels of LA (0, 0.2 and 0.4 g LA). Inset in (a) shows an as-deposited photoanode (labelled FeOOH) and photoanodes after heating to $800^\circ$C for 20 min (labelled 0 g, 0.2 g and 0.4 g, according to LA levels). The light shield mask with a circular aperture used to cover the hematite coating in PEC measurements is also shown; (b) Corresponding Tauc plot of $(h\nu)^2$ against photon energy showing direct band gaps of $E_g$ 2.05-2.08 eV (605-596nm); (c) Corresponding Tauc plot of $(h\nu)^{1/2}$ against photon energy, showing indirect band gaps of $E_g$ ~2.04 eV (608nm).

Light absorption properties and band gap energies of hematite photoanodes were also studied by IPCE measurements (Fig. 5-53). The IPCE curves were consistent with photocurrent density results: the $Fe_2O_3$ (0 g LA) gave 6% maximum IPCE, $Fe_2O_3$–$FeO_x$ (0.4 g LA) gave 13%, and $Fe_2O_3$–$FeO_x$ (0.2 g LA) gave a marked improved IPCE maximum efficiency of 23%. The low IPCE for photoanodes lacking an $FeO_x$ amorphous coating further suggests that the majority of electron–hole pairs recombine and thus no significant free charge carriers are transferred to the electrolyte. However, in the presence of an $FeO_x$ amorphous coating behaving as an FeOOH electrocatalyst, higher IPCE efficiencies are obtained due to a better utilization of the photoinduced charges.
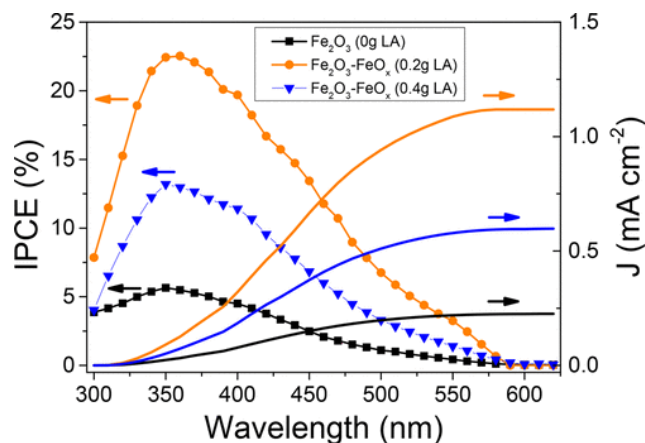
Fig. 5-53 IPCE curves of hematite photoanodes prepared with FeOOH powders synthesized with different levels of LA. Integrated photocurrent density profiles with AM1.5G solar spectrum are also shown on the right *y*-axis.

**Faradaic Efficiency Measurement**

$O_2$ evolution and photocurrent measurements were performed on the best photoanode [$Fe_2O_3$–$FeO_x$ (0.2 g LA)] at 1.23 $V_{RHE}$ under 1 sun illumination (Fig. 5-54a). The amount of $O_2$ in the headspace of a gastight PEC cell increased linearly with time during irradiation. Using the photocurrent–time curve obtained (Fig. 5-54b), the theoretical amount of $O_2$ expected for a water oxidation reaction with 100% faradaic efficiency was calculated and also represented in Fig. 5-54. Comparison between values indicated that the $Fe_2O_3$–$FeO_x$ (0.2 g LA) photoanode has a Faradaic efficiency of approximately 70%. This level is typical of high performing hematite photoanodes and is consistent with a high level of the photogenerated charges being employed in water splitting and hydrogen/oxygen production.[120]
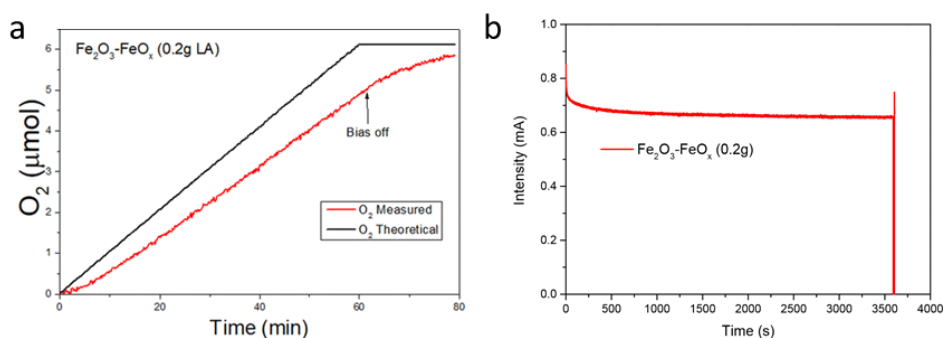


Fig. 5-54 (a) Amount of $O_2$ gas evolved at 1.23 $V_{RHE}$ under simulated sunlight (AM1.5G, 100 mW cm$^{-2}$) using the best-performing $Fe_2O_3$–$FeO_x$ (0.2 g LA) sample photoanode. The amount of $O_2$ quantified with a fluorescence probe is represented by the red line, whereas the theoretical amount of $O_2$ calculated assuming a 100% faradaic efficiency is shown by the black line. (b) Current of $Fe_2O_3$-$FeO_x$ (0.2g)

148

photoanode slide over 1h, conducted with continuous simulated sunlight in 1 M KOH at an applied potential 1.23$V_{RHE}$. $O_2$ evolution was simultaneously monitored.

**Conclusions**

We investigated the effect the preparation of FeOOH precursors has on final hematite photoanodes prepared by a simple doctor-blading deposition and heating step. We found that addition of lactic acid to the formation of FeOOH lepidocrocite nanorods changed its crystallinity and type of crystal phase, obtaining instead amorphous and goethite FeOOH. When used as a precursor for the preparation of films on a conductive support, the amorphous and goethite FeOOH resulted in the simultaneous formation of particulate hematite films with particles covered with a conductive amorphous $FeO_x$ coating. The thickness of this $FeO_x$ coating with excellent coverage and interface quality was effectively controlled by the addition of lactic acid to the FeOOH precursor preparation, being optimal at a ~3:1 Fe:LA ratio. Such an $FeO_x$ coating had a profound effect on the photoelectrochemical properties of films, producing a more than 4-fold enhancement in photocurrent density, from 0.32 to 1.39 mA cm$^{-2}$ at 1.23 $V_{RHE}$ under simulated sunlight. Detailed characterization demonstrated that the photocurrent enhancement resulted from an increase in both electrochemically active surface area and surface state capacitance. Importantly, all the characterization indicated that the formed amorphous $FeO_x$ coating has catalytic behavior equivalent to the very active FeOOH electrocatalyst. Like many successful electrocatalysts, it increased charged transfer efficiency by significantly reducing surface charge recombination. Finally, we found that an excess of lactic acid decreases surface area, but this is partly compensated by graphitic carbon sheets trapped between the crystalline hematite and $FeO_x$ amorphous coating that increase conductivity and photoelectrochemical performance. Our findings have opened a new approach to produce more efficient hematite photoanodes with a tuned semiconductor–electrolyte interface without extra steps of electrocatalyst addition and streamlined methodology. Further work to understand the mechanism of formation of the amorphous $FeO_x$ layer and the potential of this approach for other semiconductor types is currently under way.

**Author Contributions**

The manuscript was written through contributions of all authors. All authors have given approval to the final version of the manuscript.

**Data Access Statement**

All data created during this research are openly available from the University of Bath data archive at https://doi.org/10.15125/BATH-00599.

### 5.2.5 Commentary

*IPCE in deep UV region*

In Fig. 5-53 of manuscript, we recorded IPCE of our electrodes. The response rapidly decreased in deep UV region beyond 350 nm. During the measurement, substrate side illumination was used. Therefore, light must be first absorbed by FTO before reaching hematite. Although photons can generate electron hole pairs in FTO, they do not result in current because FTO is not in direct contact in electrolyte.

*IMPS response*

In addition to the PEC measurements demonstrated in the manuscript. IMPS was also carried out to explore the reaction kinetics in three types of hematite electrodes (0 g LA, 0.2 g LA and 0.4 g LA). The measurements were carried out in the same cell setup as described in the manuscript, while illumination was provided by a Modulight LED (523 nm, 20.5 mW cm$^{-2}$). The light perturbation was set to 10%, while the working electrode potential was set from 0.7 to 1.4 V$_{RHE}$ with a step of 0.1 V. Explanation of the features of IMPS complex plots and rate constants calculation steps for surface processes can be found in Note S3 Section 5.1.5. Data for three electrodes of different LA addition are shown in Fig. 5-55. The semicircles are flattened possibly due to distribution of electrode surface potential.[330]
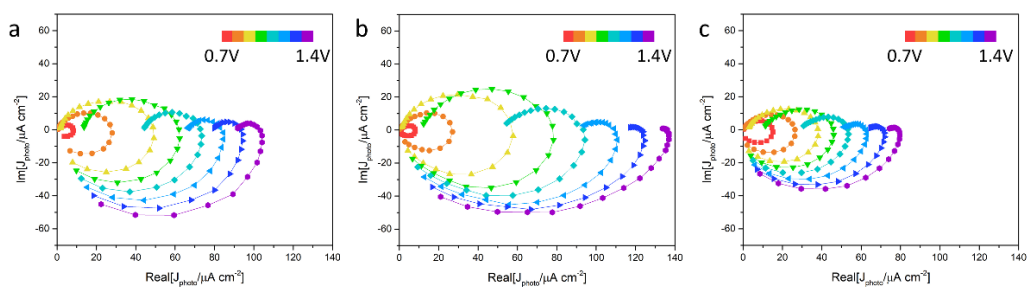


Fig. 5-55 IMPS responses of Fe$_2$O$_3$-FeO$_x$ electrodes: (a) 0 g LA, (b) 0.2 g LA and (c) 0.4 g LA.

According to fitting results based on rate constant model, we first noticed that the charge transfer efficiencies of these three electrodes are surprisingly similar (Fig. 5-56a). The value calculated for 0 g LA of 79% at 1.2 V$_{RHE}$ is in stark contrast with that obtained by hole scavenger method (49% at 1.23 V$_{RHE}$) described in the manuscript. This is probably the result of spontaneous decomposition of H$_2$O$_2$ at the

presence of Pt or photocurrent doubling as observed for CuWO$_4$ electrodes.[331] However, it is unclear why the discrepancy did not occur for the other two samples. In this section, we give an alternative set of propositions based on IMPS results.

Since $\eta_{ct}$ are highly close for all three electrodes, differences in photocurrent densities must come from the hole flux that reaches the surface, which is indeed found to diverge. Sample 0.2 g LA shows the highest hole flux (Fig. 5-56b), indicating that it is not at least directly related to the FeO$_x$ layer thickness. Another possible cause is the preference of crystal orientation along (110), which has been found to have four orders of magnitude higher conductivity than along (001). However, this possibility is also ruled out according to Grave and co-workers, where the hole flux was found to be hardly different.[137] Thus, it leaves us with the possibility that 0.2 g LA sample has a higher porosity. The relative magnitudes of hole flux are in line with ECSA. Notably, external assistance by applied potential to drive holes toward the surface is only effective at higher potentials. The drop of exerted potential away from substrate due to the low conductivity of hematite plus the longer electron paths leads to the surface potential distribution and thus the flattened semicircles in IMPS.
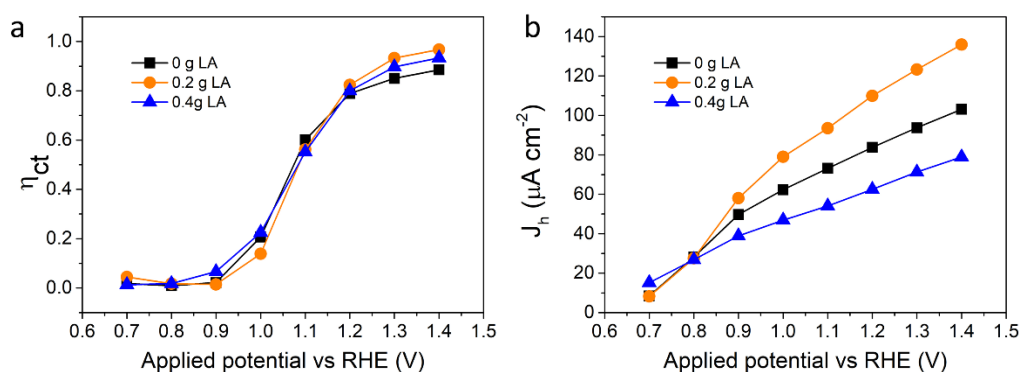


Fig. 5-56 (a) Charge transfer efficiencies and (b) hole fluxes of photoanodes 0 g LA (black squares), 0.2 g LA (orange circles) and 0.4 g LA (blue triangles) obtained from IMPS.

*Rate constants calculation from IMPS*

More interesting results are observed after calculating the charge transfer and recombination rate constants. First, charge transfer rate constants ($k_{ct}$) are noticeably lower for FeO$_x$ coated samples than bare hematite for a wide range of potentials, and surface recombination rate constants ($k_{rec}$) are also lower at all potentials. This situation resembles the changes in rate constants when CoPi is coated, thus we

speculate that the FeO$_x$ is acting as a co-catalyst. Although its chemical nature is unknown at this point, stoichiometric FeOOH can be ruled out since the films have been calcined at 800 °C.

The trends of rate constants for 0 g LA and 0.4 g LA films fit in one of the two categories proposed by Peter et al. where surface states are mobile and high in concentration,[270] which also agrees with results reported in the manuscript. Nevertheless, 0.2 g LA film shows a more complicated picture: its $k_{ct}$ starts to drop instead of reaching a plateau and $k_{rec}$ drops more rapidly above 1.1 V$_{RHE}$. This observation is in fact in line with the other category in Peter's paper where surface states are immobile and low in concentration. Hence, a transformation in reaction mechanism is expected.
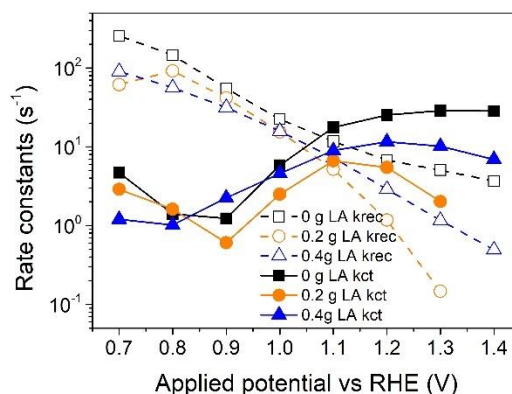


Fig. 5-57 Charge transfer rate constants ($k_{ct}$, solid symbols) and surface recombination rate constants ($k_{rec}$, open symbols) for photoanodes 0 g LA (black squares), 0.2 g LA (orange circles) and 0.4 g LA (blue triangles) calculated using IMPS data.

The cause for such a transformation is, unfortunately, still unclear, but we believe that it is not associated with the thickness of FeO$_x$ layer since that for 0.2 g LA sample is between those for 0 g LA and 0.4 g LA sample. Instead, a difference in surface area could be responsible because as mentioned before, photovoltage is inversely related to electrode surface area. A smaller photovoltage means less driving force and thereby charge transfer rate, although recombination is not enhanced due to the higher surface area that can accommodate more charges, which is evidenced by high surface states capacitance above 1.1 V$_{RHE}$ (Fig. 5-58).
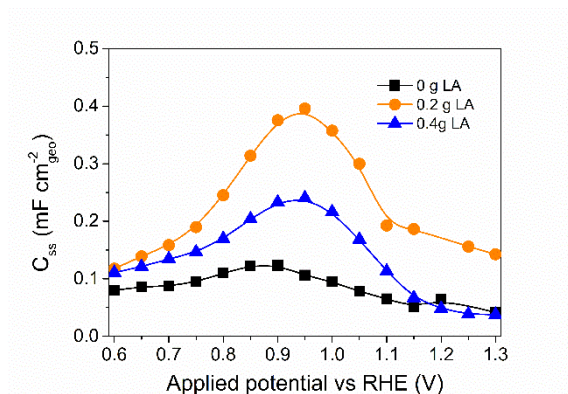
Fig. 5-58 Surface capacitances of photoanodes 0 g LA (black squares), 0.2 g LA (orange circles) and 0.4 g LA (blue triangles) for extended a potential range calculated using PEIS data.

*Chemical nature of FeO$_x$*

Whether the amorphous FeO$_x$ is catalytically more active than hematite surface requires further investigation. Although in Fig. 5-49a, the dark current density curve for 0.2 g LA sample shows a much lower onset, this advantage could be attributed to a higher surface area. If the current density is corrected with ECSA, their differences are clearly diminished (Fig. 5-59a). Moreover, the performance of 0.4 g LA sample with the thickest FeO$_x$ is poorest whether ECSA-uncorrected or corrected. Some clues on the chemical nature of this overlayer can be found in XPS results on the photoanodes. We note that Sn 3d peak intensities considerably increase with more LA addition (Fig. 5-59b), which means this FeO$_x$ layer is possibly highly Sn-doped (from FTO substrate) Fe$_2$O$_3$. Hence, the higher brightness of FeO$_x$ layer from electron microscopy images may be a result of better conductivity. Moreover, the high doping levels may explain the loss of crystallinity. In spite of deductions from IMS and XPS, firm validation of FeO$_x$ chemistry would require more advance physical characterizations such as electron energy loss spectroscopy.

154
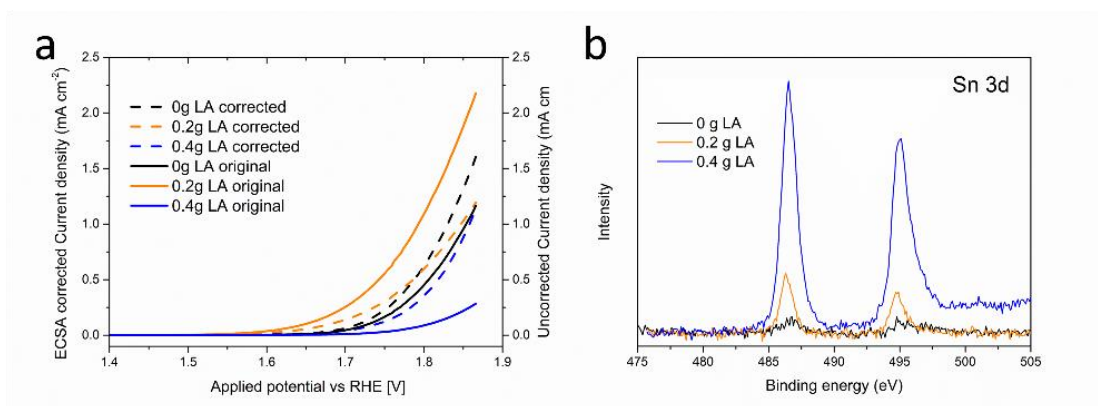
Fig. 5-59 (a) Original (solid) and ECSA-corrected (dashed) current density curves for photoanodes 0 g LA (black squares), 0.4 g LA (orange circles) and 0.4 g LA (blue triangles). (b) XPS Sn 3d spectra for the three photoanodes.

# Chapter 6 Anodized Tungsten Trioxide (WO₃) Photoanodes

## 6.1 Overview of WO₃ Photoanodes

Tungsten trioxide exist in several crystallographic forms in different temperature ranges: tetragonal (α-WO₃, above 720 °C), orthorhombic (β-WO₃, from 320 to 720 °C), monoclinic I (γ-WO₃, from 17 to 320 °C), triclinic (δ-WO₃, from -43 to 17 °C), and monoclinic II (ε-WO₃, below -43 °C).[332] Octahedral coordination dominates for $W^{6+}$, which can be deformed or collapse when WO₃ is reduced to its sub-stoichiometric forms, such as $WO_{2.9}$ and $WO_{2.72}$.[333] Of these polymorphs listed above, monoclinic γ-WO₃ is the most common phase for photoanodes, followed by triclinic δ-WO₃.[334–336]

As an n-type semiconductor for photoelectrode, WO₃ has a band gap of 2.6 eV. Although it is within visible light region, it can only absorb 12% of the solar spectrum, projecting to a theoretical maximum photocurrent density of around 4 mA cm⁻².[16,332] Its advantages include a charge diffusion length of 150 nm, good stability in neutral and acidic conditions (except HF), and elemental abundance.[337] Note that its CB edge lies slightly below HER potential so an external potential input is necessary for overall water splitting.

Deposition and solution-based techniques are common methods to fabricate WO₃ photoanodes. For deposition methods, chemical vapor deposition, radio frequency sputtering, and aerosol flame deposition among others have been attempted, often producing photocurrent densities between 1-2 mA cm⁻² at 1.23 $V_{RHE}$.[338–340] A more recent work using pulsed laser deposition achieved 2.4 mA cm⁻² at the same potential.[341] More interestingly, two layers of WO₃ on both sides of conductive glass yield a photocurrent density surpassing 3 mA cm⁻² at 1.23 $V_{RHE}$, because it was found that double stacking lessens the discrepancy between charge diffusion length and light penetration depth.[341]

Solution-based syntheses, including sol-gel and hydrothermal methods, have often resulted in films with highly nanostructured morphologies thanks to the wide selection of precursors and careful control of reaction conditions.[334,335,342] The principles of different solution-based methods can be fundamentally different, which vary for example from decomposition of peroxotungstic acid to chemical oxidation of tungsten foil.[342,343] High photocurrent densities have been more frequently reported with these

solution-based methods. Structures such as mesoporous spherical nanoparticles or plates have demonstrated photocurrent density approaching 3 mA cm$^{-2}$ at 1.23 V$_{RHE}$ under solar simulation.[344]

Electrochemical oxidation, commonly referred to as anodization, is an alternative of thermal oxidation, which have also been attempted in many cases.[345] A systematic literature survey is contained in the manuscript (Section 6.2.4). Most anodization studies used fluoride containing electrolytes because F ions migrate toward the anode end, forms HF in aqueous solution and rapidly etches tungsten oxides.[346,347] It should be noted that the use of fluorides causes health and safety issues. Several attempts have been made in anodization without fluorides in electrolyte, but reliable PEC performance measurement has been lacking.[348,349]

Anodization is an efficient way to produce self-organized nanostructures. A compact or porous layer of metal oxides (e.g. Al$_2$O$_3$, TiO$_2$, ZrO$_2$) can be formed. The compact layer is sometimes called barrier layer.[350] During an anodization process, a metal substrate is ionized upon application of a strong potential (or current). The metal cations then migrate outward to the interface; on the other hand, O$^{2-}$/OH$^-$ reach the surface under the influence of electric field and migrate further inward, forming metal oxide. (Fig. 6-1)
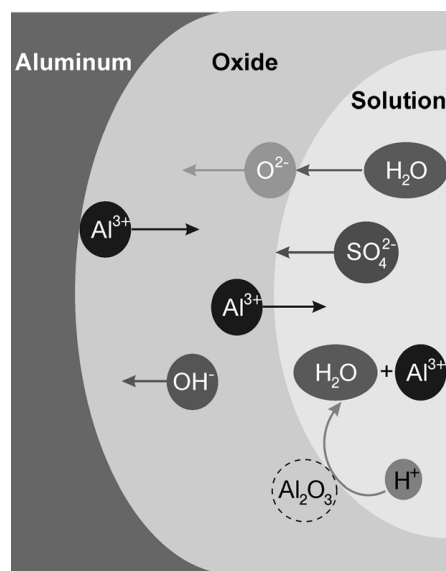


Fig. 6-1 Oxide formation process exemplified with anodization of Al.[350] From Grzegorz D. Sulka, Nanostructured Materials in Electrochemistry, Chapter 1. Copyright © 2008 Wiley‑VCH Verlag GmbH & Co. KGaA. Reprinted by permission of John Wiley & Sons, Inc.

Most commonly anodized material is aluminum. The resulting porous $Al_2O_3$ layer is frequently used as a hard template for production of 1D nanostructures.[351] For PEC applications, direct anodization of Ti for $TiO_2$ nanotubes for photoanodes has been reported.[352] Different morphologies can be obtained for other metals, such as mesoporous $WO_3$ mentioned previously.[346,348] More important consideration to obtain desirable morphologies involves the control of anodizing conditions: applied potential/current, duration, and electrolyte type.

The oxide layer produced by electrochemical anodization is usually amorphous and non-stoichiometric, thus a follow-up annealing is required to remove defects and convert it into crystalline metal oxide photoanodes. Liu et al. found that the optimum annealing temperature for $WO_3$ is 450 °C, which is adopted in this work.[353] Higher temperature, on the other hand, led to larger crystallite sizes. Measurements of photocurrent density of films made in this work confirmed the qualitative increase in photoactivity.

## 6.2 Publication: Nanostructured WO₃ Photoanodes for Efficient Water Splitting via Anodization in Citric Acid
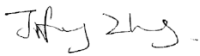
### 6.2.1 Preface

There has been plenty of research on nanostructuring photoanodes and photocatalysts. It often requires high temperatures, expensive chemicals, dangerous chemicals, or sophisticated deposition techniques, which have been mentioned in Section 6.1. These drawbacks will limit the future application in solar energy harvesting and the upscaling of devices. In this paper we demonstrate for the first time that citric acid, a less hazardous acid with environmental benefits in terms of its production and waste disposal, can be effectively used as an anodizing electrolyte for the preparation of nanostructured $WO_3$ photoanodes. Citric acid is demonstrated to be a greener alternative to the commonly used hydrofluoric-based anodizing electrolytes employed for $WO_3$ photoanode preparation by anodization. Citric acid is not only less hazardous and more environmentally friendly, but also is demonstrated in this paper to produce photoanodes with a higher photoresponse at low applied voltages and a better stability. This discovery opens new avenues in the green synthesis of semiconductor materials.

These breakthroughs are of interest to materials scientists, engineers and chemists. These results will stimulate new research on materials chemistry and manufacturing.

## 6.2.2 Declaration of Authorship

| This declaration concerns the article entitled: | | | | | |
|---|---|---|---|---|---|
| Nanostructured WO$_3$ Photoanodes for Efficient Water Splitting via Anodisation in Citric Acid | | | | | |
| Publication status | | | | | |
| In preparation | Manuscript | Submitted | In review | Accepted | <u>Published</u> |
| Publication details (reference): | RSC Advances, 2017, 7, 35221 | | | | |
| Candidate's contribution to the paper (detailed, and also given as a percentage). | <ul><li>Formulation of ideas: 20 %<br>The candidate has developed the research incentive proposed by the supervisory team.</li><li>Design of methodology: 80%<br>The candidate is responsible for the majority of experimental design and planning.</li><li>Experimental work: 90%<br>The candidate carried out most of the work, including sample fabrication, characterization on the basis of preliminary work of a previous student. Guidance in experimental setup was kindly given by Prof. Davide Mattia's group members. Training and minor assistance in characterization instrumentation were provided by staff from Department of Physics and Department of Chemistry.</li><li>Manuscript writing and editing: 70%<br>The candidate wrote the manuscript draft, which was edited by the candidate and supervisory team.</li></ul> | | | | |
| Statement from Candidate: This paper reports on original research I conducted during the period of my Higher Degree by Research candidature. | | | | | |

| Signed | | Dec. 2018 |
|---|---|---|
| | *Jeffrey Zhang* | |

## 6.2.3 Copyright Agreement

This article is licensed under a Creative Commons Attribution 3.0 Unported Licence. Reproduced from RSC Adv., 2017, 7, 35221 with permission from The Royal Society of Chemistry.

**6.2.4 Manuscript**

# Nanostructured WO₃ photoanodes for efficient water splitting *via* anodisation in citric acid

**Jifang Zhang**[a], **Ivette Salles**[b], **Sam Pering**[c], **Petra J. Cameron**[c], **Davide Mattia**[a] **and Salvador Eslava**\*[a]

[a]*Department of Chemical Engineering, University of Bath, Bath, UK. E-mail: s.eslava@bath.ac.uk*

[b]*Departament d'Enginyeria Química, Biològica i Ambiental, Universitat Autònoma de Barcelona, Bellaterra 08193, Spain*

[c]*Department of Chemistry, University of Bath, BA2 7AY, UK*

**ABSTRACT:** In this work we report the production of nanostructured WO₃ photoanodes for solar water splitting produced *via* anodisation using for the first time citric acid (CA), a safer and more environmentally friendly alternative to fluoride-based electrolytes. Photoelectrochemical solar water splitting has shown potential as a renewable method for hydrogen production, a key ingredient to advance the de-carbonisation of our economy. Many methods to produce WO₃ photoanodes are time-consuming and require high temperatures and/or toxic chemicals, such as fluoride-based electrolytes. Here we report on a systematic investigation of the anodisation of tungsten using CA to establish a relation between (i) anodisation parameters (current, time and electrolyte), (ii) the resulting nanostructured morphology and (iii) its performance as a photoanode for water splitting. Characterisation was carried out by X-ray diffraction, scanning electron microscopy, linear sweep voltammetry, and ultraviolet-visible spectroscopy. After optimisation, the obtained WO₃ photoanodes produced a photocurrent of 0.88 mA cm$^{-2}$ at 1.0 V *vs.* Ag/AgCl in 0.5 M aqueous H₂SO₄ under AM1.5 solar irradiation. At low applied potentials (below 0.67 V *vs.* Ag/AgCl), closer to practical conditions, the photoanodes produced in CA outperformed a conventional counterpart made using a NH₄F electrolyte. The CA-anodised photoanodes also showed higher stability, retaining 90% of their activity

after 1 h of chopped solar illumination. This work demonstrates the promise of anodisation in citric acid as an efficient and more sustainable method for the production of $WO_3$ photoanodes for solar water splitting.

---

**Introduction**

Photoelectrochemical (PEC) water splitting is a promising approach to produce hydrogen, a sustainable clean fuel, and significant progress has been made since its first advent.[34] In a PEC cell, the choice of materials for electrodes is essential. Among different metal oxide semiconductors, tungsten trioxide ($WO_3$) has received much attention due to its band gap of 2.7 eV within the visible-light region, the relatively long diffusion length (150 nm) of its hole carriers, and its excellent stability in acidic conditions.[354] Many methods, including chemical vapour deposition, solvothermal, sol–gel and anodisation have been deployed to produce nanostructured $WO_3$.[335,338,355–360] Their optimised performance is associated with the production of larger active surface areas, better light harvesting capability, and more effective transport of charge carriers. However, many deposition methods such as chemical vapour deposition and flame deposition involve complex experimental setups or conditions which compromise the large scale production.[338,355] Sol–gel and solvothermal methods are relatively simpler to carry out, and $WO_3$ nanostructures can be formed too with careful selection of solvents and reaction conditions.[335,356–358] Nevertheless, long hours at high temperatures are often required. Anodisation, compared to other preparation techniques for photoelectrodes, is inexpensive and simple, making it suitable for large scale fabrication. It consists of growing a natural oxide layer of a metal foil by electrolytic passivation, followed by crystallisation at adequate temperatures (typically 400 to 600 °C). As the metal oxide layer grown on top is tightly bound to the metal support, the efficacy of charge collection is high. However, there is one major disadvantage in the anodisation of tungsten. Current reports exclusively use electrolytes that contain one or more fluorides (*e.g.* NaF, HF or $NH_4F$) as etching agents, which potentially bring serious safety issues due to the presence or formation of HF.[32,359,361,362] Few F-free alternative electrolytes have been reported to successfully anodise tungsten, such as oxalic acid and $NH_4NO_3$, which have shown highly porous nanostructures.[336,363] Therefore, it is meaningful to explore more F-free

electrolytes and approaches for safer, faster and more scalable anodisation for the production of $WO_3$ photoanodes.

An ideal anodising electrolyte for the formation of photoanodes needs to assist the oxidation of the top surface of the precursor metal foil under an electric field and promote a morphology and porosity that eventually enhance the photoresponse. Citric acid (CA, $C_6H_8O_7$) is known for its chelating properties and is widely used to soften water due to its ability to bind metals.[364] It is also used as a structure-directing agent in solution-based synthesis methods.[365,366]

Here, we demonstrate for the first time that CA offers a sustainable, fast and effective replacement of fluoride-containing electrolytes for the anodisation of tungsten foil and the preparation of nanostructured $WO_3$ photoanodes for solar water splitting. We report the results of different anodising conditions using CA and compare the performance of the resulting photoanodes with that using $NH_4F$ as electrolyte. The comparison is made by analyses of their structural as well as photoelectrochemical properties, including photocurrent density under solar simulation measured by linear sweep voltammetry (LSV), applied bias photon-to-current efficiency (ABPE), and incident photon-to-current conversion efficiency (IPCE). The stability of the photoanodes is also tested.

**Experimental**

Materials

Tungsten foil (0.1 mm, 99.95%) was purchased from Alfa Aesar. Citric acid (CA, 99%) and *N*-methylformamide (NMF, 99%) were purchased from Sigma-Aldrich. Ammonium fluoride ($NH_4F$, 98+%) and sulfuric acid ($H_2SO_4$, 5 M) were supplied by Acros Organics and Fluka Analytical, respectively. Analytical acetone was obtained from VWR Chemicals and deionised water was used.

Anodisation

Tungsten foil was cut into $15 \times 30$ mm rectangles and sonicated for 15 minutes in acetone. After sonication, the foil pieces were rinsed with $H_2O$ and dried under pressurised air. The anodisation was carried out by using the cleaned foil pieces as the anode of a two-electrode cell and a 3 mm-thick stainless steel piece as the cathode. Teflon and rubber templates were used to limit the anodisation to a circular area of

13 mm in diameter. The anode and cathode were held in parallel at a distance of 10 mm and immersed in electrolytes consisting of 0.1 M CA in either $H_2O$ or a solution of 80 vol% NMF and 20 vol% $H_2O$. A jacketed beaker connected to a refrigerated circulating bath (DC-10, Thermo) kept the electrolyte at a constant temperature of 0 °C. Samples were anodised for 30 minutes at constant currents, controlled by a DC power supply (Agilent 6675A). One of the previously published procedures using fluoride electrolyte[360] was repeated for comparison: tungsten pieces were anodised for 6 h under 40 V at 40 °C in NMF solution including 20 vol% $H_2O$ and 0.05 wt% $NH_4F$. After anodisation, all samples were rinsed with $H_2O$, dried in air, and calcined in air at 450 °C for 4 h.

Physical characterisations

Morphology of photoanodes after fabrication processes was characterised by Field Emission Scanning Electron Microscopy (FESEM), JEOL 6301F, with an acceleration voltage of 5 keV. Film thicknesses were measured at ten different sites to calculate the mean value and standard deviation (quoted with a ± sign). Area fraction is measured using ImageJ. X-ray diffraction was performed with a BRUKER AXS D8 advance diffractometer using a Vantec-1 detector and CuKα radiation.

Photoelectrochemical performance

Photoelectrochemical measurements were carried out in a three-electrode photoelectrochemical quartz cell using the prepared $WO_3$ electrode as the working electrode, a Pt wire counter electrode, a Ag/AgCl (in 3.5 M KCl) reference electrode, and 0.5 M $H_2SO_4$ electrolyte. Solar simulated light on an 8 mm-diameter area was provided by a 300 W Xe Lamp (LOT Quantum Design) equipped with an AM1.5G filter. The irradiation intensity was set to 1 sun (100 mW $cm^{-2}$). An external potential (provided by Ivium CompactStat) was linearly swept from 0 to 1.2 V *vs.* Ag/AgCl at a rate of 20 mV $s^{-1}$. Applied bias photon-to-current efficiency (ABPE) was obtained using the following equation:

$$\text{ABPE} = \left[ \frac{\left| j_{\text{ph}} \; (\text{mA} \; \text{cm}^{-2}) \right| \times \left( E_{H_2O/O_2} - |V_{\text{b}}| \right) \; (\text{V})}{P_{\text{total}} \; (\text{mW} \; \text{cm}^{-2})} \right]_{\text{AM1.5G}} \qquad \text{Eq. 6-1}$$

where $j_{\text{ph}}$ is the net photocurrent density measured at an applied bias $V_{\text{b}}$ and $P_{\text{total}}$ is the total solar incident irradiation.

Incident photon-to-current efficiency (IPCE) measurements were performed from 300 to 500 nm with the same light source and a triple grating Czerny-Turner monochromator. The intensity of monochromatic light was measured at the working electrode position with a SEL033/U photodetector (International Light Technologies). The values of IPCE were then calculated using the formula below:

$$\text{IPCE}(\lambda) = \frac{|j \ (\text{mA} \ \text{cm}^{-2})| \times 1239.8 \ (\text{V} \ \text{nm})}{P_{\text{mono}} \ (\text{mW} \ \text{cm}^{-2}) \times \lambda \ (\text{nm})} \qquad \text{Eq. 6-2}$$

where $j$ is the photocurrent density measured under single wavelength ($\lambda$) light illumination and $P_{\text{mono}}$ is its incident irradiation power.

Photoelectrochemically active surface area (PECSA) values were calculated by measuring double layer capacitances with cyclic voltammetry. Potential was scanned at rates from 5 to 160 mV s$^{-1}$ in a window of 0.2 V around open-circuit potential. The active surface area was then calculated using equation: PECSA $= C_{\text{DL}}/C_{\text{S}}$,[367] where $C_{\text{DL}}$ is the slope for the fitted line plotted from measured currents against scanning rates, and $C_{\text{S}}$ (specific capacitance) took the value of the unit area $C_{\text{DL}}$ for a photoanode that has compact oxide layer produced from a controlled weak anodisation. The same electrochemical and light irradiation setup used for photocurrent density measurements was also used herein.

**Results and discussion**

Anodisation was carried out in two selected types of solvents: $H_2O$ and a mixture of NMF and $H_2O$. NMF is added for its high dielectric constant which can favour higher charge density and assist oxide growth,[368] and $H_2O$ is added as an oxygen donor and to assist the dissolution of CA, which is not soluble in NMF and unstable in other anodising solvents such as ethylene glycol or glycerol. Although it is sometimes argued that $H_2O$ concentration should be minimal for fast and deep anodisation and that $H_2O$ content in air is sufficient to act as oxygen source, adding $H_2O$ ensures the formation of a porous oxide.[32,369] We used a mixture of $H_2O$ and NMF in a 20 and 80 vol% proportion, as this was found to be optimal by Tacca et al.[360] The same solvents were used with $NH_4F$ for reference of the effectiveness of CA as etching agent.

The morphology of $WO_3$ films on the tungsten foil surface after anodisation was examined by FESEM. In the $H_2O$ solution, the CA-assisted anodisation etched the

tungsten foil into a canyon-like nanostructure with valleys and corrugated $WO_3$ walls and rods occupying approximately 70% of the area (Fig. 6-2a and b). This differs from the commonly seen $WO_3$ mesoporous mesh-like structures observed after anodisation in fluoride-containing media.[32,359,361,362]
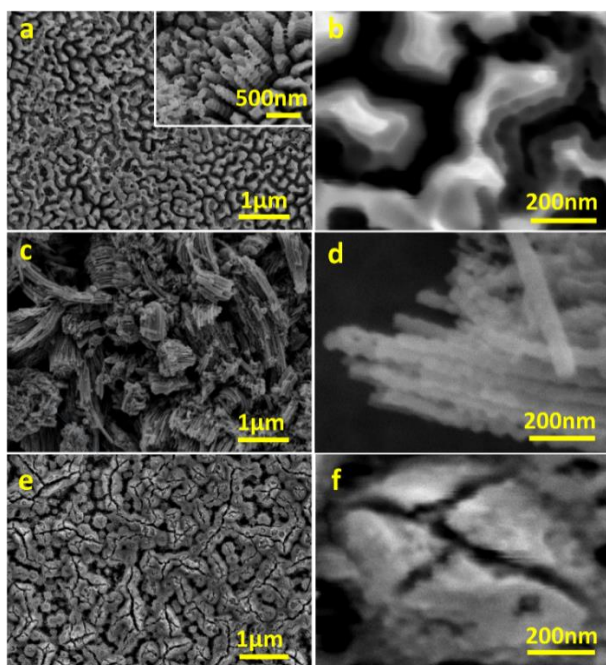


Fig. 6-2 Representative FESEM micrographs of $WO_3$ photoanodes anodised in $CA/H_2O$ at 0.1 A for 30 min (a, b), in $CA/NMF/H_2O$ at 0.015 A for 30 min (c, d), and in $NH_4F/NMF/H_2O$ at 40 V for 6 h (e, f).

The height of the nanostructured valleys is estimated to be around 500 nm, below which there is a thin, compact layer of $WO_3$, which adds up to a total thickness of *ca.* $3.7 \pm 1.5$ μm (Fig. 6-3a). The width of the walls and rods are between 100 and 200 nm. It is worth noting that their corrugated features should allow for stronger light scattering and absorption, as has been demonstrated in $WO_3$ photoanodes with helical nanostructure produced with oblique angle deposition.[51]
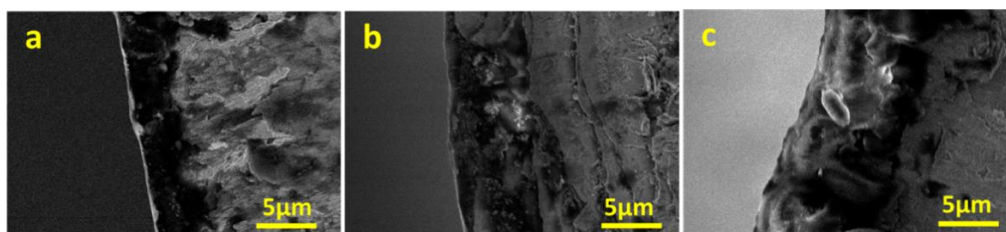


Fig. 6-3 Representative cross sectional FESEM images for $WO_3$ photoanodes produced in $CA/H_2O$ at 0.1 A for 30 min (a), in $CA/NMF/H_2O$ at 0.015 A for 30 min (b), and in $NH_4F/NMF/H_2O$ at 40 V for 6 h (c). The average thicknesses of each film

are 3.7±1.5, 5.8±1.7 and 7.4±2.7 µm, respectively. Cross-sections were prepared by cutting the photoanodes with tongs.

The etching of the tungsten foil top surface during the anodisation in CA/H$_2$O was investigated at different times by FESEM to understand the formation of the canyon-like nanostructure. First, a compact layer of tungsten oxide is formed under electrochemical oxidation, where cracks appear due to the difference in density of the oxide layer compared to tungsten, inducing strong local stresses (Fig. 6-4a). Next, field-assisted dissolution starts to play an important role in the vicinity of the cracks, rendering the formation of holes of several hundred nanometres across (Fig. 6-4b). The relatively compact oxide is then carved into nanowalls/nanorods (Fig. 6-4c). The existence of nanorods is a result of horizontal dissolution as demonstrated by the "natural bridges" between two nanorods on the top right corner of Fig. 6-2a inset. Extended anodisation time can cause total dissolution of tungsten foil and hence a less effective working area. (Fig. 6-4d). The morphological migration observed here is akin to the formation mechanism proposed by Chai and co-workers using oxalic acid anodisation, although they obtained a different porous structure consisting of spherical voids.[370]
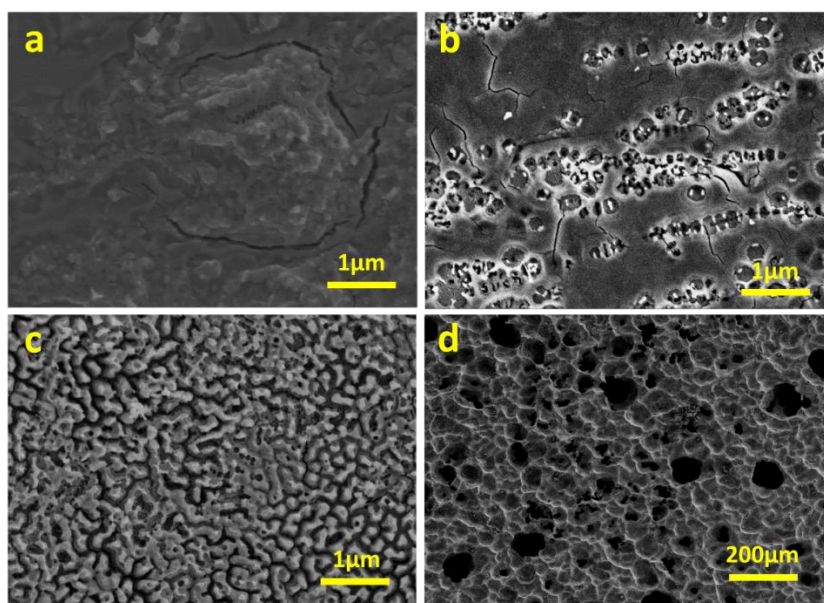


Fig. 6-4 FESEM micrographs of the morphological transformation of WO$_3$ layer anodized in CA/H$_2$O at 0.10 A. (a) Compact oxide layer with cracks forms in a few minutes; (b) field assisted dissolution gradually induces holes mainly along cracks; (c) canyon-like structures composed of nanorods/nanowalls spreads uniformly after anodization for ca. 30min; (d) pitting corrosion takes place after long anodization time (>30min).

The morphology can also be controlled by changing the anodisation current. Results for a series of specimens anodised at different current values (0.05, 0.08 and 0.10 A) for 30 min indicate further features in the formation of the $WO_3$ layer (Fig. 6-5). When anodised at 0.05 A, cracks (deep valleys) dominate the morphology of the layer, which appears to be rougher and with a less uniform porosity (Fig. 6-5a). At 0.08 A, more shallow valleys spread over the majority of the surface, with relatively limited flat domains (Fig. 6-5b). Anodisation at 0.10 A obtains the most uniform porosity and finer features (Fig. 6-5c). Above 0.10 A, large cavities up to 100 μm arise due to pitting corrosion (Fig. 6-5d). The higher porosity gained from nanorods/nanowalls compared to other structures is beneficial for its photoresponse.
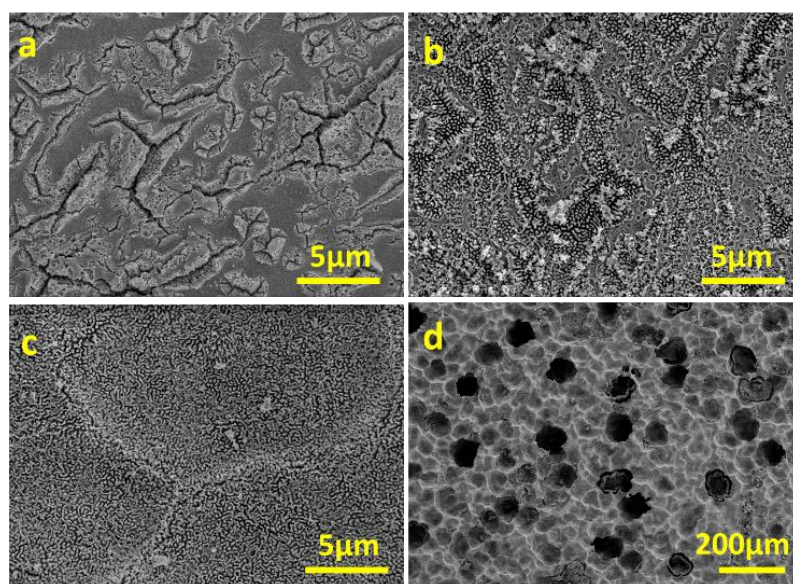


Fig. 6-5 FESEM micrographs of photoanodes after anodisation in $CA/H_2O$ for 30 min at 0.05 A (a), 0.08 A (b), 0.10 A (c) and 0.15 A (d).

The morphology of CA-anodised films was found to depend also on the choice of solvents. When anodised in $CA/NMF/H_2O$, a different morphology was obtained where nanowires of *ca.* 50 nm in diameter with different lengths and random orientation are predominant (Fig. 6-2c and d). This indicates that the high dielectric constant of NMF solvent compared to water has an effect on the final morphology.

For comparison to literature, we anodised the same tungsten foil in $NH_4F/NMF/H_2O$ and obtained a worm-like porous morphology (Fig. 6-2e and f), as reported in the literature, different to the canyon-like nanostructure or the nanowire structures obtained with CA.[360] Cross sectional FESEM micrographs show that the thicknesses of the films under study are *ca.* 5.8 ± 1.7 μm for $CA/NMF/H_2O$ anodised

film and *ca.* 7.4 ± 2.7 μm for NH$_4$F/NMF/H$_2$O anodised film (Fig. 6-3b and c). Therefore, CA has a similar etching capability with NH$_4$F, despite the citrate ligand being bulkier.

Fig. 6-6 shows the XRD patterns of anodised films after calcination. The phases of the oxide layer in all cases are monoclinic (JCPDS no. 43-1035), which is the typical phase encountered upon various anodisation methods[32,360,362,363,371] and has proved to be superior to other phases including orthorhombic and hexagonal in photocatalysis.[372] Despite the fact that calcination temperature and dwell time are the same, the oxide formed using NH$_4$F as electrolyte has preferential orientation along (−222)/(222), which was also observed elsewhere and found to be the most stable orientation during aging tests.[337,360] Notably, the calcination step after anodisation is essential because for uncalcined photoanodes, the oxide formed has poor crystallinity and is not photoresponsive (see Fig. 6-7).
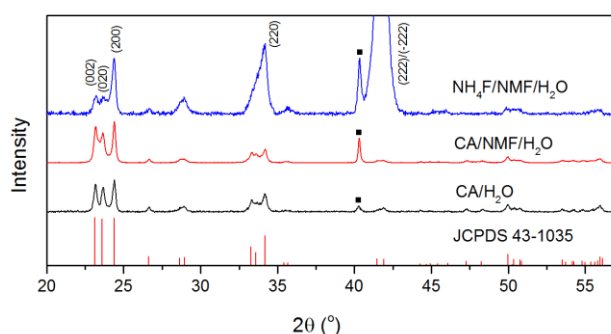


Fig. 6-6 XRD patterns of calcined WO$_3$ photoanodes anodised in CA/H$_2$O at 0.1 A for 30 min (black), in CA/NMF/H$_2$O at 0.015 A for 30 min (red), and in NH$_4$F/NMF/H$_2$O at 40 V for 6 h (blue) with reference to monoclinic WO$_3$ (JCPDS no. 43-1035). Squares indicate diffraction from metallic tungsten (110) under WO$_3$.
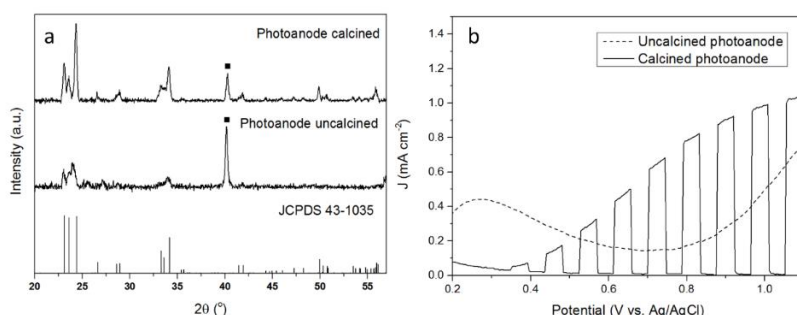


Fig. 6-7 (a) XRD patterns of calcined and uncalcined WO$_3$ electrodes prepared by anodization in CA/H$_2$O at 0.10 A for 30 min and (b) their current densities under chopped solar simulated light (AM1.5, 100 mWcm$^{-2}$). Squares indicate diffraction from metallic tungsten (110) under WO$_3$.

Kubelka–Munk conversion of UV-visible diffuse reflectance spectroscopy of anodised films after calcination is shown in Fig. 6-8. All anodised films show the $WO_3$ bandgap absorbing at wavelengths below 450 nm. For wavelengths above 450 nm, the $NH_4F/NMF/H_2O$ anodised films absorb more light, which could be due to F doping originated from the electrolyte, as observed in F-doped $TiO_2$ powders.[373] Lower, but still evident is the absorption at those high wavelengths in $CA/H_2O$ and $CA/NMF/H_2O$ films, which could be due to minor carbon doping from CA or NMF. Although the Kubelka–Munk conversion compensates for specular reflectance, this cannot be completely ruled out in these measurements.
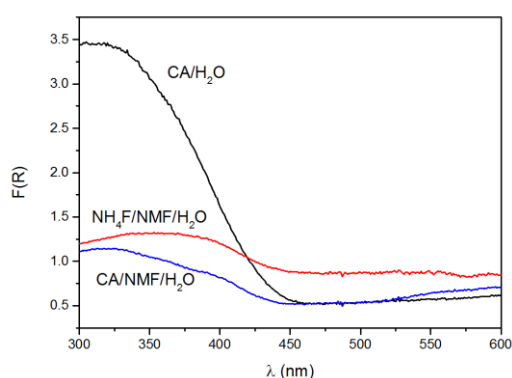


Fig. 6-8 Kubelka–Munk function, $F(R)$, of films anodised in $CA/H_2O$ at 0.1 A for 30 min (black), in $CA/NMF/H_2O$ at 0.015 A for 30 min (blue), and in $NH_4F/NMF/H_2O$ at 40 V for 6 h (red) obtained from UV-visible diffuse reflectance spectroscopy.

Anodised films were tested for photoelectrochemical water splitting. The photocurrent densities under solar illumination measured on films are found to be optimal when anodised at 0.1 A for 30 min in $CA/H_2O$ and 0.015 A for 30 min in $CA/NMF/H_2O$ (Fig. 6-9)
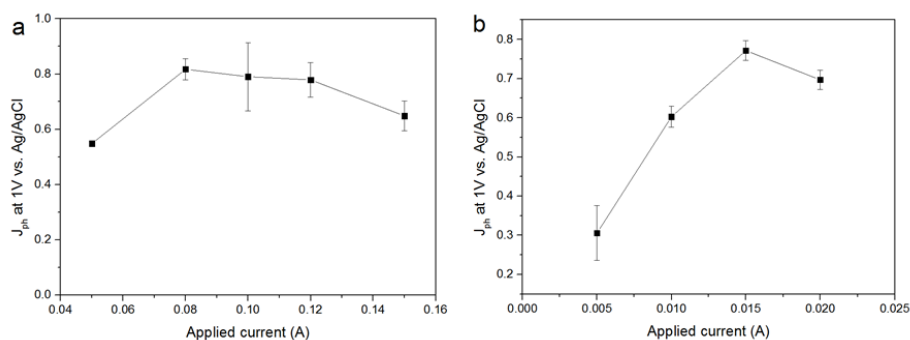


Fig. 6-9. Photocurrent density measured at 1.0 V vs. Ag/AgCl in 0.5 M $H_2SO_4$ under 1 sun illumination (AM1.5G, 100 mW cm$^{-2}$) for $WO_3$ photoanodes produced

with CA/H$_2$O (a) and CA/NMF/H$_2$O (b) solutions for 30 min; the optimized anodising currents were found to be 0.10A and 0.015A, respectively.

Fig. 6-10a shows representative LSV curves of these optimised WO$_3$ films, with or without solar illumination in a three-electrode system. In spite of differences in WO$_3$ thickness between the CA/H$_2$O- and the CA/NMF/H$_2$O-anodised photoanodes (3.7 ± 1.5 *vs.* 5.8 ± 1.7 μm, resp.), they show similar performance: the net photocurrent densities measured at 1.0 V *vs.* Ag/AgCl in 0.5 M H$_2$SO$_4$ are 0.88 mA cm$^{-2}$ and 0.77 mA cm$^{-2}$, respectively. This could be assigned to a stronger light scattering effect in the corrugated canyon-like nanostructure (formed in CA/H$_2$O) compared to the thin nanowires (formed in CA/NMF/H$_2$O). Another cause is that the ordered structure favours a more facile charge collection between the oxide and the metal basis than the randomly oriented nanowires. These values are comparable with published data for fluoride-based anodisations,[32,362,371] while using a more benign electrolyte. The film prepared with NH$_4$F/NMF/H$_2$O, used here as a competitive benchmark, showed a higher photocurrent at 1 V *vs.* Ag/AgCl. Accordingly, ABPE values show higher efficiencies below 0.67 V *vs.* Ag/AgCl for CA-anodised samples (Fig. 6-10b). These differences can be ascribed to their different morphology and crystal orientation, observed by FESEM and XRD, which could affect their light absorption, charge transfer efficiency, and amount of surface states. One should note that a higher response at lower onset potential can be advantageous for tandem PEC cells working with little or no applied potentials.
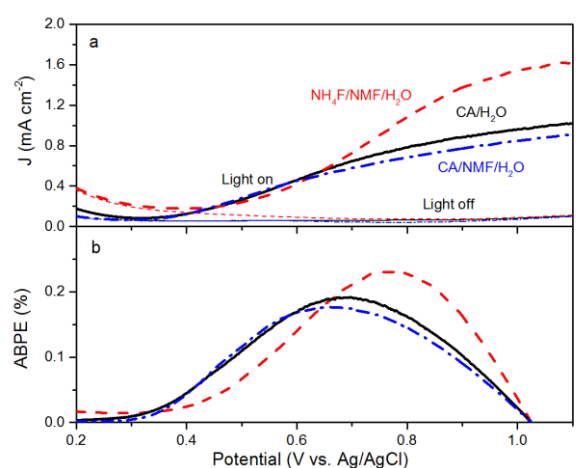


Fig. 6-10 (a) Current densities of WO$_3$ photoanodes in the presence and absence of AM1.5G illumination (100 mW cm$^{-2}$). (b) Calculated ABPE of WO$_3$ electrodes. Electrodes were prepared by anodising tungsten foils in CA/H$_2$O at 0.1 A for 30 min (black solid line), in CA/NMF/H$_2$O at 0.015 A for 30 min (blue dash-dot line), and in NH$_4$F/NMF/H$_2$O at 40 V for 6 h (red dashed line).

The trends from LSV measurements were further confirmed by IPCE measured at 0.55 V and 1 V *vs.* Ag/AgCl (Fig. 6-11a). Photoanodes prepared using CA have similar performance at both conditions and at all wavelengths. When $NH_4F$ was used, the response was not as high as using CA at 0.55 V *vs.* Ag/AgCl, which is consistent with the photocurrent and ABPE results in Fig. 6-10. Tauc plot based on IPCE spectra at 1 V *vs.* Ag/AgCl shows estimated band gaps of about 2.7 eV for all three photoanodes (Fig. 6-11b). It is notable that at 1 V *vs.* Ag/AgCl there is an IPCE maximum between 350 and 420 nm, centred at 375 nm, for $WO_3$ prepared in $NH_4F/NMF/H_2O$. This IPCE maximum is not present at 0.55 V *vs.* Ag/AgCl for the same film. This agrees with and confirms the higher photocurrent density observed in LSV measurements at higher applied potentials.
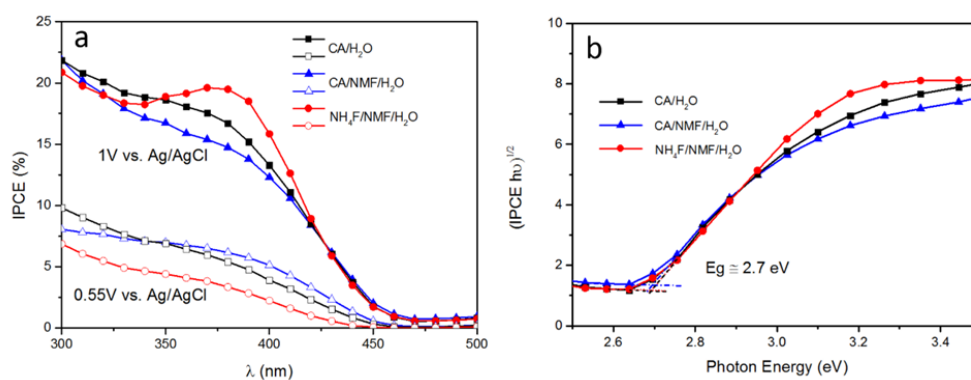


Fig. 6-11 (a) Incident photon-to-current conversion efficiency (IPCE) results for photoanodes subjected to anodisations in $CA/H_2O$ at 0.1 A for 30 min (black squares), in $CA/NMF/H_2O$ at 0.015 A for 30 min (blue triangles), and in $NH_4F/NMF/H_2O$ at 40 V for 6 h (red circles). Filled shapes indicate measurements at an applied bias of 1 V and hollow shapes at 0.55 V *vs.* Ag/AgCl. Both measurements were carried out in 0.5 M $H_2SO_4$. (b) Band gaps for $WO_3$ on all photoanodes are estimated to be ~2.7 eV based on IPCE spectra at 1 V *vs.* Ag/AgCl.

The stability of $WO_3$ photoanodes was tested at 1 V *vs.* Ag/AgCl in 0.5 M $H_2SO_4$ solution for 60 min with 6 min cycles of light chopping (Fig. 6-12). The photoanode anodised in $CA/H_2O$ shows a decay of 0.14 mA cm$^{-2}$ in photocurrent density within the first two cycles, which can be attributed to photoelectrochemical instability caused by corrosion from accumulating holes at electrode–electrolyte interface.[373] After two cycles, the decay slows down and, overall, 69% of its initial stability is retained. For the $CA/NMF/H_2O$ anodised sample, 90% of its initial photoresponse is maintained after the test. We attribute this superior result to its morphology consisting of thin nanowires having a higher photoelectrochemically active surface area (3.8 cm$^2$ *vs.* 1.7

cm$^2$), which is in favour of faster charge transfer. This leads to less accumulation of holes at the semiconductor–liquid junction and thereby higher photoelectrochemical stability.[374] On the other hand, for the sample anodised in NH$_4$F/NMF/H$_2$O, poorer stability is observed. The photocurrent density suffers from gradual decline throughout the amount of time being tested, meaning a low photoelectrochemical stability. In addition, the photocurrent densities cannot reach its previous level after each dark period, which represents poor chemical stability. The photocurrent density is almost halved (53%) after one hour. Therefore, the stability test shows a clear advantage of CA-anodised photoanode over the fluoride-anodised photoanode.
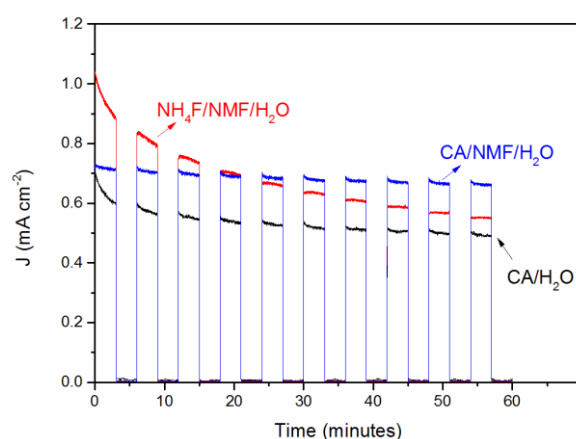


Fig. 6-12 Stability test of WO$_3$ electrodes prepared using CA/H$_2$O at 0.1 A for 30 min (black), in CA/NMF/H$_2$O at 0.015 A for 30 min (blue), and in NH$_4$F/NMF/H$_2$O at 40 V for 6 h (red) at 1 V *vs.* Ag/AgCl in 0.5 M H$_2$SO$_4$ under AM1.5G illumination (100 mW cm$^{-2}$). Light was chopped with 3 min intervals.

The performance of several porous anodic WO$_3$ films is listed in Table 6-1 along with their synthesis and characterisation conditions. The nanowalls/nanorods structures formed here by CA anodisation in aqueous solution bear much resemblance to Ng's work where corrugated nanorods of 450 nm in height were obtained using Na$_2$SO$_4$ and NaF as an electrolyte.[375] Moreover, the reported formation process is similar to that observed herein, which proves the success of CA as an effective electrolyte to replace fluorides. Fluoride-free anodisations have been explored in other works, with the formation of WO$_3$ layers with different morphologies and dimensions. For example, a slow growth of a "nanosponge" was achieved in a 10 wt% K$_2$HPO$_4$/glycerol electrolyte.[336] The thickness was up to 8.7 μm for a long 26 h anodisation. A 7.5 μm film of WO$_3$ nanotubes was reported for 0.2 M NH$_4$NO$_3$/ethylene glycol by Wei *et al.*[363] The plateau photocurrent density under solar

irradiation was 2.5 mA cm$^{-2}$ in the presence of HCOONa as a hole scavenger. More ordered and higher-aspect-ratio nanotubes were also recently formed anodising in molten H$_3$PO$_4$, although no photoresponse was reported.[376] To the best of our knowledge, the present work is the first to report the formation of WO$_3$ nanostructures using CA.

Table 6-1 Properties of photoanodes formed by various anodisation methods$^a$

| Anodising media | Anodising voltage and time | Morphology | Phase | Electrolyte | $J$ (mA cm$^{-2}$) at 1.23$V_{RHE}$ | Onset (V) vs. RHE | Light source and intensity |
|---|---|---|---|---|---|---|---|
| 80 v% NMF/20 v% H$_2$O/0.05 wt% NH$_4$F[10] | 40 V, 6 h | Crispy surface crust | Monoclinic | 1 M H$_2$SO$_4$ | 3.6 | 0.5 | AM1.5, 300 mW cm$^{-2}$ |
| 1.5 M HNO$_3$/40 mg NH$_4$F[24] | 30 V, 4 h | Triple-layered | Monoclinic | 0.5 M Na$_2$SO$_4$ | 0.9 | 0.4 | Xe lamp, 100 mW cm$^{-2}$ |
| 0.1 M NaF[12] | 60 V, 24 h | Mesh-like | Monoclinic | 0.1 M HCl | 0.75 | 0.45 | AM1.5, 100 mW cm$^{-2}$ |
| 1 M Na$_2$SO$_4$/ 0.5 wt% NaF[29] | 50 V, 30 min | Mesh-like | n.d. | 0.5 M H$_2$SO$_4$ | 1.0 | 0.6 | Xe lamp $\lambda$ > 400 nm, 100 mW cm$^{-2}$ |
| 0.1 M Na$_2$SO$_4$/ 0.5 wt% NaF[13] | 50 V, 30 min | Mesh-like | Monoclinic | 0.1 M KH$_2$PO$_4$ + KOH (pH 7) | 0.9 | 0.7 | AM1.5, 100 mW cm$^{-2}$ |
| 0.2 M NH$_4$NO$_3$/ ethylene glycol[14] | 10 V, 35 min | Nanochannel | Monoclinic | 0.5 M Na$_2$SO$_4$ + 0.1 M HCOONa | 2.5 | 0.52 | AM1.5, 100 mW cm$^{-2}$ |
| 0.1 M CA (this work) | 0.1 A 30 min | Nanowalls/ nano-rods | Monoclinic | 0.5 M H$_2$SO$_4$ | 0.88 | 0.5 | AM1.5, 100 mW cm$^{-2}$ |

$^a$ Photocurrent densities and onset potentials listed were approximatively read on figures from references.

## Conclusion

In this work, citric acid (CA) was studied for the anodisation of tungsten foil as an alternative to fluoride-based electrolytes such as NH$_4$F. A systematic investigation of anodisation process parameters (time, currents and solvents) was performed to establish a relation between the obtained morphology and its performance in solar water splitting. We demonstrated, for the first time, that a CA/H$_2$O electrolyte can produce porous canyon-like nanostructure consisting of WO$_3$ nanowalls and nanorods. Using a mixture of CA, H$_2$O and NMF, a different porous nanostructure was obtained consisting of randomly oriented ~50 nm wide WO$_3$nanowires. These morphologies differ from the classic mesh-like porous nanostructures obtained with NH$_4$F as an anodising electrolyte. The performance of these anodised films was tested for photoelectrochemical water splitting using a three-electrode system and simulated sunlight. The CA-anodised films obtained photocurrent densities around 0.8 mA cm$^{-2}$ at 1 V $vs.$ Ag/AgCl in 0.5 M H$_2$SO$_4$. These CA-anodised films outperformed NH$_4$F-anodised films at low applied potentials (below 0.67 V $vs.$ Ag/AgCl) and showed much better photoelectrochemical stability. As such, CA represents a safer and more environmentally friendly alternative to fluoride-based electrolytes for the production of nanostructured WO$_3$ photoanodes with comparable or superior performance. This

work also opens an avenue for sustainable anodisation procedures for the production of other nanostructured metal oxides as photoelectrodes using CA.

**Acknowledgements**

**Data Access Statement**

All data created during this research are openly available from the University of Bath data archive at https://doi.org/10.15125/BATH-00418

### 6.2.5 Commentary

*Thickness of the nanoporous layer*

In the manuscript, we stated that the nanostructured valleys are around 500 nm deep without giving evidence. The relevant SEM images are presented inFig. 6-13. These valleys can also take the form of "Christmas trees".
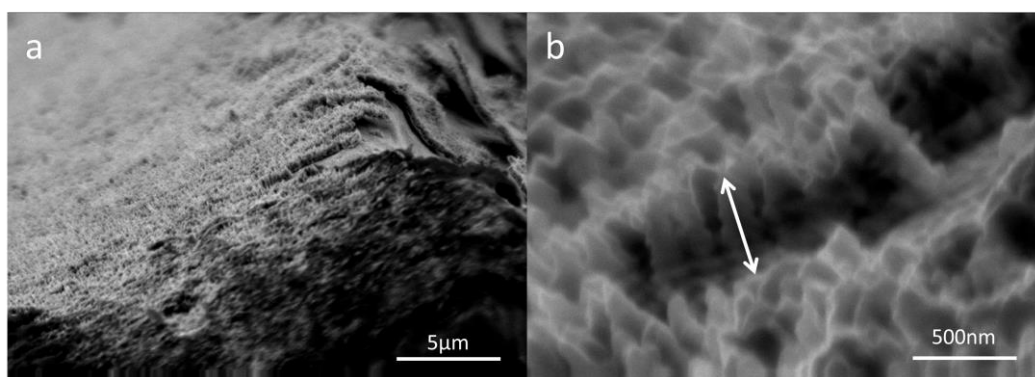


Fig. 6-13 SEM images of the nanostructures of a $WO_3$ photoanode fabricated in $CA/H_2O$ with low (a) and high (b) magnifications.

*Optical absorption profile comparison*

In Fig. 6-8 of the manuscript, three electrodes showed different UV-visible absorption profiles. The $NH_4F$-anodized samples showed a much higher platform in visible region than CA-anodized counterparts. We attributed it to unintentional F doping that originated from surface residual fluoride ions that diffuse into $WO_3$ bulk upon calcination. This kind of behavior is typically a result of formation intragap states after F substitution of O sites. The effect is intensified with higher F concentration as observed by Fang et al.[377]
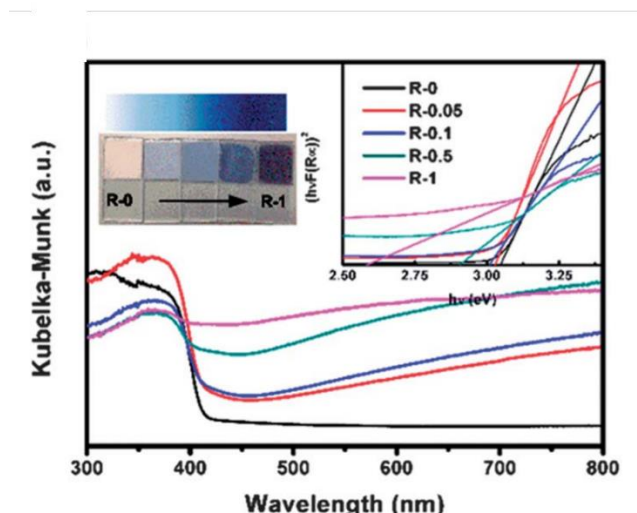
Fig. 6-14 UV-visible absorption of F-doped $TiO_2$ photocatalysts with different F:Ti molar ratios of reaction precursors.[377] Reproduced from ref. [377] with permission from The Royal Society of Chemistry.

*Choosing the optimal anodization conditions*

In this work, we have optimized the anodization conditions in CA electrolyte with and without adding NMF. From Fig. 6-9 we can see that photocurrent stayed high for a wide window of applied current at anodization in $CA/H_2O$ electrolyte. Here we selected the middle point 0.1 A as standard condition for further research. On the other hand, a clear peak exists in the case of $CA/NMF/H_2O$, which means it is less advantaged for industrialized production. However, considering that the stability of $CA/NMF/H_2O$ was apparently superior, which method is more appropriate does not seem to have a straight answer.

*Stability of WO$_3$ photoanodes*

The stabilities of the photoanodes studied in this work is worth some further investigation. In Fig. 6-12 of the article, the $NH_4F/NMF/H_2O$ sample shows the poorest stability over 1 h with intermittent illumination. We have pointed out that the photocurrent drops even during the dark periods, meaning poor chemical stability. The most probable cause is that the residual F ions at the electrodes forms HF again with $H^+$ in the PEC cell (0.5 M $H_2SO_4$ electrolyte) during the chronoamperometry measurement and keeps etching $WO_3$ akin to the oxide dissolution process during anodization. In contrast, $CA/NMF/H_2O$ and $CA/H_2O$ samples do not present chemical instability.

Interestingly, the stability of CA/NMF/H$_2$O is also superior than CA/H$_2$O sample photoelectrochemically, which can be ascribed to photocorrosion. Several papers have indicated that W$^{5+}$ are more resistant to photocorrosion by peroxo-intermediates formed during water oxidation.[378,379] Considering that formamide (NMF) is a reducing agent,[380] it is likely that the CA/NMF/H$_2$O sample possesses more W$^{5+}$ states. The suggestion that the better stability is associated with morphology, on a hindsight, seems to be much less likely.

*Practicality of WO$_3$ as photoanode material*

Several groups have thoroughly summarized the synthesis of WO$_3$ by all these methods mentioned above.[332,345] The performance of bare WO$_3$ photoanodes has not seemed to advance significantly in recent years; however, WO$_3$ has become a popular choice to be integrated in a complex photoanode. In particular, coupling with BiVO$_4$ alone has resulted in a number of reports and even a review article.[381] The performance of the heterostructure WO$_3$/BiVO$_4$ has increased substantially in a few years from about 0.1 to 6.72 mA cm$^{-2}$ at 1.23 V$_{RHE}$.[51,382,383] Many other works have also reported photocurrent densities above 5 mA cm$^{-2}$ at the same potential.[384,385] According to Shi et al., charge separation was improved not only by establishment of heterojunction, but also by diffusion of W into BiVO$_4$.[51] It should be noted that when coupled with a lower band gap semiconductor (e.g., Fe$_2$O$_3$), WO$_3$ is usually used as the host despite its shorter absorption length due to its good electronic properties and to establish favorable band alignment.[243] In short, the expectation of WO$_3$ as independent photoanode is low but it is a good candidate to supplement other materials.

# Chapter 7 Conclusion and Outlook

This PhD work has investigated multiple aspects of metal oxide photoanodes for solar water splitting, mainly using hematite as an example. Firstly, an in-depth literature survey was carried out to reveal how similarly and differently n-type doping and oxygen vacancy elimination affect the photoresponse of hematite. We also revealed the identity of one important type of surface states and how they interact with two types of photo-generated charges. This work bridged the gap between the major subdivisions of PEC research on hematite. It also opened the door to understanding the influences of defects on both bulk and surface properties of semiconductors.

Some valuable outcomes are obtained from two experimental works on hematite photoanodes. In the first, interaction between an efficient oxygen evolution catalyst $CoFeO_x$ and hematite photoanodes populated with high concentration of surface states was investigated. Although it has been widely observed that co-catalysts such as CoPi reduces surface charge recombination to facilitate photocurrent at lower potentials, we found evidence that charge transfer can indeed be accelerated. We also argued that the co-catalyst layer thickness must be carefully controlled to avoid parasitic redox reaction by photo-generated holes. In the second, we discovered a facile method of making surface-modified hematite photoanodes. Here, lactic acid dramatically increased the electrochemically active surface area and led to the formation of a very thin amorphous iron oxide ($FeO_x$) coating, although the causes remained unclear. According to PEC characterizations, the main role of this $FeO_x$ coating was to raise the surface hole flux by enlarging surface area, while reducing both the charge transfer and charge recombination rate. These two studies have pointed out the intricate roles of surface modification layers. Further research on surface reaction kinetics remain worthwhile. Additionally, we fabricated on nanostructured $WO_3$ photoanodes by anodization in citric acid. The resulting photoactivity was comparable with state-of-the-art anodized $WO_3$ electrodes, while showing superior stability.

At present, the power conversion efficiencies of these two oxides appear to be rather low. As an independently operating photoanode, $WO_3$ does not appear to have promise to achieve high photocurrents. Integration with other photoanode materials such as $BiVO_4$ consequently has become more common and will remain to be of interest in the future. The major setbacks for hematite, on the other hand, are its short

diffusion length and poor surface reaction kinetics. The history of PEC research of hematite has witnessed significant improvements in its onset potential achieved by various surface treatment methodologies, but far less effort has been put into improving the mobility and lifetime of minority charge carriers in the bulk, which in my opinion is the essence of limited performance.

For PEC water splitting, the record setting devices, as well as those with solar-to-hydrogen efficiencies over 10%, have been almost exclusively using PV materials such as II-VI and III-V semiconductors. This is most likely because diffusion lengths of these materials are orders of magnitude higher than many binary oxides ($\mu$m vs. nm). Therefore, before PV materials find a way to overcome its stability problem, I believe it is well worth exploring the world of multinary oxides in search of candidates with long minority carrier diffusion lengths.

# References

1       J. A. Herron, J. Kim, A. A. Upadhye, G. W. Huber and C. T. Maravelias, *Energy Environ. Sci.*, 2014, **8**, 126–157.

2       R. Wurster and W. Zittel, Hydrogen Energy, Energy technologies to reduce CO2 emissions in Europe: prospects, competition, synergy, Energieonderzoek Centrum Nederland ECN, Petten, April 11-12, 1994.

3       Solar Fuels, http://nsl.caltech.edu/home/solar-fuels/, (accessed 20 November 2018).

4       R. V. de Krol and M. Gratzel, *Photoelectrochemical Hydrogen Production*, Springer, 2012.

5       B. Kumar, M. Llorente, J. Froehlich, T. Dang, A. Sathrum and C. P. Kubiak, *Annu. Rev. Phys. Chem.*, 2012, **63**, 541–569.

6       H.-J. Lewrenz and L. Peter, *Photoelectrochemical Water Splitting: Materials, Processes and Arhitectures*, RSC Publishing, 2013.

7       C.-H. Yu, C.-H. Huang and C.-S. Tan, *Aerosol Air Qual Res*, 2012, **12**, 745–769.

8       M. Pagliaro and A. G. Konstandopoulos, *Solar Hydrogen*, 2012.

9       J. Dufour, D. P. Serrano, J. L. Gálvez, J. Moreno and C. García, *Int. J. Hydrog. Energy*, 2009, **34**, 1370–1376.

10      K. L. Lim, H. Kazemian, Z. Yaakob and W. R. W. Daud, *Chem. Eng. Technol.*, 2010, **33**, 213–226.

11      H. L. Tuller, *Mater. Renew. Sustain. Energy*, 2017, **6**, 1–16.

12      M. R. Shaner, H. A. Atwater, N. S. Lewis and E. W. McFarland, *Energy Environ. Sci.*, 2016, **9**, 2354–2371.

13      J. Jia, L. C. Seitz, J. D. Benck, Y. Huo, Y. Chen, J. W. D. Ng, T. Bilir, J. S. Harris and T. F. Jaramillo, *Nat. Commun.*, 2016, **7**, 13237.

14      Y. Chen, K. Sun, H. Audesirk, C. Xiang and N. S. Lewis, *Energy Environ. Sci.*, 2015, **8**, 1736–1747.

15      O. Khaselev and J. A. Turner, *Science*, 1998, **280**, 425–427.

16      M. S. Prevot and K. Sivula, *J. Phys. Chem. C*, 2013, **117**, 17879–17893.

17      A. Rothschild and H. Dotan, *ACS Energy Lett.*, 2017, **2**, 45–51.

18      J. R. Bolton, S. J. Strickler and J. S. Connolly, *Nature*, 1985, **316**, 495–500.

19      J. H. Kim, J.-W. Jang, Y. H. Jo, F. F. Abdi, Y. H. Lee, R. van de Krol and J. S. Lee, *Nat. Commun.*, 2016, **7**, 13380.

20      H. M. Fan, G. J. You, Y. Li, Z. Zheng, H. R. Tan, Z. X. Shen, S. H. Tang and Y. P. Feng, *J. Phys. Chem. C*, 2009, **113**, 9928–9935.

21      N. J. Cherepy, D. B. Liston, J. A. Lovejoy, H. Deng and J. Z. Zhang, *J. Phys. Chem. B*, 1998, **102**, 770–776.

22      Z. Zhou, J. Liu, R. Long, L. Li, L. Guo and O. V. Prezhdo, *J. Am. Chem. Soc.*, 2017, **139**, 6707–6717.

23      P. Salvador, *J. Appl. Phys.*, 1984, **55**, 2977–2985.

24      S. J. A. Moniz, S. A. Shevlin, D. J. Martin, Z. Guo and J. Tang, *Energy Env. Sci*, 2015, **8**, 731–759.

25      M. G. Walter, E. L. Warren, J. R. McKone, S. W. Boettcher, Q. Mi, E. A. Santori and N. S. Lewis, *Chem. Rev.*, 2010, **110**, 6446–6473.

26      W. W. Gärtner, *Phys. Rev.*, 1959, **116**, 84.

27      Z. Zhang and J. T. Yates, *Chem. Rev.*, 2012, **112**, 5520–5551.

28      R. Peat and L. M. Peter, *Appl. Phys. Lett.*, 1987, **51**, 328–330.

29    Z. Chen, H. N. Dinh and E. Miller, *Photoelectrochemical water splitting: standards, experimental methods, and protocols*, Springer, New York, 2013.

30    S. Kment, F. Riboni, S. Pausova, L. Wang, L. Wang, H. Han, Z. Hubicka, J. Krysa, P. Schmuki and R. Zboril, *Chem Soc Rev*, 2017, **46**, 3716–3769.

31    L. M. Peter, Gurudayal, L. H. Wong and F. F. Abdi, *J. Electroanal. Chem.*, 2018, **819**, 447–458.

32    K. R. Reyes-Gil, C. Wiggenhorn, B. S. Brunschwig and N. S. Lewis, *J. Phys. Chem. C*, 2013, **117**, 14947–14957.

33    D. A. Grave, N. Yatom, D. S. Ellis, M. C. Toroker and A. Rothschild, *Adv. Mater.*, 2018, **1706577**, 1–10.

34    A. Fujishima and K. Honda, *Nature*, 1972, **238**, 37–38.

35    S. K. Mohapatra, M. Misra, V. K. Mahajan and K. S. Raja, *J. Phys. Chem. C*, 2007, **111**, 8677–8685.

36    M. M. Momeni and Y. Ghayeb, *J. Alloys Compd.*, 2015, **637**, 393–400.

37    K. G. Upul Wijayantha, S. Saremi-Yarahmadi and L. M. Peter, *Phys. Chem. Chem. Phys.*, 2011, **13**, 5264–5270.

38    Y. Ling, G. Wang, D. A. Wheeler, J. Z. Zhang and Y. Li, *Nano Lett.*, 2011, **11**, 2119–2125.

39    K. Sivula, R. Zboril, F. Le Formal, R. Robert, A. Weidenkaff, J. Tucek, J. Frydrych and M. Grätzel, *J. Am. Chem. Soc.*, 2010, **132**, 7436–7444.

40    X. Chen, M. Wang, J. Chen and S. Shen, *J. Mater. Res.*, 2016, **31**, 1547–1553.

41    S. Li, J. Cai, Y. Mei, Y. Ren and G. Qin, *Int. J. Photoenergy*, 2014, **2014**, 794370.

42    P. Liao, M. C. Toroker and E. A. Carter, *Nano Lett.*, 2011, **11**, 1775–1781.

43    J. Deng, X. Lv, K. Nie, X. Lv, X. Sun and J. Zhong, *ACS Catal.*, 2017, **7**, 4062–4069.

44    Y. Lin, Y. Xu, M. T. Mayer, Z. I. Simpson, G. McMahon, S. Zhou and D. Wang, *J. Am. Chem. Soc.*, 2012, **134**, 5508–5511.

45    H. Li, Y. Yu, M. B. Starr, Z. Li and X. Wang, *J. Phys. Chem. Lett.*, 2015, **6**, 3410–3416.

46    W. Yang, Y. Yu, M. B. Starr, X. Yin, Z. Li, A. Kvit, S. Wang, P. Zhao and X. Wang, *Nano Lett.*, 2015, **15**, 7574–7580.

47    A. Tsyganok, D. Klotz, K. D. Malviya, A. Rothschild and D. A. Grave, *ACS Catal.*, 2018, **8**, 2754–2759.

48    S. K. Choi, G. Piao, W. Choi and H. Park, *Appl. Catal. B Environ.*, 2017, **217**, 615–621.

49    S. Hu, M. R. Shaner, J. A. Beardslee, M. Lichterman, B. S. Brunschwig and N. S. Lewis, *Science*, 2014, **344**, 1005–1009.

50    L. Wu, L. Tsui, N. Swami and G. Zangari, *J. Phys. Chem. C*, 2010, **114**, 11551–11556.

51    X. Shi, I. Y. Choi, K. Zhang, J. Kwon, D. Y. Kim, J. K. Lee, S. H. Oh, J. K. Kim and J. H. Park, *Nat. Commun.*, 2014, **5**, 4775.

52    Y. Nakato, H. Yano, S. Nishiura, T. Ueda and H. Tsubomura, *J. Electroanal. Chem. Interfacial Electrochem.*, 1987, **228**, 97–108.

53    R. N. Dominey, N. S. Lewis, J. A. Bruce, D. C. Bookbinder and M. S. Wrighton, *J. Am. Chem. Soc.*, 1982, **104**, 467–482.

54    R. Fan, W. Dong, L. Fang, F. Zheng and M. Shen, *J. Mater. Chem. A*, 2017, **5**, 18744–18751.

55    L. M. Peter, A. M. Borazio, H. J. Lewerenz and J. Stumper, *J. Electroanal. Chem. Interfacial Electrochem.*, 1990, **290**, 229–248.

56      H. J. Lewerenz, J. Stumper and L. M. Peter, *Phys. Rev. Lett.*, 1988, **61**, 1989–1992.

57      R. Fan, J. Mao, Z. Yin, J. Jie, W. Dong, L. Fang, F. Zheng and M. Shen, *ACS Appl. Mater. Interfaces*, 2017, **9**, 6123–6129.

58      W.-H. Cheng, M. H. Richter, M. M. May, J. Ohlmann, D. Lackner, F. Dimroth, T. Hannappel, H. A. Atwater and H.-J. Lewerenz, *ACS Energy Lett.*, 2018, **3**, 1795–1800.

59      E. Verlage, S. Hu, R. Liu, R. J. R. Jones, K. Sun, C. Xiang, N. S. Lewis and H. A. Atwater, *Energy Environ. Sci.*, 2015, **8**, 3166–3172.

60      T. J. Jacobsson, C. Platzer-Björkman, M. Edoff and T. Edvinsson, *Int. J. Hydrog. Energy*, 2013, **38**, 15027–15035.

61      Y. F. Tay, H. Kaneko, S. Y. Chiam, S. Lie, Q. Zheng, B. Wu, S. S. Hadke, Z. Su, P. S. Bassi, D. Bishop, T. C. Sum, T. Minegishi, J. Barber, K. Domen and L. H. Wong, *Joule*, 2018, **2**, 537–548.

62      Y.-J. Oh, G.-S. Park and C.-H. Chung, *J. Electrochem. Soc.*, 2006, **153**, G617.

63      A. Paracchino, V. Laporte, K. Sivula, M. Grätzel and E. Thimsen, *Nat. Mater.*, 2011, **10**, 456–461.

64      J. W. Schultze and M. M. Lohrengel, *Electrochimica Acta*, 2000, **45**, 2499–2513.

65      R. Wick and S. D. Tilley, *J. Phys. Chem. C*, 2015, **119**, 26243–26257.

66      W. Niu, T. Moehl, W. Cui, R. Wick-Joliat, L. Zhu and S. D. Tilley, *Adv. Energy Mater.*, 2018, **8**, 1702323.

67      G. Hodes, D. Cahen and J. Manassen, *Nature*, 1976, **260**, 312–313.

68      Z. Zhao, Z. Li and Z. Zou, *Phys. Chem. Chem. Phys.*, 2011, **13**, 4746–4753.

69      F. F. Abdi, T. J. Savenije, M. M. May, B. Dam and R. van de Krol, *J. Phys. Chem. Lett.*, 2013, **4**, 2752–2757.

70      H. S. Han, S. Shin, D. H. Kim, I. J. Park, J. S. Kim, P.-S. Huang, J.-K. Lee, I. S. Cho and X. Zheng, *Energy Environ. Sci.*, 2018, **11**, 1299–1306.

71      Y. Ma, S. R. Pendlebury, A. Reynal, F. le Formal and J. R. Durrant, *Chem. Sci.*, 2014, **5**, 2964–2973.

72      C. Zachäus, F. F. Abdi, L. M. Peter and R. van de Krol, *Chem Sci*, 2017, **8**, 3712–3719.

73      E. A. Mohamed, Z. N. Zahran and Y. Naruta, *J. Mater. Chem. A*, 2017, **5**, 6825–6831.

74      N. Guijarro, P. Bornoz, M. Prévot, X. Yu, X. Zhu, M. Johnson, X. Jeanbourquin, F. Le Formal and K. Sivula, *Sustain. Energy Fuels*, 2018, **2**, 103–117.

75      X. Zhu, N. Guijarro, Y. Liu, P. Schouwink, R. A. Wells, F. Le Formal, S. Sun, C. Gao and K. Sivula, *Adv. Mater.*, 2018, **30**, 1801612.

76      O. Zandi and T. W. Hamann, *J. Phys. Chem. Lett.*, 2014, **5**, 1522–1526.

77      J. Deng, X. Lv, J. Liu, H. Zhang, K. Nie, C. Hong, J. Wang, X. Sun, J. Zhong and S.-T. Lee, *ACS Nano*, 2015, **9**, 5348–5356.

78      M. Osada, K. Nishio, H. Y. Hwang and Y. Hikita, *APL Mater.*, 2018, **6**, 056101.

79      Q. Liu, J. He, T. Yao, Z. Sun, W. Cheng, S. He, Y. Xie, Y. Peng, H. Cheng, Y. Sun, Y. Jiang, F. Hu, Z. Xie, W. Yan, Z. Pan, Z. Wu and S. Wei, *Nat. Commun.*, 2014, **5**, 5122.

80      Y. He, J. E. Thorne, C. H. Wu, P. Ma, C. Du, Q. Dong, J. Guo and D. Wang, *Chem*, 2016, **1**, 640–655.

81      G. Liu, S. Ye, P. Yan, F. Xiong, P. Fu, Z. Wang, Z. Chen, J. Shi and C. Li, *Energy Environ. Sci.*, 2016, **9**, 1327–1334.

82      Y. He, P. Ma, S. Zhu, M. Liu, Q. Dong, J. Espano, X. Yao and D. Wang, *Joule*, 2017, **1**, 831–842.

83      L. M. Peter, *J. Solid State Electrochem.*, 2013, **17**, 315–326.

84      L. Liu, Z. Mei, A. Tang, A. Azarov, A. Kuznetsov, Q.-K. Xue and X. Du, *Phys. Rev. B*, 2016, **93**, 235305.

85      S. Giménez and J. Bisquert, *Photoelectrochemical solar fuel production: From basic principles to advanced devices*, Springer, 2016.

86      S. M. Sze and K. K. Ng, *Physics of semiconductor devices*, Wiley-Interscience, Hoboken, N.J, 3rd ed., 2007.

87      R. A. Marcus, *J. Chem. Phys.*, 1956, **24**, 966–978.

88      R. A. Marcus, *Annu. Rev. Phys. Chem.*, 1964, **15**, 155–196.

89      H.-J. Lewerenz and L. Peter, Eds., *Photoelectrochemical Water Splitting: Materials, Processes and Architectures*, Royal Society of Chemistry, Cambridge, 2013.

90      R. G. Compton and G. Hancock, Eds., *Comprehensive Chemical Kinetics Vol. 37*, Elsevier Pub. Co, Amsterdam, New York, 1969.

91      J. Reichman, *Appl. Phys. Lett.*, 1980, **36**, 574–577.

92      L. M. Peter, J. Li and R. Peat, *J. Electroanal. Chem.*, 1984, **165**, 29–40.

93      P. Cendula, S. D. Tilley, S. Gimenez, J. Bisquert, M. Schmid, M. Grätzel and J. O. Schumacher, *J. Phys. Chem. C*, 2014, **118**, 29599–29607.

94      D. Klotz, D. A. Grave and A. Rothschild, *Phys. Chem. Chem. Phys.*, 2017, **19**, 20383–20392.

95      D. Klotz, D. S. Ellis, H. Dotan and A. Rothschild, *Phys. Chem. Chem. Phys.*, 2016, **18**, 23438–23457.

96      E. Barsoukov and J. R. Macdonald, Eds., *Impedance spectroscopy: theory, experiment, and applications*, Wiley-Interscience, Hoboken, N.J, 2nd ed., 2005.

97      J. Bisquert, M. Grätzel, Q. Wang and F. Fabregat-Santiago, *J. Phys. Chem. B*, 2006, **110**, 11284–11290.

98      B. Klahr, S. Gimenez, F. Fabregat-Santiago, T. Hamann and J. Bisquert, *J. Am. Chem. Soc.*, 2012, **134**, 4294–4302.

99      R. Franking, L. Li, M. A. Lukowski, F. Meng, Y. Tan, R. J. Hamers and S. Jin, *Energy Environ. Sci.*, 2013, **6**, 500–512.

100     O. Zandi and T. W. Hamann, *Nat. Chem.*, 2016, **8**, 778–783.

101     R. Peat and L. M. Peter, *J. Electroanal. Chem. Interfacial Electrochem.*, 1987, **228**, 351–364.

102     J. Li and L. M. Peter, *J. Electroanal. Chem. Interfacial Electrochem.*, 1985, **193**, 27–47.

103     E. A. Ponomarev and L. M. Peter, *J. Electroanal. Chem.*, 1995, **396**, 219–226.

104     J. Schefold, *J. Electroanal. Chem.*, 1992, **341**, 111–136.

105     R. M. Cornell and U. Schwertmann, *The iron oxides: structure, properties, reactions, occurences and uses*, Wiley-VCH, Weinheim, 2003.

106     A. Murphy, P. Barnes, L. Randeniya, I. Plumb, I. Grey, M. Horne and J. Glasscock, *Int. J. Hydrog. Energy*, 2006, **31**, 1999–2017.

107     L. A. Marusak, R. Messier and W. B. White, *J. Phys. Chem. Solids*, 1980, **41**, 981–984.

108     J. Brillet, M. Grätzel and K. Sivula, *Nano Lett.*, 2010, **10**, 4155–4160.

109     A. Kay, D. A. Grave, K. Deo Malviya, D. S. Ellis, H. Dotan and A. Rothschild, *J. Phys. Chem. C*, 2017, **121**, 28287–28292.

110     B. Warnes, F. Aplan and G. Simkovich, *Solid State Ion.*, 1984, **12**, 271–276.

111    M. Barroso, S. R. Pendlebury, A. J. Cowan and J. R. Durrant, *Chem. Sci.*, 2013, **4**, 2724–2734.

112    K. Sivula and R. Van De Krol, *Nat. Rev. Mater.*, 2016, **1**, 15010.

113    A. G. Tamirat, J. Rick, A. A. Dubale, W.-N. Su and B.-J. Hwang, *Nanoscale Horiz.*, 2016, **1**, 243–267.

114    S. Shen, S. A. Lindley, X. Chen and J. Z. Zhang, *Energy Environ. Sci.*, 2016, **9**, 2744–2775.

115    J.-C. Chou, S.-A. Lin, C.-Y. Lee and J.-Y. Gan, *J. Mater. Chem. A*, 2013, **1**, 5908–5914.

116    X. Zhao, J. Feng, S. Chen, Y. Huang, T. C. Sum and Z. Chen, *Phys. Chem. Chem. Phys.*, 2017, **19**, 1074–1082.

117    J. Y. Zheng, M. J. Kang, G. Song, S. I. Son, S. P. Suh, C. W. Kim and Y. S. Kang, *CrystEngComm*, 2012, **14**, 6957–6961.

118    L. Fu, H. Yu, Y. Li, C. Zhang, X. Wang, Z. Shao and B. Yi, *Phys. Chem. Chem. Phys.*, 2014, **16**, 4284–4290.

119    R. H. Gonçalves, B. H. R. Lima and E. R. Leite, *J. Am. Chem. Soc.*, 2011, **133**, 6012–6019.

120    J. Y. Kim, G. Magesh, D. H. Youn, J. W. Jang, J. Kubota, K. Domen and J. S. Lee, *Sci. Rep.*, 2013, **3**, 2681.

121    S. K. Mohapatra, S. E. John, S. Banerjee and M. Misra, *Chem. Mater.*, 2009, **21**, 3048–3055.

122    P. Peerakiatkhajohn, J.-H. Yun, H. Chen, M. Lyu, T. Butburee and L. Wang, *Adv. Mater.*, 2016, **28**, 6405–6410.

123    S. D. Tilley, M. Cornuz, K. Sivula and M. Gr??tzel, *Angew. Chem. - Int. Ed.*, 2010, **49**, 6405–6408.

124    L. Li, H. Zhang, C. Liu, P. Liang, N. Mitsuzaki and Z. Chen, *J. Photochem. Photobiol. Chem.*, 2019, **369**, 8–15.

125    S. C. Warren, K. Voïtchovsky, H. Dotan, C. M. Leroy, M. Cornuz, F. Stellacci, C. Hébert, A. Rothschild and M. Grätzel, *Nat. Mater.*, 2013, **12**, 842–849.

126    L. Vayssieres, N. Beermann, S.-E. Lindquist and A. Hagfeldt, *Chem. Mater.*, 2001, **13**, 233–235.

127    J. K. Nørskov, J. Rossmeisl, A. Logadottir, L. Lindqvist, J. R. Kitchin, T. Bligaard and H. Jónsson, *J. Phys. Chem. B*, 2004, **108**, 17886–17892.

128    J. O. Bockris and T. Otagawa, *J. Electrochem. Soc.*, 1984, **131**, 290.

129    M. C. Toroker, *J. Phys. Chem. C*, 2014, **118**, 23162–23167.

130    P. Liao, J. A. Keith and E. A. Carter, *J. Am. Chem. Soc.*, 2012, **134**, 13296–13309.

131    J. Rossmeisl, Z.-W. Qu, H. Zhu, G.-J. Kroes and J. K. Nørskov, *J. Electroanal. Chem.*, 2007, **607**, 83–89.

132    X. Zhang, P. Klaver, R. Van Santen, M. C. M. Van De Sanden and A. Bieberle-Hütter, *J. Phys. Chem. C*, 2016, **120**, 18201–18208.

133    C. Y. Cummings, F. Marken, L. M. Peter, K. G. Upul Wijayantha and A. A. Tahir, *J. Am. Chem. Soc.*, 2012, **134**, 1228–1234.

134    B. M. Hunter, N. B. Thompson, A. M. Müller, G. R. Rossman, M. G. Hill, J. R. Winkler and H. B. Gray, *Joule*, 2018, **2**, 747–763.

135    Z. Wang, F. Fan, S. Wang, C. Ding, Y. Zhao and C. Li, *RSC Adv*, 2016, **6**, 85582–85586.

136    N. Iordanova, M. Dupuis and K. M. Rosso, *J. Chem. Phys.*, 2005, **122**, 144305.

137    D. A. Grave, D. Klotz, A. Kay, H. Dotan, B. Gupta, I. Visoly-Fisher and A. Rothschild, *J. Phys. Chem. C*, 2016, **120**, 28961–28970.

138    H. Srivastava, P. Tiwari, A. K. Srivastava, S. Rai, T. Ganguli and S. K. Deb, *Appl. Surf. Sci.*, 2011, **258**, 494–500.

139    I. Cesar, K. Sivula, A. Kay, R. Zboril and M. Grätzel, *J. Phys. Chem. C*, 2009, **113**, 772–782.

140    Gurudayal, L. M. Peter, L. H. Wong and F. F. Abdi, *ACS Appl. Mater. Interfaces*, 2017, **9**, 41265–41272.

141    J. W. Jang, C. Du, Y. Ye, Y. Lin, X. Yao, J. Thorne, E. Liu, G. McMahon, J. Zhu, A. Javey, J. Guo and D. Wang, *Nat. Commun.*, 2015, **6**, 7447.

142    T. Chao, Y. Hu, X. Hong and Y. Li, *ChemElectroChem*, 2018, **5**, 1–16.

143    A. Wang, J. Li and T. Zhang, *Nat. Rev. Chem.*, 2018, **2**, 65–81.

144    B. M. Hunter, H. B. Gray and A. M. Müller, *Chem. Rev.*, 2016, **116**, 14120–14136.

145    C. C. L. McCrory, S. Jung, J. C. Peters and T. F. Jaramillo, *J. Am. Chem. Soc.*, 2013, **135**, 16977–16987.

146    J. Li, Z. Zhao, Y. Ma and Y. Qu, *ChemCatChem*, 2017, **9**, 1554–1568.

147    J. D. Blakemore, R. H. Crabtree and G. W. Brudvig, *Chem. Rev.*, 2015, **115**, 12974–13005.

148    M. Zhang, M. De Respinis and H. Frei, *Nat. Chem.*, 2014, **6**, 362–367.

149    M. W. Kanan and D. G. Nocera, *Science*, 2008, **321**, 1072–1075.

150    W. Luo, C. Jiang, Y. Li, S. A. Shevlin, X. Han, K. Qiu, Y. Cheng, Z. Guo, W. Huang and J. Tang, *J. Mater. Chem. A*, 2017, **5**, 2021–2028.

151    M. S. Burke, M. G. Kast, L. Trotochaud, A. M. Smith and S. W. Boettcher, *J. Am. Chem. Soc.*, 2015, **137**, 3638–3648.

152    M. D. Merrill and R. C. Dougherty, *J. Phys. Chem. C*, 2008, **112**, 3655–3666.

153    C. G. Morales-Guio, L. Liardet and X. Hu, *J. Am. Chem. Soc.*, 2016, **138**, 8946–8957.

154    C. G. Morales-Guio, M. T. Mayer, A. Yella, S. D. Tilley, M. Grätzel and X. Hu, *J. Am. Chem. Soc.*, 2015, **137**, 9927–9936.

155    G. M. Carroll and D. R. Gamelin, *J. Mater. Chem. A*, 2016, **4**, 2986–2994.

156    M. Barroso, A. J. Cowan, S. R. Pendlebury, M. Grätzel, D. R. Klug and J. R. Durrant, *J. Am. Chem. Soc.*, 2011, **133**, 14868–14871.

157    M. Barroso, C. a Mesa, S. R. Pendlebury, A. J. Cowan, T. Hisatomi and K. Sivula, *PNAS*, 2012, **109**, 15640–15645.

158    B. Klahr, S. Gimenez, F. Fabregat-Santiago, J. Bisquert and T. W. Hamann, *J. Am. Chem. Soc.*, 2012, **134**, 16693–16700.

159    J. Qiu, H. Hajibabaei, M. R. Nellist, F. A. L. Laskowski, T. W. Hamann and S. W. Boettcher, *ACS Cent. Sci.*, 2017, **3**, 1015–1025.

160    G. M. Carroll, D. K. Zhong and D. R. Gamelin, *Energy Environ. Sci.*, 2015, **8**, 577–584.

161    L. Steier, I. Herraiz-Cardona, S. Gimenez, F. Fabregat-Santiago, J. Bisquert, S. D. Tilley and M. Grätzel, *Adv. Funct. Mater.*, 2014, **24**, 7681–7688.

162    K. Ulman, M.-T. Nguyen, N. Seriani, S. Piccinin and R. Gebauer, *ACS Catal.*, 2017, **7**, 1793–1804.

163    F. Le Formal, N. Tétreault, M. Cornuz, T. Moehl, M. Grätzel and K. Sivula, *Chem Sci*, 2011, **2**, 737–743.

164    M. Barroso, S. R. Pendlebury, A. J. Cowan and J. R. Durrant, *Chem. Sci.*, 2013, **4**, 2724–2734.

165    G. M. Carroll and D. R. Gamelin, *J. Mater. Chem. A*, 2016, **4**, 2986–2994.

166    Gurudayal, L. M. Peter, L. H. Wong and F. F. Abdi, *ACS Appl. Mater. Interfaces*, 2017, **9**, 41265–41272.

167     D. A. Grave, N. Yatom, D. S. Ellis, M. C. Toroker and A. Rothschild, *Adv. Mater.*, 2018, **1706577**, 1–10.

168     P. Liao, M. C. Toroker and E. A. Carter, *Nano Lett.*, 2011, **11**, 1775–1781.

169     R. F. G. Gardner, R. L. Moss and D. W. Tanner, *Br. J. Appl. Phys.*, 1966, **17**, 55–61.

170     D. Monllor-Satoca, M. Bärtsch, C. Fàbrega, A. Genç, S. Reinhard, T. Andreu, J. Arbiol, M. Niederberger and J. R. Morante, *Energy Environ. Sci.*, 2015, **8**, 3242–3254.

171     Y. Lin, Y. Xu, M. T. Mayer, Z. I. Simpson, G. McMahon, S. Zhou and D. Wang, *J. Am. Chem. Soc.*, 2012, **134**, 5508–5511.

172     X. Zhao, J. Feng, S. Chen, Y. Huang, T. C. Sum and Z. Chen, *Phys. Chem. Chem. Phys.*, 2017, **19**, 1074–1082.

173     Z. Wang, G. Liu, C. Ding, Z. Chen, F. Zhang, J. Shi and C. Li, *J. Phys. Chem. C*, 2015, **119**, 19607–19612.

174     J. Zhang, R. García-Rodríguez, P. Cameron and S. Eslava, *Energy Environ. Sci.*, , DOI:10.1039/C8EE01346B.

175     C. Zachäus, F. F. Abdi, L. M. Peter and R. van de Krol, *Chem Sci*, 2017, **8**, 3712–3719.

176     A. Pu, J. Deng, M. Li, J. Gao, H. Zhang, Y. Hao, J. Zhong and X. Sun, *J. Mater. Chem. A*, 2014, **2**, 2491–2497.

177     T. Y. Yang, H. Y. Kang, U. Sim, Y. J. Lee, J. H. Lee, B. Koo, K. T. Nam and Y. C. Joo, *Phys. Chem. Chem. Phys.*, 2013, **15**, 2117–2124.

178     A. Annamalai, H. H. Lee, S. H. Choi, S. Y. Lee, E. Gracia-Espino, A. Subramanian, J. Park, K. J. Kong and J. S. Jang, *Sci. Rep.*, 2016, **6**, 23183.

179     A. Braun, K. Sivula, D. K. Bora, J. Zhu, L. Zhang, M. Grätzel, J. Guo and E. C. Constable, *J. Phys. Chem. C*, 2012, **116**, 16870–16875.

180     O. Zandi and T. W. Hamann, *Nat. Chem.*, 2016, **8**, 778–783.

181     P. Liao and E. A. Carter, *J. Phys. Chem. C*, 2011, **115**, 20795–20805.

182     R. F. G. Gardner, F. Sweett and D. W. Tanner, *J. Phys. Chem. Solids*, 1963, **24**, 1183–1196.

183     J. H. Kennedy and K. W. Frese, *J. Electrochem. Soc.*, 1978, **125**, 709–714.

184     J. C. Papaioannou, G. S. Patermarakis and H. S. Karayianni, *J. Phys. Chem. Solids*, 2005, **66**, 839–844.

185     R. F. G. Gardner, F. Sweett and D. W. Tanner, *J. Phys. Chem. Solids*, 1963, **24**, 1183–1196.

186     S. R. Pendlebury, X. Wang, F. Le Formal, M. Cornuz, A. Kafizas, S. D. Tilley, M. Grätzel and J. R. Durrant, *J. Am. Chem. Soc.*, 2014, **136**, 9854–9857.

187     B. Klahr, S. Gimenez, F. Fabregat-Santiago, T. Hamann and J. Bisquert, *J. Am. Chem. Soc.*, 2012, **134**, 4294–4302.

188     M. Pyeon, T. P. Ruoko, J. Leduc, Y. Gönüllü, M. Deo, N. V. Tkachenko and S. Mathur, *J. Mater. Res.*, 2018, **33**, 455–466.

189     Y. Hu, F. Boudoire, I. Hermann-Geppert, P. Bogdanoff, G. Tsekouras, B. S. Mun, G. Fortunato, M. Graetzel and A. Braun, *J. Phys. Chem. C*, 2016, **120**, 3250–3258.

190     R. Van de Krol and M. Gratzel, *Photoelectrochemical Hydrogen Production*, Springer, 2012.

191     C. Zhu, C. Li, M. Zheng and J. J. Delaunay, *ACS Appl. Mater. Interfaces*, 2015, **7**, 22355–22363.

192     M. Rioult, D. Stanescu, E. Fonda, A. Barbier and H. Magnan, *J. Phys. Chem. C*, 2016, **120**, 7482–7490.

193     X. Zhang, P. Klaver, R. Van Santen, M. C. M. Van De Sanden and A. Bieberle-Hütter, *J. Phys. Chem. C*, 2016, **120**, 18201–18208.

194     Z. Zhou, P. Huo, L. Guo and O. V. Prezhdo, *J. Phys. Chem. C*, 2015, **119**, 26303–26310.

195     K. D. Malviya, D. Klotz, H. Dotan, D. Shlenkevich, A. Tsyganok, H. Mor and A. Rothschild, *J. Phys. Chem. C*, 2017, **121**, 4206–4213.

196     M. C. Toroker, *J. Phys. Chem. C*, 2014, **118**, 23162–23167.

197     N. Mirbagheri, D. Wang, C. Peng, J. Wang, Q. Huang, C. Fan and E. E. Ferapontova, *ACS Catal.*, 2014, **4**, 2006–2015.

198     R. Franking, L. Li, M. A. Lukowski, F. Meng, Y. Tan, R. J. Hamers and S. Jin, *Energy Environ. Sci.*, 2013, **6**, 500–512.

199     M. Rioult, H. Magnan, D. Stanescu and A. Barbier, *J. Phys. Chem. C*, 2014, **118**, 3007–3014.

200     J. Engel and H. L. Tuller, *Phys. Chem. Chem. Phys.*, 2014, **16**, 11374–11380.

201     M. T. Nguyen, S. Piccinin, N. Seriani and R. Gebauer, *ACS Catal.*, 2015, **5**, 715–721.

202     J. Lee and S. Han, *Phys. Chem. Chem. Phys.*, 2013, **15**, 18906–18914.

203     Y. Ling and Y. Li, *Nano Lett.*, 2011, **11**, 2119–2125.

204     M. Barroso, C. a Mesa, S. R. Pendlebury, A. J. Cowan, T. Hisatomi and K. Sivula, *Pnas*, 2012, **109**, 15640–15645.

205     O. Zandi and T. W. Hamann, *J. Phys. Chem. Lett.*, 2014, **5**, 1522–1526.

206     J. Han, X. Zong, Z. Wang and C. Li, *Phys Chem Chem Phys*, 2014, **16**, 23544–23548.

207     P. Liao, J. A. Keith and E. A. Carter, *J. Am. Chem. Soc.*, 2012, **134**, 13296–13309.

208     P. Liao and E. A. Carter, *J. Appl. Phys.*, 2012, **112**, 1–13.

209     Y. Tong, J. Wu, P. Chen, H. Liu, W. Chu, C. Wu and Y. Xie, *J. Am. Chem. Soc.*, 2018, jacs.8b06108.

210     J. Simfukwe, R. E. Mapasha, A. Braun and M. Diale, *MRS Adv.*, 2018, **3**, 669–678.

211     H. K. Dunn, J. M. Feckl, A. Müller, D. Fattakhova-Rohlfing, S. G. Morehead, J. Roos, L. M. Peter, C. Scheu and T. Bein, *Phys Chem Chem Phys*, 2014, **16**, 24610–24620.

212     O. Zandi and T. W. Hamann, *J. Phys. Chem. Lett.*, 2014, **5**, 1522–1526.

213     A. Kay, D. A. Grave, D. S. Ellis, H. Dotan and A. Rothschild, *ACS Energy Lett.*, 2016, **1**, 827–833.

214     A. Kleiman-Shwarscstein, M. N. Huda, A. Walsh, Y. Yan, G. D. Stuckyst, Y. S. Hu, M. M. Al-Jassim and E. W. McMland, *Chem. Mater.*, 2010, **22**, 510–517.

215     L. Steier, I. Herraiz-Cardona, S. Gimenez, F. Fabregat-Santiago, J. Bisquert, S. D. Tilley and M. Grätzel, *Adv. Funct. Mater.*, 2014, **24**, 7681–7688.

216     W. Clark and P. Broadhead, *J. Phys. C Solid State Phys.*, 1970, **3**, 1047–1054.

217     Z. Zhou, J. Liu, R. Long, L. Li, L. Guo and O. V. Prezhdo, *J. Am. Chem. Soc.*, 2017, **139**, 6707–6717.

218     S. R. Pendlebury, A. J. Cowan, M. Barroso, K. Sivula, J. Ye, M. Grätzel, D. R. Klug, J. Tang and J. R. Durrant, *Energy Environ. Sci.*, 2012, **5**, 6304–6312.

219     Y. Hu, F. Boudoire, I. Hermann-Geppert, P. Bogdanoff, G. Tsekouras, B. S. Mun, G. Fortunato, M. Graetzel and A. Braun, *J. Phys. Chem. C*, 2016, **120**, 3250–3258.

220     A. Bandyopadhyay, J. Velev, W. H. Butler, S. K. Sarker and O. Bengone, *Phys. Rev. B*, 2004, **69**, 174429.

221     I. Cesar, A. Kay, J. A. Gonzalez Martinez and M. Grätzel, *J. Am. Chem. Soc.*, 2006, **128**, 4582–4583.

222     G. S. Parkinson, *Surf. Sci. Rep.*, 2016, **71**, 272–365.

223     L. Xi, S. Y. Chiam, W. F. Mak, P. D. Tran, J. Barber, S. C. J. Loo and L. H. Wong, *Chem Sci*, 2013, **4**, 164–169.

224     W. Cheng, J. He, Z. Sun, Y. Peng, T. Yao, Q. Liu, Y. Jiang, F. Hu, Z. Xie, B. He and S. Wei, *J. Phys. Chem. C*, 2012, **116**, 24060–24067.

225     L. M. Peter, K. G. U. Wijayantha and A. A. Tahir, *Faraday Discuss.*, 2012, **155**, 309–322.

226     N. Yatom, O. Neufeld and M. Caspary Toroker, *J. Phys. Chem. C*, 2015, **119**, 24789–24795.

227     B. M. Hunter, N. B. Thompson, A. M. Müller, G. R. Rossman, M. G. Hill, J. R. Winkler and H. B. Gray, *Joule*, 2018, **2**, 747–763.

228     M. Gratzel, *Nature*, 2001, **414**, 338–344.

229     M. P. Dare-Edwards, J. B. Goodenough, A. Hamnett and P. R. Trevellick, *J. Chem. Soc. Faraday Trans. 1 Phys. Chem. Condens. Phases*, 1983, **79**, 2027.

196     F. Le Formal, S. R. Pendlebury, M. Cornuz, S. D. Tilley, M. Grätzel and J. R. Durrant, *J. Am. Chem. Soc.*, 2014, **136**, 2564-2574.

231     J. Bao, X. Zhang, B. Fan, J. Zhang, M. Zhou, W. Yang, X. Hu, H. Wang, B. Pan and Y. Xie, *Angew. Chem. - Int. Ed.*, 2015, **54**, 7399–7404.

232     T. Hisatomi, F. Le Formal, M. Cornuz, J. Brillet, N. Tétreault, K. Sivula and M. Grätzel, *Energy Environ. Sci.*, 2011, **4**, 2512–2515.

233     M. S. Burke, S. Zou, L. J. Enman, J. E. Kellon, C. A. Gabor, E. Pledger and S. W. Boettcher, *J. Phys. Chem. Lett.*, 2015, **6**, 3737–3742.

234     F. Jiao and H. Frei, *Energy Environ. Sci.*, 2010, **3**, 1018–1027.

235     J. Y. Kim, G. Magesh, D. H. Youn, J. W. Jang, J. Kubota, K. Domen and J. S. Lee, *Sci. Rep.*, 2013, **3**, 1–8.

236     P. Peerakiatkhajohn, J. H. Yun, H. Chen, M. Lyu, T. Butburee and L. Wang, *Adv. Mater.*, 2016, **28**, 6405–6410.

237     K. Sivula, F. Le Formal and M. Grätzel, *ChemSusChem*, 2011, **4**, 432–449.

238     T. H. Jeon, G. Moon, H. Park and W. Choi, *Nano Energy*, 2017, **39**, 211–218.

239     X. Ye, J. Yang, M. Boloor, N. A. Melosh and W. C. Chueh, *J. Mater. Chem. A*, 2015, **3**, 10801–10810.

240     K. Sivula, *J. Phys. Chem. Lett.*, 2015, **6**, 975–976.

241     G. Wang, Y. Ling, D. a. Wheeler, K. E. N. George, K. Horsley, C. Heske, J. Z. Zhang and Y. Li, *Nano Lett.*, 2011, **11**, 3503–3509.

242     S. Shen, J. Zhou, C. L. Dong, Y. Hu, E. N. Tseng, P. Guo, L. Guo and S. S. Mao, *Sci. Rep.*, 2014, **4**, 1–9.

243     K. Sivula, F. L. Formal and M. Gratzel, *Chem. Mater.*, 2009, **21**, 2862–2867.

244     I. Roger, M. A. Shipman and M. D. Symes, *Nat. Rev. Chem.*, 2017, **1**, 0003.

245     N.-T. Suen, S.-F. Hung, Q. Quan, N. Zhang, Y.-J. Xu and H. M. Chen, *Chem Soc Rev*, 2017, **46**, 337–365.

246     Z. W. Seh, J. Kibsgaard, C. F. Dickens, I. Chorkendorff, J. K. Nørskov and T. F. Jaramillo, *Science*, 2017, **355**, eaad4998.

247     L. Cai, J. Zhao, H. Li, J. Park, I. S. Cho, H. S. Han and X. Zheng, *ACS Energy Lett.*, 2016, **1**, 624–632.

248     J. A. Seabold and K. S. Choi, *J. Am. Chem. Soc.*, 2012, **134**, 2186–2192.

249     L. Trotochaud, S. L. Young, J. K. Ranney and S. W. Boettcher, *J. Am. Chem. Soc.*, 2014, **136**, 6744–6753.

250     M. W. Louie and A. T. Bell, *J. Am. Chem. Soc.*, 2013, **135**, 12329–12337.

251    C. Du, X. Yang, M. T. Mayer, H. Hoyt, J. Xie, G. McMahon, G. Bischoping and D. Wang, *Angew. Chem. - Int. Ed.*, 2013, **52**, 12692–12695.

252    M. Bajdich, M. García-Mota, A. Vojvodic, J. K. Nørskov and A. T. Bell, *J. Am. Chem. Soc.*, 2013, **135**, 13521–13530.

253    D. Friebel, M. W. Louie, M. Bajdich, K. E. Sanwald, Y. Cai, A. M. Wise, M. J. Cheng, D. Sokaras, T. C. Weng, R. Alonso-Mori, R. C. Davis, J. R. Bargar, J. K. Nørskov, A. Nilsson and A. T. Bell, *J. Am. Chem. Soc.*, 2015, **137**, 1305–1313.

254    N. Guijarro, M. S. Prévot and K. Sivula, *Phys Chem Chem Phys*, 2015, **17**, 15655–15674.

255    M. R. Nellist, F. A. L. Laskowski, F. Lin, T. J. Mills and S. W. Boettcher, *Acc. Chem. Res.*, 2016, **49**, 733–740.

256    M. G. Ahmed, T. a. Kandiel, A. Y. Ahmed, I. Kretschmer, F. Rashwan and D. Bahnemann, *J. Phys. Chem. C*, 2015, **119**, 5864–5871.

257    A. Y. Ahmed, M. G. Ahmed and T. a. Kandiel, *J. Phys. Chem. C*, 2016, **120**, 23415–23420.

258    A. J. Abel, A. M. Patel, S. Y. Smolin, B. Opasanont and J. B. Baxter, *J Mater Chem A*, 2016, **4**, 6495–6504.

259    F. Malara, A. Minguzzi, M. Marelli, S. Morandi, R. Psaro, V. Dal Santo and A. Naldoni, *ACS Catal.*, 2015, **5**, 5292–5300.

260    J. W. Moir, E. V. Sackville, U. Hintermair and G. A. Ozin, *J. Phys. Chem. C*, 2016, **120**, 12999–13012.

261    L. Wang, N. T. Nguyen and P. Schmuki, *ChemSusChem*, 2016, **9**, 2048–2053.

262    M. Chhetri, S. Dey and C. N. R. Rao, *ACS Energy Lett.*, 2017, **2**, 1062–1069.

263    L. Badia-Bou, E. Mas-Marza, P. Rodenas, E. M. Barea, F. Fabregat-Santiago, S. Gimenez, E. Peris and J. Bisquert, *J. Phys. Chem. C*, 2013, **117**, 3826–3833.

264    Y. B. Hu, C. F. Dong, M. Sun, K. Xiao, P. Zhong and X. G. Li, *Corros. Sci.*, 2011, **53**, 4159–4165.

265    R. Wang, X. Yan, J. Lang, Z. Zheng and P. Zhang, *J. Mater. Chem. A*, 2014, **2**, 12724–12732.

266    F. Lin, B. F. Bachman and S. W. Boettcher, *J. Phys. Chem. Lett.*, 2015, **6**, 2427–2433.

195    K. G. Upul Wijayantha, S. Saremi-Yarahmadi and L. M. Peter, *Phys. Chem. Chem. Phys.*, 2011, **13**, 5264-5270.

268    B. Klahr, S. Gimenez, F. Fabregat-Santiago, J. Bisquert and T. W. Hamann, *Energy Environ. Sci.*, 2012, **5**, 7626–7636.

269    L. M. Peter, L. H. Wong and F. F. Abdi, *J. Electroanal. Chem.*, 2018, **819**, 447–458.

270    L. M. Peter, E. A. Ponomarev and D. J. Fermín, *J. Electroanal. Chem.*, 1997, **427**, 79–96.

271    L. M. Peter, *Chem. Rev.*, 1990, **90**, 753–769.

272    E. A. Ponomarev and L. M. Peter, *J. Electroanal. Chem.*, 1995, **397**, 45–52.

273    D. Tafalla, P. Salvador and R. M. Benito, *J Electrochem Soc*, 1990, **137**, 1810–1815.

274    J. E. Thorne, J.-W. Jang, E. Y. Liu and D. Wang, *Chem Sci*, 2016, **7**, 3347–3354.

275    R. A. Lunt, A. J. Jackson and A. Walsh, *Chem. Phys. Lett.*, 2013, **586**, 67–69.

276    M. Grundmann, *The physics of semiconductors: An introduction including devices and nanophysics*, 2006.

277    L. Liardet, J. E. Katz, J. Luo, M. Grätzel and X. Hu, *J. Mater. Chem. A*, 2019, **7**, 6012–6020.

278    C. Y. Cummings, F. Marken, L. M. Peter, A. A. Tahir and K. G. U. Wijayantha, *Chem. Commun.*, 2012, **48**, 2027–2029.

279    R. M. Cornell and P. W. Schindler, *Colloid Polym. Sci.*, 1980, **258**, 1171–1175.

280    T. Ishikawa, S. Kataoka and K. Kandori, *J. Mater. Sci.*, 1993, **28**, 2693–2698.

281    *BP Statistical Review of World Energy 2017, 66th ed.; British Petroleum: 2017,* .

282    E. L. Miller, *Energy Environ. Sci.*, 2015, **8**, 2809–2810.

283    Z. Shi, X. Wen, Z. Guan, D. Cao, W. Luo and Z. Zou, *Ann. Phys.*, 2015, **358**, 236–247.

284    J. Joy, J. Mathew and S. C. George, *Int. J. Hydrog. Energy*, 2018, **43**, 4804–4817.

285    Y. Lin, G. Yuan, S. Sheehan, S. Zhou and D. Wang, *Energy Environ. Sci.*, 2011, **4**, 4862.

286    D. K. Bora, A. Braun and E. C. Constable, *Energy Env. Sci*, 2013, **6**, 407–425.

287    K. Itoh, *J. Electrochem. Soc.*, 1984, **131**, 1266.

288    M. Mishra and D.-M. Chun, *Appl. Catal. Gen.*, 2015, **498**, 126–141.

289    Y. Li, N. Guijarro, X. Zhang, M. S. Prévot, X. A. Jeanbourquin, K. Sivula, H. Chen and Y. Li, *ACS Appl. Mater. Interfaces*, 2015, **7**, 16999–17007.

290    D. Barreca, G. Carraro, A. Gasparotto, C. Maccato, M. E. A. Warwick, K. Kaunisto, C. Sada, S. Turner, Y. Gönüllü, T.-P. Ruoko, L. Borgese, E. Bontempi, G. Van Tendeloo, H. Lemmetyinen and S. Mathur, *Adv. Mater. Interfaces*, 2015, **2**, 1500313.

291    G. Carraro, C. Maccato, A. Gasparotto, M. E. A. Warwick, C. Sada, S. Turner, A. Bazzo, T. Andreu, O. Pliekhova, D. Korte, U. Lavrenčič Štangar, G. Van Tendeloo, J. R. Morante and D. Barreca, *Sol. Energy Mater. Sol. Cells*, 2017, **159**, 456–466.

292    A. P. Singh, N. Saini, B. R. Mehta, G. Carraro and D. Barreca, *J. Nanosci. Nanotechnol.*, 2017, **17**, 8959–8966.

293    K. Sivula, F. Le Formal and M. Grätzel, *ChemSusChem*, 2011, **4**, 432.

294    D. K. Zhong, M. Cornuz, K. Sivula, M. Grätzel and D. R. Gamelin, *Energy Environ. Sci.*, 2011, **4**, 1759.

295    Y. Qiu, S.-F. Leung, Q. Zhang, B. Hua, Q. Lin, Z. Wei, K.-H. Tsui, Y. Zhang, S. Yang and Z. Fan, *Nano Lett.*, 2014, **14**, 2123–2129.

296    J. Yang, D. Wang, H. Han and C. Li, *Acc. Chem. Res.*, 2013, **46**, 1900–1909.

297    M. Hesari, X. Mao and P. Chen, *J. Am. Chem. Soc.*, 2018, **140**, 6729–6740.

298    M. E. A. Warwick, D. Barreca, E. Bontempi, G. Carraro, A. Gasparotto, C. Maccato, K. Kaunisto, T.-P. Ruoko, H. Lemmetyinen, C. Sada, Y. Gönüllü and S. Mathur, *Phys. Chem. Chem. Phys.*, 2015, **17**, 12899–12907.

299    J. Zhang, R. García-Rodríguez, P. Cameron and S. Eslava, *Energy Environ. Sci.*, 2018, **11**, 2972–2984.

300    J. G. McAlpin, Y. Surendranath, M. Dincă, T. A. Stich, S. A. Stoian, W. H. Casey, D. G. Nocera and R. D. Britt, *J. Am. Chem. Soc.*, 2010, **132**, 6882–6883.

301    C. T. Bowmer, R. N. Hooftman, A. O. Hanstveit, P. W. M. Venderbosch and N. van der Hoeven, *Chemosphere*, 1998, **37**, 1317–1333.

302    C. Blanco-Andujar, D. Ortega, Q. A. Pankhurst and N. T. K. Thanh, *J. Mater. Chem.*, 2012, **22**, 12498.

303    M. S. Park, D. Walsh, J. Zhang, J. H. Kim and S. Eslava, *J. Power Sources*, 2018, **404**, 149–158.

304    A. J. Bard and L. R. Faulkner, *Electrochemical Method: Fundamentals and Applications*, John Wiley and Sons, New York, 2nd Edition., 2001.

305     B. K. Kang, G. S. Han, J. H. Baek, D. G. Lee, Y. H. Song, S. B. Kwon, I. S. Cho, H. S. Jung and D. H. Yoon, *Adv. Mater. Interfaces*, 2017, **4**, 1700323.

306     Y. Duan, S. Zhou, Z. Chen, J. Luo, M. Zhang, F. Wang, T. Xu and C. Wang, *Catal. Sci. Technol.*, 2018, **8**, 1395–1403.

307     M. Regue, K. Armstrong, D. Walsh, E. Richards, A. L. Johnson and S. Eslava, *Sustain. Energy Fuels*, 2018, **2**, 2674–2686.

308     H. Dotan, K. Sivula, M. Gratzel, A. Rothschild and S. C. Warren, *Energy Environ. Sci.*, 2011, **4**, 958.

309     C. R. Lhermitte, J. Garret Verwer and B. M. Bartlett, *J. Mater. Chem. A*, 2016, **4**, 2960–2968.

310     H. Jia, J. Stark, L. Q. Zhou, C. Ling, T. Sekito and Z. Markin, *RSC Adv.*, 2012, **2**, 10874.

311     W. Littmann, in *Developments in Petroleum Science*, Elsevier, 1988, vol. 24, pp. 204–205.

312     L. A. Thomas, L. Dekker, M. Kallumadil, P. Southern, M. Wilson, S. P. Nair, Q. A. Pankhurst and I. P. Parkin, *J. Mater. Chem.*, 2009, **19**, 6529.

313     S. Palanikumar, L. Kannammal, B. Meenarathi and R. Anbarasan, *Int. Nano Lett.*, , DOI:10.1007/s40089-014-0104-9.

314     F. Xiao, W. Li, L. Fang and D. Wang, *J. Hazard. Mater.*, 2016, **308**, 11–20.

315     M. Hanesch, *Geophys. J. Int.*, 2009, **177**, 941–948.

316     D. L. A. de Faria and F. N. Lopes, *Vib. Spectrosc.*, 2007, **45**, 117–121.

317     D. Santos-Carballal, Z. Du, H. E. King and N. H. de Leeuw, *RSC Adv.*, 2016, **6**, 91893–91903.

318     B. Lafuente, R. T. Downs, H. Yang and N. Stone, in *Highlights in Mineralogical Crystallography*, eds. T. Armbruster and R. M. Danisi, DE GRUYTER, Berlin, München, Boston, 2015, pp. 1–30.

319     S. Kment, P. Schmuki, Z. Hubicka, L. Machala, R. Kirchgeorg, N. Liu, L. Wang, K. Lee, J. Olejnicek, M. Cada, I. Gregora and R. Zboril, *ACS Nano*, 2015, **9**, 7113–7123.

320     X. Zhang, C. Cao and A. Bieberle-Hütter, *J. Phys. Chem. C*, 2016, **120**, 28694–28700.

321     J. Deng, X. Lv, J. Gao, A. Pu, M. Li, X. Sun and J. Zhong, *Energy Environ. Sci.*, 2013, **6**, 1965.

322     N. S. McIntyre and D. G. Zetaruk, *Anal. Chem.*, 1977, **49**, 1521–1529.

323     J. M. Cerrato, M. F. Hochella, W. R. Knocke, A. M. Dietrich and T. F. Cromer, *Environ. Sci. Technol.*, 2010, **44**, 5881–5886.

324     J. Su, J. Wang, C. Liu, B. Feng, Y. Chen and L. Guo, *RSC Adv.*, 2016, **6**, 101745–101751.

325     C. Vaalma, D. Buchholz, M. Weil and S. Passerini, *Nat. Rev. Mater.*, 2018, **3**, 18013.

326     O. S. Hammond, S. Eslava, A. J. Smith, J. Zhang and K. J. Edler, *J Mater Chem A*, 2017, **5**, 16189–16199.

327     J. Xie, W. Liu, J. Xin, F. Lei, L. Gao, H. Qu, X. Zhang and Y. Xie, *ChemSusChem*, 2017, **10**, 4465–4471.

328     J. Tauc, R. Grigorovici and A. Vancu, *Phys. Status Solidi B*, 1966, **15**, 627–637.

329     H. Wang and J. A. Turner, *J. Electrochem. Soc.*, 2010, **157**, F173.

330     J. Li and L. M. Peter, *J. Electroanal. Chem. Interfacial Electrochem.*, 1986, **199**, 1–26.

331     Y. Gao and T. W. Hamann, *Chem. Commun.*, 2017, **53**, 1285–1288.

332    X. Liu, F. Wang and Q. Wang, *Phys. Chem. Chem. Phys.*, 2012, **14**, 7894–7911.

333    E. Lassner and W.-D. Schubert, *Tungsten: properties, chemistry, technology of the element, alloys, and chemical compounds*, Kluwer Academic/Plenum Publishers, New York, 1999.

334    C. Santato, M. Ulmann and J. Augustynski, *J. Phys. Chem. B*, 2001, **105**, 936–940.

335    C. Santato, M. Odziemkowski, M. Ulmann and J. Augustynski, *J. Am. Chem. Soc.*, 2001, **123**, 10639–10649.

336    W. Lee, D. Kim, K. Lee, P. Roy and P. Schmuki, *Electrochimica Acta*, 2010, **56**, 828–833.

337    P. Dias, T. Lopes, L. Meda, L. Andrade and A. Mendes, *Phys. Chem. Chem. Phys.*, 2016, **18**, 5232–5243.

338    V. Chakrapani, J. Thangala and M. K. Sunkara, *Int. J. Hydrog. Energy*, 2009, **34**, 9050–9059.

339    X. Zhang, X. Lu, Y. Shen, J. Han, L. Yuan, L. Gong, Z. Xu, X. Bai, M. Wei, Y. Tong, Y. Gao, J. Chen, J. Zhou and Z. L. Wang, *Chem. Commun. Camb. Engl.*, 2011, **47**, 5804–5806.

340    H. Zheng, A. Z. Sadek, K. Latham and K. Kalantar-Zadeh, *Electrochem. Commun.*, 2009, **11**, 768–771.

341    C. Fàbrega, S. Murcia-López, D. Monllor-Satoca, J. D. Prades, M. D. Hernández-Alonso, G. Penelas, J. R. Morante and T. Andreu, *Appl. Catal. B Environ.*, 2016, **189**, 133–140.

342    F. Amano, M. Tian, G. Wu, B. Ohtani and A. Chen, *ACS Appl. Mater. Interfaces*, 2011, **3**, 4047–4052.

343    B. Yang and V. Luca, *Chem. Commun.*, 2008, **0**, 4454–4456.

344    J. K. Kim, K. Shin, S. M. Cho, T.-W. Lee and J. H. Park, *Energy Environ. Sci.*, 2011, **4**, 1465–1470.

345    T. Zhu, M. N. Chong and E. S. Chan, *ChemSusChem*, 2014, **7**, 2974–2997.

346    L. E. Fraga and M. V. B. Zanoni, *J. Braz. Chem. Soc.*, 2011, **22**, 718–725.

347    Y.-C. Nah, I. Paramasivam, R. Hahn, N. K. Shrestha and P. Schmuki, *Nanotechnology*, 2010, **21**, 105704.

348    N. Mukherjee, M. Paulose, O. K. Varghese, G. K. Mor and C. A. Grimes, *J. Mater. Res.*, 2003, **18**, 2296–2299.

349    R. Hahn, J. M. Macak and P. Schmuki, *Electrochem. Commun.*, 2007, **9**, 947–952.

350    G. D. Sulka, in *Nanostructured Materials in Electrochemistry*, ed. A. Eftekhari, Wiley-VCH Verlag GmbH & Co. KGaA, Weinheim, Germany, 2008, pp. 1–116.

351    A. Mao, G. Y. Han and J. H. Park, *J. Mater. Chem.*, 2010, **20**, 2247–2250.

352    J. Hu, M. Noked, E. Gillette, F. Han, Z. Gui, C. Wang and S. B. Lee, *J. Mater. Chem. A*, 2015, **3**, 21501–21510.

353    Y. Liu, Y. Li, W. Li, S. Han and C. Liu, *Appl. Surf. Sci.*, 2012, **258**, 5038–5045.

354    J. Lin, P. Hu, Y. Zhang, M. Fan, Z. He, C. K. Ngaw, J. S. C. Loo, D. Liao and T. T. Y. Tan, *RSC Adv.*, 2013, **3**, 9330.

355    J. Ding and K. Kim, *J. Nanosci. Nanotechnol.*, 2016, **16**, 1578.

356    J. Su, X. Feng, J. D. Sloppy, L. Guo and C. A. Grimes, *Nano Lett.*, 2011, **11**, 203.

357    D. Qin, C. Tao, S. A. Friesen, T. Wang, O. K. Varghese, N. Bao, Z. Yang, T. E. Mallouk and C. A. Grimes, *Chem. Commun.*, 2012, **48**, 729.

358    Y. Hou, F. Zuo, A. P. Dagg, J. Liu and P. Feng, *Adv. Mater.*, 2014, **26**, 5043.

359    A. Watcharenwong, W. Chanmanee, N. R. de Tacconi, C. R. Chenthamarakshan, P. Kajitvichyanukul and K. Rajeshwar, *J. Electroanal. Chem.*, 2008, **612**, 112.

360    A. Tacca, L. Meda, G. Marra, A. Savoini, S. Caramori, V. Cristino, C. A. Bignozzi, V. Gonzalez Pedro, P. P. Boix, S. Gimenez and J. Bisquert, *Chemphyschem Eur. J. Chem. Phys. Phys. Chem.*, 2012, **13**, 3025.

361    N. R. De Tacconi, C. R. Chenthamarakshan, G. Yogeeswaran, A. Watcharenwong, R. S. De Zoysa, N. A. Basit and K. Rajeshwar, *J. Phys. Chem. B*, 2006, **110**, 25347.

362    Q. Liu, Q. Chen, J. Bai, J. Li, J. Li and B. Zhou, *J. Solid State Electrochem.*, 2014, **18**, 157.

363    W. Wei, S. Shaw, K. Lee and P. Schmuki, *Chem. - Eur. J.*, 2012, **18**, 14622.

364    K. Kirimura, Y. Honda and T. Hattori, *Compr. Biotechnol.*, 2011, **3**, 135.

365    Q. Han, X. Wu, Y. Liao, D. Li, R. Yue, H. Liu and Y. Chen, *Mater. Lett.*, 2013, **95**, 9.

366    A. E. Danks, S. R. Hall and Z. Schnepp, *Mater Horiz*, 2016, **3**, 91.

367    S. Trasatti and O. A. Petrii, *Pure Appl Chem*, 1991, **63**, 711.

368    V. Cristino, S. Caramori, R. Argazzi, L. Meda, G. L. Marra and C. A. Bignozzi, *Langmuir*, 2011, **27**, 7276.

369    M. Paulose, K. Shankar, S. Yoriya, H. E. Prakasam, O. K. Varghese, G. K. Mor, T. A. Latempa, A. Fitzgerald and C. A. Grimes, *J. Phys. Chem. B*, 2006, **110**, 16179.

370    Y. Chai, C. W. Tam, K. P. Beh, F. K. Yam and Z. Hassan, *J. Porous Mater.*, 2013, **20**, 997.

371    H. Qi, J. Wolfe, D. Wang, H. J. Fan, D. Fichou and Z. Chen, *Nanoscale*, 2014, **6**, 13457.

372    S. S. Kalanur, Y. J. Hwang, S. Y. Chae and O. S. Joo, *J. Mater. Chem. A*, 2013, **1**, 3479.

373    T. W. Kim and K. S. Choi, *J. Phys. Chem. Lett.*, 2016, **7**, 447.

374    D. Bae, B. Seger, P. C. K. Vesborg, O. Hansen and I. Chorkendorff, *Chem. Soc. Rev.*, 2017, **46**, 1933.

375    C. Y. Ng, K. Abdul Razak and Z. Lockman, *J. Porous Mater.*, 2015, **22**, 537.

376    M. Altomare, O. Pfoch, A. Tighineanu, R. Kirchgeorg, K. Lee, E. Selli and P. Schmuki, *J. Am. Chem. Soc.*, 2015, **137**, 5646.

377    W. Q. Fang, X. L. Wang, H. Zhang, Y. Jia, Z. Huo, Z. Li, H. Zhao, H. G. Yang and X. Yao, *J. Mater. Chem. A*, 2014, **2**, 3513.

378    J. Zhao, E. Olide and F. E. Osterloh, *J. Electrochem. Soc.*, 2015, **162**, H65–H71.

379    G. Wang, Y. Ling, H. Wang, X. Yang, C. Wang, J. Z. Zhang and Y. Li, *Energy Environ. Sci.*, 2012, **5**, 6180–6187.

380    C. B. Pollard and D. C. Young, *J. Org. Chem.*, 1951, **16**, 661–672.

381    B. S. Kalanoor, H. Seo and S. S. Kalanur, *Mater. Sci. Energy Technol.*, 2018, **1**, 49–62.

382    P. Chatchai, S. Kishioka, Y. Murakami, A. Y. Nosaka and Y. Nosaka, *Electrochimica Acta*, 2010, **55**, 592–596.

383    P. Chatchai, Y. Murakami, S. Kishioka, A. Y. Nosaka and Y. Nosaka, *Electrochimica Acta*, 2009, **54**, 1147–1152.

384    S. K. Pilli, R. Janarthanan, T. G. Deutsch, T. E. Furtak, L. D. Brown, J. A. Turner and A. M. Herring, *Phys. Chem. Chem. Phys.*, 2013, **15**, 14723–14728.

385    X. Shi, I. Herraiz-Cardona, L. Bertoluzzi, P. Lopez-Varo, J. Bisquert, J. H. Park and S. Gimenez, *Phys. Chem. Chem. Phys.*, 2016, **18**, 9255–9261.